

OUT-OF-PLANE FIBER WAVINESS IN COMPOSITE MATERIALS:
ORIGINS, DETECTION AND MECHANICAL EVALUATION

DISSERTATION

zur Erlangung des akademischen Grades

Dr.-Ing.

eingereicht an der

Mathematisch-Naturwissenschaftlich-Technischen Fakultät

der Universität Augsburg

von

Michael Thor

Augsburg, April 2021



Erstgutachter: Prof. Dr. habil. Markus Sause

Zweitgutachter: Prof. Dr.-Ing. Michael Kupke

Tag der mündlichen Prüfung: 5. August 2021

*Many thanks to Prof. Dr. habil. Markus Sause and
FH-Prof. DI Dr. techn. Roland Hinterhölzl for providing guidance, feedback, and patience
throughout this project. I would also like to thank Prof. Dr.-Ing. Michael Kupke for serving as
second reviewer.*

*A big thank you to my wife, Sabine, who has had my back during this time so I could focus on
work.*

TABLE OF CONTENT

1. Introduction.....	1
1.1. Definition of terms	2
1.2. Parameters.....	3
1.3. Non-destructive detection of out-of-plane fiber waviness	4
1.4. Mechanical response of wavy composites	7
1.5. Objectives and research questions.....	8
1.6. Outline of the thesis.....	9
1.7. Notation convention.....	10
2. Occurrence of fiber waviness.....	11
2.1. Mechanical loading and behavior of dry and impregnated fiber reinforcements.....	11
2.1.1. Basic material behavior.....	11
2.1.2. Mechanical deformation of layers due to manual handling of preforms, moving sliders and closing tools.....	13
2.2. Path length differences.....	13
2.2.1. Micro/meso scale deformation at the material level.....	13
2.2.2. Global deformation on structural level at double curved and joggled geometries.....	13
2.2.3. Steering.....	17
2.2.4. Consolidation in corner areas, external radii, stepped or tapered laminates	20
2.3. Non-uniform pressure distribution.....	24
2.3.1. Co-bonding (or pre-cured parts in LCM process)	24
2.3.2. Telegraphing effect of face sheets at honeycomb core	24
2.3.3. Welding spots.....	25
2.3.4. Ply and vacuum bag bridging	26
2.4. Interaction between tool-ply and ply-ply.....	27
2.4.1. Inter-ply slippage.....	27
2.4.2. CTE mismatch	29
2.5. Lay-up sequence	30

2.5.1.	Gaps and overlaps.....	30
2.5.2.	Ply drops in tapered laminates	31
2.6.	Textile architecture	32
2.6.1.	Inherent undulations in woven and braided fabrics	32
2.6.2.	Shear locking angle of woven fabrics.....	32
2.6.3.	Stitches in non-crimped fabrics.....	34
2.6.4.	Stitches in dry fiber placements	35
2.7.	Foreign objects	36
2.7.1.	Intended foreign objects (e.g. optical sensors, pins, inserts).....	36
2.7.2.	Unintended foreign objects (e.g. foils, blades, etc.).....	37
2.8.	Flow induced waviness	37
2.8.1.	Fiber wash-out.....	37
2.8.2.	Hydraulic effects (squeezing, transverse flow)	38
2.9.	Cure induced waviness	38
2.9.1.	Volumetric shrinkage	39
2.9.2.	Large temperature gradient in thick laminates	39
2.10.	Unique characteristics of fabrication processes	40
2.10.1.	Filament winding	40
2.10.2.	Pultrusion	41
3.	Classification scheme.....	42
3.1.	Number and distribution of waves.....	42
3.2.	Traditional differentiation of wave types – constant or changing wave amplitude	42
3.3.	Phase characteristics of the wave form	43
3.4.	Visibility.....	44
3.5.	Dimensional characteristics	44
3.6.	Continuity of layers/laminate	45
3.7.	Portion and position of the wavy region in the laminate.....	45
3.8.	Phase characteristics of the material.....	46
3.9.	Influence of t/A ratio	46
3.10.	Geometric position of the wavy region in the part	47

3.11. Examples for waviness classification	48
4. Non-destructive testing	49
4.1. Experimental non-destructive testing	49
4.1.1. Test plate fabrication	49
4.1.2. Optical microscopy on polished samples	51
4.1.3. X-ray computed tomography (CT)	51
4.1.3.1. Talbot-Lau grating interferometer CT (TLGI-CT).....	52
4.1.4. Ultrasonic testing (UT).....	53
4.1.4.1. Ultrasonic microscopy.....	53
4.1.4.2. Pulse-echo and through-transmission inspection	53
4.1.5. Infrared thermography (IRT).....	55
4.1.6. Digital shearography.....	59
4.1.7. Eddy current testing (ET)	62
4.1.8. Results and discussion	64
4.1.8.1. Optical microscopy on polished samples.....	64
4.1.8.2. X-ray computed tomography (CT).....	65
4.1.8.3. Ultrasonic testing (UT)	66
4.1.8.4. Infrared thermography (IRT)	68
4.1.8.5. Digital shearography	74
4.1.8.6. Eddy current testing (ET).....	76
4.1.8.7. Comparison of test methods	78
4.2. Finite element analysis of NDT methods	84
4.2.1. General modelling	84
4.2.2. Infrared thermography (heat transfer)	85
4.2.3. Digital shearography (deformation).....	85
4.2.4. Results	85
4.2.4.1. Infrared thermography (heat transfer)	85
4.2.4.2. Digital shearography (deformation)	89
4.3. Conclusion on the non-destructive testing of wrinkles in composites	90
5. Mechanical testing	92
5.1. Experiments under room temperature and dry conditions.....	92
5.1.1. Experimental methods and test set-ups	92

5.1.1.1.	Specimen preparation	92
5.1.1.2.	Tensile and compression testing	93
5.1.1.3.	Digital image correlation.....	94
5.1.1.4.	Passive infrared thermography	95
5.1.1.5.	Acoustic emission.....	96
5.1.2.	Results and discussion	98
5.1.2.1.	Mechanical behavior of planar reference and wavy specimen	98
5.1.2.2.	Passive thermography	105
5.1.2.3.	Acoustic emission.....	109
5.1.3.	Assessment of test methods.....	112
5.2.	Influence of hot-wet conditioning.....	113
5.2.1.	Environmental influences on composite materials	113
5.2.2.	Experimental methods and test set-ups.....	114
5.2.2.1.	Specimen preparation	114
5.2.2.2.	Tensile and compression testing	115
5.2.2.3.	Thermal and thermo-mechanical analysis.....	116
5.2.2.4.	Scanning electron microscope	116
5.2.3.	Results and discussion	117
5.2.3.1.	Moisture absorption.....	117
5.2.3.2.	Mechanical behavior of planar specimens with matrix dominated properties	119
5.2.3.3.	Mechanical behavior of both unaged and hot-wet conditioned planar and wavy specimens.....	121
5.3.	Conclusions on mechanical testing and the influence of hot-wet conditioning 127	
6.	Assessment strategies in engineering practice	129
6.1.	Challenges in assessing fiber waviness.....	129
6.2.	Knockdown factor (KDF)	129
6.3.	Simulation based approaches	131
6.3.1.	Simplified simulations.....	131
6.3.2.	Numerical and experimental assessment on sub-component level	131
7.	Analytical modelling.....	133

7.1.	Effective elastic properties	133
7.2.	Local stresses and strains	140
7.3.	Local elastic properties	142
7.4.	Damage initiation	143
7.5.	Validation of analytical results	144
7.6.	Comparison with experimental results	147
7.7.	Conclusions on the analytical model	152
8.	Numerical simulation	154
8.1.	Constitutive material behavior	154
8.1.1.	Non-linearity in the elasto-plastic hardening regime	155
8.2.	Continuum damage model	157
8.2.1.	Damage variables	157
8.2.2.	Damage initiation	160
8.2.3.	Damage evolution law	161
8.2.4.	Energy consideration and element size regularization	162
8.3.	Finite element model	166
8.4.	Results and discussion	168
8.4.1.	Model validation	168
8.4.2.	Virtual testing	172
8.5.	Conclusion on the numerical simulation	174
9.	Summary and conclusions	176
10.	Outlook	181
	References	182

1. INTRODUCTION

Out-of-plane fiber waviness, also referred to as wrinkling, is considered one of the most significant effects that occur in composite materials. It significantly affects mechanical properties, such as stiffness, strength and fatigue and, therefore, dramatically reduces the load carrying capacity of the material. Fiber waviness is inherent to various manufacturing processes of fiber-reinforced composite parts. They cannot be completely avoided and thus have to be tolerated and considered as an integral part of the structure. Because of this influenceable but in many cases unavoidable nature of fiber waviness, it might be more appropriate to consider fiber waviness as effects or features rather than defects. Hence, it is important to understand the impact of different process parameters on the formation of fiber waviness in order to reduce or, in the best case, completely avoid them as early as possible in the product and process development phases. Mostly depending on the chosen geometry of the part and the specific manufacturing process used, different types of fiber waviness result.

Fiber-reinforced composite materials allow for a significant mass reduction due to the comparably low density (c.f. 4-5 times less than steel) and, in addition, fibers can be aligned in accordance with the load paths. This possibility of alignment allows the fibers to be placed at the exact position where they are needed to provide the component with the required stiffness and strength. However, this can lead to a load path-optimized composite structure, which is not necessarily easy to produce and free of defects. The placement of the fibers or semi-finished textile products is still often carried out by hand-lay-up, especially in the aviation industry. This allows a diverse draping of the unidirectional (UD) layers, woven textiles or non-crimped fabrics (NCF) onto the production tool. However, manufacturing effects such as fiber waviness, porosity, delamination and distortion cannot be completely avoided. The increased demand for composite components and their production process stability for the aviation and automotive industries requires a transition to at least partially automated manufacturing processes. Those systems come with a higher deposition rate and ensure reproducible quality, but also imply production effects, e.g. fiber waviness [1,2]. This necessitates a sophisticated understanding of those implicit effects on the mechanical properties of the manufactured structure.

The decision as to whether these unwanted irregularities are considered as manufacturing features (effects), or as defects, depends on the size, number and location in the component. Those allowance limits depend on the strength and stiffness reserve at the location of the feature, as well as on functional requirements, e.g. water tightness. The assessment of manufacturing effects further depends on the industry. In the aviation industry, the allowance limits for defects are very restricted, while in the automotive industry the need for short cycle times leads to a trade-off between robust processes and tolerated manufacturing imperfections. To this point, there is still

1.1 DEFINITION OF TERMS

no generally accepted approach to quantitatively support accept/reject/repair-decisions and make a consistent assessment of wavy layers in composites. If the effect is termed to be a defect, typically a deviation from design must be requested in the aviation industry and an individual decision must be made on "use as is", repair or reject entirely. In some cases, experiments on representative test samples are performed at the subcomponent-level on a statistical basis. However, this is both time consuming and cost intensive. It is necessary to strive for a fiber-oriented and in particular a manufacturing-oriented design and construction of composite components. Towards this goal, design and production engineers aim to expand the permissible margin of safety by assessing the effect on stiffness and strength of those production effects, i.e. fiber waviness, porosity, delamination etc. Additionally, they aim to reduce or, in the best case, avoid them on the process side, increasingly with the help of finite element based process simulations, such as in [3–5].

1.1. Definition of terms

There is no universally accepted terminology and consistent use for the differentiation between waves, wrinkles, folds, undulations and misalignments (Figure 1). Definitions of these terms are given below for the sake of clarity. Ply/Fiber waviness or wrinkling is a commonly observed manufacturing effect in composite parts resulting in decreased mechanical performances. Fiber waviness is denoted as a wave-formed ply and/or fiber deviation from a straight alignment in a unidirectional laminate. This may arise as an undesirable manufacturing effect that commonly occurs during draping, infiltration and/or consolidation/curing process steps. Sometimes these waves are also referred to as marcells. If the out-of-plane fiber waviness occurs due to stability issues when the ply is loaded under compression, it is also referred to as buckles or fiber buckling.

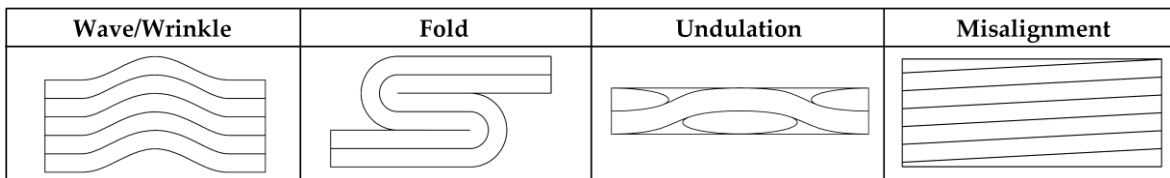


Figure 1. General definition of deviations from a straight fiber orientation, i.e. wave/wrinkle, fold, undulation and misalignment.

Wavy plies can appear in arbitrary shapes and locations and can principally be classified into in-plane and out-of-plane waves, whereas Nelson et al. [6] stated, that both show similar strength degradations. This thesis aims to investigate out-of-plane waviness because of its more frequent occurrence compared to in-plane waviness. In this work, folds are considered as a special type of waviness with a maximum deviation of the fiber misalignment where a layer comes into contact with itself. Undulations are considered to be small-sized fiber misalignments at the mesoscopic

level in the form of waves inherent to various preform manufacturing processes, such as woven textiles where fibers are undulated between warp and weft directions. Due to the undulations, woven fabrics show a systematically lower stiffness and different damage behavior compared to UD layers. This influence has been intensely investigated by [7–10]. Fiber misalignment is the general description for the angular deviation of nominal, intended fiber directions and therefore not corresponding to the designed fiber path. Misaligned fibers remain straight compared to curved fibers in waves, wrinkles or undulations. Nevertheless, in many publications the term fiber misalignment is used as an umbrella term including waves, wrinkles and undulations.

1.2. Parameters

In general, the shape of fiber waviness is described by the ratio of amplitude to wavelength. Davidson and Waas [11] introduced 6 parameters to characterize the wave, indirectly including the laminate thickness. While amplitude A and wavelength L are most commonly used to describe the wave (Figure 2), the maximum deviation θ_{\max} is considered to have the greatest impact on the mechanical properties. Important influencing parameters such as maximum deviation of the fiber orientation from the original orientation, as well as the laminate thickness [12], have received little attention in previous investigations. The wave pattern is typically represented mathematically as sinusoidal waves [13,14]. El-Hajjar and Petersen [15] used a Gaussian function to capture the bell curve of wavy plies, which was found to better represent the wave geometry. Nevertheless, there are a few more parameters, which can influence the mechanical behavior, and have to be considered. Results in [16] show that the position of wavy layers in the cross-section of a laminate also has a significant influence on the strength reduction. A more outward position of wavy layer leads to a greater decrease in strength, since the layers on the edge of the laminate are supported only one-sided and therefore fail earlier.

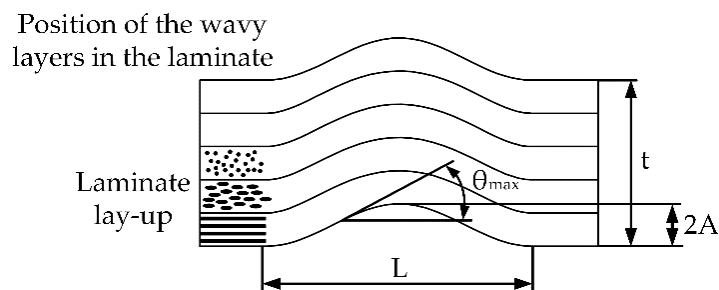


Figure 2. Parameters influencing the mechanical properties, e.g. amplitude A , wavelength L , laminate thickness t , maximum fiber misalignment angle θ_{\max} , layup and the position of wavy layers within the laminate.

1.3. Non-destructive detection of out-of-plane fiber waviness

Along the value chain of carbon fiber reinforced polymer (CFRP) products many different physical testing methods are successfully applied for the detection of flaws in composite materials [17]. The early detection of manufacturing effects such as out-of-plane fiber waviness is of great importance for the production in order to reduce rejects and for the stress department which needs an exact representation of the manufacturing effect in order to conduct further mechanical analysis. The possibilities of online and in-situ process monitoring to detect manufacturing effects in the CFRP manufacturing process are manifold. Völtzer [18] used an infrared camera for monitoring the automated fiber placement (AFP) process which tends to cause gaps and overlaps, which in turn leads to fiber waviness. Berger *et al.* [19] used eddy current sensors for process integrated inspection of the preforming of the semi-finished fiber materials for resin transfer molding (RTM) processes. By entering the measured values in a common coordinate system, a histogram can be generated that provides information about the impedance changes as a function of depth and thus about the fiber direction of the CFRP layup. However, an in-depth comparison of different NDT methods applied on the same fiber waviness is not investigated explicit in current literature.

Optical microscopy on polished samples was used by Sutcliffe *et al.* [20] to determine the fiber orientation using an image analysis technique. Joyce *et al.* [21] used optical microscopy for the characterization of localized fiber waviness in composite materials. In general, optical microscopy is a time-consuming and destructive method which is used as a reference method in this study.

In addition to optical microscopy, **X-ray computed tomography (CT)** is regarded as a reference in terms of the detectability of fiber waviness. CT images offer a high level of detail down to the resolution of individual fibers that cannot be achieved with any other NDT technique so far. When using robot-based CT methods [22], which are under continuous development, large components of > 3 m can also be investigated, especially at neuralgic and structurally critical regions of the part. The application of CT for the investigation of fiber orientations in a laminate have been shown in various studies [23,24].

Ultrasonic testing [25] represents the standard NDT method used for the inspection of aircraft components and serves as a baseline for comparing other methods. Ultrasonic inspection using traditional approaches has great difficulties in identifying waviness due to dependency on impedance changes in the material [26]. When an ultrasonic wave meets a discontinuity inside a component, as can be the case with interfaces between plies of different orientation, scattering occurs. This scattered field carries information about the shape, orientation and size of the discontinuity. Fiber waviness can often appear to be porosity as both defects cause diffuse scatter and cause close similarity of the ultrasonic signal [27,28]. Pain and Drinkwater [28] used an ultrasonic array for both imaging the composite material and extract information

that characterizes the scattering of the interior structure. The scattering information is encoded in the scattering matrix (or S-matrix). It is defined as a matrix containing all far-field amplitudes of the scattered signals from a defect as a function of the incidence and scattering angle. This proof of principle study using an ultrasonic array based scattering matrix shows potential for the detection and quantification of small-scale out-of-plane fiber waviness in carbon fiber composite components. James *et al.* [29] carried out ultrasonic tests on test plates containing embedded out-of-plane fiber waviness which were accompanied by eddy current tests. For some test specimens the results from ultrasonic testing using a 10 MHz, 1" focused, 0.375" diameter transducer show a good detectability of the fiber waviness in C-scans and also a clear indication of the wave characteristics in the B-scan. For others, the ultrasonic signals do not indicate fiber waviness whereas eddy current method was able to detect the flaw. In general, waviness originating from embedded foreign materials or resin accumulations are easier to detect, e.g. shown in [30]. Smith *et al.* [31] have shown the possibility for obtaining a quantitative map of 3D fiber orientations in test plates containing in-plane and out-of-plane fiber waviness from ultrasonic test data. Based on this work, Nelson and Smith [32] applied additional promising methods to extract the fiber orientation based on B- and C-scans. The three methods investigated were: Image gradient methods, represented by Canny operators, rotated periodic filters, represented by Gabor (periodic filter) operators, and the Radon transform method using the variance of the first derivative to retrieve the angular dependence. In systematic studies on simulated images, the image gradient method (Canny operator) showed stronger dependence on kernel size than the other two methods. In comparison with real ultrasonic data, the angle-measurement maps from Radon method was more consistent with the original image than the other two methods using Canny or Gabor operators. Chakrapani *et al.* [33] used air-coupled ultrasonics to detect waviness with different aspect ratios in thick composites used in wind turbine blades. They developed a three-step process to ensure the in-field use of the technique.

Based on **infrared thermographic** test principles, Elhajjar *et al.* [26] proposed and successfully applied a full-field thermoelastic stress analysis infrared method (TSA-IR) with promising results for being capable of detecting out-of-plane fiber waviness under both tension and compression mean stress conditions with applied sinusoidal loading within the elastic loading region. Although the results indicate the possibility of deriving the wave amplitude from the signal strength, they are not conclusive. A method for non-destructive inspection of composite structures containing fiber waviness is presented in the US patent US 10 094 794 B2 [34]. This method is based on the development of calibration/correlation curves for an infrared imaging system based on correlation of infrared image data and optical cross-section measurement data acquired from reference standards containing fiber waviness. By using this calibration curves, the maximum amplitude (i.e. height) of an out-of-plane wrinkle can be determined. A calibration curve is needed because the amplitude measurement from the infrared thermography is a temperature-related value, not a spatial value.

1.3 NON-DESTRUCTIVE DETECTION OF OUT-OF-PLANE FIBER WAVINESS

The wrinkle wavelength is determined by measuring the infrared image and applying a transfer function, which is a correction factor that accounts for heat loss due to convection or smearing of the thermal data due to lateral heat flows. This transfer functions were also obtained by numerous measurements on reference standards containing known fiber waviness. Furthermore, the transfer functions are dependent on the depth of the waviness (i.e. the position of the waviness in the laminate), since lateral heat transfer occurs preferentially in the plane of the part (e.g. in fiber direction). Consequently, it is expected that the wavelength signal will become fuzzier with increasing depth.

Numerous studies have shown the possibilities for the detection of local fiber orientations in the laminate [35–37] and in-plane fiber waviness [38–42] using **eddy current** methods. Zeng *et al.* [38] used eddy current testing for the detection of in-plane fiber waviness, where they showed to be able to detect waviness with deviations of 0.5°. Mizukami *et al.* [40,42] stated, that surface waviness can be detected exactly, whereas the size of subsurface waviness are underestimated. In [43], Mizukami carried out finite element studies to evaluate the deformation of the magnetic field in relation to the size of waviness. A nonlinear relationship was shown between the signals and positions of the waviness in the laminate. The amplitude or peak-to-peak height of the magnetic field deformation becomes smaller as the depth of the waviness increases. In [44], Mizukami *et al.* proposed a specialized probe for the detection of in-plane and out-of-plane fiber waviness in UD composites using eddy current technique. Experimental tests have shown the ability to detect in-plane fiber waviness with an amplitude of 1.1 mm and height of 15.9 mm in a thin unidirectional carbon fiber reinforced plastic at sufficiently high drive frequency. Three-dimensional finite element method analysis was carried out to proof the validity of the proposed method. Out-of-plane fiber waviness induced in a thick unidirectional laminate could also be detected. It was found that output signals in complex plane obtained by scanning a material containing out-of-plane fiber waviness lead to ring-shaped plots. Those plots in the complex plane are used to identify the presence and location of out-of-plane fiber waviness.

In this thesis, a comprehensive investigation on the detectability and characterization of embedded out-of-plane fiber waviness was carried out. Test plates with varying artificially embedded waviness in different depth positions were produced. The study includes standard methods used in NDT of aerospace structures, i.e. ultrasonic methods, as well as other advanced methods and sophisticated evaluation methodologies, i.e. ultrasonic microscopy, X-ray computed tomography, infrared thermography, digital shearography and eddy current testing.

1.4. Mechanical response of wavy composites

Even simple global loading cases, e.g. uniaxial extension, of wavy layers in a composite material locally induce a complex three-dimensional stress state consisting of a combination of interlaminar normal and shear stresses. Interlaminar tensile stresses normal to the lamina plane are induced as a consequence of transverse strains caused by the wave geometry [45]. Groundbreaking experimental and analytical studies on the influence of fiber waviness on mechanical properties were performed by Hsiao and Daniel [13,46] and Piggott [47].

It has been shown that compressive strength and stiffness are especially sensitive to the presence of fiber waviness. The initial misalignment can decrease the compressive strength by up to 60% [48].

Experimental studies under compression load for fiber waviness were carried out by [49–52], all reporting a significant reduction on compression properties. Lemanski and Sutcliffe [53] numerically investigated the influence of fiber waviness under compression load. It was shown that the compressive strength falls rapidly with the proportion of laminate width covered by the wavy region. The effect of length and position of the wavy region was found to have a smaller effect on the compressive strength. Zhu et al. [54] developed a three-dimensional analytical method based on the classical lamination theory. Li et al. [55] have dealt with the determination of the reduced stiffness due to fiber waviness by proposing a micro-sphere based homogenization approach.

In a numerical and experimental study conducted by Vogler et al. [56] a strong interaction between compressive and shear stresses on compressive strength could be demonstrated. The general failure behavior of composites under compression and its resulting failure mechanisms, i.e. elastic microbuckling, plastic microbuckling, delamination, fiber crushing and longitudinal cracking, have been studied in [11,56–64], and similar mechanisms can be observed in composites containing fiber waviness. It has been shown that the nonlinear matrix properties dominate the damage initiation and the stiffness and strength decrease [48,65].

The formation of a shear kink-band is induced by local fiber buckling or matrix flow induced by initial or as-delivered fiber misalignments in the UD material, which continue to rotate under load. In the case of fiber waviness, this effect is further intensified due to the characteristics of the waviness. A very detailed study on experimental, analytical and numerical aspects on the formation of kink-bands can be found in [66,67]. Davidson and Waas [11] have shown that under compression load this is the critical failure mode also for laminates containing fiber waviness. They used a local-global approach, where the local FE-based micromechanical analyses for fiber kinking are integrated into the global macroscopic FE model of fiber waviness, which exactly maps the geometry of the fiber waviness. The World-Wide Failure Exercise of Hinton et al. [68] have shown that the failure criteria show significant weaknesses,

1.5 OBJECTIVES AND RESEARCH QUESTIONS

partly due to not considering fiber kinking under combined compression and shear stresses.

Under tensile loading, the fibers are pulled "straight", resulting in a stiffening effect and a failure of the interface between fiber and matrix due to local interlaminar normal and shear stresses and finally to delamination [69,70].

For shear loading in the laminate plane of a laminate with fiber waviness, few experimental and simulative investigations are known. In the few available literature references [71,72] an influence of up to 12% on the reduction of the shear strength is determined. Similar to shear stresses in laminates without fiber waviness [73], a strong influence of the nonlinear shear behavior on the failure process is assumed for laminates containing fiber waviness.

In recent publications the simulations are validated on strain field measurement to record damage initiation and progression [11,74]. Previous studies have mainly focused on UD laminates, all oriented in the same direction, and have concentrated on the effect of fiber waviness on the stiffness. Quasi-isotropic (QI) laminates containing wavy layers have been rarely investigated so far. Mukhopadhyay et al. published work on compressive [75], tensile [76] and fatigue behavior [77] of QI laminates containing embedded wrinkles using 3D finite element modelling approaches reporting a more complex failure behavior due to multiple active damage mechanisms and their interaction. The study of Wilhelmsson et al. [78] has shown a considerable influence of embedded out-of-plane waviness on the bending during compression testing.

1.5. Objectives and research questions

The overall objective of this thesis is to contribute to a fundamental understanding of the origins of out-of-plane fiber waviness, i.e. waviness in the thickness direction and the resulting failure phenomena of loaded laminates containing out-of-plane fiber waviness. This will provide the basis for a cost reduction in quality assurance and repair. In detail, the following fundamental questions are addressed:

- What are the characteristic cases of out-of-plane fiber waviness in industrial applications such as hand lay-up of layers, hot-drape forming (HDF), resin transfer molding (RTM) or automated fiber placement (AFP)?
- How can these resulting wrinkles be classified (e.g. via geometric parameters such as amplitude, wavelength, location in the laminate, ply lay-up, etc.)?
- Besides ultrasonic testing (UT), which is the standard non-destructive testing (NDT) method used in the aviation industry, are there other NDT methods available, that could provide a better detectability and characterization of out-of-plane fiber waviness?
- How large is the influence of the determined parameters, such as amplitude, wavelength, inclination, thickness, ply lay-up, etc., on the stiffness and strength of the laminate and what are the mutual dependencies between the parameters?

- What is the influence of the matrix, especially under elevated temperatures and relative humidity (i.e. hot/wet conditions)?
- How good is the prediction quality of simple and more complex analytical and numerical approaches in comparison with each other and, above all, with the experiments?
- Is a reliable and computationally efficient study over the large parameter space of out-of-plane fiber waviness possible using a virtual testing approach (analytical or numerical) as a substitute to a very high experimental effort?

1.6. Outline of the thesis

Any composite manufacturing process is associated with a number of specific effects. In **Section 2**, numerous mechanisms of wrinkling were analyzed, leading to several recommendations to prevent wrinkle formation not only during composite processing, but also at an earlier design stage, where generally several influencing factors are defined.

Based on that, an overview of typically occurring wave shapes is presented and a classification scheme based on ten characteristic features is suggested for categorization purposes in **Section 3**.

The assessment of out-of-plane fiber waviness in composite materials is strongly dependent on the accuracy of detection and quantification of the wave parameters such as amplitude, wavelength and position in the laminate. In the aviation industry, ultrasonic testing (UT) is the preferred method for the evaluation of composite materials. The evaluation of the ultrasound signal from different manufacturing effects is difficult and it often cannot be clearly determined whether there are actually wavy regions in the laminate or not. In **Section 4**, different non-destructive testing (NDT) methods, such as infrared thermography (IRT), digital shearography, eddy current testing (ET) and X-ray computed tomography (CT) have been used to assess their potential for the detection and characterization of embedded out-of-plane fiber waviness in composite materials. These methods were applied on test plates with artificially embedded waviness with varying amplitudes, wavelengths and positions in the laminate and evaluated with respect to their ability of detecting the wrinkle morphology. The experimental non-destructive procedures of infrared thermography and digital shearography were simulated using the Finite Element Method (FEM) to gain a deeper understanding on the influence of fiber waviness on the measured results.

To understand the complex failure behaviour of composite materials containing out-of-plane fiber waviness under compressive and tensile loading, numerous experimental tests have been carried out in **Section 5**. Digital image correlation (DIC), passive thermography (IRT) and acoustic emission (AE) test methods have been used to investigate damage initiation and propagation on specimen level. In addition to that, an extensive material characterization on planar specimens was also performed.

1.7 NOTATION CONVENTION

Composite materials exposed to harsh environmental conditions, i.e. hot-wet, show considerably reduced mechanical properties, governed by a degrading matrix. To investigate the effect of fiber waviness on the mechanical properties at both room temperature and after 12 months hot-wet conditioning at 70°C and 85% relative humidity, mechanical tests (compressive and tensile loading) were conducted.

The basic strategies for the assessment of fiber waviness are briefly described in **Section 6**. In engineering practice several approaches are used, i.e. empirical, generic, and semi-empirical. These include experimentally obtained knockdown factors, simplified simulations or extensive testing on subcomponent level, both experimentally and numerically.

In **Section 7**, a developed micromechanical model, which represents an extension of the models of Hsiao & Daniel [46] and Altmann et al. [79] for the application on multidirectional laminates, is presented. It is implemented in a MATLAB GUI to determine the effective elastic properties as well as the resulting complex stress state of uniform and graded fiber waviness. The well-established Puck failure criterion [80] was implemented and applied on the calculated stresses to predict local ply failure and determine the strength of wavy plies.

Section 8 aims to investigate the mechanical behavior of out-of-plane fiber waviness of both unidirectional and quasi-isotropic laminates by numerically simulating damage initiation and propagation. A nonlinear material model was implemented in ABAQUS/Explicit as a material user-subroutine, which is able to capture the material behavior including shear nonlinearities, failure initiation and propagation in unidirectional laminates reasonably accurate.

1.7. Notation convention

Both the tensor notation, D_{ijkl} , and matrix notation, \mathbf{D} , is used in this thesis.

2. OCCURRENCE OF FIBER WAVINESS

The origins of fiber waviness are manifold and can be caused by several factors. These effects can occur in manual hand lay-up processes, which are strongly influenced by the skills of the operators, but also in highly automated production processes. Any composite manufacturing process is associated with a number of specific effects. The classification of waviness-inducing effects serves as an overview of the numerous origins and influence factors on the formation of out-of-plane fiber waviness and provides a general guideline on how to reduce and, in the best case, even avoid the occurrence of wavy layers at an early stage of product and process development.

2.1. Mechanical loading and behavior of dry and impregnated fiber reinforcements

2.1.1. *Basic material behavior*

The deformation behavior of fiber reinforced plastics is very different from that of isotropic materials. With isotropic materials, normal stresses only cause normal strains and shear stresses only shear strains. Within consolidated/cured fiber reinforced plastics, this decoupling is only possible under certain conditions, if symmetries are introduced in the stacking sequence. In the most general case all elements of the $[ABD]$ matrix [81] that relates cross-sectional forces and moments to mid-plane strains and curvatures are occupied and thereby extensional, shear, bending and twisting behavior are coupled. However, during the process, the matrix is either absent, e.g. in initially dry reinforcements in LCM processes, melted, e.g. in thermoforming processes using thermoplastic matrices, or in an uncured sticky stage when using thermoset pre-impregnated reinforcements. In dry or pre-impregnated composites, independent if a thermoplastic or thermoset matrix is used, the extensional and bending behavior is decoupled, which makes the use of the $[ABD]$ matrix in fact not appropriate. Classical plate and shell theories do not apply in their standard form for dry or non-cured composites, since, opposite to continuous materials, there is no direct relation between the extensional and bending stiffness. According to Boisse et al. [4], the quasi-inextensibility and the possible slippage between fibers are the two main reasons for the very specific mechanical behavior of fiber reinforcements. The relative slippage between fibers, which is described in detail in Section 4.4.1, leads to a much lower bending stiffness than for continuous materials such as cured composites, metals or polymers.

When considering a single ply, the thickness of a typical ply is much smaller than the width, and therefore the bending stiffness out-of-plane is much smaller than in-plane, consequently out-of-plane is the predominantly occurring case of waviness. In

2.1 MECHANICAL LOADING AND BEHAVIOR OF DRY AND IMPREGNATED FIBER REINFORCEMENTS

[82] it is stated, that thermoset prepregs are more prone to fiber buckling in form of wavy layers because of their lower bending stiffness compared to layers used for liquid composite molding processes which are usually thicker. As shown in Figure 3, plies with higher bending stiffness tend to single wave formation, whereas low bending stiffness plies tend to form a higher number of waves.

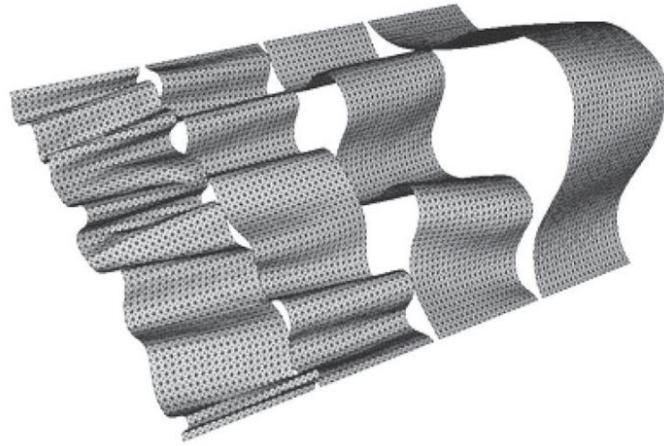


Figure 3. Wrinkling in compression of a woven reinforcement strip with different bending stiffness (from left to right 1, 10, 10^2 , 10^3 N mm⁻¹) [83]. Reprinted from Phil. Trans. R. Soc. A, Vol. 374, Modelling the development of defects during composite reinforcements and prepreg forming, page 5, (2016), with permission from The Royal Society Publishing.

An instability phenomenon, known as shear-buckling, can occur in forming composite materials leading to pronounced out-of-plane wrinkling. An example of this mechanism can be also observed, for example, in simple off-axis tensile tests of unidirectional prepregs (Figure 4). However, this phenomenon is not limited to single unidirectional laminates and may also occur in cross-ply or quasi-isotropic laminates mainly dependent on the forming rate and the preform dimensions, i.e. the ratio of the initial preform size to the formed surface area [84,85].



Figure 4. Wrinkling of initially planar UD ply due to shear buckling in off-axis tensile test.

2.1.2. *Mechanical deformation of layers due to manual handling of preforms, moving sliders and closing tools*

Fiber misalignment in general, and fiber waviness specifically, often originate from the labor-intensive preform placement into the mold cavity prior to infiltration and curing steps. The quality of draping is therefore strongly dependent on the skill and experience of the operator. Fiber waviness may be also formed due to mold closure effects when the fiber preform is compressed during mold closing, inducing tension forces around curvatures and bends, particularly in massive, geometrically-complex parts or when sliders move the plies away from its intentional position [86,87]. [48,74] stated that fiber waviness can also occur when slightly oversized preforms are forced to fit into a mold cavity. This is not considered to be a manufacturing effect but more a design issue, as this problem can be solved by adapting the size of the ply.

2.2. Path length differences

2.2.1. *Micro/meso scale deformation at the material level*

Bended continuous fiber-reinforcements tends to form out-of-plane waviness as a result of path length differences between the upper and lower side of the ply [1]. This effect is considered to be caused at the material level (micro/meso scale). When forming a multiple-ply stack, each ply is exposed to these path length differences. In addition to that, waviness can occur if the ability of the plies to slip between each other is too low or even constrained. This effect can be controlled by the forming rate, temperature control and the distance of the point of forming to the free edge where the necessary slip between the plies must be accommodated [1].

2.2.2. *Global deformation on structural level at double curved and joggled geometries*

When a material, regardless of whether it is dry or pre-impregnated, is draped around a double curved surface, e.g. hemispheres [1,88] or joggled geometries [5,89–93], the path length difference of the reinforcement and the path on the geometry to which the material must map on the surface can vary significantly, thus leading to a pronounced risk of wrinkling of the layers due to path length differences at the structural level (macro scale). The drapeability of a material describes its ability to conform to the mold surface without fiber distortion, movement, and out-of-plane buckling. The complexity of the final part tremendously influences the occurrence of fiber waviness. Potter et al. [1] stated that only a slight difference in path length can lead to obvious fiber waviness. A schematic illustration of path length differences between the edges of tows on the surface of a hemisphere is shown in Figure 5.

2.2 PATH LENGTH DIFFERENCES

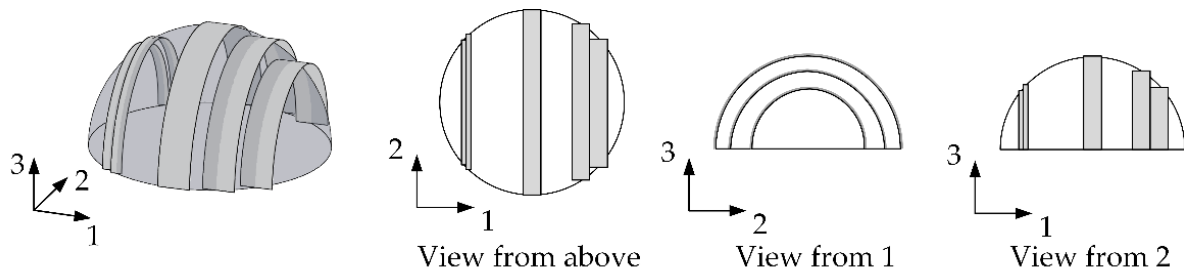


Figure 5. Path length differences between the edges of tows on the surface of a hemisphere / a double curved surface; adapted from [1].

Furthermore, the probability of fiber waviness is strongly dependent on the pathway, as there are generally several ways by which the draping can be achieved [94]. Especially the placement of fiber reinforcements by hand allows for a very diverse draping into the production tool, but the occurrence of fiber waviness cannot be completely avoided. Depending on the pathway, higher or lesser skills of the operators are required to achieve a defect free part. The effect of differences in the path length strongly depends on the choice of material and the geometry design. During the deformation of the material, the curvature and the stresses generated in the material change. These are, according to Lin et al. [95], functions of time, temperature, processing rate and holding force. Wrinkling may occur by buckling of the tows along the circumference of the hemisphere if the compressive force exceeds the critical buckling force. Several experimental studies [96–101] have reported that, amongst other factors, stress conditions induced by manufacturing boundary conditions, deforming rates, original blank dimensions and strain gradients play a role in their development. Boisse et al. [88] have also shown that the formation of out-of-plane wrinkles is a global phenomenon dependent on process conditions, e.g. blank-holder pressure, and all types of strains and rigidities of the composite material. Low forming speeds also reduce the possibility of wrinkling by generating lower resistance to inter-ply and intra-ply shearing, thus allowing the blank to deform more easily [102,103]. Generally, when the draped reinforcement arrives at a flat region, the distortions in the tows needed to accommodate the curvature continue across the flat regions [1]. The tendency of wrinkling, occurring from a so-called drape run-out, is significantly reduced if the layers to be formed have a shape and size which results in as little excess material as possible at the edges [104]. These wrinkles can be, at least partially, avoided by blank holder forces to keep the plies under slight tension during molding in forming processes. As shown in numerous studies [88,95,102,105,106], keeping the blank under suitable in-plane tension by the presence of blank holder forces can, significantly minimize the occurrence of fiber waviness and increase the quality of the formed parts. The clamping force depends on both reinforcement architecture (e.g., unidirectional or fabric) and forming ratio (i.e., ratio of blank area and the projected area of the die cavity) [106]. The type of holding fixture and the position of springs is usually determined by prior experience and considerable trial and error or,

increasingly, with the help of process simulations. The blank holder may induce tensile stresses by spring elements or vertical clamping rings used to keep the flange flat.

In diaphragm forming, the outer edges of the blank are pressed onto the mold flanges before the central area is drawn into the cavity when using female tools. In addition, the friction between the blank surfaces and the diaphragm create biaxial tensile stresses in the blank as the diaphragm is stretched, which prevent wrinkle formation due to out-of-plane buckling [106]. Additional forces that can reduce the formation of wrinkles in diaphragm forming processes originate from the inherent resistance of the material itself and from the restraining force supplied by the diaphragm when it is stretched [107]. The combination of both prevents out-of-plane wrinkling in diaphragm formed components even in the absence of clamping or blank holder forces [106]. In addition to the suppression of wrinkle formation during press forming, according to [108], blank holders serve several more functions, e.g. they prevent the shrinkage of the blank during preheating, they maintain the fiber orientation in the softened blank when it is transferred from the oven to the mold, and they allow for a rapid transfer of the preheated blank to the mold without significant heat loss. Lin et al. [95] used experimental and numerical (FE) approaches to determine the effects of clamping and blank holding forces on the wrinkling behavior. In an example of 3D stamp forming [106], schematically illustrated in Figure 6, a reduction in area of the individual sections occurs when travelling into the cavity of the mold [109,110], inducing hoop forces, which resolve into compressive stresses perpendicular to the radius of the circular laminate. Fiber wrinkling and distortions are observed around the periphery of the cavity and in the flange area if stamping forces generated during forming exceed the critical buckling stress.

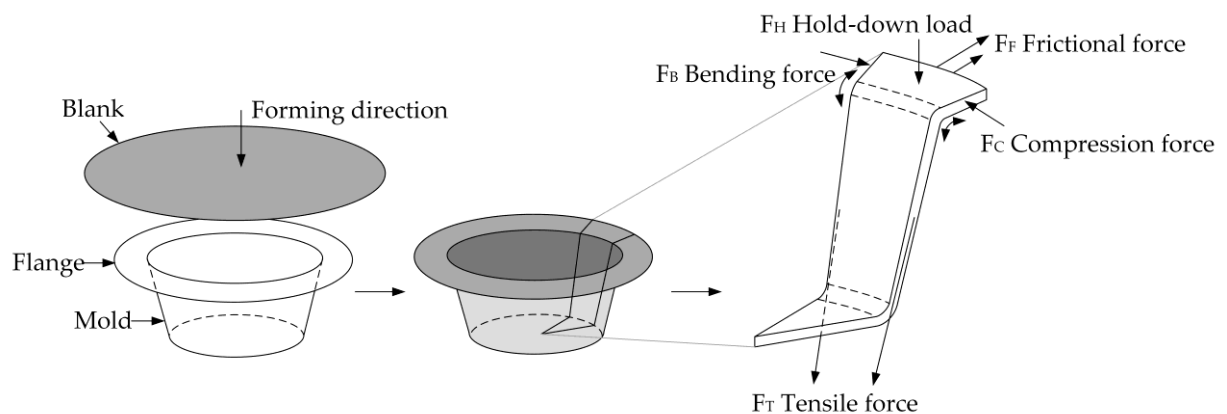


Figure 6. Force analysis in 3D stamp forming, modified from [106].

Clamping forces create desirable frictional forces, F_R , which act in opposite direction to the material flow as the material is drawn into the cavity. Since the material cannot stretch in fiber direction due to virtually inextensible fibers, the fibers have to move from the outer edges of the sheet towards the center causing tensile stresses in fiber direction. According to Friedrich et al. [106], the decrease in area when moving

2.2 PATH LENGTH DIFFERENCES

towards the apex of the dome section simultaneously leads to compressive hoop stresses in the bisecting direction of the reinforcements which are resolved in out-of-plane buckles appearing in the direction away from the fibers. Dependent on the mold geometry inter-ply slip, inter-ply rotation and transverse matrix flow are necessary in order to form a component without instabilities such as out-of-plane buckling.

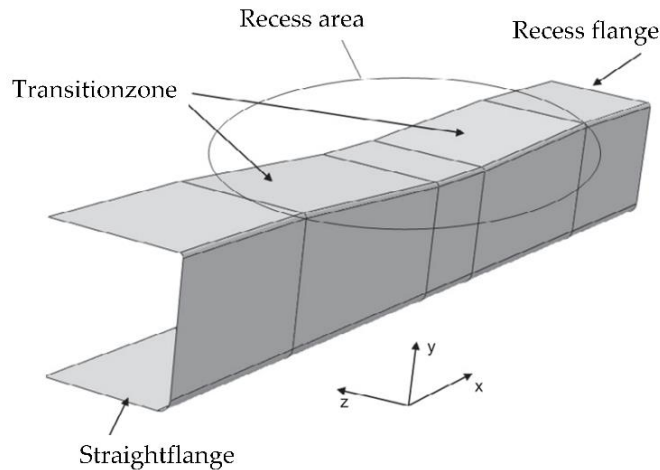


Figure 7. Spar geometry with a flange recess area [90]. Reprinted from *Composites: Part A*, Vol. 50, An experimental study of mechanisms behind wrinkle development during forming of composite laminates, page 56, (2013), with permission from Elsevier.

The forming behavior of pre-stacked prepregs subsequently formed in a Hot Drape Forming (HDF) process using a spar geometry with a flange recess area (varying cross section), shown in Figure 7, was investigated by [5,90–93]. Hallander et al. [90] experimentally studied the out-of-plane defect behavior during forming in the recess area investigating various parameters, e.g. lay-up sequence, prepreg ply thickness, inter-ply friction and prepreg ply impregnation. The lay-up sequence was shown to have a dominant effect. $[0/90]$ and $[45/-45]$ layups in a UD prepreg are less sensitive for out-of-plane defects compared to a quasi-isotropic lay-up. The lay-up that is more prone to shear, also deforms better during forming without visible defects. The study further shows the existence of compression in the laminate in the recess area that is globally under tension during forming. Åkermo et al. [91] and building on this, Sjölander et al. [5] studied the inter-ply friction by performing numerical simulations on the same geometry using the software AniForm. They modelled the rubber like diaphragm by the hyperelastic Mooney-Rivlin material model. The fibers are modelled as linearly elastic and the matrix by a combination of a viscous and an iso-elastic material model, a so-called Kelvin-Voigt model. The inter-ply friction was modelled by two different friction models, a penalty model that combines viscous and Coulomb friction and a penalty polymer friction model. The simulations confirmed the presence of compressive stresses across the recess area of the considered spar. The bending stiffness was modelled with an orthotropic elastic model to simulate the difference in bending stiffness in the fiber direction and the transverse fiber direction. In [92],

Hallander and colleagues investigated the influence of locally changed ply properties or cuts on the wrinkling behavior during forming. Local cuts of layers were used to reduce the stresses that develop in the recess area. In [93], Hallander et al. experimentally studied the forming behavior by locally manipulating the prepreg interfacial characteristics, i.e. primarily increasing prepreg surface friction, in order to cause different pairs of plies to interact during forming. This manipulation is performed by using either Multi Wall Carbon Nano Tubes (MWCNT) or thermoplastic veil at the desired interlayers.

Additionally, wrinkles originating from the forming of pre-stacked prepregs, can be, at least partially, reduced by higher consolidation pressure during a subsequent autoclave curing.

For parts with significant double curvature and requiring the use of a large area draped reinforcement layer, the selection of a woven fabric with a narrow rather than a wide tow reduces the level of fiber waviness [86]. By including these influencing factors in the design decisions, this effect can be reduced.

2.2.3. *Steering*

In automated fiber placement (AFP) [111], a fully automated manufacturing process for ribs or flat composite components, robot-guided fiber-reinforced prepreg tows are placed along a predetermined path on the three-dimensional tool surface using pressure and temperature. Due to the path steering of the head, the layers can be ideally orientated according to a pre-defined load path. However, different defects may occur, e.g. bridging, gaps between the deposited tow, in-plane or out-of-plane buckling of the tow or a lifting of the tow on the outside of the tow as the radius narrows. Overall, the formation of these defects is a function of the steering radius chosen in the design process.

A schematic overview of tow steering defects is given in Figure 8. During steering, the tow is bent in the plane of the surface, which causes the fibers along the inner edge to be under compression and the outer edge to be under tension [112]. The inner edge of a tow placed along a curved trajectory tends to buckle in the form of localized out-of-plane waviness when the radius reaches a specific limit. This limit depends on parameters such as tow width and thickness, material, temperature control, etc. The tape/tow pull-off/pull-up [112,113] is caused by the tension state at the outer edge of the steered tow. The mechanical behavior of the fiber mainly determines the resulting cylindrical deformation mode. The fiber can be assumed to be almost inextensible, causing high tensile stresses. In combination with an insufficient prepreg tack, the tow starts to fold at the outer edge. In-plane fiber waviness and out-of-plane tow buckling are two effects that are assumed to occur subsequently [113].

2.2 PATH LENGTH DIFFERENCES

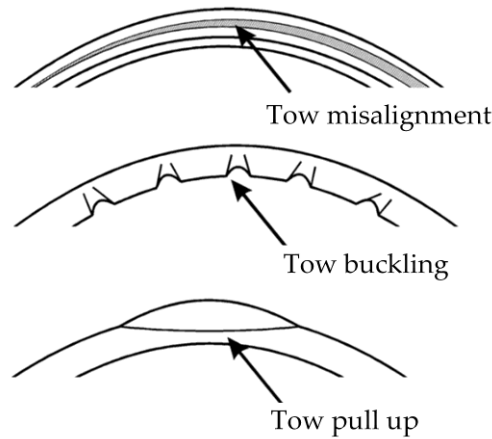


Figure 8. Overview of tow steering defects leading to out-of-plane fiber waviness [114]. Reprinted from *Composites: Part B, Vol. 43, The engineering aspects of automated prepreg layup: History, present and future*, page 1005, (2012), with permission from Elsevier.

Hörmann [113] states, that in a first step, the compression at the inner edge of the tow due to the in-plane curvature causes in-plane fiber waviness by shearing the non-cured, thermoset matrix between the fibers. Subsequently, the tows start to form out-of-plane buckles, if the in-plane curvature reaches a particular, material-dependent limit and the prepreg tack is insufficient to hold the tow on the substrate surface. A comprehensive review on manufacturing-induced imperfections in composite parts manufactured via AFP is given by Heinecke and Willberg [115].

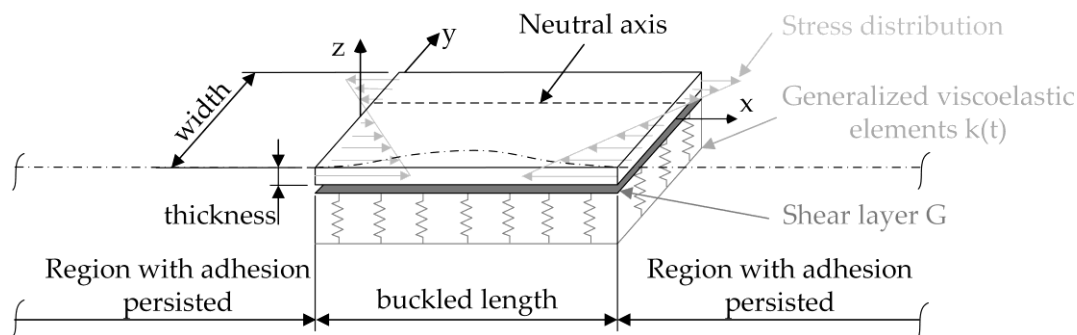


Figure 9. Schematic illustration of an anisotropic plate on elastic foundation illustrating an approach by Béakou et al. [116] and Hörmann [113] to describe out-of-plane tape buckling for a steered tape during automated fiber placement, modified from [113,116,117].

A careful control and selection of process parameters [118–120] (i.e. heating temperature, compaction pressure, deposition rate), machine trajectories (i.e. steering radius), together with material parameter (i.e. tackiness and tow width), is of crucial importance for obtaining a high quality, defect-free laminate. Bakhshi et al. [117] carried out experimental and analytical studies to understand the time-dependent wrinkle formation during tow steering in AFP. The analytical model to describe wrinkle formation accounts for process parameters (e.g. temperature, radius,

compaction force, speed) together with interface properties (tack). An analytical model (Ritz) was developed by Beakou et al. [116] to estimate the critical buckling load of a tow and, consequently, the minimum steering radius for a circular fiber path. The analytical approach accounts for prepreg tack and stress distribution, however, two important parameters, i.e. lay-down rate and delay in tow wrinkling recovery were additionally found to be important to describe tow wrinkling. Sensitivity studies by Beakou et al. [116] have shown that the prepreg tack and the tow width strongly affect the critical buckling load. However, care must be taken to avoid stretching of the outer fiber of the tow to prevent lateral compressive stresses leading to a transverse buckling phenomenon. Lower compaction forces lead to placement without tow wrinkling, however a minimum force must exist to ensure tack. For productivity reasons, manufacturers strive for high deposition rates. Figure 9 shows an anisotropic plate on elastic foundation illustrating an approach by Béakou et al. [116] and Hörmann [113] to describe out-of-plane tape buckling for a steered tape during automated fiber placement. An anisotropic plate which is geometrically defined by its length l , width h and thickness d , rests on an elastic foundation defined by its elastic stiffness k . The plate is subjected to combined in-plane bending and tension, causing the position of the neutral axis to deviate from the position of the symmetric axis. The inner edge is assumed to be under compression and out-of-plane buckling is allowed. However, it was observed by Beakou et al. [116], that high deposition rates promote the occurrence of tow wrinkling. As a rule, the minimum steering radius without tow wrinkling increases from 1.5 to 4 m when the lay-down rate increases from 12 to 30 m/min. Depending on processing parameters, tow wrinkling may also return many hours after fiber deposition. Matveev et al. [121] developed an analytical framework for the prediction of wrinkling in tow steering during Automated Dry Fiber Placement (ADFP). Experimental results were used for estimation of the model parameters and to validate the analytical model. The tackiness was shown to have the greatest influence on critical steering radius. The lay-up temperature influence tack stiffness and hence can improve wrinkle formation, respectively decrease the steering radius. Kim et al. [122] found that the key factor causing all process-induced defects in Automated Fiber Placement (AFP) and Tailored Fiber Placement (TFP) is the in-plane bending deformation of the tow.

Table 1, taken from Blom [112], shows process limits for minimum steering radii as a function of the tape width. The given values are purely kinematic and do not consider the process-material interaction. However, according to Blom, much smaller steering radii are possible depending on the used material system, the lay-up speed and compaction force.

2.2 PATH LENGTH DIFFERENCES

Table 1. Variation of minimum steering radius with slit-tape width for a 102 mm track width [112]

Slit-tape width	Typical minimum steering radius
3.175 mm 1/8"	635.0 mm 25"
6.350 mm 1/4"	1778 mm 70"
12.70 mm 1/2"	8890 mm 350"

Rajan et al. [123] performed experimental studies using Stereo-DIC to obtain in-situ measurements for quantifying out-of-plane wrinkle formation and in-plane deformations occurring during Automated Fiber Placement (AFP). Viisainen et al. [124] used in-situ Stereo-DIC during forming experiments on a double curved hemisphere. Rajan et al. [123] found, that tow wrinkling can be observed in all tows at each location where the underlying laminate substrate showed surface defects such as gaps and overlaps. It has been observed, that the wrinkle amplitude increases during the first hour of lay-up to almost twice the amplitude of the wrinkle immediately after placement, apparently due to viscoelastic effects in the prepreg tack. Another mechanism observed, is that after applying heating to the steered tape, close adjacent wrinkles tend to merge into one large wrinkle, apparently due to considerable loss in stiffness of the cohesive layer between the tape and substrate.

2.2.4. Consolidation in corner areas, external radii, stepped or tapered laminates

The autoclave consolidation of thick laminates in inner corner geometries can force the plies to move in the corner direction and form wrinkles due to the pressure acting at the end of the layup (Figure 10). This effect depends on the length of the laminate arm (limb length) as it influences the possibility of ply slippage and, therefore, can be addressed in design decisions and manufacturing planning. Further mechanisms of fiber waviness in internal radii are described in Section 4.3.4 which may occur due to ply or vacuum bag bridging.

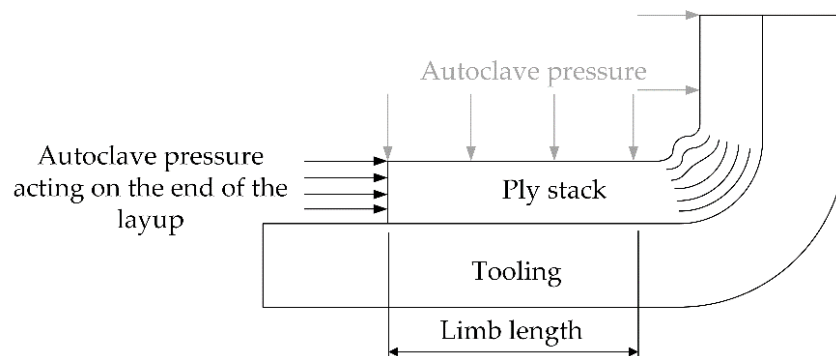


Figure 10. Fiber waviness due to autoclave pressure acting on the end of the layup.

In V-bending [106], the compressed fibers in the bend region can lead to wrinkling provided the compressive stresses exceed a certain limit. In contrast, Potter et al. [1] state that even a small amount of consolidation of the plies over an external corner can lead to an excess length that must be accommodated by the forming of wrinkles if no slippage can occur.

The debulking of the plies over an external radius during the consolidation process ensures a correct fit on the tool geometry and improves adhesion between the layers. The outermost plies are forced into a tighter geometry, leading to an excess length. Figure 11 a) and b) shows these two possible scenarios when a laminate is consolidated over a corner radius and the excess length is accommodated by slippage of the plies or the occurrence of waviness.

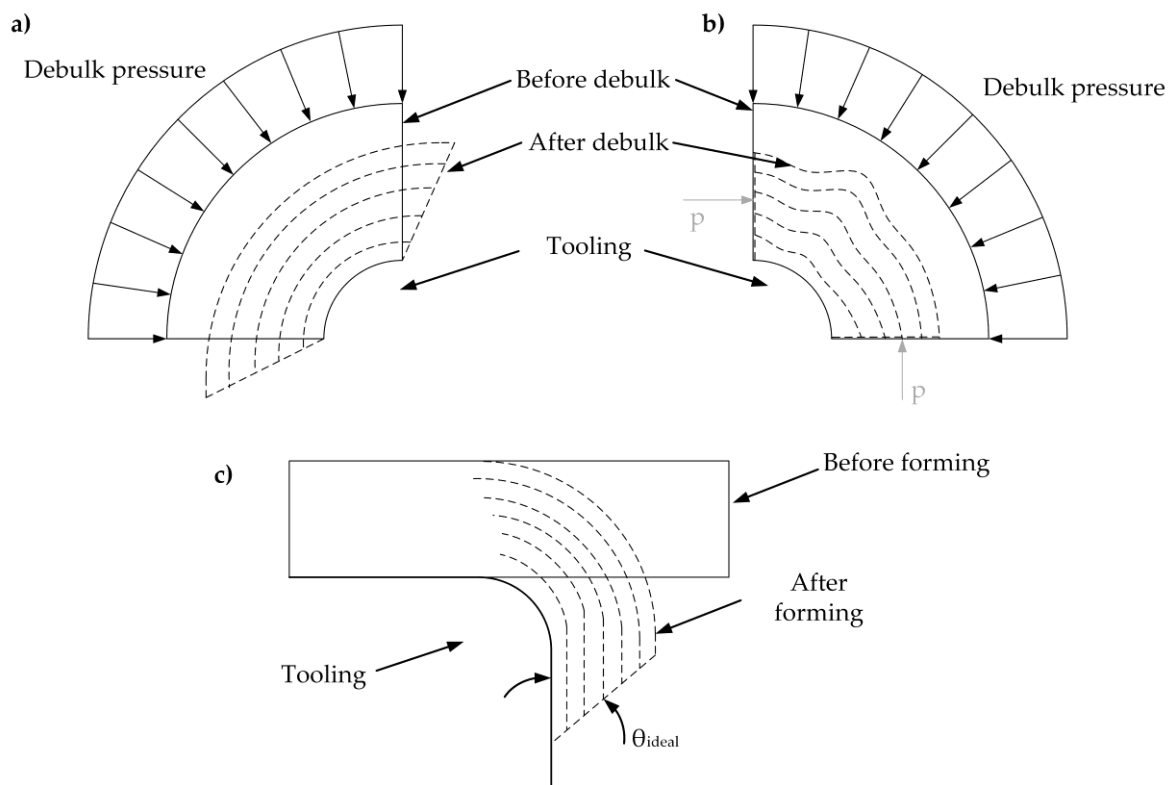


Figure 11. a) representation of the book-end effect, created when a laminate is consolidated unconstrained over a corner radius and slippage occurs; b) constrained consolidation due to high shear resistance leading to fiber waviness; c) book-end resulting from forming process illustrating the termination angle θ .

If layers can shear/slip over one another, the additional length can be accommodated by producing so-called “bookends” [82], which are shown in Figure 11 (c). However, if the tack between the plies is too high, axial compressive stresses are built up in the layers which may form wrinkles.

Dodwell et al. [82] developed an analytical model for the description of out-of-plane wrinkling due to consolidation over non-trivial geometries. The model determines the critical strain energy at which the layers begin to buckle. Several

2.2 PATH LENGTH DIFFERENCES

assumptions and simplifications have been made for this analytical approach. In reality wrinkling is dependent on a complex mix of non-linear geometry and viscoelastic temperature-dependent rheological behavior. A critical limb length L_{crit} is derived from the model, which depends mainly on layer thickness and shear properties and less on the tool radius.

$$L_{crit} = \frac{\delta p^c}{\tau(\gamma)} \quad (1)$$

where p^c is the critical load and $\tau(\gamma)$ the shear stress.

During many advanced composite processes, e.g. autoclave process or compression molding, bulk compressive stresses [125] are applied to the reinforcement in thickness direction leading to an increased fiber volume fraction. During consolidation, the fiber reinforcement begins to take up an increasing amount of the applied compression load. Bulk compressive stresses that are applied in the absence of any axial stress $\sigma_1 = 0$ represent similar conditions occurring during autoclave processes. For this case, an expression [125] can be obtained that relates the bulk compressive stress with the fiber volume fraction,

$$\sigma_b = \frac{3\pi E}{\beta^4} \frac{1 - \sqrt{\frac{V_f}{V_o}}}{\left(\sqrt{\frac{V_a}{V_f}} - 1\right)^4} \quad (2)$$

with V_o initial fiber volume fraction, V_a maximum allowable fiber volume fraction and V_f current fiber volume fraction, respectively. If the axial extension $\varepsilon_1 > 0$ induced by transverse compression is constrained, the applied compression bulk stress would lead to an induced axial compression increasing the potential for fiber wrinkling [125].

The size of radius plays an important role, especially in internal corners. It becomes more difficult to place the prepregs accurately into internal corners with decreasing radius. The quality of the layup strongly depends on the size of radius, the ply thickness and the final laminate thickness. Larger corner radii are less likely to be bridged and, according to [86], will definitely have lower levels of fiber waviness induced by the curvature of the prepreg. Although heavier grades of prepregs potentially reduce the labour cost due to a reduced number of plies, the level of fiber waviness induced by the curvature would increase. When processing out-of-autoclave prepregs using vacuum bag only, the challenge is to extract the remaining air from the part prior to curing. For this purpose, these prepregs, also called semipregs, have a dry area ensuring a connected flow path, but resulting in a very high bulk factor.

$$\beta = \frac{t_i}{t_f} \quad (3)$$

The bulk factor β [126], which describes the ratio of the initial laminate thickness t_i to the final thickness t_f of the fully impregnated part after curing, is an inherent characteristic of the material. Materials with high bulk factors, e.g. out-of-autoclave semipregs, are more prone to wrinkling compared to low bulk factor plies, e.g. traditional prepregs. To improve the laminate quality and reduce the risk of fiber waviness, pre-consolidation every 4-5 layers using a vacuum bag is recommended. This is especially important for reinforcements with high bulk factors. However, Lightfoot et al. [127] reported that frequently conducted debulks during hand lay-up had no influence on the wrinkle formation compared to non-intermediate debulks.

The relationship shown in Eqn. (3) is not valid in corner regions, because of the curvature, the material undergoes a more complex compaction, i.e. corner thinning and thickening. Typical values for the bulk factor [126] range between 1.08-1.17 for unidirectional plies and 1.15-1.4 for woven fabrics, meaning a ~8-17 %, respectively ~15-40 % lower final thickness compared to initial laminate thickness. Levy and Hubert [128] developed an analytical model for the prediction of thickness deviation in both male and female corner regions by distinguishing between two phenomena. The friction dominated mechanism describes the interply friction which can hinder the layers from adapting to the mold geometry, thus preventing a proper compaction in the corner [82]. In a previous work by Hubert & Poursartip [129], they stated that even if interply slippage occurs, the bagged surface may differ from the facing mold surface due to the curvature in the corner. The available consolidation pressure in the part then differs from the expected vacuum bag pressure. Levy and Hubert [128] called this the pressure dominated phenomenon. The pressure dominated model predicts a lower bound, which is even negative (e.g. corner thinning) for the male case, and the friction dominated model predicts a higher bound.

The friction coefficient μ between the prepreg plies can be identified by characterization techniques using specially designed devices, i.e. pull-out tests and friction sleds, or by adapted rheometers [101,130,131]. Typical values for the friction coefficient μ of 5320 resin system range between higher values of approximately 0.17 for woven fabrics and lower values of 0.1 for unidirectional plies [128]. However, more important than absolute values of the friction coefficient are dependencies like temperature, normal pressure and relative motion speed.

Farnand et al. [132] studied the micro-level mechanisms for wrinkle formation of partial impregnated out-of-autoclave prepregs systems with 'Engineered Vacuum Channels' in Hot Drape Forming (HDF) consolidation over an external radius. The combination of these channels and low forming temperature, promotes intra-ply separation of fibers in 0° plies that leads to partial waviness of the ply during forming. For 90° plies, rolling of fibers was observed as the micro-level mechanism that leads to wrinkle formation during bending-induced compression.

2.3 NON-UNIFORM PRESSURE DISTRIBUTION

2.3. Non-uniform pressure distribution

2.3.1. Co-bonding (or pre-cured parts in LCM process)

Large stiffened composite panels used in aircraft, e.g. pressure bulkheads, are often produced in a co-bonding process, i.e. pre-cured skins are co-bonded with wet stringers or also vice-versa, when pre-cured stiffeners are co-bonded to the wet skins and webs in an autoclave process. The co-bonding allows for an integral design that reduces or even eliminates drilled holes and mechanical fasteners. This, in turn, reduces complexity, weight, material and tooling costs etc. However, co-bonding may also lead to undesirable effects such as fiber waviness, voids, adhesive pockets and resin pockets. These effects typically occur at the stiffener edges, as shown in Figure 12 [133].

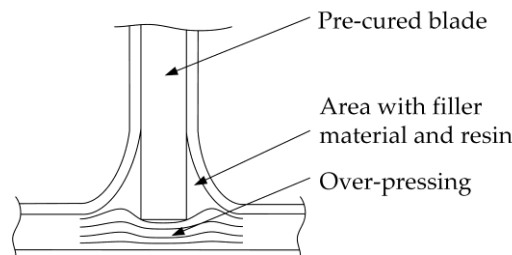


Figure 12. Example of co-bonding of a pre-cured stringer onto wet face layers leading to fiber waviness due to non-uniform consolidation pressure distribution.

Rubber pads can be used to achieve better pressure distribution [134,135]. Similarly, rubber-die molding processes [104], which are closely related to matched-die molding but at significantly cheaper mold costs, may reduce the risk of wrinkles in the part through more evenly applied pressure.

2.3.2. Telegraphing effect of face sheets at honeycomb core

The telegraphing effect [136] is a result of the integral fabrication of sandwich structures. In production, the face sheets are placed directly on the honeycomb core in a wet lay-up process. The sandwich structure is then cured in the autoclave at elevated pressure. The use of large cell size honeycomb cores in sandwich structures in combination with thin skins may result in telegraphing effects, which are characterized by a dimpled outer surface, illustrated in Figure 13 (a). Waviness in form of indentions, Figure 13 (b), can also occur in the face sheets located at the tool side of the sandwich structure due to a high local consolidation pressure at the contact zone. These dimples are treated as small-sized waviness. A smaller cell size also improves the surface appearance and bonding quality due to its larger bonding area, but also increases its weight and cost. Secondary-bonded face sheets can completely eliminate telegraphing

[137]. Riss et al. [138] developed an anti-telegraphing solution with additive layer manufactured honeycombs.

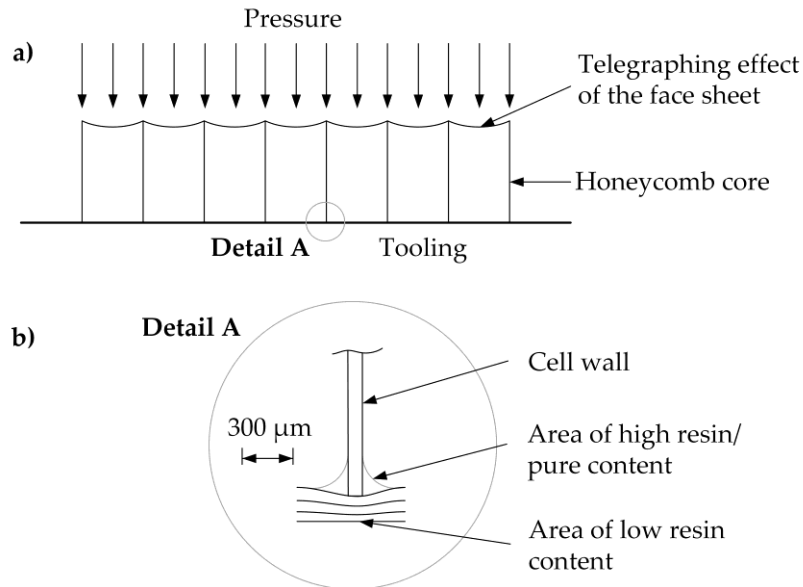


Figure 13. a) Telegraphing effect of thin layers on top of a honeycomb core; b) waviness in tool side face layers due to non-uniform consolidation pressure.

2.3.3. *Welding spots*

During spot welding of thermoplastic laminate stacks, indentations in form of wavy layers can occur due to the local elevated contact pressure of the welding horn and resulting softening material behavior caused by increased temperatures (Figure 14).

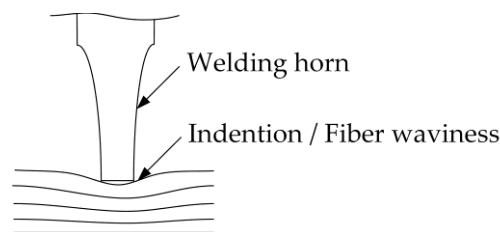


Figure 14. Illustration of a horn locally welding the laminate stack leading to fiber waviness due to uneven pressure distributions.

These ply stacks are primarily positioned by the welding spots and further processed in a forming step. Fischer et al. [139] reported that after consolidation, the imprints remain distinct atop the compacted sample, and the previously disrupted fibers are clearly recognizable. If possible, these welding spots may be positioned in non-critical areas of the part.

2.3 NON-UNIFORM PRESSURE DISTRIBUTION

2.3.4. Ply and vacuum bag bridging

Bridging is an effect of unsuccessful draping where the reinforcement [127,140] and/or layers of the vacuum bag [27,135,141] are not in contact with the mold surface potentially caused by improper lay-up and debulking. Some bridging is often inevitable and causes wrinkling [1]. Bridging can be observed in smaller corner radii with a longer limb length (distance from the corner to a free edge, shown in Figure 15) which would allow for a necessary slip of the plies into the corner, transitions of ply numbers (tapered laminates), resulting from gaps and overlaps. At low resin viscosities and high consolidation pressures, matrix migration can be observed in bridged areas in radii when resin is squeezed into the outer area. Friedrich et al. [106] explains this phenomenon as a lack of time for the inter-ply slip deformation mechanism to occur.

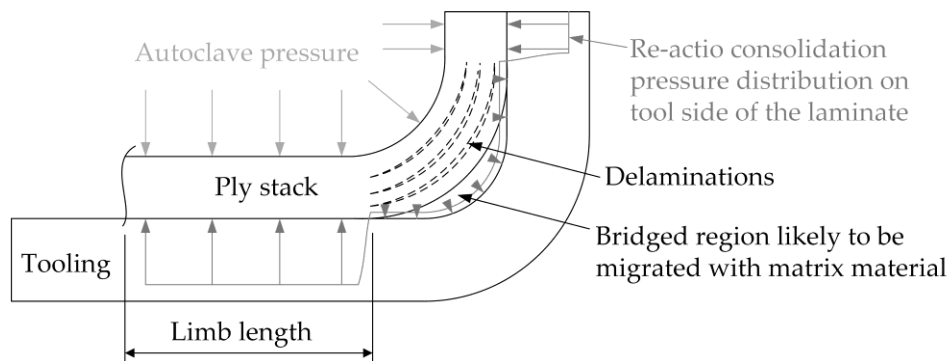


Figure 15. Ply bridging in internal corner radius leading to matrix migration.

Incorrectly placed vacuum bags, illustrated in Figure 16, can cause wrinkles to form in female corners when the vacuum bag is bridged [141]. Flexible silicon rubber pads or “dog ears” can be used to avoid bag bridging compared to a conventional vacuum bag lay-up [27,135]. The vacuum bag may not be able to follow the deformation that occurs during the consolidation of the laminate. This influence is increased when prepreg systems with a high bulk factor are used, e.g. semi-impregnated out-of-autoclave (OOA) prepreps. For this reason, there may be a lack of pressure in the resin in the corner area, leading to void growth. When atmospheric pressure prevails on the outside, the vacuum bag does not deform and does not slip due to the low compaction pressure. Increased consolidation pressures in autoclave processes can cause the vacuum bag to slip and reduce the amount of bridging, although shear forces due to the friction between vacuum bag and plies may force the layers into the corner radius thus leading to fiber waviness. Lightfoot *et al.* [127] achieved an elimination of wrinkles in autoclave cured laminates with bridged 0° plies in the radii of a female U-shaped tool by increasing the frictional shear stress between part and tool through the removal of the release film slip layer between the first ply and the tool.

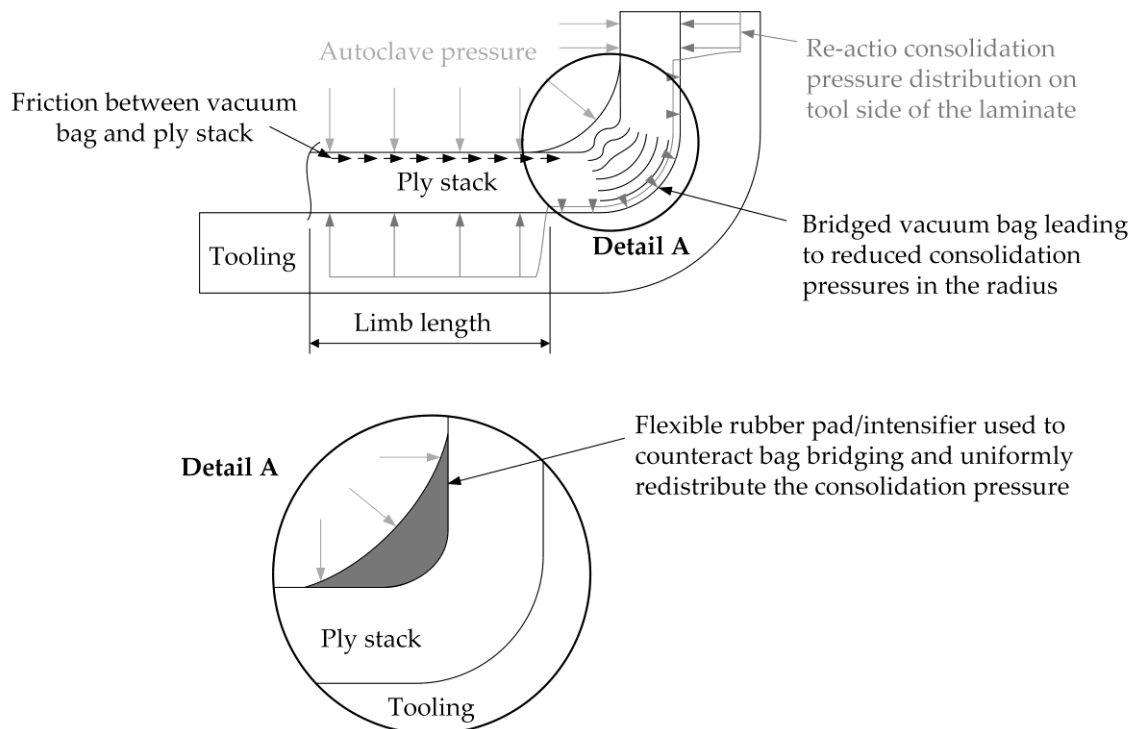


Figure 16. Vacuum bag bridging leading to low compaction pressure in the corner area, fiber waviness and increased void growth.

2.4. Interaction between tool-ply and ply-ply

Tool-ply and ply-ply interactions can be described by viscous friction laws. The sliding between ply and ply as well as ply and tool is affected at the interface by the coefficient of friction [102]. High frictional forces can cause in-plane buckling of the fiber tows and out-of-plane wrinkling of the fabric. The parameters that influence the friction coefficients are mold surface roughness, fiber tow surface roughness, presence of binders, presence of liquid resin, and processing temperature, which causes viscosity changes. Tack and drapeability [102] are also important quality characteristics of prepregs. Tack or stickiness is defined as the ability of a partially cured prepreg layer to adhere to the mold surface and to another partially cured prepreg layer without forming chemical bonds. Prepreg with too little resin on the surfaces has low tack and may need to be heated to increase its tack during layup. On the other hand, if the surfaces are resin rich and there is less resin inside (e.g. vacuum channels in out-of-autoclave prepregs), the prepreg may separate at the center during the layup process.

2.4.1. *Inter-ply slippage*

The formation of waviness is dependent on the frictional behavior between the plies. If the friction is sufficiently low, the excess length (limb length) can be dissipated

2.4 INTERACTION BETWEEN TOOL-PLY AND PLY-PLY

into the rest of the part by shearing in the layer interphase. At the beginning of the curing process, the shear and Young's moduli of the resin are very low [142]. These may decrease even further when temperature increases and viscosity drops in the first step, which allows a certain amount of ply movement to occur before cross-linking increases the material properties. The two major inter-ply forming mechanisms, namely inter-laminar slip and inter-laminar rotation/shear, are illustrated in Figure 17.

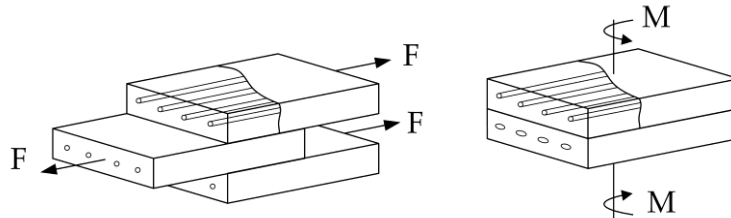


Figure 17. Inter-ply forming mechanisms (Inter-laminar slip and inter-laminar rotation/shear).

Inter-ply slip or inter-laminar slip [91,106,143–147] is a relative shear movement of two adjacent laminate layers. It occurs when layers slip or slide relative to each other when the flat prepreg stack is deformed over a single curved surface, e.g. a corner radius. In liquid composite molding processes, the inter-ply slip is supported by the liquid resin, which acts as a lubricant between adjacent plies, especially in low viscosity resins. According to [143], inter-ply slippage is considered to be the principal mechanism that prevents the occurrence of wrinkles during the shape change. Inter-ply slip can also occur between plies of woven fabric [97]. Woven fabrics are more extensible compared to unidirectional materials due to the undulations which allow a certain straightening of the fibers when forming over a radius. According to Murtagh et al. [97], inter-ply slip only occurs once the fiber tows have been straightened and become inextensible. Conversely, the crimped nature of the tows also means that the plies exposed to compressive stress tend to buckle. When the ply stack is deformed over a double-curved surface, e.g. a spherical dome, (see 4.2.2), the mechanism of intra-ply shearing is more common. This is an in-plane shearing mechanism where the fibers move past each other within each ply. For woven fabrics, intra-ply shearing occurs in the form of a trellis effect (see shear locking of woven fabrics in Section 4.6.2) in which the angle between the initially orthogonal fiber directions is decreased. Stresses are, according to [148], a function of time, temperature and processing rate. The stress needed to induce inter-ply slippage and shear, decreases with increasing temperature and increases with increasing deformation rate, and is significantly higher than the shear stress needed for inter-ply slippage [143]. Researchers [103,148,149] have identified the dependence of buckling on deformation rate and temperature during forming of composite sheets. The stresses during forming may be partially or fully relaxed by inter-laminar slippage, if given enough time to do so, as shown in Figure 18. According to Friedrich et al. [106], inter-ply shear can be regarded as the result of a pressure/velocity gradient between adjacent plies of the laminate. However, if the

forming velocity is too low in forming processes of reinforced thermoplastic materials, the actual temperature of the laminate may drop below a temperature level where inter-ply slip can no longer occur. In this case, the shear stress acting on the plies does not exceed the shear yield stress of the matrix material, which ultimately leads to fiber wrinkling at the compressed inner face during bending.

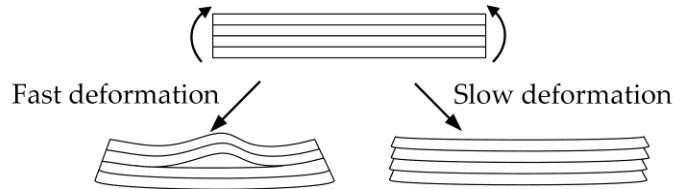


Figure 18. Formation of wrinkles as a result of deformation rate, adapted from [148].

2.4.2. CTE mismatch

The longitudinal stiffness of unidirectional composites is much higher than the transverse stiffness, and the longitudinal coefficient of thermal expansion (CTE) is much lower than the transverse CTE [87]. Typical coefficients of thermal expansion for composite materials and metals are given in Table 2. The anisotropy of composite materials may be an advantage from a structural point of view, but is also a main reason for process-induced deformations. The curing of high-performance composites typically happens at elevated temperatures. Especially the cool-down process/rate leads to a significant CTE mismatch.

Table 2. Typical coefficients of thermal expansion for composite materials and metals.

	Coefficient of thermal expansion [$10^{-6}/^{\circ}\text{C}$]	
CFR-Epoxy – UD longitudinal	0.3	[150,151]
CFR-Epoxy – UD transverse	35	[150,151]
CFR-PEEK – UD longitudinal	0.4 (23-143°C) – solid state 0 (143-343°C) – rubbery region	[152]
CFR-PEEK – UD transverse	30 (23-143°C) – solid state 80 (143-343°C) – rubbery region	[152]
CFR-PEEK – quasi isotropic	2.9 (23-143°C) – solid state 7 (143-343°C) – rubbery region	[152]
Neat epoxy resin	55 - 76	[150,153,154]
Carbon fiber - longitudinal	-0.4 - -0.75 (High strength - High modulus fibers)	[27,154]
Carbon fiber – transverse	8	[154]
Glass fiber	5	[27,153]
Aluminum	12-25	[27,155]
Steel	7-12	[27,150]

Residual stresses can also occur due to a CTE difference between fiber and matrix [87,156]. Several studies [127,157] have identified the CTE mismatch and, consequently, the tool/part friction (slippage) as the main phenomena leading to fiber

2.5 LAY-UP SEQUENCE

wrinkling. Additionally, Kugler and Moon [157] have shown the significant influence of the cooling rate and length. The prediction of instabilities originating from the differences in CTE is very complex, as shown in the studies of Dodwell *et al.* [82] and Belnoue *et al.* [158].

2.5. Lay-up sequence

In general, the lay-up sequence has a strong influence on the formability and resulting out-of-plane deformations. In [159] it is reported that the stacking sequence has a strong influence on the formability of thermo-stamped parts. They observed out-of-plane wrinkles and ply separation in quasi-isotropic 0/90/45/-45 laminates, but not in [0/90] laminates. Hallander *et al.* [90] also stated that [0/90] and [45/-45] lay-ups in a UD prepreg are less sensitive to out-of-plane defects compared to a quasi-isotropic lay-up. The results of forming studies carried out by Friedrich *et al.* [106] have shown that the instabilities such as in-plane wrinkles and out-of-plane buckles, only occur in distinctive areas of diaphragm-formed parts which can be directly related to the lay-up of the laminate.

2.5.1. Gaps and overlaps

Whenever individual plies are butt-spliced, whether manually or automatically, gaps or overlaps can occur. However, the phenomenon of gaps and overlaps is strongly related to automated fiber placement (AFP) and automated tape laying (ATL) processes and its steering methods. When locally placing tape layers in a laminate according to the load path, the resulting laminate typically consists of a large number of gaps and overlaps, which can be of different sizes and complex combinations [3]. Overlapping plies lead to humps and gaps may force subsequently positioned plies to move into the gaps during the consolidation step, both resulting in fiber waviness. These effects on the mechanical properties of the laminate are still under investigation and the existing results spread between 5-30 % [71,111]. Lukaszewicz *et al.* [118] reported that the tolerance in head movement, steered fibers and row width variations contributes to gaps and overlaps. Lan *et al.* [72,160] experimentally and numerically studied the mechanical properties of AFP laminates containing gaps and overlaps, which were cured with and without caul plates. The use of caul plates is critical during polymerization, as it can prevent thickness variations and allows defects to heal. Belnoue *et al.* [3] stated that the influence on the final fiber path and ply geometry from gaps and overlaps is not their nominal as-deposited position, but a function of what happens to the laminate in the subsequent processes, such as debulking or consolidation. This should be taken into account in manufacturing practices and the analysis of such defects.

According to Elhajjar *et al.* [141], a special form of gaps which may lead to wrinkles can be found in sandwich structures which are resulting from core splicing.

2.5.2. *Ply drops in tapered laminates*

The majority of real composite components contain ply terminations, also called ply drops in tapered laminates, within the part due to varying numbers of plies between two adjacent regions of the part and e.g. the requirement for local reinforcements. Examples of tapered composites containing fiber waviness and their mechanical evaluation can be found in [161]. Possible manufacturing effects leading to fiber waviness in ply runout (tapered) regions are shown in Figure 19. Design rules for thickness transitions are generally well established [86]. However, Hart-Smith [162] stated, that poorly made ply drop regions, where the consolidation of the ply drop region can lead to additional fiber waviness, can affect the components properties more negatively than a set of well-made external ply drops. The mechanism of wave formation is similar to that in a corner radius as described in Section 4.2.4. The change in part thickness generates an excess length of the plies, which can be dissipated by slipping between the plies or, if the friction between the layers is too high, by an out-of-plane movement that accommodates for this additional length. According to Potter et al. [86], fiber wrinkling tends to occur when the fibers are deformed out-of-plane to match the ply edges of the dropped plies. The obvious discontinuity of the thickness can also lead to small areas of resin accumulations due to bridging effects. The strength reductions are associated with out of plane stresses and resulting delamination emanating from the cut ply ends and the small resin-rich zones at the ends of the terminated plies.

Belnoue et al. [158] investigated the wrinkle formation in tapered laminates under double-sided rigid tooling due to variabilities in the ply thickness, which would lead to a mismatch between mold and preform. The thickness variation of the laminate upon consolidation is responsible for the generation of excess length. Processed in an autoclave using single-sided tooling and a vacuum bag, the tapered specimen would not exhibit any substantial wrinkles. Steeves et al. [50] carried out experimental studies on the compressive strength of composite laminates with terminated internal plies. The first mode of failure was shown to be fiber micro-buckling, which is governed by the induced fiber waviness of longitudinal fiber in the vicinity of the ply drop.

2.6 TEXTILE ARCHITECTURE

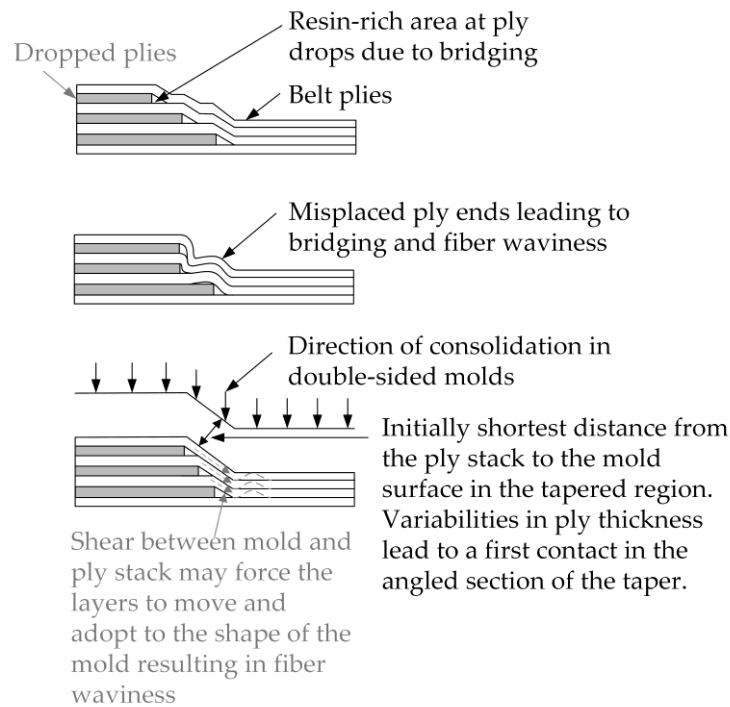


Figure 19. Possible manufacturing effects leading to fiber waviness in ply runout (tapered) regions, modified from [1].

2.6. Textile architecture

2.6.1. *Inherent undulations in woven and braided fabrics*

Undulations or crimped fibers are inherent to the internal structure of woven and braided fabrics due to the textile manufacturing processes with recurring undulations of warp and weft fiber bundles [163] and therefore have to be considered as a feature rather than a defect. The resulting uniform undulation depends on the selected weaving architecture, i.e. the most common weaving patterns plain, twill and satin. 3D fabrics that are reinforced through the thickness can be used to improve inter-laminar properties of the composite part. However, these interlocks induce additional distortions in the internal architecture, such as in-plane waviness, and reduce the mechanical properties [164] similar to stitches in non-crimped fabrics, as described in Section 4.6.3.

2.6.2. *Shear locking angle of woven fabrics*

Considering deformations on the micro/meso scale, in-plane and inter-ply shear, have been identified by several researchers as the important parameters governing the formation of aligned fiber composites [95,165]. Figure 20 schematically shows a shear load vs. shear angle plot obtained from a picture frame test carried out on a dry fabric.

Before shearing fabrics, the yarns are initially orthogonal to each other. As the intra-ply shear is initiated, the yarns begin to rotate and slide over each other. The friction between the yarns at the crossovers and viscous drag if a liquid resin is present contributes to the resistance to shear deformation, which is still relatively low at this level of loading. As loading increases, the adjacent yarns come in contact and press against each other, resulting in yarn compaction and increased shear stiffness. When the load is further increased, the yarns become locked. Loading beyond this locking point causes out-of-plane buckling of the fabric and the resulting deformation is not only due to shearing. The load increases very quickly to a high value after the locking of the yarns. [95,102,166,167]

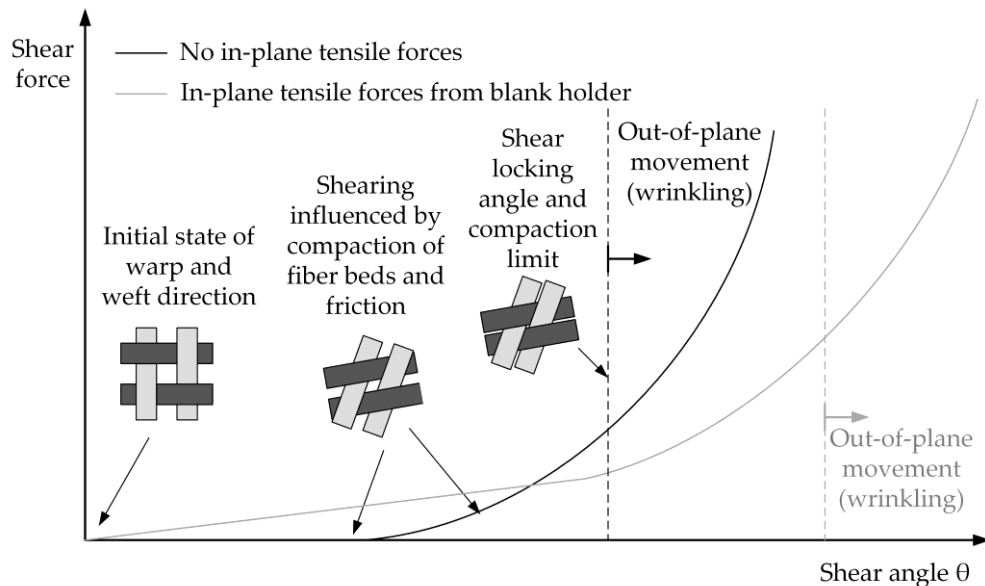


Figure 20. Shear force vs. shear angle plot of a picture frame test showing shear locking (trellis effect) with resulting increased load and out-of-plane movement in form of wrinkling.

The shear locking angle is mainly a function of the weave style and thickness of the tow. Beyond this angle, further deformation may cause out-of-plane buckling in the part. Tam and Gutowski [89] demonstrated that wrinkling will occur when the shear required to accommodate the material to a specific geometry is too high. In their analytical study, Prodromou and Chen [166] postulated, that woven fabrics wrinkle when they exceed a critical shear angle at which the tows “lock up”. They showed a number of driving parameters behind wrinkling, including high friction coefficients and inter-ply interactions. Since then, most work in the field has focused on shear angle measurement to predict wrinkle formation. Wrinkling is an out-of-plane phenomenon that occurs when less energy is needed for an out-of-plane deformation than for an in-plane deformation. Therefore, the concept of a locking angle is not necessarily sufficient to predict the occurrence of wrinkles, since wrinkling (position, shape, number, etc.) is strongly related not only to the bending stiffness but also to the tensile loading on the woven fabric [168,169]. Experimental and numerical results of Allaoui

2.6 TEXTILE ARCHITECTURE

et al. [170] also confirmed the statement, that wrinkling does not necessarily occur when the critical locking angle of woven fabrics is exceeded. They used blank holder loads to increase the in-plane tension and for the simulation they took the bending stiffness of the reinforcement into account. A sole determination of the onset of wrinkling based on the shear locking angle is also questioned by Boisse et al. [83] as the occurrence of out-of-plane movement is not directly related to locking angle. They carried out studies on the wrinkling behavior investigating the influence of different rigidities of textile, the onset of peculiar transition zones due to bending stiffness of fiber, and the slippage during forming using meso-level finite element models [83]. By applying tension to the reinforcement, it is possible to achieve a higher shear deformation, than one could expect if only the locking angle is considered. As a result, an increase in the tension applied on the interlock fabric tends to delay the onset of wrinkles [169]. A schematic illustration of this shift of out-of-plane wrinkling to higher shear angles is shown in Figure 20. The coupling between shear and tension is an effect related to the woven fabric and has been discussed in different papers, all showing a delay in the onset of wrinkling during pre-tensioned shear tests [171–173]. However, an increased tensile load on the yarns can lead to considerable (residual) stresses in the fabric. The integrity of the fibers may then be undermined by broken yarns and/or the ‘weave pattern heterogeneity’ phenomenon [169,174]. In a previous study, Boisse et al. [88] analyzed the wrinkling of textile reinforcements during forming processes using a simplified form of the internal virtual work where the tension, in-plane shear and bending parts are separated and related to load resultants on a unit woven cell. The importance of considering these terms have been already mentioned in Section 4.2.2. Hosseini et al. [167] performed an analytical-experimental study on the shear wrinkling behavior, i.e. locking and wrinkling onset, of plain woven composite preforms using bias extension test and picture frame test.

2.6.3. *Stitches in non-crimped fabrics*

Even if the term non-crimped fabrics (NCFs) [175–177] refers to semi-finished fiber products that do not contain any fiber misalignment, they usually contain small level in-plane fiber waviness due to stitches or binder yarns. This is an inherent feature of the material similar to undulations in woven fabrics. Amongst many other studies, Cao et al. [176] numerically studied the effect of in-plane fiber distortions in quadriaxial non-crimped fabrics (QNCF) induced by the stitching yarn on the mechanical properties using meso-scale finite element simulations. The effects of in-plane fiber distortions on the longitudinal elastic modulus were found to be insignificant. The modulus of the QNCF lamina resulted in a difference of 3.34% compared to the un-stitched composite with the same UD type. Cao also stated that this conclusion on the stiffness of QNCF composites is different from the open structure NCF composite in which the stitching may reduce in-plane elastic properties

by 10%-20%. Stitching induces a traceable effect on the longitudinal strength of QNCF lamina, but only a slight effect on transverse stiffness and transverse strength.

2.6.4. Stitches in dry fiber placements

Using dry tows in tailored fiber placement (TFP) methods [122,178] overcomes the disadvantages of the pre-impregnated tape placement techniques. Both methods use in-plane bending deformation of the tow/tape to achieve a curved tow path, but the dry and typically thinner tows in TFP tend to bend or shear much easier. Because dry tows do not have tackiness, they cannot be deposited without a suitable fixing method. The most common method uses an embroidery technique in which a numerically controlled stitching head stitches the tows onto a backup fabric, generally used together with an additional backup felt, to hold the preform together. Similar to ATL, curved tow paths can lead to local buckling of the fibers induced by the in-plane bending deformations. Additionally, the fabric may be wrinkled if the tension of the stitching yarn is too high and the softness of the backup felt allows the stitching yarn to move upward. In this case, the placed tows cannot be firmly attached to the substrate. Machine heads that operate without a tow feeding mechanism have to pull the tow by applying slight tension.

This tension force makes the placed tow move toward the origin of the curvature under the influence of the looseness of the stitching yarn, which increases the buckling intensity of the fibers inside the tow path and significantly enlarges the tow gap area outside the tow path [122]. A schematic illustration of fiber waviness induced by zig-zag stitches in TFP processes is shown in Figure 21.

To overcome the problem of fiber waviness induced by stitches in TFP, Hazra et al. [179] investigated the applicability of a soluble stitching yarn. The in-plane fiber misalignment was observed to still exist, but the out-of-plane crimp was reduced.

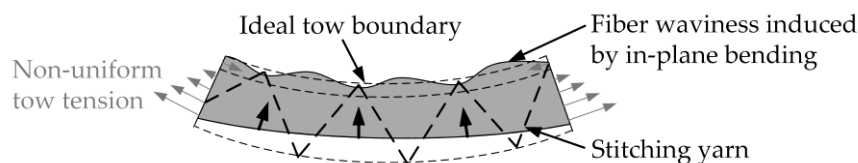


Figure 21. Schematic illustration of fiber waviness induced by zig-zag stitches in TFP process; adapted from [122].

2.7 FOREIGN OBJECTS

2.7. Foreign objects

2.7.1. Intended foreign objects (e.g. optical sensors, pins, inserts)

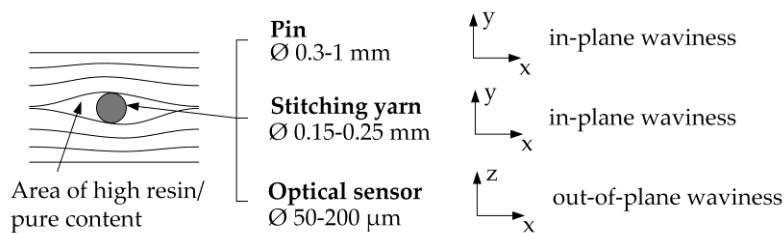


Figure 22. Schematic illustration of waviness induced by foreign objects, e.g. optical sensors, pins, inserts, or inherent to NCFs due to stitching yarns. This kind of waviness can be, dependent on the orientation of the embedded object, in-plane and out-of-plane.

In many cases, foreign objects (Figure 22) may be intentionally integrated into the material, e.g. optical sensors for strain measurements or structural health monitoring, metal pins for joining parts, or inserts, which in turn can interfere with the fiber orientation inevitably causing local fiber waviness. The wave characteristic depends on the size (diameter) of the embedded object. Typical values range between 0.3-1 mm for pins [180], 0.15-0.25 mm for stitching yarns [181] and 50-200 µm for optical sensors [182,183]. Embedded optical sensors lead to out-of-plane waviness, whereas stitches or pins lead to in-plane waviness. The diameter of optical Fiber Bragg Grating (FBG) sensors ranges from 52 µm to 125 µm [182]. The diameter of optical fiber sensors is a multiple compared to the most commonly used reinforcement fibers (glass: 5–50 µm, carbon: 5–10 µm). The reduction of the optical fiber diameter minimizes the distortion of the reinforcement fibers. However, not only size difference between optical and reinforcement fibers, but also the type of composite material used (unidirectional, woven fabric, stitched, braided, etc.) and the relative orientation of the optical fiber with respect to the reinforcement fibers influences the distortion [184].

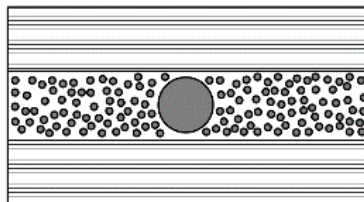


Figure 23. Optical fibers embedded parallel to the orientation of the reinforcement fibers can avoid fiber waviness as long as the diameter is small or the thickness of the composite layer is thick enough.

Several studies [183–187] have shown that there is little effect on the ultimate load carrying capacity of composites as long as small diameter optical fibers are embedded

between similar layers, i.e. avoiding stress concentrations when the optical fiber is predominantly oriented in the fiber direction of these layers (Figure 23).

By using z-pinning, the microstructure of laminates can be changed both beneficial due to the through-thickness reinforcement and also adverse due to distorted fibers in form of fiber waviness on the damage tolerance and mechanical properties. For the joining of hybrid components, e.g. composite/metal parts, 3D reinforcement technologies use for example cold metal transfer (CMT) welded pins (~ 0.8 mm diameter) or additive manufactured (AM) pins with specifically formed heads. The formed heads, e.g. spherically, improve the damage tolerance and give the joint additional resistance against the through-thickness separation of the two different materials. A comprehensive literature review of through-the-thickness reinforcements is given by Mouritz [180] and Sarantinos et al. [188].

2.7.2. *Unintended foreign objects (e.g. foils, blades, etc.)*

Unintentionally embedded foreign objects, like release film, tapes and tools (knife blades) are flaws during ply collation [27,189]. These defects lead to fiber waviness, similar to the intentionally embedded sensors or inserts, but can be avoided by strict compliance with process instructions and stringent quality controls.

2.8. Flow induced waviness

2.8.1. *Fiber wash-out*

If, in infiltration processes, the resin feed velocity and/or the injection pressure is too high, the resin viscosity is not low enough, or the fibers are only held loose due to low fiber volume fractions or poor tolerances of the mold, the fibers may be deformed by the flow of the resin [27,141]. Hallander et al. [90] stated, that materials with lower inter-ply friction are also more sensitive to fiber wash-out. In infiltration processes, especially when using higher pressures such as in Resin Transfer Molding (RTM), the injected resin can force the fibers to be locally 'washed' (Figure 24) mainly occurring at the injection port and also wholesale movements of plies leading to wavy regions and resin rich zones [1,190]. Due to the compaction of the layers in thickness direction by double-sided RTM molds, the layers are more prone to in-plane waviness. A basic method used to prevent fiber waviness is to choose optimized process parameters to minimize or totally eliminate fiber washing. By carefully choosing the LCM process parameters such as resin viscosity, pressure, and molding temperature, fiber movement during resin injection can be minimized [191].

2.9 CURE INDUCED WAVINESS

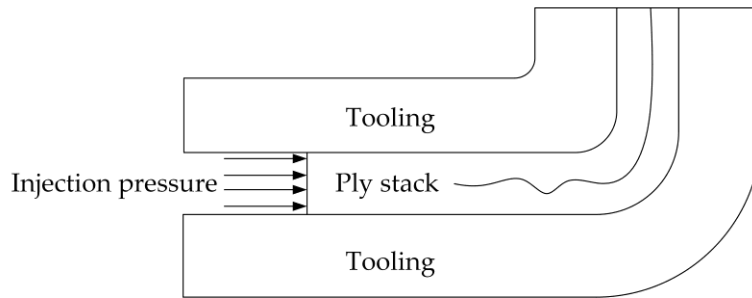


Figure 24. Schematic illustration of fiber washing effect.

2.8.2. Hydraulic effects (squeezing, transverse flow)

In forming processes such as thermoforming or compression molding, a non-hydrostatic pressure, similar to RTM processes, can lead to a fiber movement away from their original position and result in a wavy misalignment. Squeeze flow [137], as shown in Figure 25, describes the transverse flow of the fiber/resin/voids mixture as a function of the pressure distribution across the tow to yield the reduction in height and the increase in width.

Friedrich et al. [106] stated, that the local pressure gradients can arise from small variations in the laminate thickness and mold clearances. Further shear stresses that develop between the thermoplastic material and the mold surface may also result in transverse flow. The transverse flow is, according to Barnes [192], responsible for apparent stretching that can occur in a unidirectional laminate in perpendicular direction of the reinforcements. According to [193], this squeezing mechanism typically occurs at low temperature and low pressure, until a locking of the material occurs, the point at which the fiber bed reaches a configuration where it no longer deform. The squeezing flow, i.e. the laminate, behaves as a highly viscous incompressible fluid, according to Hubert and Poursartip [129]. After that, a transition from transverse squeezing to bleeding takes place corresponding with a change from transverse resin flow direction to bleeding. In Hot Drape Forming (HDF), the usage of stiffer diaphragms increases the squeeze flow due to higher forming pressure, however, the risk of out-of-plane deformations, e.g. wrinkling, is reduced [99].

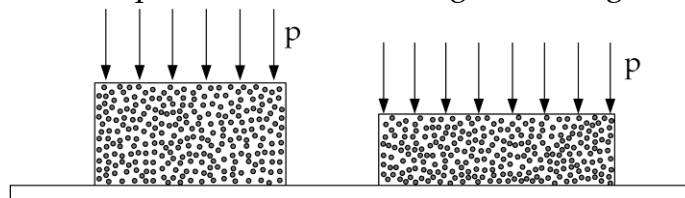


Figure 25. Schematic illustration of transverse squeeze flow.

2.9. Cure induced waviness

Parlevliet et al. [194] and Baran et al. [195] give comprehensive overviews of residual stresses in composite materials. Parlevliet et al. [194] states that fiber waviness

can be regarded as a defect, which has formed due to residual stresses. In part I of the publication series by Parlevliet et al. [196], three mechanical levels of residual stress formation were identified: micromechanical residual stresses (resulting from the shrinkage mismatch between the matrix and the fiber), interlaminar residual stresses (resulting from ply anisotropy in angle-ply composites) and residual stress gradients through the thickness (resulting from gradients in cooling rate, material density, thermal gradients, etc.). One method used to prevent ply wrinkling during curing is to keep the laminate thickness below certain limits in order to minimize exothermal heat generation. In general, the curing should be carried out at carefully controlled temperature gradients to minimize differences in the thermal expansion.

2.9.1. Volumetric shrinkage

Another important aspect in processing composite materials is the cross-linking of the resin. Chemical reactions during the curing process lead to shrinkage. In contrast to the resin, fibers exhibit no chemical shrinkage. Deformations are likely induced by the CTE mismatch, described in Section 4.4.2, between fiber and matrix, and the curing shrinkage of resin. The exothermic reaction during curing and the corresponding shrinkage in thermoset systems, or physical shrinkage in fiber reinforced thermoplastics, affects the formation of sink marks which result in fiber waviness. The temperature changes experienced by the composite and the volumetric shrinkage of the matrix are also reported to induce waviness [157,194]. The fiber waviness can occur due to both the bulk factor (see Section 4.2.4) and shrinkage in the thick-walled areas of transitions, e.g. T-joint shown in Figure 26.

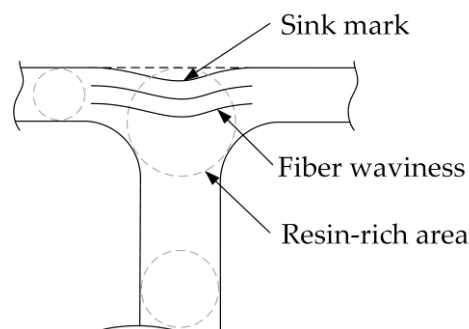


Figure 26. Shrinkage in resin-rich areas, e.g. T-joints.

2.9.2. Large temperature gradient in thick laminates

Besides the ply-tool CTE mismatch, sufficiently high temperature gradients that are present through the thickness of the laminate can cause fiber waviness. Since thick laminates are prone to large temperature gradients throughout the thickness, wrinkling is often induced in thick laminates [194,197], e.g. those found in wind turbine blades. Parlevliet et al. [194] concluded, that one of the results of residual

2.10 UNIQUE CHARACTERISTICS OF FABRICATION PROCESSES

stresses is fiber waviness. The presence of sufficiently high thermal residual stresses can lead to fiber waviness during the curing due to a mismatch between the coefficients of thermal expansion of the composite constituents [157]. The difference between the coefficients of thermal expansion of fiber, matrix, and mold can be several orders of magnitude. This often leads to residual stresses in the composite during the cooling step of the process. When the fibers experience axial loads during processing, e.g. due to thermal residual stresses, then fiber waviness may be observed due to micro-buckling. This mechanism was described by Bhalerao [198] who has developed a stress analysis model to obtain the laminate's in-process thermo-viscoelastic stress state and the fibers' thermo-elastic stress state. The fiber stress state can then be computed and used in the micromechanical fiber stability model to predict the viscoelastic buckling of elastic fibers. This phenomenon leads to the so-called "growth-of-waviness" in composite laminates. Elevated cooling rates can lead to compressive stresses on the laminate surface, while slower cooling rates avoid significant temperature gradients through-the-thickness of the part and allow time for stresses to relax [157].

2.10. Unique characteristics of fabrication processes

2.10.1. *Filament winding*

Fiber waviness is one of the most significant manufacturing effects in filament winding processes, however, the mechanism behind the occurrence is not completely clear. Fiber waviness in filament winding processes may result from insufficient winding tension [102], due to local fiber micro-buckling arising from the compression load caused by the shrinkage of a metal jig [199], or due to the volumetric changes during resin bleed-out in thick wound structures [200]. Parlevliet et al. [194] advised to use a sufficiently high tow-tension when winding composite cylinders as well as a low as possible mismatch between the composite and mandrel materials' CTE. According to Mallick [102], an inadequate winding tension and misaligned rovings can be caused by unstable fiber paths that cause fibers to slip on the mandrel and may cause fibers to bunch together, bridge, and improperly orient in the filament-wound part. Studies [201,202] have shown, that fiber waviness found in wound thermoplastic cylinders, are primarily affected by the mandrel material, not the cooling rate. According to Baker et al. [200], the waviness is mainly caused by volumetric changes during resin bleed-out in thick wound structures. It can be avoided by minimizing the amount of resin that needs to be removed and by maintaining the correct tension of the filaments during winding. Waviness can also occur in thick filament wound structures where the buckling of fibers results from the pressure exerted by the over-wrapped layers [203]. Springer et al. [204,205] developed a model which is able to

describe changes in fiber tension and fiber position due to moving fibers during processing.

2.10.2. *Pultrusion*

Fiber waviness originating from pultrusion processes represent a special characteristic due to manufacturing specific mechanisms. Pultrusion is a process for manufacturing composite profiles with a constant cross section. The process is characterized by low labor input and a high efficiency in the conversion of raw materials, as it is a continuous processing technique that does not require any secondary finishing steps. The reinforcements, e.g. UD rovings or filament mats are continuously fed through a guiding system. The dimensional changes must be controlled during processing to improve the product quality in terms of geometrical tolerances. The thermal and cure history together with highly non-linear resin phase transitions (viscous-rubbery-glassy), described in [206], make the process complex to control and have a significant influence on the quality of the final composite part. The resin undergoes large changes in its material properties during phase transitions, most significantly in its thermal expansion and elastic modulus [207]. The principal mechanisms causing process induced stresses and shape distortions in pultruded composites are summarized in [206–209]. Some of the defects found in pultruded products, such as fiber bunching, fiber shifting, wrinkles, and folding of mats or woven rovings, are examples of fiber misalignment that can reduce the structural properties of pultruded products [102]. Coogler et al. [210] examined the various process-induced imperfections that can occur in the cross sectional areas of pultruded GFRP profiles for bridge decks. In general, fiber waviness can be particularly pronounced within the flange-web joints/junctions in pultruded profiles [210–216], to the extent that the fibers often return upon themselves, essentially describing U-trajectories, as a web lamina transitions from the vertical to horizontal direction. Sebastian [211] characterized fiber waviness in pultruded profiles and experimentally investigated the ultimate mechanical behavior. Elhajjar [141] stated, that random in-plane waviness can occur in pultrusion due to temporarily/locally insufficient tow tension, e.g. from one of the feeding spools. An example of random waviness in pultrusion processes due to insufficient tow tension is schematically illustrated in Figure 27.

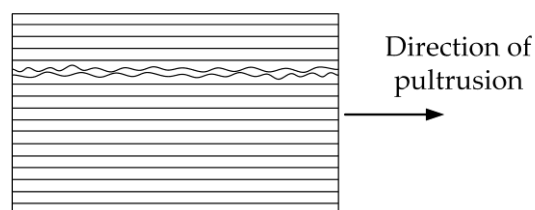


Figure 27. Random (stochastic distributed) waviness in pultrusion direction due to insufficient tow tension.

3. CLASSIFICATION SCHEME

The following section provides an overview of typically occurring wave shapes and suggests a classification scheme based on ten characteristic features.

3.1. Number and distribution of waves

Generally, waviness can be distinguished by whether there is a single wave, or a higher number of waves that can be either stochastically distributed (i.e., consisting of varying amplitudes and wavelengths) or in-phase distributed (i.e., with constant amplitudes and wavelength; Figure 28). The occurrence of single or distributed waves can be attributed to the bending stiffness of the layers.

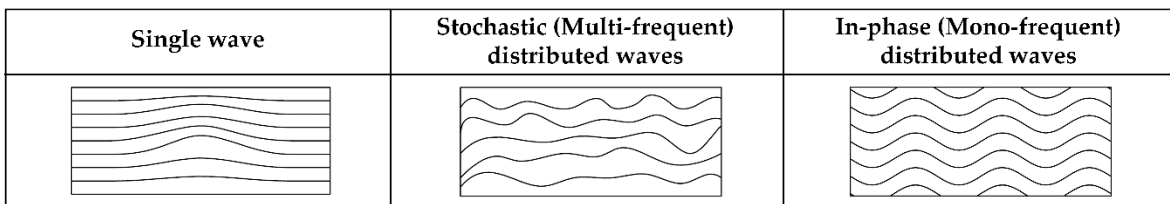


Figure 28. Single vs. distributed waviness.

3.2. Traditional differentiation of wave types – constant or changing wave amplitude

Another general distinction between uniform and graded waviness (Figure 29) is often used in literature [13,14]. In graded waviness, unlike uniform waviness, the amplitude changes in the thickness direction of the laminate. Graded waviness is typically embedded in the laminate, whereas uniform waviness is more likely to be visible on the surface. However, uniform waviness can be also fully embedded, but occur only locally and not across the entire thickness.

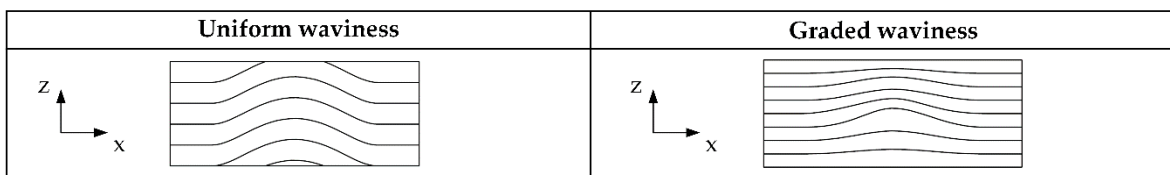


Figure 29. Uniform vs. graded waviness.

Hsiao and Daniel [13,46] mathematically described the uniform fiber waviness as a planar sinusoidal wave with an local amplitude defined by

$$v = A * \sin\left(\frac{2 * \pi * x}{L}\right) \tag{4}$$

where A is the amplitude and L is the wavelength. The deviation angle θ is described by a partial derivative of the spatial position of the wavy fibers v after x .

$$\tan \theta = \frac{dv}{dx} = \frac{2 * \pi * A}{L} \cos\left(\frac{2 * \pi * x}{L}\right) \quad (5)$$

Similarly to that, the graded waviness can be described as follows

$$v = A * \left(1 - \frac{|z|}{h}\right) \sin\left(\frac{2 * \pi * x}{L}\right) \quad (6)$$

$$\tan \theta = \frac{dv}{dx} = \frac{2 * \pi * A}{L} \left(1 - \frac{|z|}{h}\right) \cos\left(\frac{2 * \pi * x}{L}\right) \quad (7)$$

El-Hajjar and Petersen [15] alternatively used a Gaussian function to capture the bell curve of wavy plies, which was found to better represent the wave geometry.

$$f(x) = A e^{-\frac{(x-b)^2}{2c^2}} \quad (8)$$

A again describes the amplitude, i.e. the height, of the bell curve, e the Euler number, x the running coordinate, b the position of the maximum fiber deflection and c describes the width of the bell curve. This equation is further adapted by describing a wavy part A_w in a laminate with the nominal thickness h and the z -coordinate Z_k of the k^{th} ply.

$$v = A_w \left[1 - \left(\frac{Z_k - A_w}{h - A_w}\right)^2\right] e^{-\frac{x^2}{2c^2}} \quad (9)$$

The derivative after x again leads to the equation for the local fiber angle θ .

$$\tan \theta = \frac{dv}{dx} = \frac{A x e^{-\frac{x^2}{2c^2}}}{c^2} \left[\left(\frac{A - Z_k}{A - h}\right)^2 - 1 \right] \quad (10)$$

3.3. Phase characteristics of the wave form

The iso-phase model [217], also known as in-phase model, depicted in

Figure 30 (left), assumes all fibers to be in the same phase along the x -direction. Similar to uniform waviness, each small volume element of the composite between x and $x+dx$ is approximated by a unidirectional fiber composite, in which fibers are

3.4 VISIBILITY

inclined at an angle θ to the x-axis. In contrast to that, the fiber orientation θ of the random-phase waviness, shown in

Figure 30 (right), is randomly distributed at each x increment. In this case, the spatial position of wavy fibers can be described by

$$v = A * \sin\left(\frac{2 * \pi * (x - d)}{L}\right) \quad (11)$$

where d is the translation of the sinusoidally shaped fiber in the x -direction.

Although the description of the random phase waviness is a rather theoretical one, this form of waviness can be caused by shear stresses in the thickness direction of the laminate.

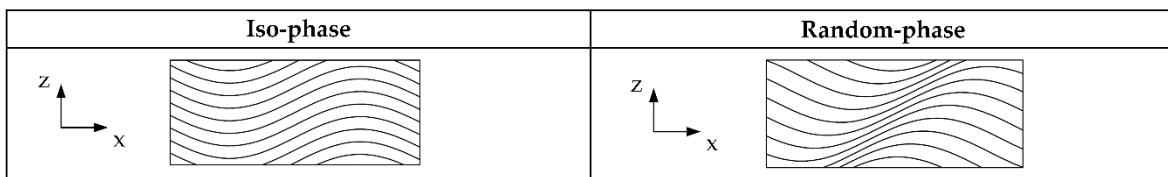


Figure 30. Iso-phase vs. random-phase waviness.

3.4. Visibility

In terms of detectability, outer visibility constitutes another classification (Figure 31). Embedded waves, i.e. not directly visible deviations of the fiber orientation from the outside surface, are more difficult to be detected compared to visible waves, due to differences in thickness t of the laminate or deviations from a planar surface.

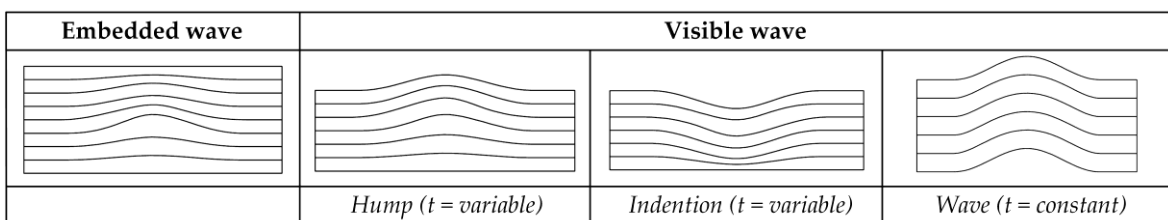


Figure 31. Embedded vs. visible waves.

3.5. Dimensional characteristics

With regard to the assessment of fiber waviness, the dimensional characteristic of waves is an important distinguishing feature. If the waviness changes one of its characteristics in the third spatial direction, this must also be taken into account. Figure 32 shows a representation of a 2D wave (left) and a 3D wave (right).

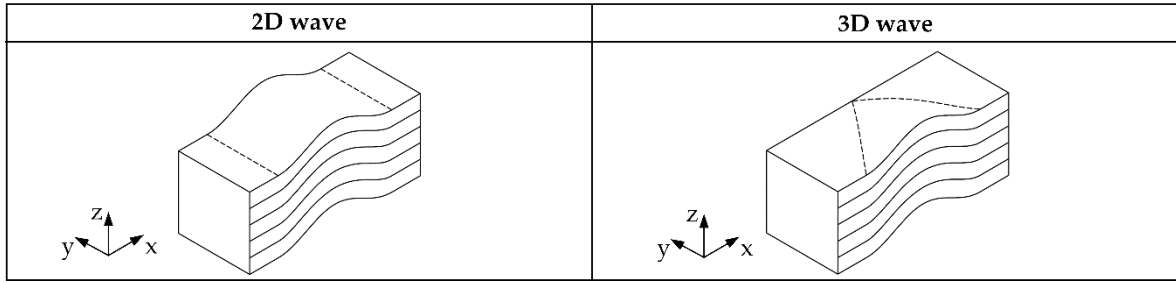


Figure 32. 2D vs. 3D waves.

The analytical description for uniform waviness in 2D, based on [13], is expanded for 3D waviness and the spatial position of the fiber v and the fiber angle θ can be written as:

$$v = \frac{A}{2} * \frac{y}{w} * \left[1 - \cos\left(\frac{2 * \pi * x}{L}\right) \right] \quad (12)$$

$$\tan \theta = \frac{dv}{dx} = \frac{A * y * \pi}{w * L} \sin\left(\frac{2 * \pi * x}{L}\right) \quad (13)$$

where w is the width of the wave in the third spatial direction.

3.6. Continuity of layers/laminate

Fiber waviness frequently occurs in laminate transition areas with varying thicknesses resulting from ply-drops, i.e. tapered laminates, or also through gaps and overlaps which are characteristically for automated fiber placement (AFP) processes. In general, these types of fiber waviness occur due to non-continuous layers compared to waviness in continuous layers or laminates (Figure 33).

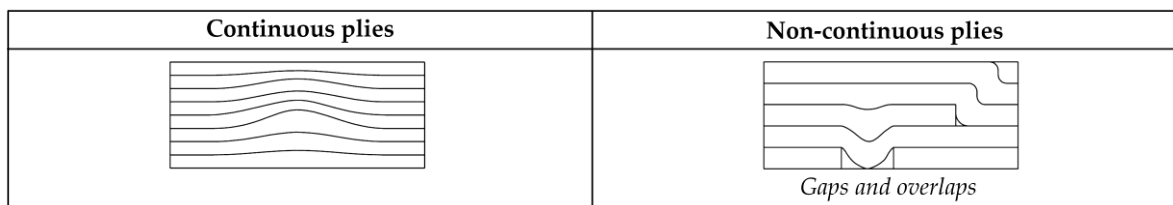


Figure 33. Waves at continuous vs. non-continuous plies.

3.7. Portion and position of the wavy region in the laminate

The ratio of wavy plies (Eqn. (14)) to the total number of plies represents a characteristic factor of local waviness where only a part of the laminate is wrinkled and the remaining layers are oriented according to the design (Figure 34).

$$\text{ratio of waviness} = \frac{\text{number of affected plies}}{\text{total number of plies}} \quad (14)$$

3.8 PHASE CHARACTERISTICS OF THE MATERIAL

Multidirectional laminates may be more prone to local fiber waviness due to varying (bending) stiffnesses of the plies. Camanho *et al.* [218] introduced strength correction factors to account for this position as well as the thickness of the layer.

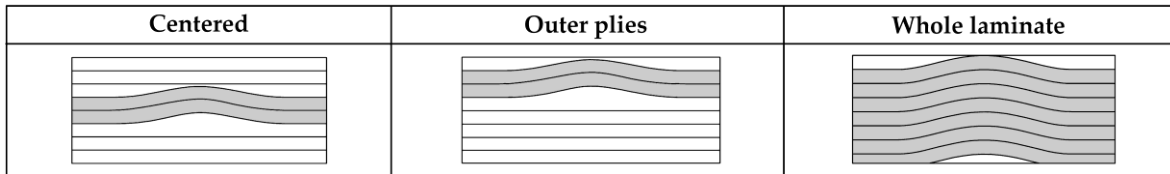


Figure 34. Portion and position of the wavy layers in the laminate.

3.8. Phase characteristics of the material

For the resolution of fiber and matrix in the undisturbed laminate the microscopic level is used. Manufacturing effects, such as bridging or fiber washing, can result in areas without fiber material that can be filled with excess resin. These areas are visible to the naked eye in many cases, i.e. in bridged corner radii, and are therefore referred to as macroscopic phases by resin accumulation. Especially in manual production steps, such as hand lay-ups, unwanted foreign bodies embedded in the laminate, such as carrier foils, knife blades, etc., can cause wrinkles which in turn can lead to additionally accumulations of resin in this area. This also leads to macroscopically different phases, in this case by foreign material. A schematic overview of this classification is shown in Figure 35.

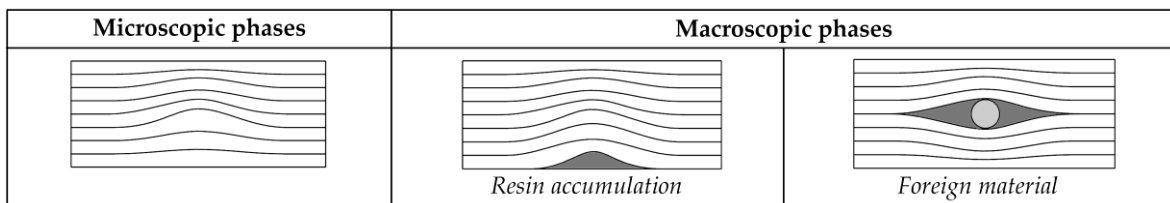


Figure 35. Microscopic vs. macroscopic distributed phases in wavy regions.

3.9. Influence of t/A ratio

The influence of wavy layers strongly depends on the affected thickness of the laminate (Figure 36). Especially in thin-walled laminates with a correspondingly large degree of waviness ($t \ll A$), in addition to the influences on the material properties, structural influences [12] become apparent. In such cases, a complex mix of both material and structural type behavior leads to strongly nonlinear geometric constraints, requiring the calculation of stresses resulting from the bending of the wave.

The substantial influence of both, the amplitude A and thickness t , in view of the resulting bending stresses are shown in a simplified analytical consideration, Eqn. (15), using the Euler-Bernoulli beam theory (neutral axis coincides with the beam centroid line, bending moment $M_B = F A = \sigma_x b t A$, where A is the amplitude, the moment of inertia for rectangular cross section $J_y = \frac{b t^3}{12}$ and $y = \frac{t}{2}$) leads to

$$\sigma_B = \frac{M_B}{J_y} y = \frac{6 \sigma_x A}{t} \quad (15)$$

Thus, the resulting bending stresses, with a maximum in the longitudinal center of the wave, increases with increasing amplitude and decreases with increasing thickness.

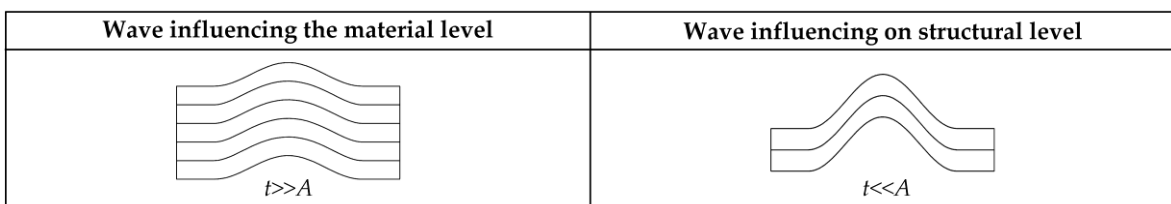


Figure 36. Material vs. structural level.

3.10. Geometric position of the wavy region in the part

There is a growing interest in the use of thick walled composite parts to replace complex metallic fittings for specific applications [219]. Additionally, the integral design of composite parts allows for an integration of several functions. However, these parts often have quite complex geometries and consist of radii, T-joints and varying wall thicknesses which are prone to fiber waviness. Examples of fiber waviness in areas of radii or T-joints are shown in Figure 37 (right).

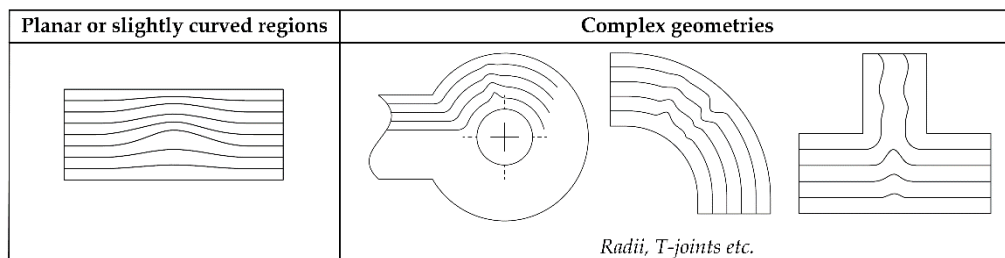




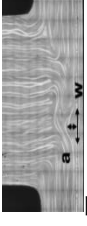

Figure 37. Waves in flat or slightly curved areas vs. complex geometries.

3.11 EXAMPLES FOR WAVINESS CLASSIFICATION

3.11. Examples for waviness classification

Some examples for waviness classification are shown in Table 3.

Table 3. Examples for waviness classification.

	Single	Uniform	Iso-phase	Wave	2D	Continuous	Whole laminate	Microscopic	Structural	Flat
	Single	Graded	Iso-phase	Embedded	2D	Continuous	Whole laminate	Microscopic	Material	Flat
	Stochastic distributed	Graded	Random-phase	Embedded	3D	Non-continuous	Whole laminate	Microscopic	Material	T-joint
	Single	Graded	Iso-phase	Hump	2D	Continuous	Whole laminate	Macroscopic	Material	Flat
	Number and distribution (single, stochastic or in-phase distributed)	Through-thickness wave form (Uniform vs. Graded)	Phase characteristics of the wave form (iso-phase, random-phase)	Visibility (embedded, hump, indentation, wave)	Dimensional characteristics (2D, 3D)	Continuity of layers/laminate (continuous, non-continuous)	Position (centered, outer plies, whole laminate)	Phase characteristics (microscopic, macroscopic)	Level of influence (material, structure)	Geometric position (flat or slightly curved areas, complex geometries)

4. NON-DESTRUCTIVE TESTING

It becomes increasingly important to be able to detect fiber waviness in composite materials as early as possible in the product development and manufacturing stages. The decision, if these irregularities are considered as manufacturing features, respectively effects, or as defects, is dependent on the size, number and location of the effects on the component. The assessment of out-of-plane fiber waviness in composite materials is strongly dependent on the accuracy of detection and quantification of the wave parameters such as amplitude, wavelength and position in the laminate. In the aviation industry, ultrasonic testing (UT) is the preferential method for the evaluation of composite materials. The evaluation of the ultrasound signal from different manufacturing effects is difficult and it often cannot be clearly decided whether there are actually wavy regions in the laminate or not. In this work, different non-destructive testing (NDT) methods were investigated, such as infrared thermography (IRT), digital shearography, eddy current testing (ET) and X-ray computed tomography (CT) to assess their potential for the detection and characterization of embedded out-of-plane fiber waviness in composite materials. These methods were applied on test plates with artificially embedded waviness with varying amplitudes, wavelengths and positions in the laminate and evaluated with respect to their ability of detecting the wrinkle morphology.

4.1. Experimental non-destructive testing

4.1.1. *Test plate fabrication*

The pre-impregnated polymer composite IM7-8552 (Hexcel Corporation, Stamford, USA) is used in this study. The nominal cured ply thickness of the unidirectional (UD) prepreg layer is 0.131 mm, according to the material data sheet. The test plates with a dimension of (400 x 150) mm² are fabricated in a two-step autoclave process following the recommended curing cycle for monolithic components. The lay-up procedure is schematically shown in Figure 38. Two wave configurations with varying depth positions in the laminate, i.e. center, top and bottom, were realized using a one-side male metal plate tooling in which the defined sinusoidal wave configurations were milled in with identical amplitudes $A=2$ mm but varying wavelengths $L_1=15$ mm (wave 1) and $L_2=10$ mm (wave 2). The thickness of the UD cross ply laminate (0/90) including the two types of sinusoidal waves was realized by 61 plies for ~8 mm laminate thickness for plate 1 and 76 plies for plate 2-4 respectively, leading to a laminate thickness of ~10 mm. The realized wave configurations and their positions in the laminate are schematically depicted in Figure 39. The laminate quality was verified by measuring the fiber volume fraction (67.2%, 0.9% STD) using wet chemical fiber extraction according to EN 2564 for 9 specimens.

4.1 EXPERIMENTAL NON-DESTRUCTIVE TESTING

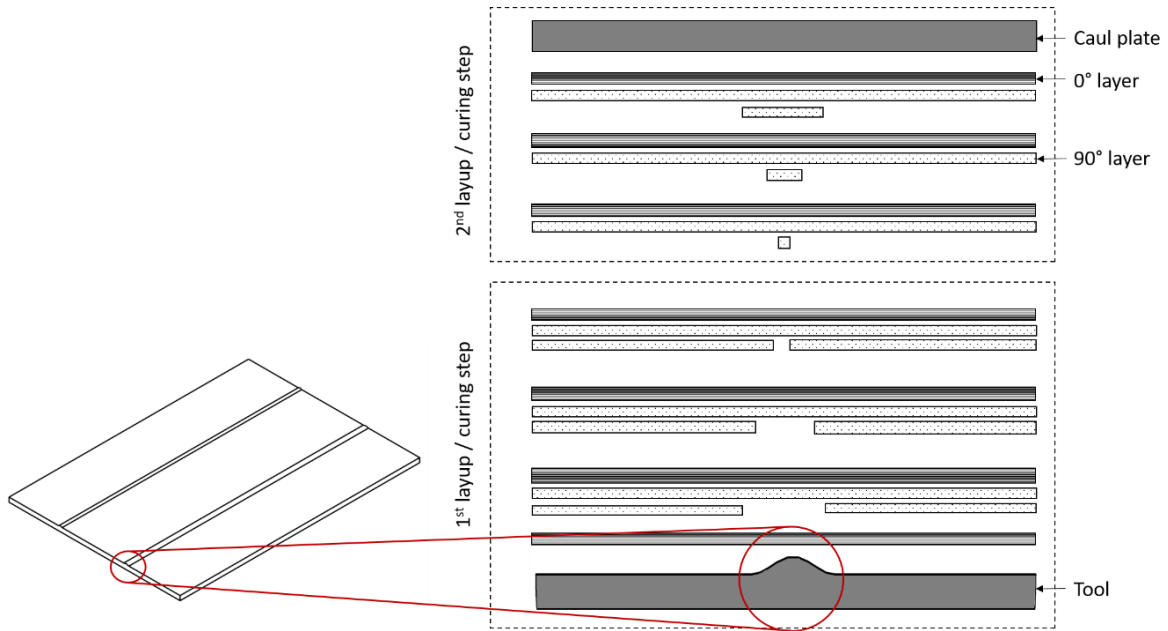


Figure 38. Two-step manufacturing method of cross-ply test plates with embedded out-of-plane fiber waviness using a male tooling.

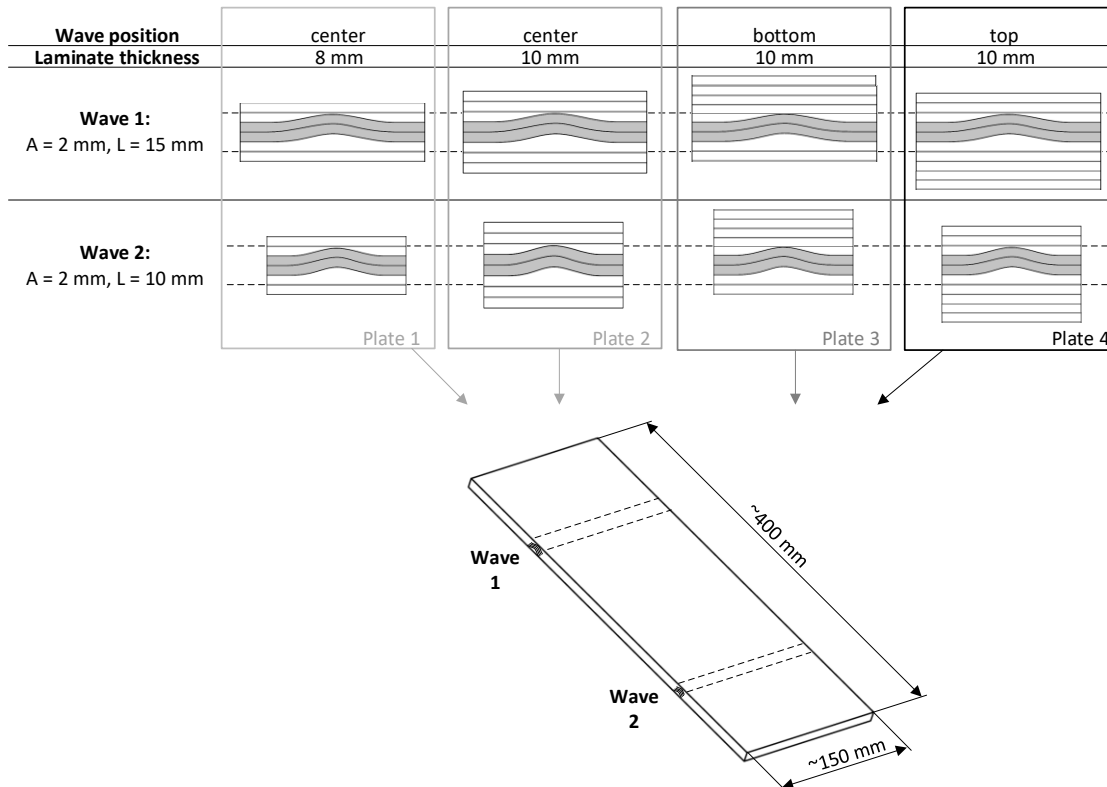


Figure 39. Realized wave configurations and their positions in the laminate.

4.1.2. Optical microscopy on polished samples

Samples were cut from each test plate and wave configuration (in total 8 images) and progressively polished using a Struers LabPol grinding and polishing machine (Struers GmbH, Willich, Germany), with a final polish using 1 μm grit paper. Microscopic images were obtained using an Olympus BX61 optical microscope (Olympus, Tokyo, Japan). To obtain an adequate image resolution enabling the identification of individual fibers, several images with a magnification of 50x were taken from the cross-sectional area and automatically stitched together using the post-processing image analysis software Olympus Stream (Olympus, Tokyo, Japan).

4.1.3. X-ray computed tomography (CT)

Inspection techniques based on X-ray absorption [220] have become standard methods for the non-destructive testing and characterization of defects in CFRP components. The basic principle of standard X-ray computed tomography (CT) is absorption, in which a three-dimensional volumetric map of the scanned part is reconstructed from a set of absorption radiographs generated at different angles. The general configuration of a CT is shown in Figure 40 and consists of a radiation source, a rotatable sample stage and a detector.

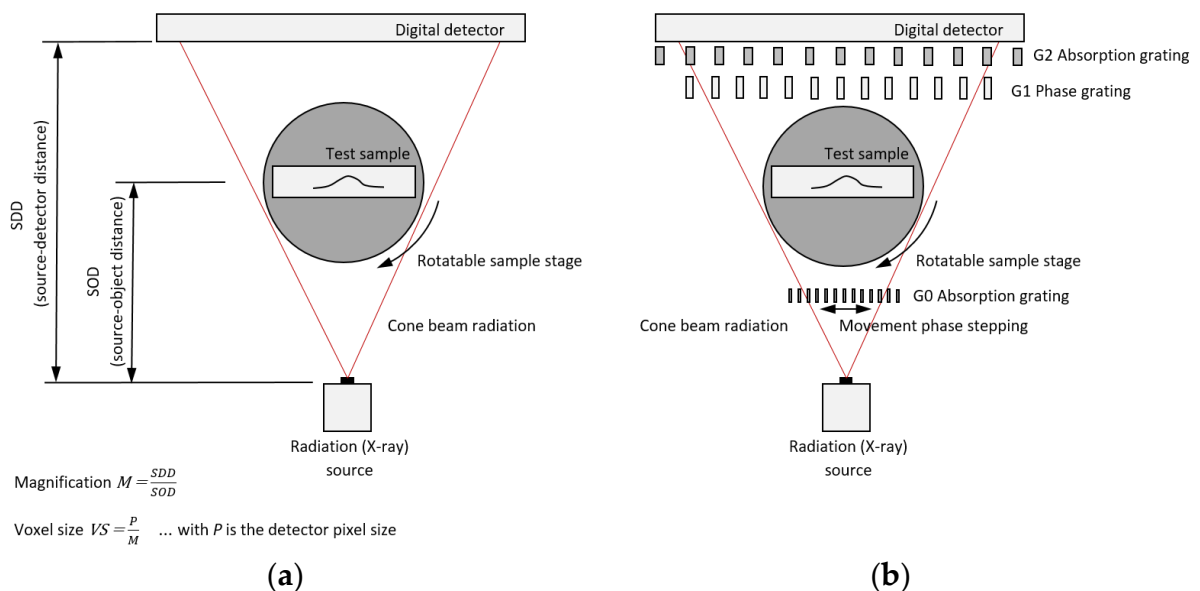


Figure 40. Test set-ups of X-ray computed tomography for the inspection of out-of-plane fiber waviness; a) conventional CT and b) Talbot-Lau grating interferometer CT.

X-ray sources with energies from 100 keV to 450 keV are used as radiation sources, generating a cone beam. The sample stage can be very precisely controlled and rotated to realize small angle differences between the projection images. The transmitted radiation is then recorded by a digital detector. The intensity of the X-ray beam

4.1 EXPERIMENTAL NON-DESTRUCTIVE TESTING

decreases exponentially with the path length x travelled in the material (Lambert-Beer law or attenuation law)

$$I = I_0 e^{-\mu x} \quad (16)$$

where the linear attenuation coefficient μ depends on the material. It applies:

$$\mu \sim \rho Z^3 \lambda^3 \quad (17)$$

with Z being the atomic number of the material, ρ the density of the material and λ the X-ray wavelength.

In industrial 3D X-ray computed tomography, resolutions down to ~ 50 nm can be achieved [221,222]. The achievable contrast of details is strongly dependent on the absorption coefficients of the transmitted materials. When scanning carbon fiber reinforced plastics, the absorption difference between resin and carbon fiber is low and a good X-ray image quality may be difficult to obtain.

4.1.3.1. Talbot-Lau grating interferometer CT (TLGI-CT)

Novel X-ray imaging methods based on the refraction and scattering of the X-ray beam passing through a material allow for a significant enhancement of the contrast. In addition to high resolution cone-beam CT measurements conducted in this study, an interferometric CT method based on the Talbot-Lau effect was used to measure the scatter caused by carbon fibers in the specimens. Compared to standard CT, reduced requirements in spatial resolution allow for visualization of fiber waviness at relatively large specimen dimensions. However, the extraction of refraction and scatter information requires increased measurement time. The specifications and chosen parameters of the devices used are listed in Table 4. The applied CT scan parameters for the individual samples are shown Table 5.

Table 4. 3D X-ray computed tomography device specifications and chosen parameters.

	μ CT RayScan 250E	High-resolution μ CT GE phoenix Nanotom 180 NF	Talbot-Lau μ CT Bruker SkyScan 1294
X-ray source	225 kV μ -focus and 450 kV mini-focus	180 kV sub- μ -focus	60 kV μ -focus
Detector system(s)	2048 x 2048 pixels (flat panel)	2304 x 2304 pixel (flat panel)	4008 x 2672 pixel (CCD camera)
Minimal voxel size	$\sim 5 \mu\text{m}$	$\sim 0.5 \mu\text{m}$	$\sim 5.7 \mu\text{m}$
Focal spot size	μ -focus adjustable mini-focus ~ 0.4 mm	adjustable	fixed $\sim 30 \mu\text{m}$
Sample diameter	< 300 mm	< 68 mm	< 20 mm
Sample height	< 2 m	< 150 mm	< 60 mm

Table 5. Applied CT scan parameters for the individual samples.

CT system	Sample (Image modalities/ CT modes)	Scanning parameters (Tube voltage; Tube current; Integration time; Nr. of images; Target-material, Pre-Filter)	Voxel size [μm]	SOD [mm]	SDD [mm]	Scanning-time [min]
RayScan 250 E	W1&W2 (AC)*	120 kV; 840 μA ; 999 ms; 720 ; W; 0.5 mm Cu;	155 μm	1030.5	1327.1	38 min
		120 kV; 450 μA ; 1999 ms;	60 μm	278.1	927.1	98 min
	W1 (AC)*	1440 ; W; 0.5 mm Cu;				
Nanotom 180 NF	W1 (AC)*	60kV; 210 μA ; 750 ms; 1900 ; Mo; none; 5/1	8 μm	40	250	146 min
	W2 (AC)*	50 kV; 340 μA ; 600 ms; 1800 ; Mo; none; 6/1	8 μm	40	250	130 min
SkyScan 1294	W1 (AC, DPC, DFC)*	40 kV, 1000 μA ; 600 ms; 900 ; W; 0.5 mm Al	22.8 μm	140	286	391 n

* AC... Attenuation contrast due to absorption
DPC... Differential phase contrast due to refraction
DFC... Dark-field contrast due to scattering

4.1.4. Ultrasonic testing (UT)

4.1.4.1. Ultrasonic microscopy

Ultrasonic/acoustic microscopy measurements were conducted using the ultrasonic microscope v8 system from KSI (Herborn, Germany) in pulse-echo technique. The system uses an ultrasonic immersion tank for transmitting the ultrasound waves to the object under investigation and to act as a delay line. This system allows measurements with frequencies up to 150 MHz. In contrast to conventional ultrasonic methods, special transducers with confocal sapphire lenses are used, which allow a lateral resolution of down to 5 μm . The frequency of the ultrasonic wave influences the lateral resolution of the examination as well as the penetration depth of the wave into the material, leading to a trade-off between penetration depth and image resolution. The lower the frequency, the higher the penetration depth, but the lower the lateral resolution. Additionally, the penetration depth also depends on the material properties. In this study, frequencies of 10, 15 and 100 MHz were used with 24, 38 and 40 dB amplification, respectively.

4.1.4.2. Pulse-echo and through-transmission inspection

Ultrasonic testing is an acoustic method where a piezoelectric transmitter sends ultrasonic pulses into the test object to identify defects due to the change of the signals in reflection (pulse-echo mode) or transmitted signals (through-transmission mode). Ultrasound starts at a frequency above the audible range of humans at ~20 kHz.

4.1 EXPERIMENTAL NON-DESTRUCTIVE TESTING

According to Smith [223], the frequency range from 0.5-50 MHz is most often employed for the ultrasonic inspection of materials. For composites of thicknesses between 2.5 and 13.0 mm, Michaels and Davidson [224] recommended to use 5-20 MHz. The ultrasonic wave is reflected at interfaces, such as inclusions, cracks, or at the end of the component. In composites containing out-of-plane fiber waviness, the ultrasonic waves undergo diffuse scattering due to the continuous change of incidence angle within the focal range of the beam, which causes signal changes quite similar to porosity [27]. To differentiate these defect types, the use of phased array ultrasonic testing is necessary. The principle of scattering at wavy layers is shown in Figure 41. As indicated by the red arrows, the reflection of the incident wave is directed towards different angles, hence causing a drop of measurable intensity of the intensity received from the backwall-echo when compared to the undisturbed regions.

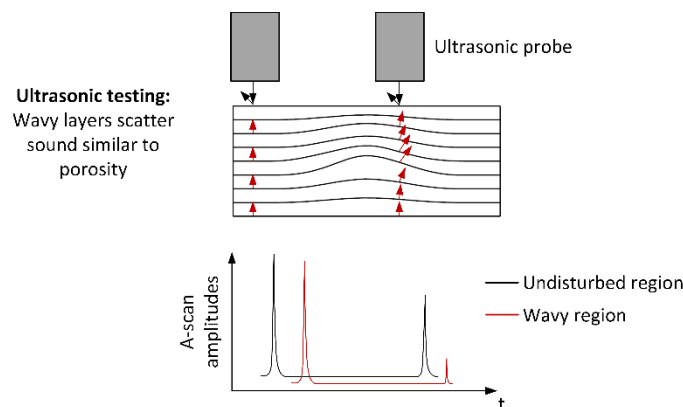


Figure 41. Principle of ultrasonic testing of out-of-plane fiber waviness. The waviness causes diffuse scatter very similar to the interaction with porosity.

A simplified representation of different ultrasonic scanning methods, i.e. A-scan, B-scan and C-scan, is given in Figure 42. Ultrasonic C-scanning is generally used to detect manufacturing effects or give an estimate of the average porosity in through-thickness direction. B-scans are needed to obtain information about the geometrical characteristics of the waviness. However, the evaluation of wrinkle morphologies from B-scans is very difficult. The test setups for ultrasonic inspection in through-transmission and pulse-echo mode are schematically shown in Figure 43. In this study, C-scans from both top and bottom side of the test plates were obtained from GE UTxx equipment (General Electric, Boston, USA) with water jet coupling in transmission mode. Transducers with 5 MHz frequency and 19 mm (0.748") diameter were used for conducting the scans. At least 175 mm water was used as a delay line. Pulse-echo (reflection) measurements used for obtaining both B- and C-scans were conducted with a GE USM35 phased-array system (General Electric, Boston, USA) combined with Krautkramer K5MN transducer. The transducer had a diameter of 6.35 mm and a delay line of 20 mm Plexiglas. The coupling agent used was Exosen 30.

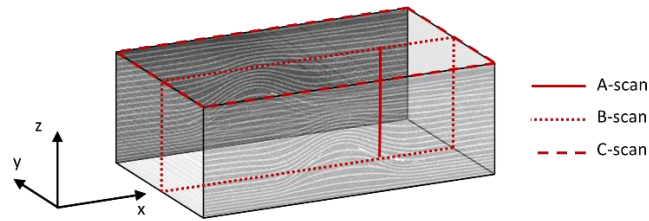


Figure 42. Schematic illustration of ultrasonic testing; **A-scan** (single signal for a specific coordinate x - y on the test object); **B-scan** (Ultrasonic linear scan - In B-scans, the echo from separate ultrasonic pulses (A-scans), which are obtained along a coordinate direction by a movement of the probe, are revealed as lines instead of signal peaks by the probe. The lines have variations in contrast depending on the amplitudes. Higher amplitude results in a better contrast. This makes the B-scan useful for the evaluation of the characteristics of fiber waviness; **C-scan** (Full-field inspection resulting in a 2D orthographic projection picture of the test object).

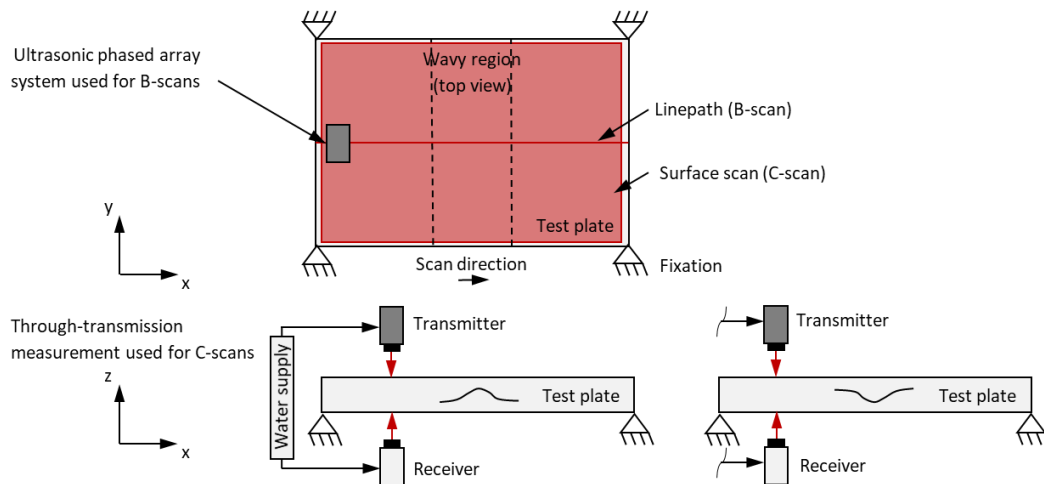


Figure 43. Test set-up of ultrasonic testing of out-of-plane fiber waviness with phased array system used for obtaining B- and C-scans and through-transmission ultrasonic testing for C-scans from top and bottom side of the test plates.

4.1.5. Infrared thermography (IRT)

In active thermographic methods [225–227] an external source of energy is actively applied to the test object in order to create a temperature gradient which drives a heat flow through the specimen. Internal defects disturb this heat-flow, which can be measured at the specimens' surface and therefore allows the detection of subsurface defects. This method works contactless and no coupling medium is needed, which makes it highly feasible for fast and automated measurements. Different excitation sources, i.e. optical flash lamps, heat lamps, air jets, electromagnetic induction, etc., can be used to achieve sufficient thermal gradients. Active thermography is a promising method for the non-destructive testing of lightweight structures made of CFRP due to its ability to inspect large areas and its depth sensitivity. Pulsed or

4.1 EXPERIMENTAL NON-DESTRUCTIVE TESTING

periodic heat excitation with appropriate signal processing in pulse-phase or lock-in thermography offers in-depth resolution, better contrast and less influence of disturbances [228,229].

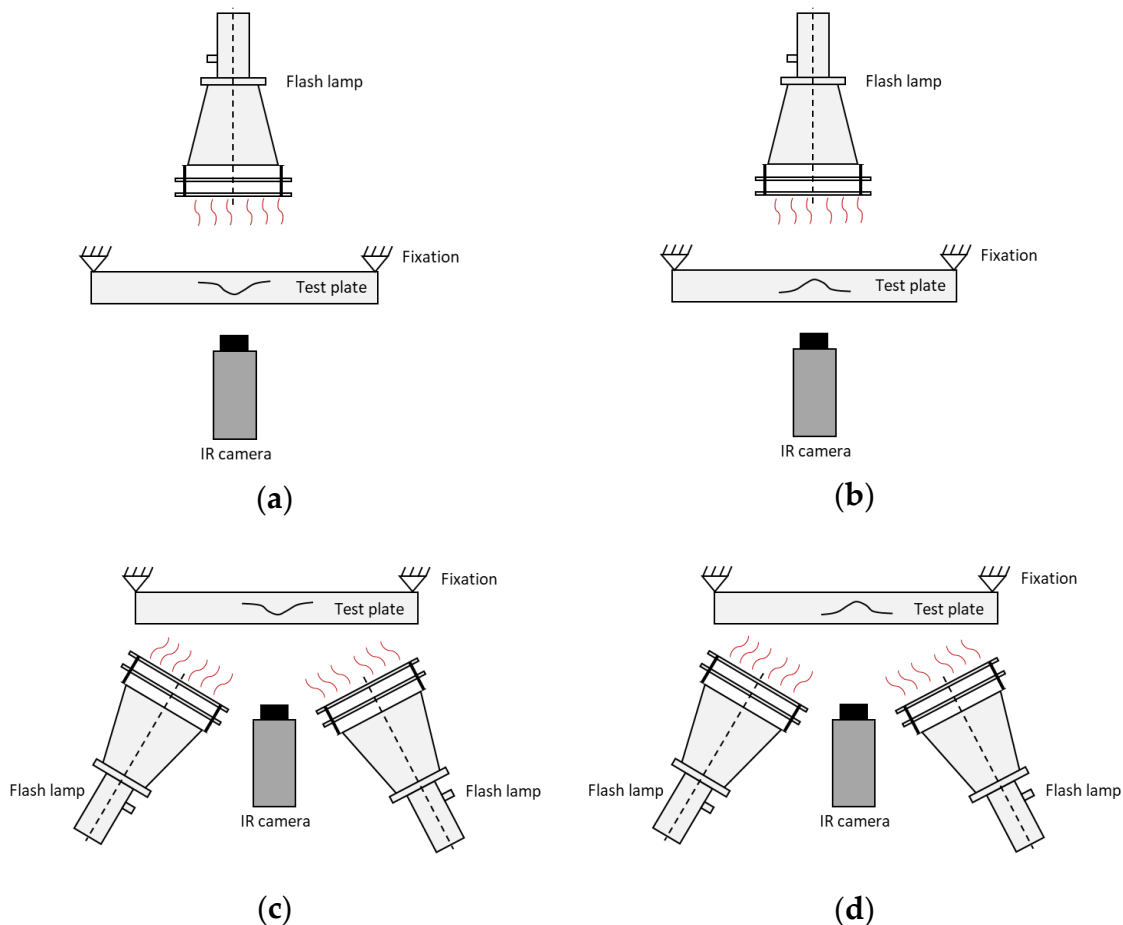


Figure 44. Test set-up of active infrared thermography testing of out-of-plane fiber waviness in transmission (a-b) and reflection mode (c-d).

In this study, pulse thermography measurements were conducted using a high-resolution infrared camera FLIR X8400sc (FLIR Inc., Wilsonville, USA) equipped with an indium antimonide (InSb) detector. The cooled 1280×1024 pixel focal plane array camera has a noise equivalent temperature difference (NETD) of about 25 mK and is sensitive in a spectral range of 1.5 to 5.1 micron. The measurements were carried out with a frame rate of 12.5 Hz for transmission mode with an approximate spatial resolution of $160 \mu\text{m}$. For the optical excitation in reflection mode, two synchronized flash lamps PB G 6000 Z (Bläsing/ELWA GmbH, Essen, Germany) with a 2 ms long flash and a nominal energy of 6 kJ each are used. They are positioned on the left and right side next to the camera with a distance and incidence angle suitable to create a strong but homogeneous illumination and to avoid direct reflexions. With transmission mode measurements to excitation is positioned on the opposite side of the IR camera. Due to a better accessibility only one flash lamp with a lower distance and a perpendicular incidence angle was used in transmission mode.

Polymethylmethacrylate (PMMA) sheets have been mounted in front of each flash lamp to reduce disturbing IR radiation of the hot lamps after flash excitation. Pulse thermography measurements (in the time domain) and pulse phase thermography measurements (in the frequency domain) were conducted in both reflection and transmission mode (Figure 44) and from both sides of the plate, i.e. top and bottom.

Pulse thermography allows the determination of the diffusion time t_d with the following relationship between the thickness L of the material and the effective thermal diffusivity α .

$$t_d = \frac{L^2}{\alpha} \quad (18)$$

The diffusion of the heat absorbed from the optical energy is dependent on the sample geometry, the existence of defects inside the material and the thermal diffusivity α . The thermal diffusivity depends on the thermal conductivity k , the density ρ and the specific heat c_p and is given by

$$\alpha = \frac{k}{\rho c_p}. \quad (19)$$

The method used for diffusion time t_d imaging in **transmission** mode, is the Linear Diffusivity Fitting (LDF) method [230], which is based on two assumptions: i) a one-dimensional time dependent heat diffusion model and ii) the assumption of a delta-like (Dirac pulse) optical excitation.

The diffusion time in **reflection** mode is determined by the Thermal Signal Reconstruction (TSR) method [231]. The TSR method is based on the analytical solutions of the one-dimensional heat conduction equation for the finite and semi-infinite body without convective losses. Both the LDF and TSR are independent of local changes in illumination, surface absorption or local thermal emission coefficients as long as they do not cause (too strong) lateral heat diffusion.

In addition to that, previous investigations have shown that flaws in general often become more visible in phase images than in temperature images. In pulse phase thermography (PPT) a wide frequency spectrum can be tested simultaneously due to the pulse excitation [226]. The evaluation of the sampled surface temperature $T(x,t)$ after the thermal pulse is transformed in the frequency domain by the Fast Fourier Transformation (FFT). The Fourier Transform is used to extract various frequencies of the temperature response by

$$F_n = \sum_{k=1}^N T(k) e^{2\pi jkn/N} = Re_n + j Im_n \quad (20)$$

4.1 EXPERIMENTAL NON-DESTRUCTIVE TESTING

with the subscript n is the frequency increment, N the number of acquired images and $T(k)$ is the k^{th} thermogram. The phase images can be analysed for various frequencies by calculating the phase angle φ for each pixel.

$$\varphi_n = \tan^{-1} \left(\frac{\text{Im}_n[\tilde{T}(x, \omega)]}{\text{Re}_n[\tilde{T}(x, \omega)]} \right) \quad (21)$$

The amplitude information is calculated by

$$A_n = \sqrt{\text{Re}_n^2 + \text{Im}_n^2}. \quad (22)$$

Table 6. Material properties of unidirectional CFRP influencing infrared thermographic inspection.

Material property	Value	
Thermal conductivity in fiber direction [W/mK]	7	[225]
Thermal conductivity in transverse direction [W/mK]	0.8	[225]

Fiber waviness diverge the heat flow due to major differences in thermal conductivities in fiber direction and transverse direction. Typical values of thermal conductivities for both fiber and transverse direction are shown in Table 6. Even though the thickness of the laminate may be constant in regions of embedded waves, the deviation of fibers in thickness direction and the often accompanying local resin accumulations and increased porosities affect the heat flow in different ways. Typical thermal signatures resulting from reflection and transmission configurations are schematically shown in Figure 45. When a wavy region is thermally excited from the bottom side, an increased temperature is measured at the center of the wave for both reflection and transmission configurations. In reflection, the elevated temperature results from the lower thermal conductivity of the CFRP in transverse direction at the center of the wave. In transmission, the thermal peak results from a bundling of the heat flux due to the higher thermal conductivity in fiber direction which is transformed in thickness direction due to the wave shape. The opposite is observed with excitation on the top side of the test plate. In reflection mode, a cold spot is located at the center of the wave because the fibers draw heat from the surface. When propagating in thickness direction, the heat flux spreads into two main directions due to the wave morphology. This spreading of heat flux leads to two local temperature maxima in the vicinity of the start and end point of the wave and a temperature minimum at the center of the wave for bottom side evaluations in transmission mode.

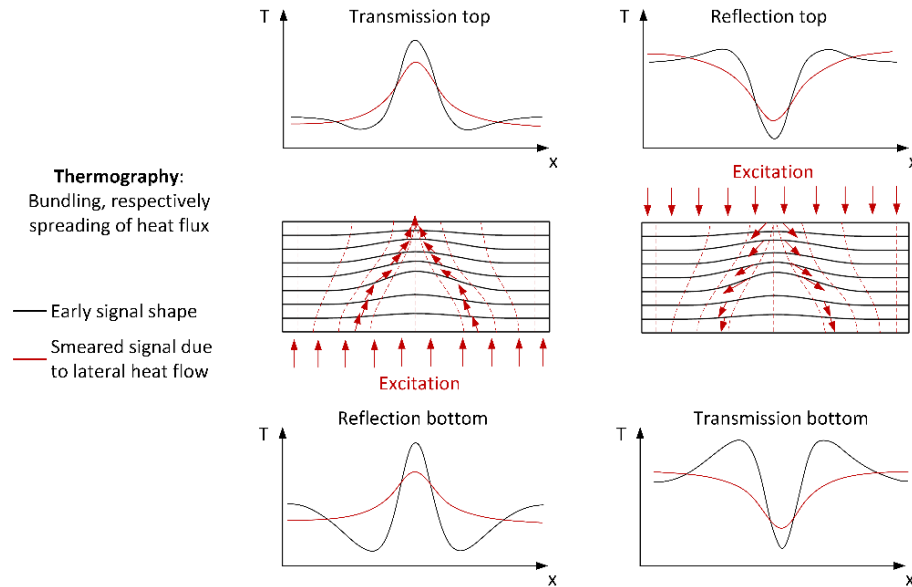


Figure 45. Principle of active infrared thermography testing of out-of-plane fiber waviness. An excitation on the bottom side of the test plate leads to a bundling of the heat flux, whereas an excitation on the top side of the test plate leads to a spreading of the heat flow along the thickness direction of the laminate. Typical resulting thermal signatures are shown for both reflection and transmission mode at the top and bottom side of the test plate. This characteristic Mexican hat shaped signatures can be obtained in both reflection and transmission configuration. The local maxima and minima of the signal very good correspond with the wavelength of the embedded wave. However, dependent on the shape of the embedded wave and laminate thickness, the Mexican hat signal gets smeared due to lateral heat flow with increasing measurement time.

4.1.6. Digital shearography

Digital imaging laser speckle interferometry (short Shearography) [232,233] is a fast non-destructive test method that is used to detect, measure and analyse surface and subsurface anomalies or defects in materials and structures by imaging very small changes to a test part surface when an appropriate stress is applied, e.g. through mechanical loading or thermal, pressure, vacuum, acoustic, vibration excitation. The selection of a suitable excitation method is of crucial importance for a successful shearographic examination. Digital shearography is contactless, doesn't need a coupling medium and allows the testing of a large area. When the test object is illuminated with coherent light, i.e. a laser point source, the scattered wave fronts from optically rough surfaces are passing through a Michelson interferometer and are focused on a charge-coupled device (CCD) detector array. Due to the so-called shearing, which is achieved e.g. by tilting one mirror of the Michelson interferometer, each pixel of the CCD array is hit by two beams emanating from two different object points. Due to the coherent illumination, these beams interfere and as a result a characteristic interference pattern is measured which changes due to a deformation induced shift in the phase relation of the two beams. The simplified mathematical

4.1 EXPERIMENTAL NON-DESTRUCTIVE TESTING

equation of the intensity on the specklegram detected on every pixel of the CCD matrix is:

$$I = I_0(1 + \mu \cos(\varphi)) \quad (23)$$

Where I is the intensity distribution of the speckle pattern at the CCD array, I_0 the intensity of the sheared images, μ the amplitude of the speckle patterns modulation and φ represents the random phase difference between scattered wavelet from two points $P(x,y)$ and $P(x+\delta x,y)$ on the object surface. When the object is deformed slightly, the intensity distribution of the speckle pattern is changed to I' , and Δ phase difference denotes the surface deformation which is shown in the following equation:

$$I' = I_0(1 + \mu \cos(\varphi + \Delta)) \quad (24)$$

By subtracting the interference speckle patterns, Eqn. (23) and (24), obtained before and after the occurrence of the deformations and by applying algorithms of signal conditioning methods, it is possible to visualize images of sub-surface defects, described as:

$$|I_d| = |I - I'| = 2I_0 \left[\mu \sin\left(\varphi + \frac{\Delta}{2}\right) \sin\left(\frac{\Delta}{2}\right) \right] \quad (25)$$

Phase-shifting shearography allows the determination of the phase difference Δ via the addition of a known phase using the controlled phase-shifting mirror in the Michelson interferometer. For each state of load four intensity images are captured, each with an additional phase of $\frac{\pi}{2}$.

$$\begin{aligned} I_1 &= I_0(1 + \mu \cos(\varphi + 0)) \\ I_2 &= I_0 \left(1 + \mu \cos\left(\frac{\varphi + \pi}{2}\right) \right) \\ I_3 &= I_0(1 + \mu \cos(\varphi + \pi)) \\ I_4 &= I_0 \left(1 + \mu \cos\left(\frac{\varphi + 3\pi}{2}\right) \right) \end{aligned} \quad (26)$$

The phase φ for the unloaded test object is then given by

$$\varphi = \arctan \frac{(I_2 - I_4)}{(I_3 - I_1)} \quad (27)$$

and for the deformed test object with intensities according to Eqn. (24) by

$$\varphi + \Delta = \arctan \frac{(I'_2 - I'_4)}{(I'_3 - I'_1)}. \quad (28)$$

This allows the determination of the phase difference Δ by subtracting Eqn. (27) and (28). Subsequent denoising and possibly necessary phase unwrapping lead to a phase-difference image [233]. Phase difference images are shown in the results overview of NDT methods in Figure 73 and Figure 74.

Surface deformations in z-axis direction (normal to the part surface) can be measured down to 2-20 nanometers with this method, depending on the environmental or background noise. Anomalies at the surface or subsurface cause changes to the thermal expansion and in the case of embedded out-of-plane fiber waviness additional effects of varying heat flows due to higher thermal conductivities in fiber direction occur. The principle of shearography testing of embedded out-of-plane fiber waviness is schematically shown in Figure 46.

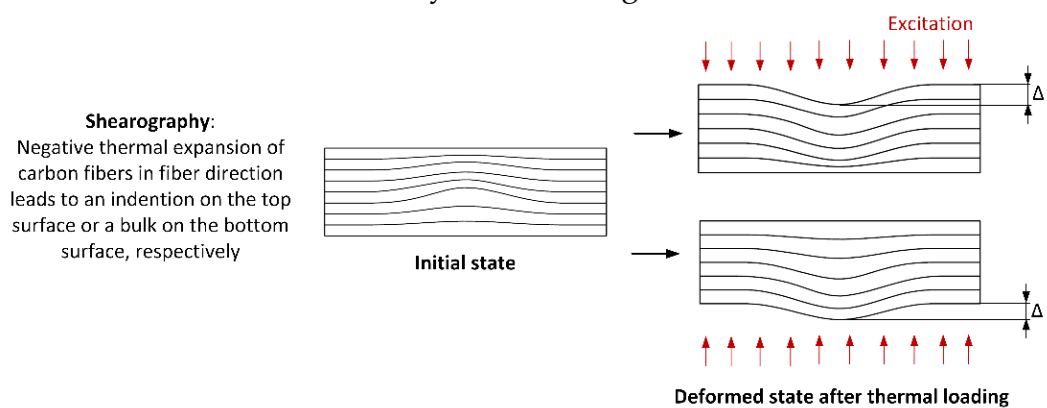


Figure 46. Principle of shearography testing of out-of-plane fiber waviness. The higher coefficient of thermal expansion in fiber direction and also temperature differences due to thermal conductivities into the laminate may lead to the formation of an indentation at the top side and/or a bulk at the bottom side of the wave due to the negative coefficient of thermal expansion of carbon fibers in fiber direction.

In this study, shearographic measurements were performed using the SE3 sensor from isi-sys GmbH (Kassel, Germany) consisting of a Michelson interferometer (shear element) and a CCD chip with a maximum resolution of 1024x768 pixel and 15 images per second. The measurements were carried out with an approximate spatial resolution of 122 μm . Out-of-plane illumination is provided by an array of 4 laser diodes which are expanded by diffusion lenses. The wavelength is 650 nm. The software isi-Studio 2008 NDT Edition from isi-sys was used to evaluate the measurement results. The measurements were conducted in reflection mode (Figure 47) with (common) halogen lamps used for a homogeneous thermal excitation of the whole test plate.

4.1 EXPERIMENTAL NON-DESTRUCTIVE TESTING

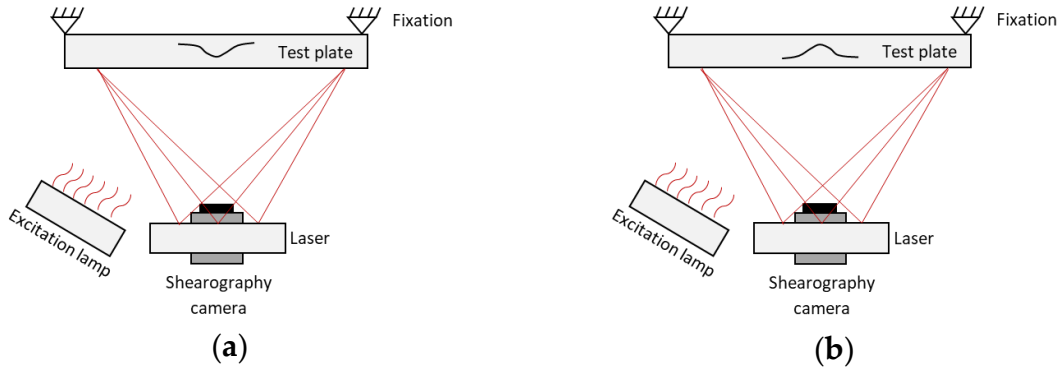


Figure 47. Test set-up of shearography testing of out-of-plane fiber waviness in reflection mode for a) top side and b) bottom side of the test plate.

4.1.7. Eddy current testing (ET)

The eddy current technique [17] is a non-destructive testing method which can be used to detect defects, e.g. missing or misaligned fiber bundles in conductive materials, e.g. in consolidated thermoplastic or thermoset CFRP as well as in dry fiber semi-finished products by using variations in the electric and dielectric properties of the materials. This method uses the property of electrical anisotropy of CFRP. Carbon fiber based materials show a low electrical conductivity [17], which is still sufficient to measure deviations in the material. Great advantage of this method is that it works without contact, and no coupling or X-ray protection is needed, unlike ultrasonic-based methods or X-ray-based methods, respectively. Because of the contactless approach, which ensures that the material properties and quality are not affected by the measurement, eddy current testing is well suited for automation and can be directly used in the process [17]. The basic set-up of an eddy current test device consists of two coils, an excitation coil and a receiver coil. The excitation coil generates an alternating magnetic field which propagates through the component and induces eddy currents. These eddy currents, in turn, generate a magnetic field which is then detected by the second coil. If there are defects in the component, such as cracks or foreign inclusions, these areas exhibit different conductivities or magnetic permeabilities compared to the base material. Thus the eddy current density changes compared to undisturbed regions in the material and therefore also the measured complex impedance of the receiver coil. Eddy currents decay exponentially with depth below the surface of a material. Important factors in eddy current testing are the coil excitation frequency and the magnetic permeability and conductivity of the test material. The depth of penetration δ in eddy current testing can be calculated by

$$\delta = \frac{503}{\sqrt{f * \mu * \sigma}} = \sim \frac{1}{\sqrt{\pi * f * \mu * \sigma}} \quad (29)$$

where f is the frequency, μ the magnetic permeability and σ the conductivity of the material. This equation indicates that at a higher frequency, permeability and/or conductivity the penetration depth decreases. Typical material properties for eddy current testing of CFRP are shown in Table 7.

Table 7. Material properties of unidirectional CFRP for eddy current testing.

Material property	Value	
Electrical conductivity in fiber direction [S/m]	34,120	[44]
Electrical conductivity transverse to fiber direction [S/m]	24	[44]
Magnetic permeability [H/m]	1.26×10^{-6}	[44]

In this study, the imaging eddy current testing electronics EddyCus® MPECS (Multi Parameter Eddy Current Scanner) for frequencies from 100 kHz to 100 MHz was used for testing the four test plates. It is a system developed by Fraunhofer Institute IKTS (Dresden, Germany) for mapping complex measurement values, i.e. magnitude and phase, with a spatial resolution of down to 100 μm . The measurement system in half-transmission configuration was equipped with two high frequency eddy current sensors S16209 P7H (sensor 1) and S17240 P2,4H (sensor 2) with sensor diameters of 7 and 2.4 mm, respectively. The used frequencies of sensor 1 were 4, 10, 15, 20 MHz and for sensor 2 4, 9, 15, 20 MHz respectively. Each of the four test plates was measured from the plates top and the bottom side as well as with both 0° and 90° sensor orientation. The test set-up is schematically shown in Figure 48.

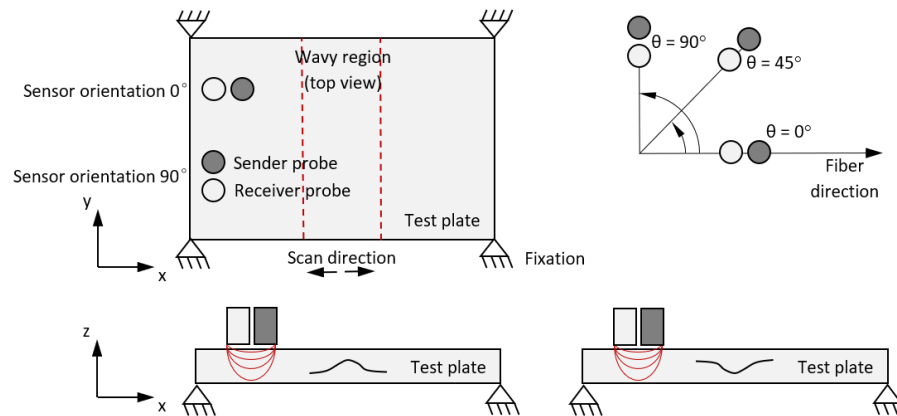


Figure 48. Test set-up of eddy current testing of out-of-plane fiber waviness in half-transmission mode from the top and bottom side of the test plate.

When the probe direction coincides with the fiber direction during the rotation of the sensor (i.e. when the angle between the fiber direction and the probe azimuth θ becomes zero, as shown in Figure 48), the output voltage of the receiver coil is at a maximum and the fiber orientation can be detected [44]. This readily describes the differences in eddy current testing of out-of-plane fiber waviness. The formation of the magnetic field lines depends on the waviness inside the material (Figure 49). When

4.1 EXPERIMENTAL NON-DESTRUCTIVE TESTING

measuring from the top side (Figure 49 left) the overall higher fraction of 0° layers at the top side leads to a locally higher conductivity and therefore to stronger signals at the wavy regions compared to undisturbed regions. Accordingly, the higher proportion of 90° layers at the bottom side (Figure 49 right) of the plate leads to a lower conductivity and therefore to lower signals compared to the undisturbed region.

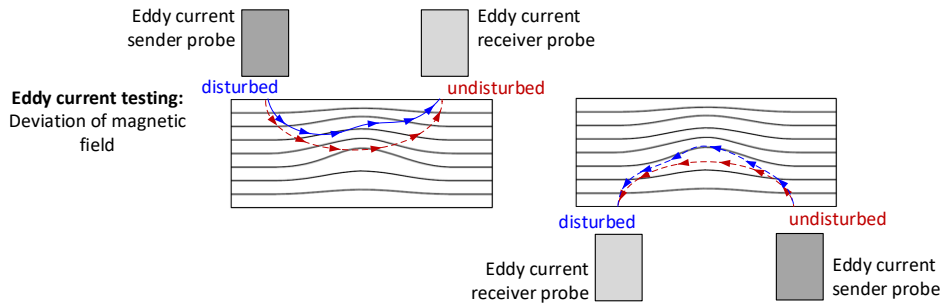


Figure 49. Principle of eddy current testing to detect out-of-plane fiber waviness.

4.1.8. Results and discussion

In the diagrams that are plotted for the evaluation of each NDT result in this section, average values in y-direction of predefined areas with a size of 40×80 mm (red rectangle in Figure 50) are evaluated in order to avoid edge effects and reduce signal noise.

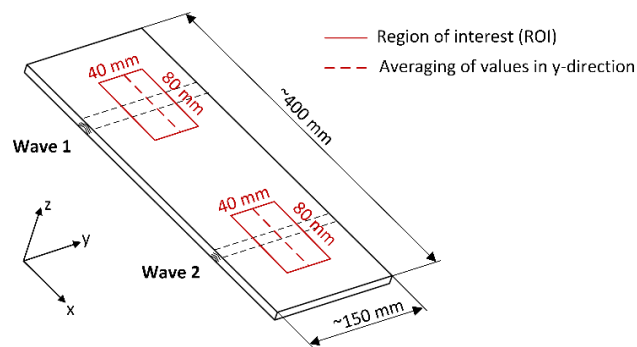


Figure 50. Region of interest (ROI) consistently used for the evaluation of NDT results in order to avoid edge effects. For plotting the resulting signals, average values are calculated along the y-direction to reduce noise.

4.1.8.1. Optical microscopy on polished samples

Figure 51 shows microscopic images of the manufactured test plates containing the two wave configurations ($A = 2$ mm, $L_1 = 15$ mm, $L_2 = 10$ mm) with varying positions in the laminate.

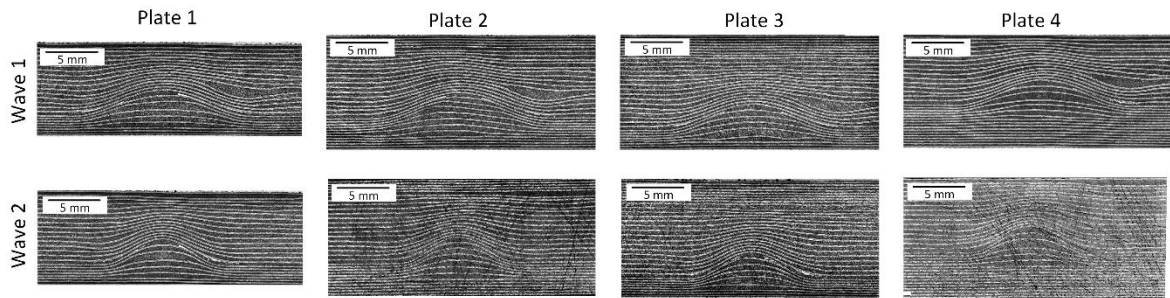


Figure 51. Optical microscopy images of polished samples.

4.1.8.2.X-ray computed tomography (CT)

Figure 52 shows results of wave 1 obtained from the conducted X-ray computed tomography scans overlaid on microscopic images. The results of the Talbot-Lau grating interferometer CT has shown the best contrast compared to results obtained from conventional CT. However, the sample sizes has to be small for both conventional and TLGI-CT to obtain a reasonable resolution of the wave characteristics.

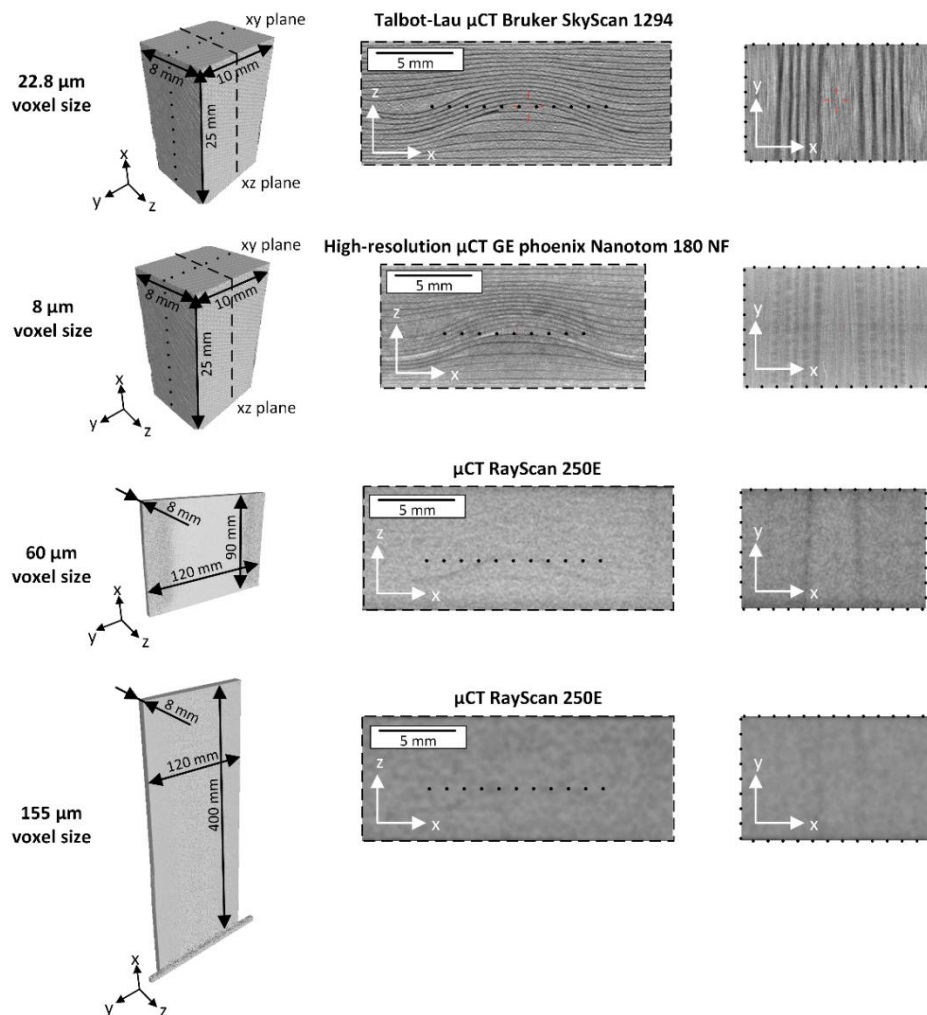


Figure 52. X-ray computed tomography results of wave 1 from high resolution cone-beam CT and Talbot-Lau grating interferometer CT overlaid on microscopic image.

4.1 EXPERIMENTAL NON-DESTRUCTIVE TESTING

4.1.8.3. Ultrasonic testing (UT)

Ultrasonic microscopy

The results from ultrasonic microscopy B-Scans have proven the method to be able to capture the morphology of the embedded waves. In Figure 53, representative results from ultrasonic microscopy obtained from the bottom side of the test samples are overlaid onto microscopic images of the corresponding polished samples. Especially the use of a higher frequency, i.e. 100 MHz, leads to high lateral resolutions as shown in Figure 53 a). However, for this clear representation of the wave, a subsequent time gain compensation (TGC) had to be carried out in order to increase the contrast of the signals through-out the thickness. The use of lower frequencies of 15 MHz and 10 MHz resulted in poor indications of the wave geometry as shown in Figure 53 b) and c) respectively.

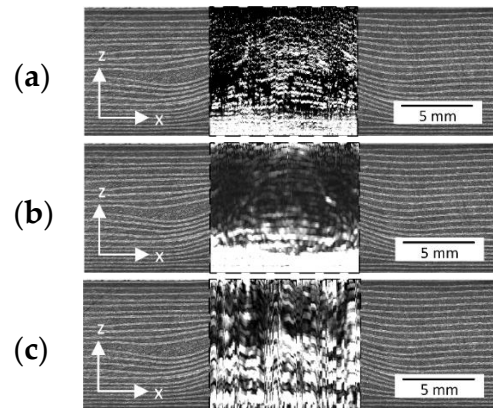


Figure 53. Ultrasonic microscopy results for wave 1 obtained from the bottom side of the test plate with different frequencies of a) 100 MHz, b) 15 MHz and c) 10 MHz.

A representative result of a C-scan obtained from ultrasonic microscopy on plate 1 at a frequency of 15 Hz and 38 dB amplification, is shown in Figure 54. It indicates the two wavy regions from the top view of the plate.

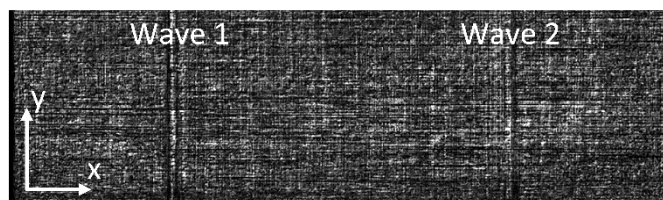


Figure 54. Ultrasonic microscopy C-scan obtained at a frequency of 15 Hz and 38 dB amplification from the top of plate 1 indicating wave 1 and wave 2.

Pulse-echo and through-transmission inspection

Results from ultrasonic testing in pulse-echo mode are shown in Figure 55 (top side) and Figure 56 (bottom side). They show clear indications of the embedded waves and their geometric extension. Similar results are obtained for through-transmission measurements shown in Figure 57 (top side) and Figure 58 (bottom side).

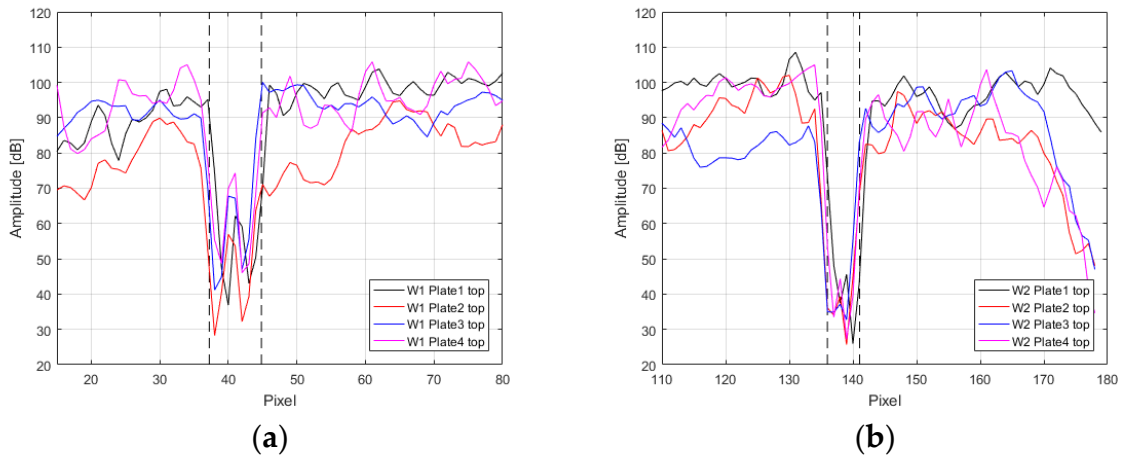


Figure 55. Ultrasonic testing results for a) wave 1 and b) wave 2 obtained in pulse-echo mode from the top side of the test plate.

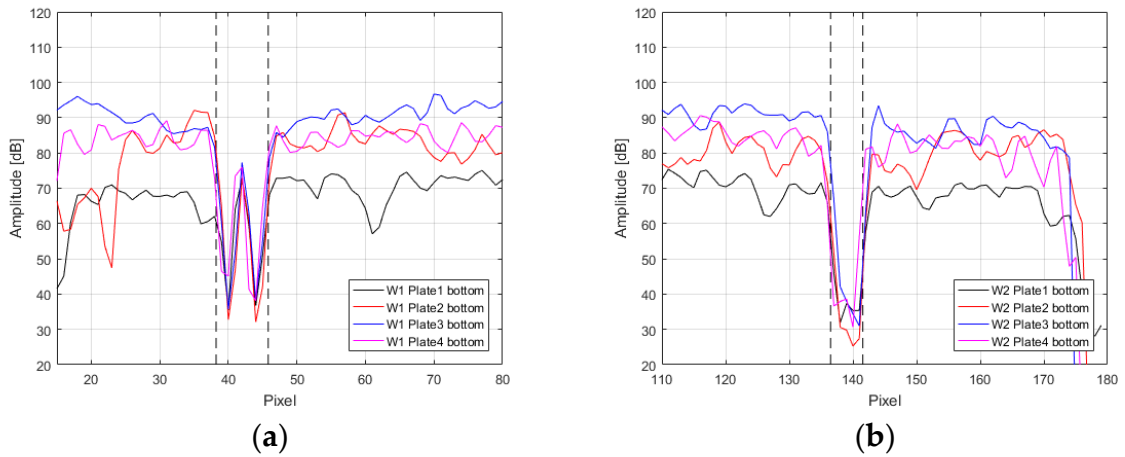


Figure 56. Ultrasonic testing results for a) wave 1 and b) wave 2 obtained in pulse-echo mode from the bottom side of the test plate.

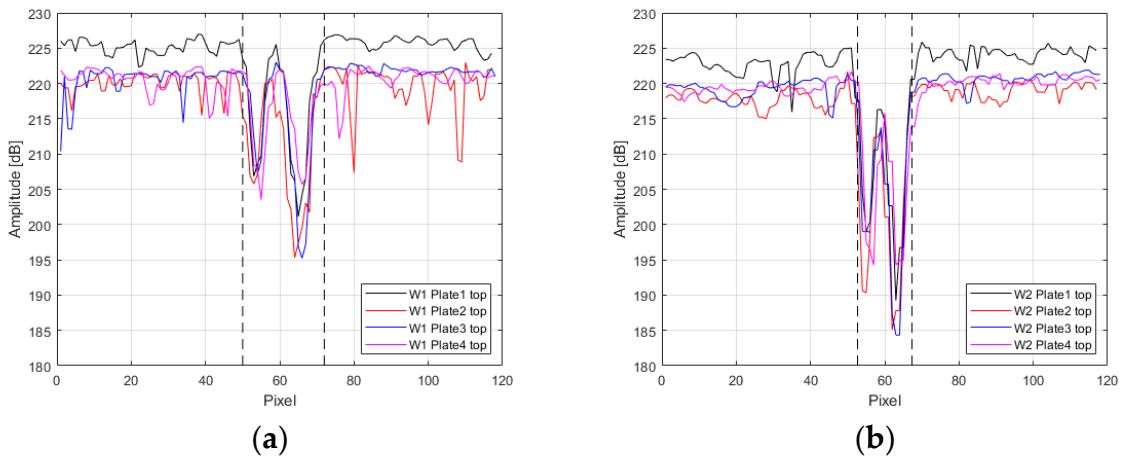


Figure 57. Ultrasonic testing results for a) wave 1 and b) wave 2 obtained in transmission mode from the top side of the test plate.

4.1 EXPERIMENTAL NON-DESTRUCTIVE TESTING

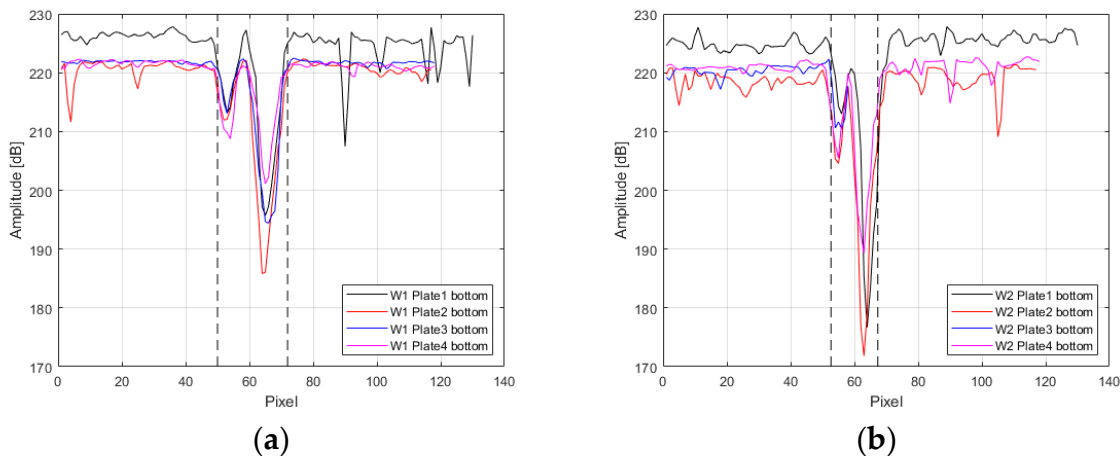


Figure 58. Ultrasonic testing results for a) wave 1 and b) wave 2 obtained in transmission mode from the bottom side of the test plate.

4.1.8.4. Infrared thermography (IRT)

The presence of a wavy region in the laminate can be clearly identified by infrared thermography using thermal signatures. The experimental determination of diffusion time t_d in transmission mode is conducted using the LDF method. The averaged temperature-over-time curve for the undisturbed and wavy region (wave 1) obtained by a measurement of plate 1 carried out in transmission mode is shown in Figure 59. The temperature rise between 30 % and 80 % of its maximum temperature is used for the evaluation. This interval is linearized using the LDF method and the gradient, which is a measure for diffusion time t_d , is determined using a linear compensation line. Figure 60 shows the averaged temperature-time evolution from a measurement of plate 1 carried out in reflection mode.

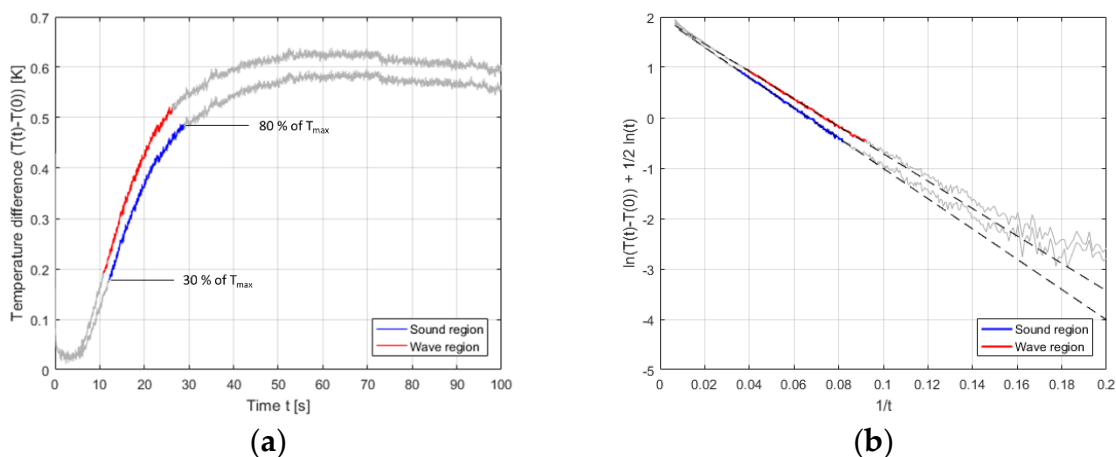


Figure 59. Transmission mode – a) averaged temperature over time curves and b) linearization of the temperature curves of undisturbed and wave region for wave 1 obtained from the top side of test plate 1. The range between 30 % and 80 % of the maximum temperature is used for the evaluation of the diffusion time t_d via the LDF method.

With the TSR method the temperature evolution gets plotted in a double logarithmic scale and fitted by a polynomial of certain order, here 9th order. The temporal position of the local maximum of the second derivation from the fitted curve is a measure for the diffusion time t_d .

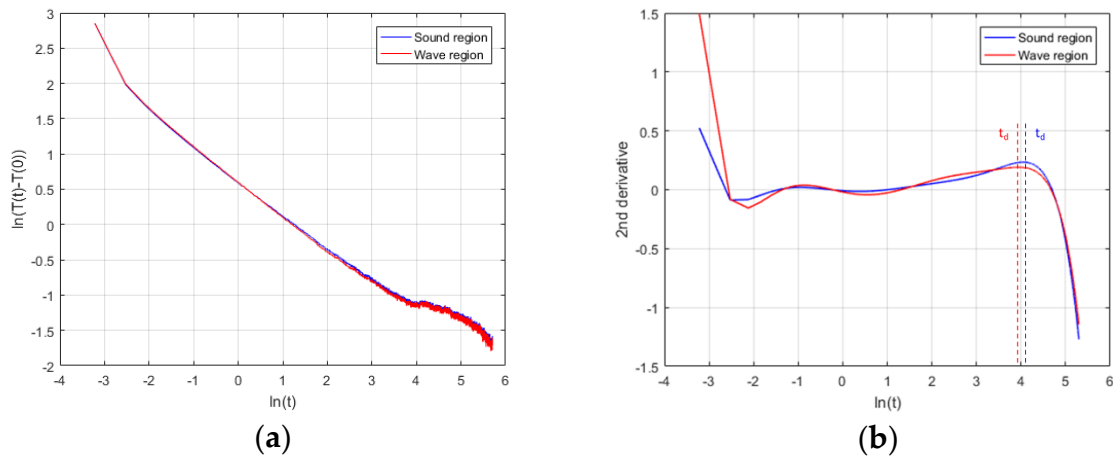


Figure 60. Reflection mode – a) double logarithmic visualization of time-dependent averaged temperature curves of undisturbed and wave region for wave 1, evaluated at the top side of plate 1. With the TSR method, the averaged temperature curves are plotted in the double-logarithmic scale and fitted with a 9th degree polynomial. b) 2nd derivative of 9th degree polynomial with t_d determined at the local maximum.

Diffusion time results for transmission IRT measurements are shown in Figure 61 (top side) and Figure 62 (bottom side) for a) wave 1 and b) wave 2 with the dashed lines indicating the wavy region. In general, the results obtained from transmission mode measurements result in Mexican hat shaped signals. The wavelength of the embedded out-of-plane fiber waviness can be determined with sufficient accuracy for both wave configurations from the top as well as bottom side of the test plates. The actual wavelengths coincide well with measured local maxima from the top side and minima from the bottom side, respectively. The wave amplitude may be approximated by the signal strength. The signal strength is assumed to be mainly dependent on the amplitude of the embedded fiber waviness and its position, i.e. depth, in the laminate.

4.1 EXPERIMENTAL NON-DESTRUCTIVE TESTING

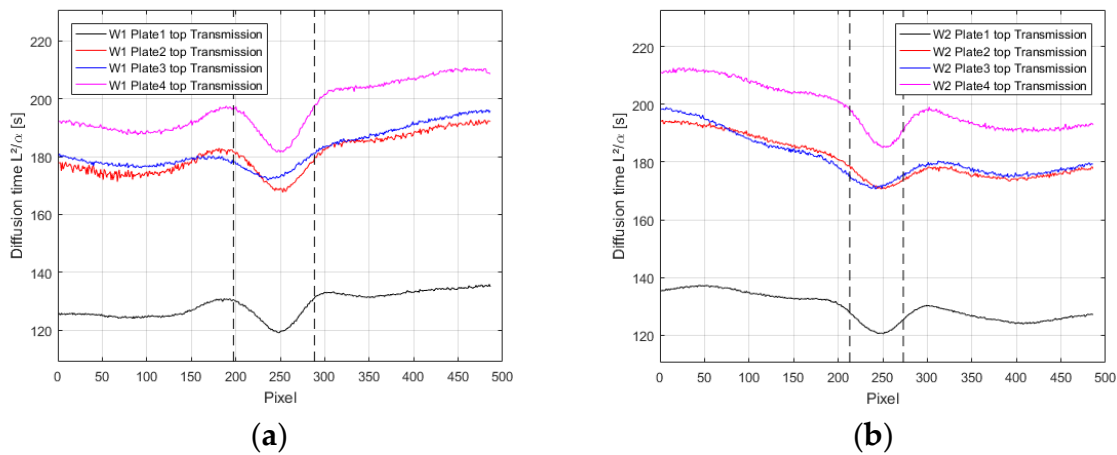


Figure 61. Infrared thermography results (diffusion time) for a) wave 1 and b) wave 2 obtained from transmission mode measurements on the plates top side.

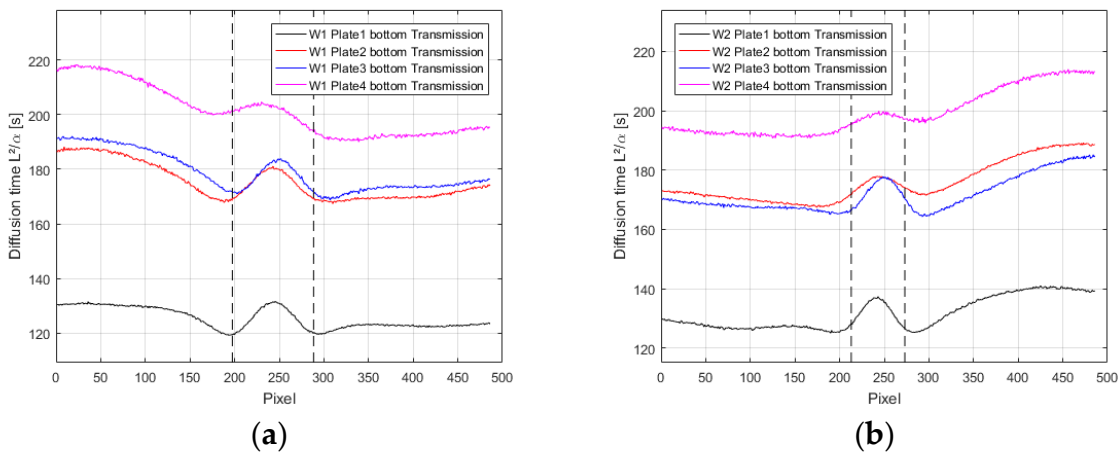


Figure 62. Infrared thermography results (diffusion time) for a) wave 1 and b) wave 2 obtained from transmission mode measurements on the plates bottom side.

The thermographic results in reflection mode (Figure 63 and Figure 64) show a significant influence of the position of the fiber waviness in the laminate. It is shown that the signals become fuzzier in view of wavelength and amplitude with increasing depth. The start and end point of the embedded out-of-plane waves (dashed lines) roughly coincide with the turning point of the measured signals in reflection mode.

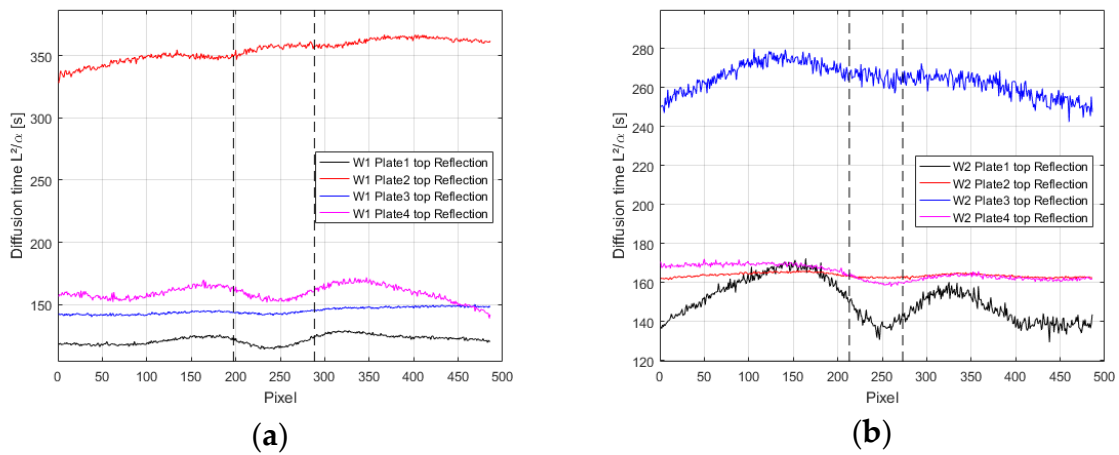


Figure 63. Infrared thermography results (diffusion time) for a) wave 1 and b) wave 2 obtained from reflection mode measurements on the plates top side.

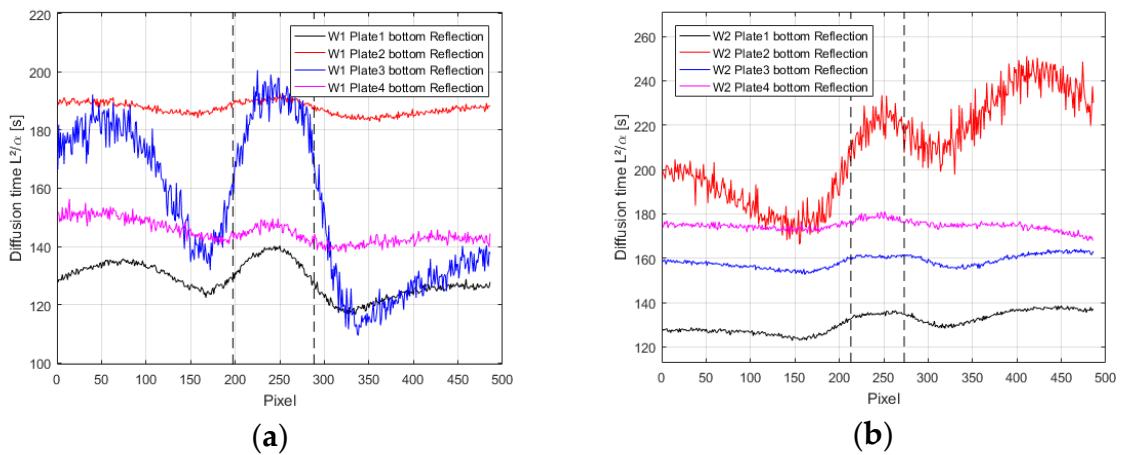


Figure 64. Infrared thermography results (diffusion time) for a) wave 1 and b) wave 2 obtained from reflection mode measurements on the plates bottom side.

The pulse phase thermography (PPT) has proven to offer deeper probing depth under the surface and better defect shape resolution compared to the thermal contrast method of pulse thermography (PT). Especially phase images of wavy regions show a clear indication of the wavelength. The evaluation of wavelength is significantly better for reflection mode measurements. In Figure 65, results from reflection measurements are shown. This figure intentionally shows wave configurations that have shown poor detectability in PT (diffusion time) in order to emphasize the considerable improvement of the results from PPT. Transmission mode results from PPT (Figure 66) also show a high contrast between undisturbed and wavy region, however no significant increase in signal quality was obtained compared to pulse thermography. The only drawback of the Fourier-based approach is the loss of temporal information making quantitative inversion procedures tricky, i.e. quantitative defect depth measurements. This is related to the fact, that Fourier transforms decompose a signal into infinite, circular functions.

4.1 EXPERIMENTAL NON-DESTRUCTIVE TESTING

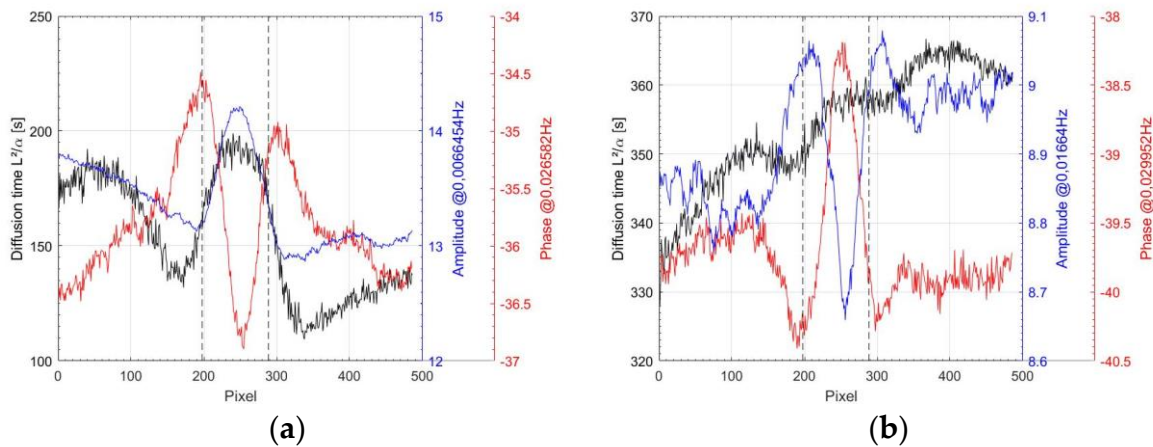


Figure 65. Comparison of pulse thermography results (diffusion time) with amplitude and phase values obtained from FFT analysis for a) wave 1 of plate 3 from bottom side in reflection mode and b) wave 1 of plate 2 from top side in reflection mode.

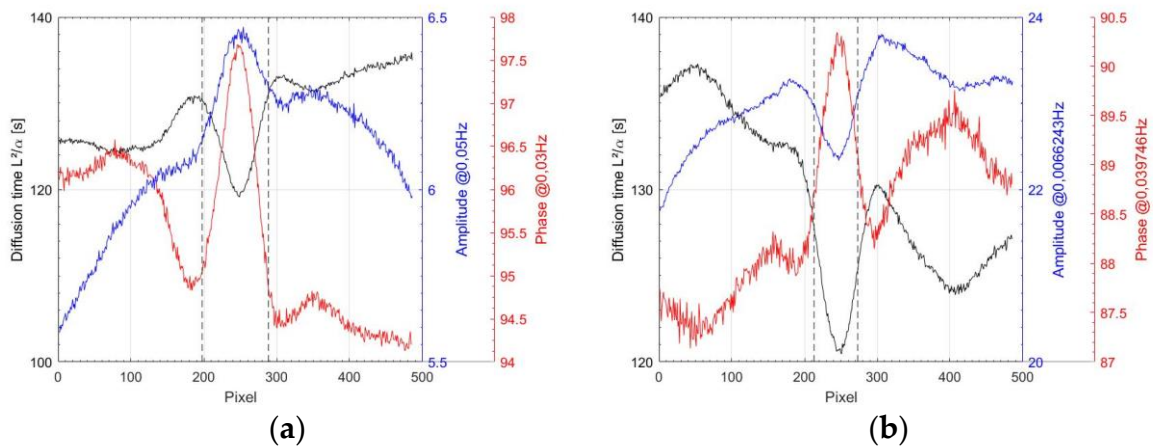


Figure 66. Comparison of diffusion time with amplitude and phase images obtained from FFT analysis for a) wave 1 of plate 1 from top side in transmission mode and b) wave 2 of plate 1 from top side in transmission mode.

To overcome the poor signal quality from reflection measurements, a Gaussian filter is applied to reduce noise and show a more clear indication of the signal. Results are shown in Figure 67 .

For the detection and evaluation of out-of-plane fiber waviness in composite materials using infrared thermography, the results of transmission mode measurements show better indications of the wavy region than those obtained from reflection mode measurements. It is found that transmission mode is more suitable than reflection mode as some wave configurations, especially waves that are not in the vicinity of the surface, can only be detected in transmission mode. This is due to the generally lower penetration depth in reflection mode than in transmission mode as the heat has to travel twice the distance. However, measurements in transmission mode are only possible if the test object is accessible from both sides. In addition to the

accessibility, both the reflection and transmission mode show advantages and disadvantages in view of detectability of fiber waviness. Measurements in reflection mode are suitable to detect wavy regions that are close to the surface with high sensitivity and high lateral resolution. The thermal contrast, i.e. the signal amplitude, between the wavy and undisturbed regions mainly depends on the depth of the wave in the laminate and the geometry of the wave, i.e. amplitude, more precisely, the maximum lateral deviation of the fiber orientation in thickness direction. As out-of-plane fiber waviness is often accompanied by increased porosities or resin accumulations, the resulting variance of the thermal diffusivities of wavy and undisturbed material may also play an important role in the signal evaluation. Results obtained in transmission mode provide integral information about the entire cross-section of the test specimen. Although almost all information about the depth resolution is lost, thicker test objects can be investigated compared to reflection configurations.

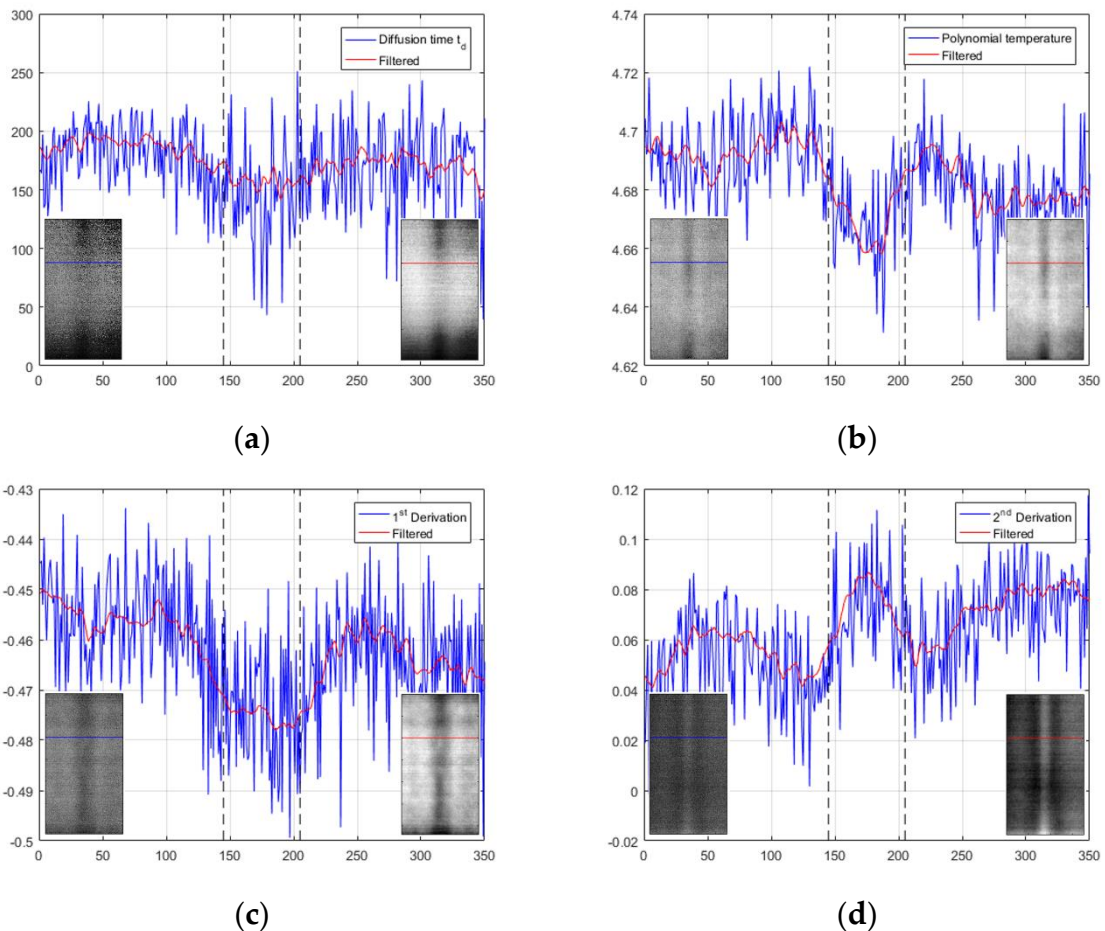


Figure 67. Improvement of infrared thermography results (blue) obtained from reflection mode measurements by applying Gaussian filters (red). a) Diffusion time t_d , b) polynomial temperature, c) 1st derivative and d) 2nd derivative of polynomial temperature for wave 2 of plate 1 measured from top side.

4.1 EXPERIMENTAL NON-DESTRUCTIVE TESTING

Furthermore, the heat loss and the smearing of the thermal data due to the lateral heat flow are expected to increase especially in thicker laminates, since longer measurement times are required. By developing transfer functions (correction factors) that incorporate these parameters, an evaluation of even the wave amplitude is within the realm of possibility. The development of transfer functions requires additional test data for different wave configurations. The characteristics of embedded waves can be determined by comparing the thermal signatures on the surface of the test object with the thermal signatures of reference standards or collected production samples containing fiber waviness of known characteristics, i.e. amplitude and wavelength. However, these data can additionally be obtained by means of finite element analyses through extensive parameter studies, which are outside the scope of this work but will be conducted in further studies.

4.1.8.5. Digital shearography

Digital shearography method has proven to be excellently applicable for the task of detecting fiber waviness from both sides of the test plates. The greatest influence on the quality of the measurement results is the use of an optimal excitation method of the object to be tested, i.e. in the case of thermal excitation there is an optimal excitation time, depending among others on the excitation power, its radiation characteristic and its distance to the sample, at which the defect signal reaches maximum contrast without artefacts (e.g. from an overall bending of the plate). The excitation time is further dependent on the geometrical characteristics of the wave and its depth beneath the laminates surface. Similar to thermographic results, the wave morphology may be characterized from signal amplitudes by using transfer functions. These functions could link the digital level (grey value) of signals with wave parameters, i.e. amplitude or position in the laminate. Figure 68 shows exemplarily results for wave 1 obtained at the top and bottom side of plate 1 with varying excitation times (5 s, 10 s, 15 s, 20 s). For all the investigated test plates a thermal excitation of 20 s has shown good results in view of signal contrast. Note: the shown greyscale values are offset-corrected in a way that the global bending of the plate was subtracted by creating a correction image based on the global gradient, i.e. a grey value change with a constant slope, which was subtracted from the original result. So only the changes due to the fiber waviness on top of this background are presented in the following.

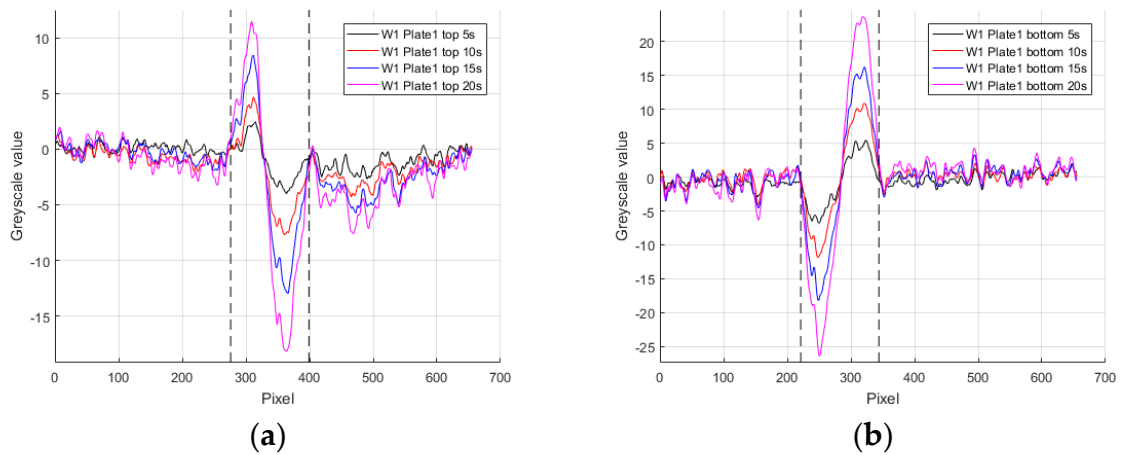


Figure 68. Results from digital shearography for varying excitation times (5 s, 10 s, 15 s, 20 s).

Figure 69 shows test results obtained at the top side of the four investigated test plates with a thermal excitation of 20 s for a) wave 1 and b) wave 2. The widths of the signals are in excellent agreement with the wavy region, i.e. wavelength, which is indicated by the dashed lines. A similar accuracy was achieved for results obtained at the bottom side (Figure 70) of the test plate. Similar to thermal signatures from IRT, it is expected that the signal from shearography will overestimate the wavelengths with increasing depth. The amplitude of the signals correlates well with the depth of the wave in the laminate. Both the wave position and amplitude are influencing the signal strength. For the evaluation of which allows the conclusion that the actual wave amplitude can be estimated via the signal strength.

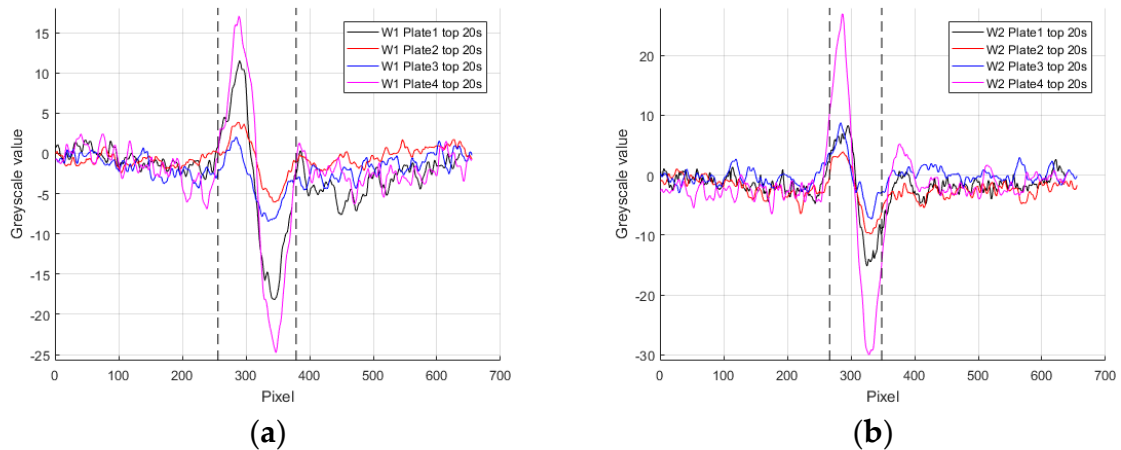


Figure 69. Digital shearography results for a) wave 1 and b) wave 2 obtained from the top side of the test plate with an excitation time of 20 s.

4.1 EXPERIMENTAL NON-DESTRUCTIVE TESTING

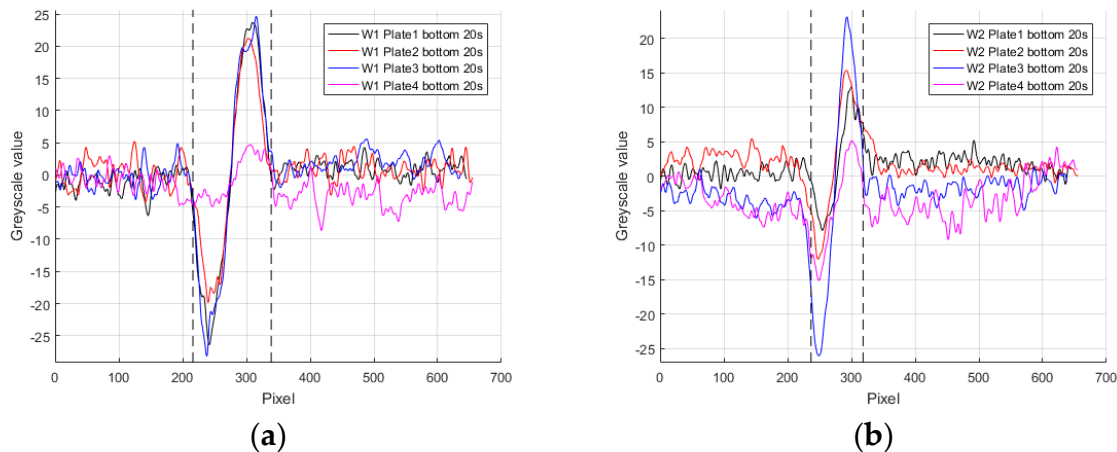


Figure 70. Digital shearography results for a) wave 1 and b) wave 2 obtained from the bottom side of the test plate with an excitation time of 20 s.

4.1.8.6. Eddy current testing (ET)

Each of the four test plates was measured from the top and the bottom side of the plate as well as with both 0° and 90° sensor orientation. From each measurement, two result images were generated from the data of the complex electrical plane for comparison: Real part (0° phase position); Imaginary part (90° phase position). When manually adjusting the phase position, better results were obtained with more clearly highlighted embedded fiber waviness due to improved image dynamics. Further improvements can be achieved by manually filtering the data, to reduce the noise level or to eliminate disturbing phenomena. An attempt was made to generate a distinctive, characteristic image for each test object.

The depth of the fiber waviness has shown significant influence on the detectability in eddy current testing. Figure 71 shows ET results for a) wave 1 and b) wave 2 obtained from the top side of the test plates. The two sensors used (sensor 1 and sensor 2) resulted in similar results, with a slightly better resolution using sensor 2 due to the smaller sensor diameter. The sensor orientation of 0° , where the transmitting and receiving probes are in parallel with the scanning direction, led to better results for measurements at the top side. In comparison to that, bottom side measurements (Figure 72) show better detectability using a 90° sensor orientation, where the probes are orthogonal to the scanning direction.

Results from plate 3 (Figure 71), where the wave is located at the lower part of the laminate with two millimeters of undisturbed layers on top, do not indicate any deviation in the ET signal obtained from the top side. In comparison, waves that are located at the upper area of the laminate (plate 4) are not detectable from the bottom side (Figure 72) of the test plate. These results clearly indicate the limits of detectability of embedded out-of-plane fiber waviness using ET.

In general, the wavelength of both waves are slightly overestimated using ET. However, results acquired from the bottom side of the test plates are slightly better,

probably due to the tendency of the waves to be located lower in the laminate, i.e. the largest deviations of the waves and higher proportions of 90° layers are located at the bottom side of the plate.

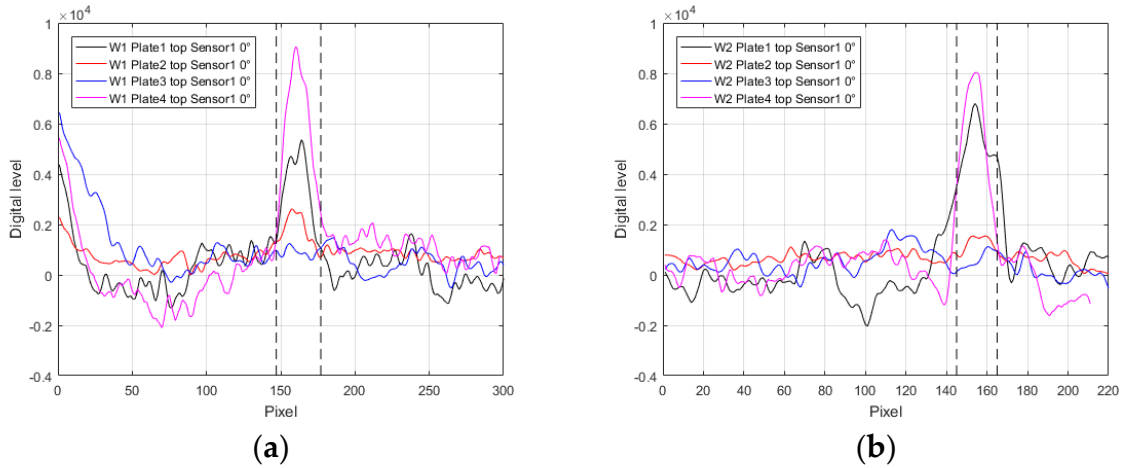


Figure 71. Eddy current test results for a) wave 1 and b) wave 2 obtained from the top side of the test plate using sensor 1 in 0° orientation.

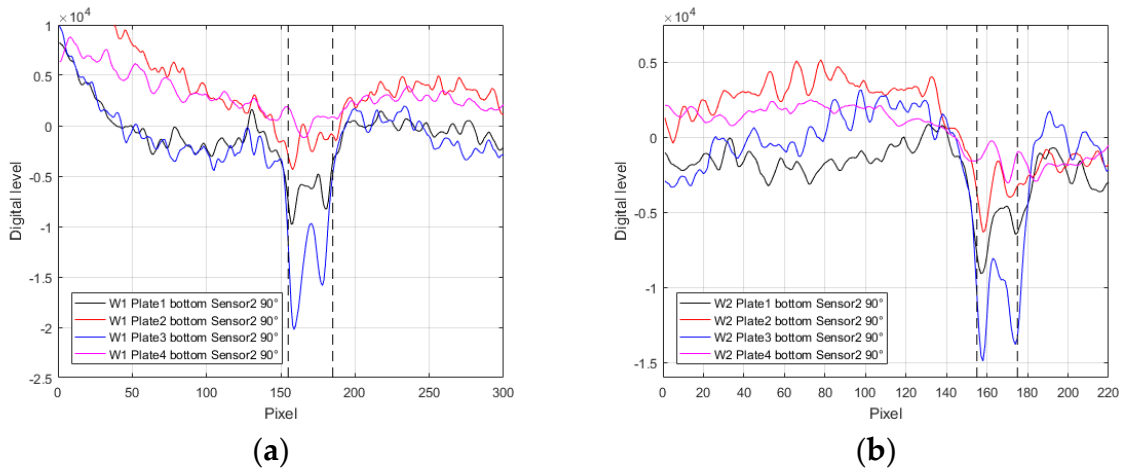


Figure 72. Eddy current test results for a) wave 1 and b) wave 2 obtained from the bottom side of the test plate using sensor 2 in 90° orientation.

4.1 EXPERIMENTAL NON-DESTRUCTIVE TESTING

4.1.8.7. Comparison of test methods

This section provides a final overview of the test results obtained from the conducted NDT methods. Figure 73 and Figure 74 show representative results from the tested samples from the bottom and top side, respectively.

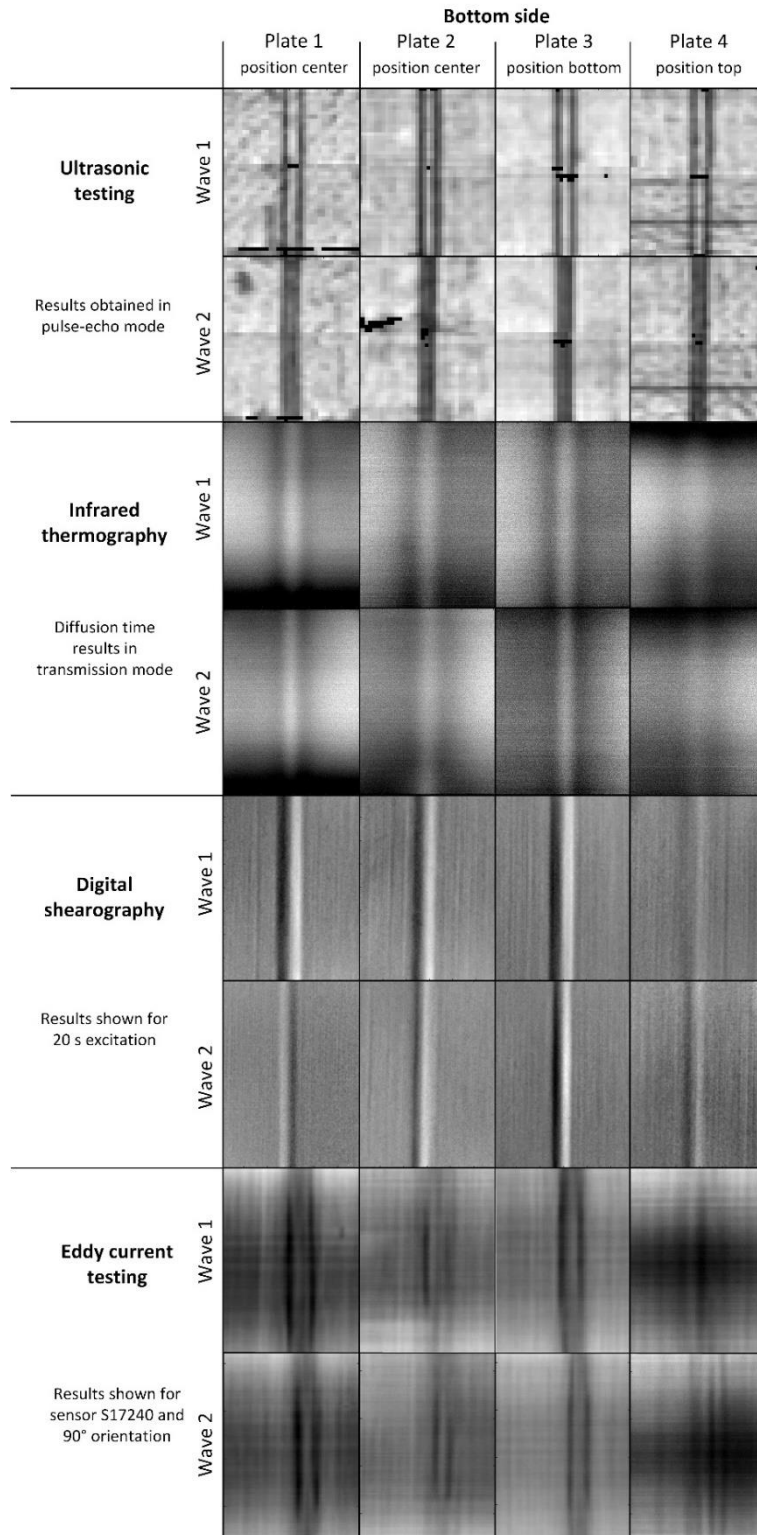


Figure 73. Overview of NDT results (bottom side).

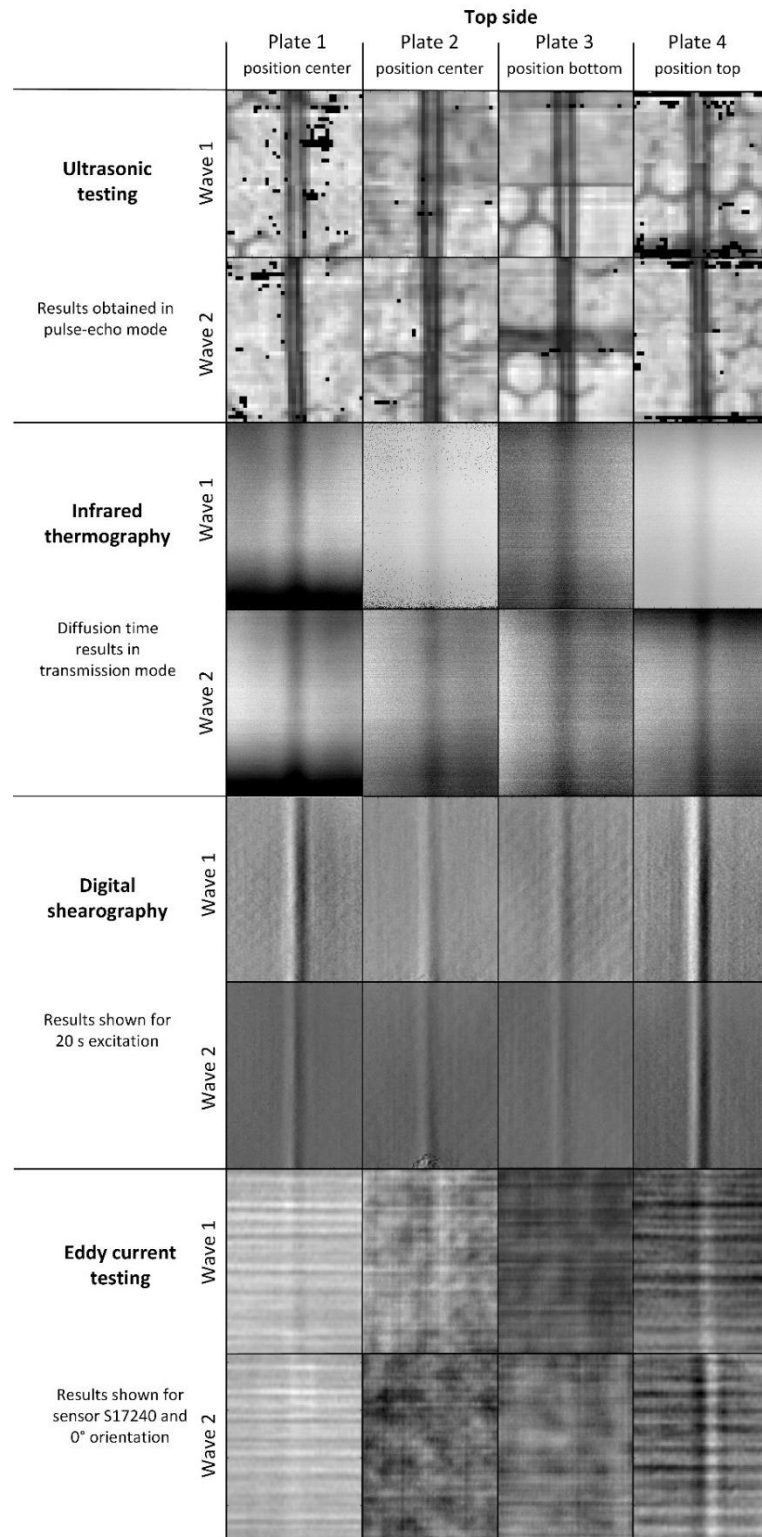


Figure 74. Overview of NDT results (top side).

In Table 8, a quantification of the fiber waviness in terms of amplitude and wavelength is shown, compared to the reference tool geometry used for manufacturing.

4.1 EXPERIMENTAL NON-DESTRUCTIVE TESTING

Table 8. Quantification of waviness in terms of amplitude and wavelength compared to tool geometry.

	Plate	Ultrasonic	Infrared thermography	Digital shearography	Eddy current	
		A _{ΔdB} [dB] L [mm]	A _{ΔID} [s] L [mm]	A _{Δgsv} [grey scale value] L [mm]	A _{Δdl} [digital level] L [mm]	
Wave 1	top	1	A _{ΔdB} = 57.25 L = 17.77	A _{ΔID} = 12.75 L = 18.11	A _{Δgsv} = 14.86 L = 16.73	A = 4145.1 L = 17.5
		2	A _{ΔdB} = 43.18 L = 17.77	A _{ΔID} = 15.35 L = 20.74	A _{Δgsv} = 4.97 L = 14.65	A = 1728.3 L = 17.5
		3	A _{ΔdB} = 50,92 L = 17.77	A _{ΔID} = 10.3 L = 23.70	A _{Δgsv} = 5.2 L = 13.92	Not detectable
		4	A _{ΔdB} = 45.84 L = 17.77	A _{ΔID} = 18.25 L = 21.07	A _{Δgsv} = 20.91 L = 17.70	A = 7970.2 L = 18.0
	bottom	1	A _{ΔdB} = 29.03 L = 15.79	A _{ΔID} = 12.1 L = 16.30	A _{Δgsv} = 25.03 L = 16.36	A = 6743.5 L = 21.5
		2	A _{ΔdB} = 52.26 L = 15.79	A _{ΔID} = 13.15 L = 18.27	A _{Δgsv} = 20.58 L = 15.51	Not detectable
		3	A _{ΔdB} = 49.64 L = 15.79	A _{ΔID} = 13.75 L = 15.80	A _{Δgsv} = 26.43 L = 16.48	A = 15625.5 L = 19.5
		4	A _{ΔdB} = 42.54 L = 15.79	A _{ΔID} = 8.0 L = 22.88	Not detectable	Not detectable
Wave 2	top	1	A _{ΔdB} = 64.39 L = 13.82	A _{ΔID} = 10.5 L = 17.94	A _{Δgsv} = 11.74 L = 16.24	A = 7000.8 L = 20.5
		2	A _{ΔdB} = 57.59 L = 13.82	A _{ΔID} = 9.95 L = 21.40	A _{Δgsv} = 6.86 L = 13.31	Not detectable
		3	A _{ΔdB} = 54.08 L = 13.82	A _{ΔID} = 10.5 L = 22.22	A _{Δgsv} = 7.87 L = 15.26	Not detectable
		4	A _{ΔdB} = 62.12 L = 13.82	A _{ΔID} = 15.05 L = 17.61	A _{Δgsv} = 28.48 L = 13.31	A = 8733.0 L = 13.5
	bottom	1	A _{ΔdB} = 36.59 L = 13.82	A _{ΔID} = 12.0 L = 13.66	A _{Δgsv} = 10.43 L = 13.19	A = 6127.0 L = 18.0
		2	A _{ΔdB} = 52.30 L = 13.82	A _{ΔID} = 8.1 L = 17.78	A _{Δgsv} = 13.7 L = 15.26	A = 4488.9 L = 19.0
		3	A _{ΔdB} = 50.13 L = 13.82	A _{ΔID} = 12.45 L = 14.65	A _{Δgsv} = 24.56 L = 12.70	A = 14197.9 L = 20.0
		4	A _{ΔdB} = 47.96 L = 13.82	A _{ΔID} = 6.0 L = 17.45	A _{Δgsv} = 10.12 L = 13.55	Not detectable

	Tool geometry (reference)	X-ray computed tomography (8 μm VS) *	X-ray computed tomography (60 μm VS) *
Wave 1	A=2 mm L ₁ =15 mm	A= 2.04 mm L=14.15 mm	A= 1.68 mm L=15.4 mm
Wave 2	A=2 mm L ₂ =10 mm	A= 1.95 mm L=10.26 mm	A= 1.78 mm L=10.68 mm

* Estimated by simple manual measurement (user depended)! At (155 μm)³ VS no quantification was possible.

Table 9 provides a summary of characteristics of the investigated NDT methods in general, but also specifically for the application to detect fiber waviness. A comparison is made for contact mode (i.e. contactless or coupling needed), (physical) measurement quantity, the type of excitation and what is captured during analysis that carry the information. Furthermore, the type of results and the advantages and disadvantages of the methods are compared.

Table 9. Comparison of NDT methods – General and specifically for fiber waviness.

	Ultrasonic	Infrared thermography	Digital shearography	Eddy current	X-ray computed tomography
Contact mode	Couplant needed	Contactless	Contactless	Contactless (> 2mm liftoff acceptable)	Contactless
Measurement quantity	Ultrasonic wave	Thermal radiation	Shearogram	Complex electrical impedance	Intensity of transmitted radiation
Excitation/ Loading	Ultrasonic wave	Short heat impulse (in Pulse Thermo-graphy)	Mechanical or thermal	Magnetic field with induced eddy currents	X-ray source
Captures ... for analysis	Amplitude and time of flight of ultrasonic wave	Sequence of thermal images	Shearogram to deduce the out-of-plane deformation gradient	Local change in impedance due to conductivity and permittivity changes	Radiographic images from numerous angle positions

4.1 EXPERIMENTAL NON-DESTRUCTIVE TESTING

	Ultrasonic	Infrared thermography	Digital shearography	Eddy current	X-ray computed tomography
Results	Evaluation of signals at specific points (A-scan), along cross-sections leading to depth information (B-scan) and 2D images of the surface yielding location and depth information of flaws (C-scan)	Image series indicating flawless regions by hotter or colder temperature distributions due to changes in the effective thermal diffusivity	Grey value image showing the deformation gradient.	Image of changes of amplitudes and phase angles resulting from variations in the material impedance	Three-dimensional representation of the test object and it's inner structure
Advantages	Accurate measurement of defect size	Fast and contactless inspection of large areas, good evaluation of wavelength	Fast and contactless inspection of large areas, good evaluation of wavelength, Possibility to detect from top or bottom side of plate.	Possibility to detect from top or bottom side of plate	Detailed three-dimensional representation of the test object and it's inner structure. Fiber waviness can be evaluated geometrically exact using voxel sizes of <math><10 \mu\text{m}</math>
Dis-advantages	Long measurement times. Difficult to differentiate between fiber waviness and porosity	Defect depth and amplitude of fiber waviness cannot be directly evaluated without	Defect depth and amplitude of fiber waviness cannot be directly evaluated. Results are strongly	Longer measurement times compared to Shearography and IRT	For detailed analysis with high resolution CT results, small samples are necessary (<math><10\text{mm}</math>). Fiber waviness

4 NON-DESTRUCTIVE TESTING

	Ultrasonic	Infrared thermography	Digital shearography	Eddy current	X-ray computed tomography
	using backwall-echo amplitude	applying transfer/correction factors.	dependent on the chosen time of thermal excitation.		cannot be detected on typical CT scans on component level (>>10mm).
Factors of influence	Choice of couplant	Material's surface thermal properties influence	Rigid body movement influence	Sensor orientation	Difference in absorption coefficients of fiber and matrix and used resolution
Detectability of fiber waviness (0-10 / low-high)	B-scan (1 conventional UT, 10 ultrasonic microscopy) C-scan (10)	9	10	7	0 ... 10 (Strongly depends on resolution)

4.2. Finite element analysis of NDT methods

The experimental non-destructive procedures of infrared thermography and digital shearography, which are described in Section 4.1, were simulated using the Finite Element Method (FEM) to gain a deeper understanding on the influence of fiber waviness on the measured results.

4.2.1. General modelling

For the comparison between simulations and experiments, the cross-sections (i.e. x-z plane) of the produced samples were reconstructed in CATIA V5R19 by using the microscopic images, as shown in Section 4.1.8.1. The 2D simplification is valid due to the fact that the characteristic of the embedded fiber waviness is constant in y-direction and no heat transfer occurs in this direction. Additionally, the y-direction is experimentally large enough to avoid additional signatures from potential edge reflections of the heat pulse. Due to anisotropic thermal and mechanical behavior of composite material, each layer is modelled separately to assign the anisotropic material properties. For the FEM simulations the software ABAQUS CAE 2019 was used.

Table 10. Material parameter.

Parameter	Value	Reference
Density, ρ [g/cm ³]	1.56	[235]
Conductivity longitudinal, k_{long} [W/mK]	7.0	[236]
Conductivity transversal, k_{trans} [W/mK]	0.7238	[237]
Specific heat, C_p [J/kgK]	895.376	[237]
Young's modulus longitudinal, E_{long} [GPa]	171.42	[238]
Young's modulus transversal, E_{trans} [GPa]	9.08	[12]
Shear stiffness, G_{12} , G_{13} [GPa]	5.29	[12]
Shear stiffness, G_{23} [GPa]	3.98	[12]
Poisson's ratio, ν_{12} , ν_{13} [-]	0.32	[12]
Poisson's ratio, ν_{23} [-]	0.43	[12]
Coefficient of thermal expansion longitudinal, α_{long} [K ⁻¹]	-5.5E-6	[238]
Coefficient of thermal expansion transversal, α_{trans} [K ⁻¹]	2.58E-5	[238]
Heat transfer coefficient (surface film coefficient), U [W/m ² K]	10.0	[238]

For the numerical analysis of infrared thermography (heat transfer) and digital shearography (coupled temperature-displacement) measurements, standard triangular elements of linear geometric order are used. The material parameters used for the simulations are shown in Table 10.

4.2.2. *Infrared thermography (heat transfer)*

The optical excitation of the test plates was modeled as a delta-like Dirac pulse. A heat flux of 3.5×10^6 [W/m²] was assumed, which shows the same temperature difference between undisturbed and wave region and approximately the same averaged temperature of experimental and simulation results. Thermal convection, conduction and radiation were assumed to be negligible due to the very small temperature differences.

4.2.3. *Digital shearography (deformation)*

As the thermal load from the experimental setup was not exactly known, it was defined in the simulation with 500 W/m² as well as with 50,000 W/m². According to literature, the applied heat fluxes vary from 100 - 400,000 W/m² [239–241] for standard heating lamps. It could be determined that the qualitative deformation as function of time remains identical for both magnitudes, i.e. 500 and 50,000 W/m². Therefore, a heat flux of 500 W/m² was used for further studies. A heat transfer coefficient of 10 W/m²K was defined on the top and bottom of the plate to account for the convection to the environment. Since a layer of polystyrene was placed between the outer edges of the test plates and the aluminum frame, where they were attached in the experimental test setup, conduction was neglected in the simulation. Thermal radiation was also neglected due to the low temperature differences. The initial plate temperature was set to 23°C.

4.2.4. *Results*

4.2.4.1. Infrared thermography (heat transfer)

Representative images from infrared thermography, i.e. diffusion time t_d , obtained from the bottom and top side of the test plates are shown in Section 4.1.8.7 in Figure 73 and Figure 74 respectively. A comparison of simulation and experimental values obtained by infrared thermography from the undisturbed region of the test plates are shown in Figure 75. On the left side, the comparison of a reflection mode measurement from the top side of the plate is shown. Whereas, on the right side, data of transmission mode measurements can be seen. The temperature profiles of the simulations perfectly correspond with those of the measurements. To investigate the temperature distribution over the entire embedded fiber waviness, the IR camera recorded the intensity of the temperature orthogonally to the cross-section of the test plates, with an excitation from the bottom and top side, respectively. This allowed an exact observation of the heat flux passing through the entire wave over time. A representative visualization of the temperature difference obtained from experimental

4.2 FINITE ELEMENT ANALYSIS OF NDT METHODS

measurements is shown in Figure 76 (a). The results of the same plate evaluated by FE analysis is shown in Figure 76 (b). This Figure shows the temperature field at $t=15$ s after excitation on the top side of the test plate 3 containing wave 1. The data of the temperature differences of the experiment were visualized using MATLAB.

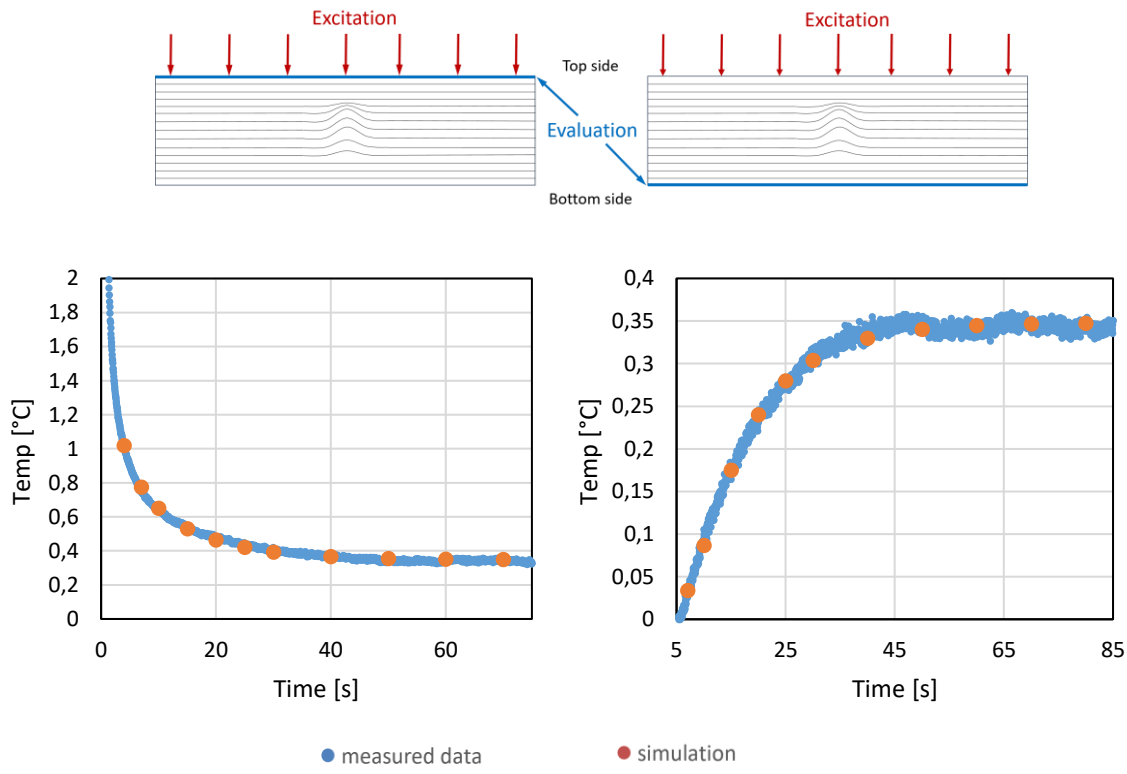


Figure 75. Comparison of the temperature profile of the experiment (blue) and simulation (red) of the undisturbed region of plate 1 in reflection mode analyzed at the top side (left) and in transmission mode analyzed on the bottom side (right) of the test plate.

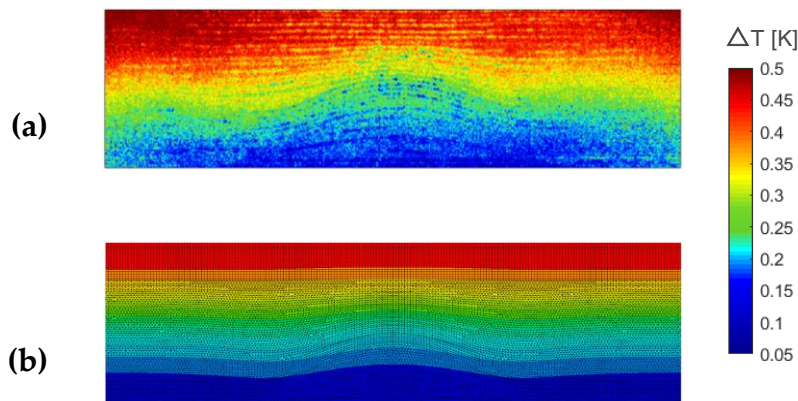


Figure 76. Temperature differences at 15 seconds of plate 3 with wave 1 obtained from a) experimental setup and b) FEM simulation.

In both images the shape of the wave can be clearly recognized. A temperature difference of 0.5 K can be determined over the entire area in both plots, although more noise is observed in the experimental data. The temperature distribution of the simulation and the measurement are in excellent agreement. Based on the signal shape, it is simple to determine the orientation of the fiber waviness. The heat flux shown in Figure 77 is either spread (a) or bundled (b), depending on the side of excitation or orientation of the fiber waviness, respectively. Thus, the orientation of the fiber waviness can be determined from the signal shape.

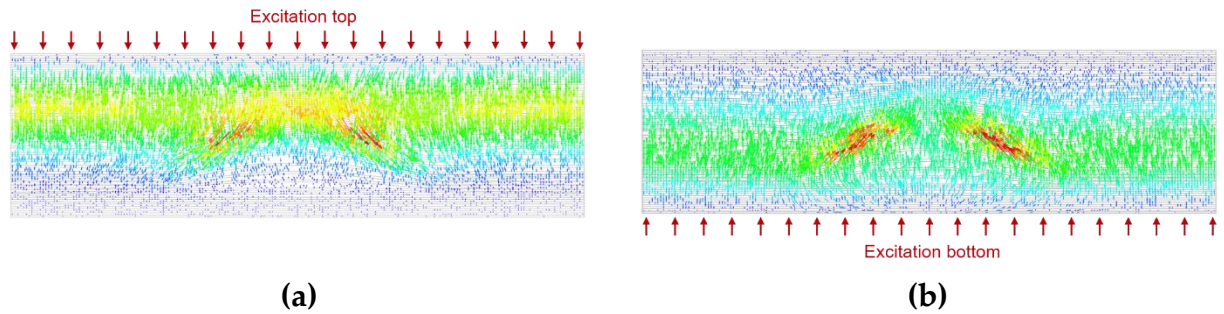


Figure 77. Representative FEM result of the spreading (a) and bundling (b) heat flux due to excitation on the top and bottom side, respectively, for plate 2 containing wave 1.

The measurement and simulation results were investigated and compared with respect to the intensity of the averaged signals from the undisturbed and wave region. Figure 78 to Figure 81 show a few representative variants of the measured and simulated waves. The x-axis shows the position of the wave and the corresponding signal is plotted on the y-axis. The dashed lines indicate the wavelength, i.e. $L_1=15$ mm, $L_2=10$ mm. The beginning and the end of the fiber waviness can be recognized clearly, as they appear in the signal exactly left and right of the characteristic Mexican hat-shaped function in the local minima and maxima, respectively.

4.2 FINITE ELEMENT ANALYSIS OF NDT METHODS

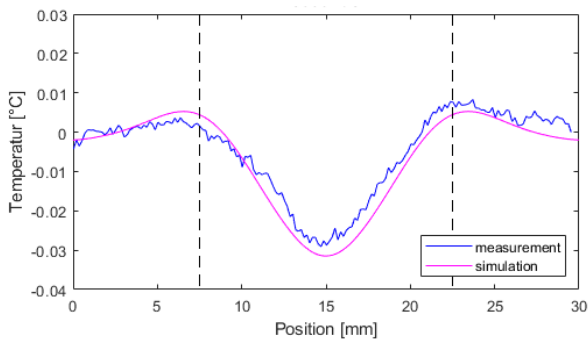


Figure 78. Comparison of measurement (blue) and simulation (purple). Plate 1, wave 1, at 10 seconds, reflection mode, analyzed on the top side.

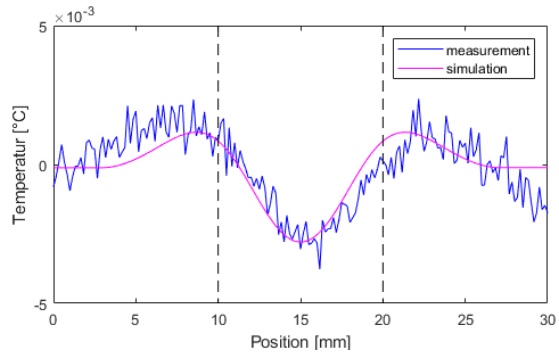


Figure 79. Comparison of measurement (blue) and simulation (purple). Plate 2, wave 2, at 10 seconds, transmission mode, analyzed on the bottom side.

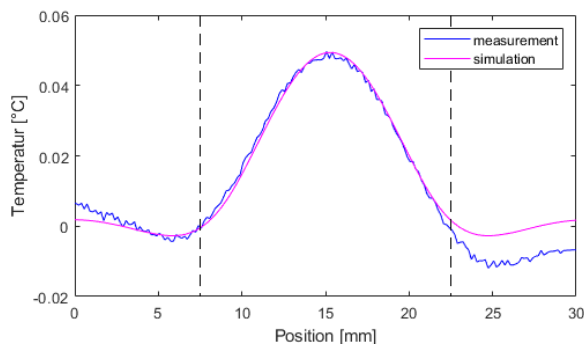


Figure 80. Comparison of measurement (blue) and simulation (purple). Plate 3, wave 1, at 10 seconds, reflection mode, analyzed on the bottom side.

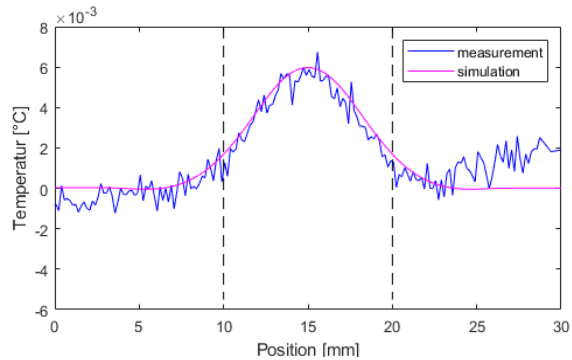


Figure 81. Comparison of measurement (blue) and simulation (purple). Plate 4, wave 2, at 10 seconds, transmission mode, analyzed on the top side.

In order to evaluate the change of the signal shape over time, representative results of plate 1 containing wave 1 in reflection and transmission mode are shown in Figure 82 and Figure 83, respectively. With longer measurement times, the typical Mexican hat function disappears due to lateral heat flows. In general, the wavelength of the embedded out-of-plane fiber waviness can be determined with sufficient accuracy for both wave configurations from the top as well as bottom side of the test plates. The wave amplitude may be approximated by the signal strength. The signal strength is assumed to be mainly dependent on the amplitude of the embedded fiber waviness and its position, i.e. depth, in the laminate. Furthermore, the heat loss and the smearing of the thermal data due to the lateral heat flow are expected to increase especially in thicker laminates, since longer measurement times are required.

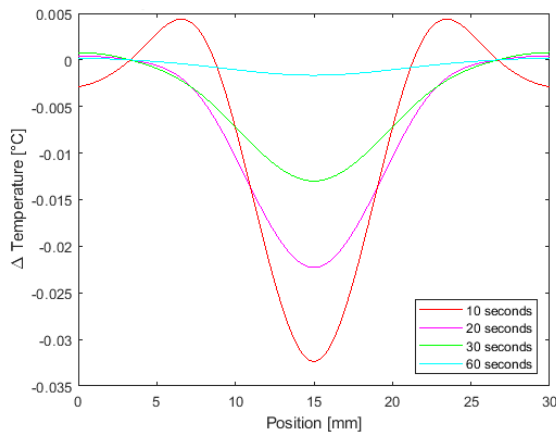


Figure 82. Resulting signals obtained from FEM simulations in reflection mode, exemplified by the simulation of plate 1 including wave 1 from the top side of the test plate for times $t=10, 20, 30$ and 60 s.

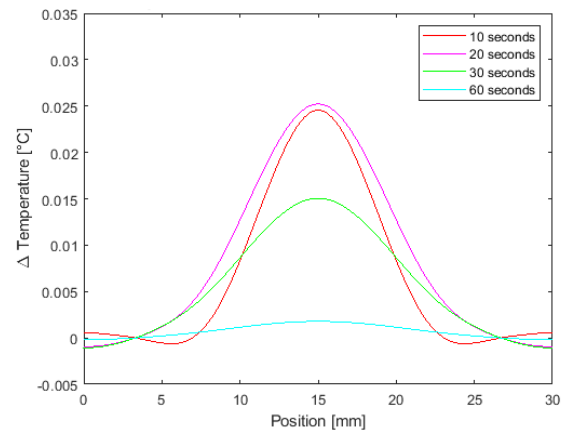


Figure 83. Resulting signals obtained from FEM simulations in transmission mode, exemplified by the simulation of plate 1 including wave 1 with an excitation at the bottom and analysis at the top side of the test plate after for various times $t=10, 20, 30$ and 60 s.

4.2.4.2. Digital shearography (deformation)

Representative images from digital shearography, i.e. grey scale values of the gradient of deformation field, obtained from the bottom and top side of the test plates are presented in Section 4.1.8.7 in Figure 73 and Figure 74 respectively. To validate the accuracy of the conducted FEM simulations, the results were compared with experimental measurements. However, there are no absolute displacement or temperature values available for the experimental measurements. Therefore, the comparison was only made on a qualitative basis. For this purpose, the resulting deformations in y -direction on the top and bottom side of the simulation were exported and converted into the gradient of the deformation. These were compared with the results of the measurements. A representative result of measured (Figure 84) and simulated (Figure 85) deformation gradients of plate 1 containing wave 1 obtained in reflection mode from the top side shows qualitatively good agreement. The measurements also show the first derivative, i.e. gradient of deformation field, but directly derived from the grey values of the interfering laser beams. Furthermore, the respective wavelengths were plotted with dashed lines in the diagrams.

Due to the negative coefficient of thermal expansion in the fiber direction [238], an indentation occurs at the top side and a bulge on the bottom side. Figure 86 shows this warpage of the test plate, where the displacement in the y -direction of plate 1 containing wave 1 after 60 seconds with an excitation at the top side is shown.

4.3 CONCLUSION ON THE NON-DESTRUCTIVE TESTING OF WRINKLES IN COMPOSITES

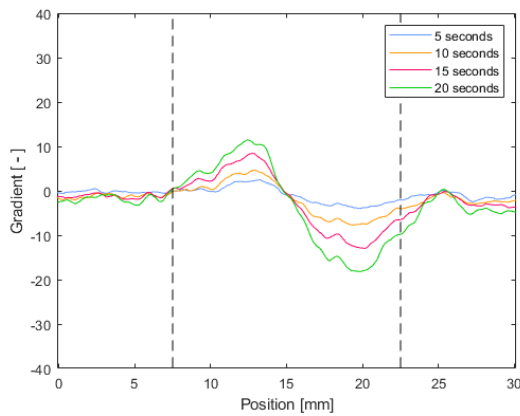


Figure 84. Result of the digital shearography measurement. Gradient of deformation field on the basis of grey values. Plate 1, wave 1, excited and evaluated on the top side.

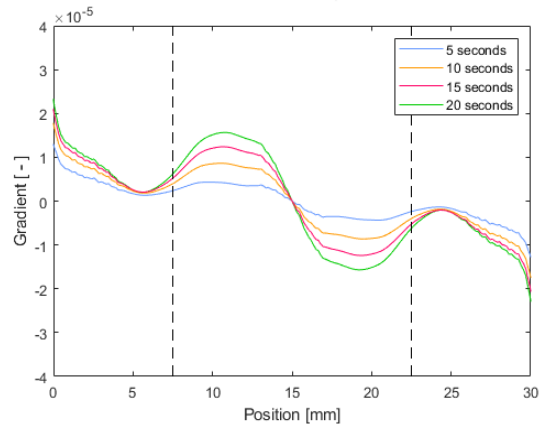


Figure 85. Result of the digital shearography simulation. Gradient of deformation field on the basis of the computed deformation. Plate 1, wave 1, excited and evaluated on the top side.

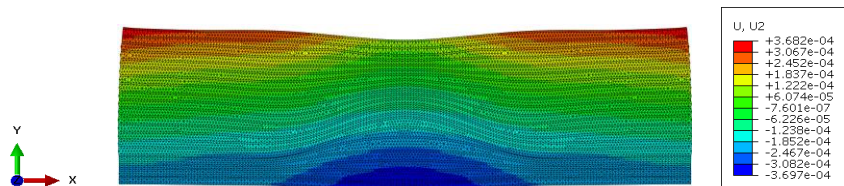


Figure 86. Representative deformation, i.e. displacement in y-direction, of a coupled temperature-displacement simulation of plate 1 containing wave 1 with an excitation from the top side at $t=60s$.

4.3. Conclusion on the non-destructive testing of wrinkles in composites

This section has focused on the non-destructive detection and evaluation of composite materials containing artificially induced out-of-plane fiber waviness from both an experimental and numerical point of view. The performed non-destructive tests have shown great potential for the detection of embedded out-of-plane fiber waviness. However, due to the various types and characteristics of fiber waviness that can occur in composite manufacturing processes, comprehensively described in Section 3, a general statement on the detectability can be hardly made without further studies. The presented results and statements are valid for the type of test samples used in this study. Results from various methods, i.e. ultrasonic testing, infrared thermography, digital shearography and eddy current testing, indicate the possibility of estimating the characteristics of the fiber waviness, i.e. amplitude and wavelength, from the strength of the signal. The wavelength has shown to be more easily determined by the conducted NDT methods. Nevertheless, for a subsequent

evaluation of the structural integrity, the amplitude was found in Section 8 to be a more important parameter than the wavelength.

Particularly, active thermography and digital shearography have shown great potential as alternative NDT methods compared to ultrasonic testing, which is currently the industry standard. Both methods allow for a fast and contactless inspection of large areas. By using active thermography, it was possible to determine the defect as well as the orientation of the fiber waviness from the appearance of the resulting signal, regardless whether the measurement was performed in transmission or reflection mode. The wavelength can also be determined accurately based on the results of the experimental measurements as well as numerical simulations. Additionally, the depth up to which the wave is detectable could also be determined. With increasing depth of the fiber waviness, a decreasing course of the signal duration above a specific threshold value could be noticed. In this thesis, a qualitative investigation of shearography was considered. Therefore, no quantitative statements about the depth of the wave can be provided. However, the wavelength was clearly visible based on the signal of the deformation gradients obtained from FEM simulations as well as from experimental measurements. In further research activities, several additional variations of wave configurations and positions, i.e. wavelengths, amplitudes and depths in the laminate, have to be investigated analytically, numerically and experimentally to describe the relationship between the depth position of the wave and the intensity and duration of the signal. Additional accompanying finite element simulations may also give a better insight into the physics and possible ranges of applicability of the methods. The experimental digital shearography test setup has to be carried out in combination with temperature measurements and digital image correlation to obtain valid data for the simulations, i.e. temperatures and deformations. This study provides a good basis for the determination of the characteristics of embedded fiber waviness, i.e. amplitude, wavelength and depth in the laminate. Moreover, the promising results point out the huge potential of these NDT methods for further research and applications in industry.

5. MECHANICAL TESTING

The currently limited capability to predict material failure in composite materials in general and in wavy composite layers specifically has led to high margins of safety for the design of composite structures. Thus, the full lightweight potential of this class of materials is left unused. To understand the complex failure behaviour of composite materials containing out-of-plane fiber waviness under compressive and tensile loading, digital image correlation (DIC), passive thermography (IRT) and acoustic emission (AE) test methods are used to investigate damage initiation and propagation on specimen level. These methods deliver qualitative trends as well as quantitative metrics about the damage behavior in wavy CFRP materials. This data can be further used in constitutive laws to gain deeper insight and understanding in the material behavior. In addition to that, an extensive material characterization on planar specimens was also performed.

5.1. Experiments under room temperature and dry conditions

5.1.1. *Experimental methods and test set-ups*

5.1.1.1. Specimen preparation

A pre-impregnated polymer composite consisting of IM7 unidirectional carbon fiber reinforcement embedded in a 8552 thermosetting epoxy matrix (Hexcel Corporation) is used. The nominal cured ply thickness of the UD prepreg layer is 0.131 mm according to the material data sheet. The laminates are fabricated in an autoclave following the recommended curing cycle for monolithic components. Reference specimen (no waviness) thickness is, consistent with test standards, kept at 2.1 mm, i.e. 16 layers of 0° (UD) or with a stacking sequence of (0/45/-45/90)_{2s} (QI). Specimen containing fiber waves were 5.1 mm, i.e. 40 plies at 0° (UD) or with a stacking sequence of (0/45/-45/90)_{5s} (QI). Two configurations of sinusoidal waves were realized using a one-side female metal plate tooling in which the defined sinusoidal wave configurations were milled in with a wavelength $L_1=27.9$ mm and amplitude $A_1=1.19$ mm (wave 1) and $L_2=14.5$ mm and $A_2=0.58$ mm (wave 2). After demolding, glass fiber reinforced (GFRP) tabs were glued onto the grinded and thoroughly cleaned surface. The process of wavy specimen preparation is shown in Figure 87. Laminate quality was verified by measuring the fiber volume fraction (61.3%, 0.95% STD) using wet chemical fiber extraction according to EN 2564 for 12 samples.

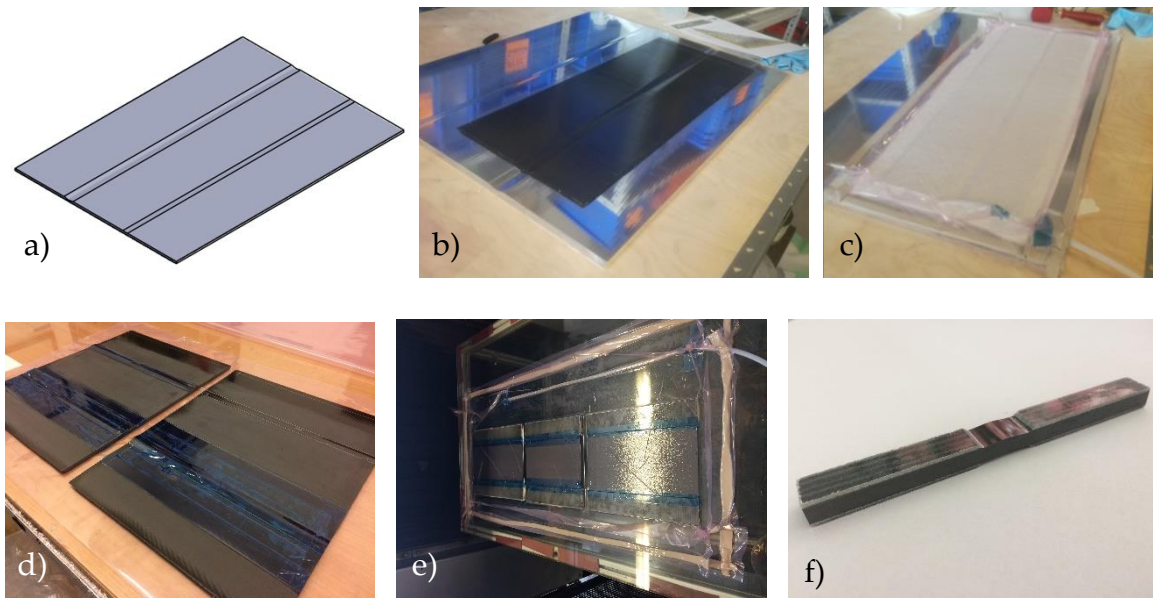


Figure 87. Autoclave fabrication process of test plate containing out-of-plane fiber waviness;

- a) isoparametric view of metal mold;
- b) stacked carbon UD prepreg layers;
- c) vacuum bagging for autoclave process;
- d) surface treated test plates prepared for bonding tabs;
- e) applied tabs under vacuum bag;
- f) cut representative specimen (wave 2, compression).

5.1.1.2. Tensile and compression testing

Tensile and compression tests are carried out in the spirit of ASTM D3039 and ASTM D6641. Material testing was conducted on universal test machines from Zwick and Messphysik with a maximum load of 150 kN and 250 kN respectively. Specimens were loaded at a rate of 2 mm/min. Coupling the DIC, IRT and AE measurement systems with the test machine via analog inputs allows for a simultaneous recording of images with the corresponding force and displacement signal. The general test plan showing configurations and number of specimens used for mechanical tests is given in Table 11. The conducted tests on wavy specimens which were accompanied by DIC, IRT and AE are summarized in the following test matrix, Table 12.

5.1 EXPERIMENTS UNDER ROOM TEMPERATURE AND DRY CONDITIONS

Table 11. Test plan showing configurations and number of specimens.

	Loading	No. of specimen	Layup	Dimension (mm)
Wave 1	Compression	5	0°	130x10
Wave 2	Compression	5	0°	115x10
Wave 1	Compression	5	QI	130x25
Wave 2	Compression	5	QI	115x25
Wave 1	Tension	5	0°	250x10
Planar reference	Compression	5	0°	110x10
Planar reference	Compression	5	90°	110x10
Planar reference	Tension	5	0°	250x10
Planar reference	Tension	5	90	250x25
Planar reference	Compression	3	QI	110x10
15° Off-axis	Tension	5	15°	250x25

Table 12. Test plan for experiments accompanied by DIC, IRT and AE (configurations and number of specimens).

	Digital image correlation	Passive thermography	Acoustic emission
Wave 1 UD compression	6	4	
Wave 2 UD compression	6	4	
Wave 1 UD tension	6	4	
Wave 1 QI tension	8		8

5.1.1.3. Digital image correlation

Digital image correlation (DIC) is a powerful tool for measuring strain distributions during mechanical testing of materials. In contrast to traditional extensometers or applied strain gauges, with a typical gauge length of several tens of millimetres, DIC delivers full-field information of the strain state for each load step. In general, DIC is based on the principle of comparing stochastic distributed speckle patterns of the undeformed reference state to any deformed state. For the strain analysis, a virtual grid of subsets (facets) is overlaid on the applied speckle pattern. The deformation during the loading process is recorded with a camera system and the subsets are tracked by the software. The in-plane strain distribution on the surface of the specimen is gained without a priori knowledge of the constitutive behaviour. When observing materials with a non-uniform microstructure and a resulting non-uniform local loading condition, like it is present in the behaviour of out-of-plane fiber waviness with a complex strain field, a full-field strain measurement is necessary. In recent

years, several studies on composite materials have been performed using DIC [1-2], also specifically on the investigation of fiber waviness in composites [3-4]. A stereo camera system with two 12 Megapixel cameras (GOM Aramis™ 3D 12M) was used for measuring the full-field through-thickness strain distribution. The DIC measurement system was triggered by the test software via analog inputs, ensuring synchronized recording of images with the force and displacement signal. Depending on the required field of view 50 mm and 100 mm lenses were used and a homogeneously distributed speckle pattern was applied on a matt white grounding using the airbrush system Minijet 4400 B RP (SATA, Kornwestheim, Germany). Images were obtained at 10 Hz. The test-set up is shown in Figure 88. To analyze the images the software GOM Correlate Professional (2016) was used. The facet size was set to (14 x 14) pixels with a point distance of 10 pixels.

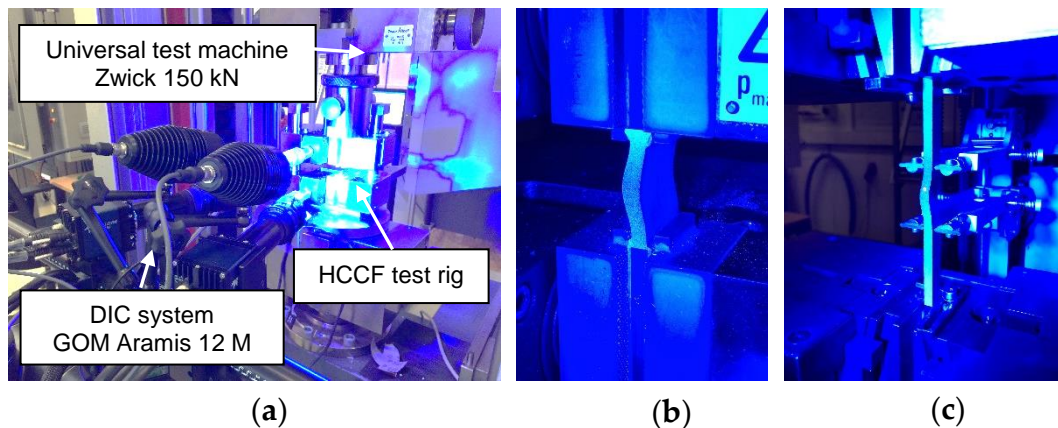


Figure 88. a) Mechanical test set-up using DIC and hydraulic composite compression fixture (HCCF); b) compression specimen; c) tensile specimen.

5.1.1.4. Passive infrared thermography

In passive thermographic methods, the temperature distribution of the test object is monitored as resulting from its regular operation. In the case of applied mechanical loads, damage events occur and dissipate heat allowing their localisation. In this study, a passive thermographic approach was used to locate the failure initiation and propagation by using a high-resolution infrared (IR) camera FLIR X8400sc equipped with an indium antimonide (InSb) detector. The cooled 1280 x 1024 pixel focal plane array camera has a noise equivalent temperature difference (NETD) of about 25 mK and is sensitive in a spectral range of 1.5 to 5.1 micron. The measurements were carried out with a frame rate of 172 Hz and an approximate spatial resolution of 70 μm . The field of view was set to be consistent with the strain field measurements. The test set-up for passive thermography is shown in Figure 89.

5.1 EXPERIMENTS UNDER ROOM TEMPERATURE AND DRY CONDITIONS

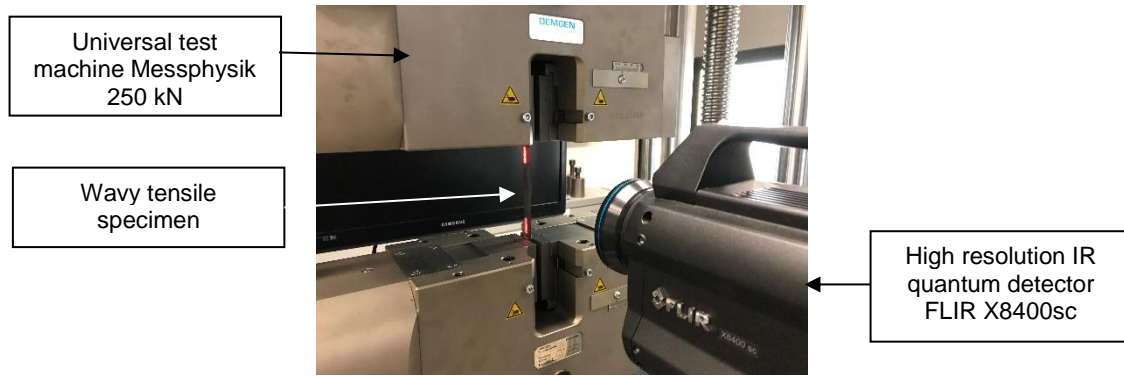


Figure 89. Passive thermography test set-up for tensile test.

5.1.1.5. Acoustic emission

The rapid microscopic displacements caused by microscopic failure mechanisms in fiber-reinforced composite materials cause an excitation of elastic waves in the ultrasonic frequency range. These transient acoustic signals can be detected and analysed using piezoelectric sensor systems. The measured acoustic emission signals can be used to detect the onset and position of microscopic failure events occurring in fiber-reinforced composite materials. [5-11]

In recent years, many attempts [6-10, 12] have been made to distinguish between different types of failures such as fiber breakage, matrix cracking and interfacial failure in fiber-reinforced materials. The analysis of the measured acoustic emission signals used in the present study is based on previous work [13,14]. It follows a recently developed pattern recognition method [15] to distinguish and quantify the above mentioned failure mechanisms in carbon fiber-reinforced polymers. The validity of the source identification by the proposed method is based on reference calculations [16-18] of the acoustic emission source, signal propagation, and signal detection process by finite element modelling.

Two wide band (WD) AE sensors were attached in linear arrangement at opposing ends of the specimen as illustrated in Figure 90 and Figure 91. In the present case, the AE test method is only used for the tensile specimens due to space limitations of the low free length in compression. AE tests are conducted on wavy as well as on flat reference tensile specimen. AE signals were acquired using a Mistras PCI-2 system with 2/4/6 preamplifiers. A threshold-based triggering mechanism using 10/80/300 μs (Peak-Definition-Time/Hit-Definition-Time/Hit-Lockout-Time) at a threshold of 35 dB_{AE} and a preamplification of 20 dB_{AE} was used. The data were recorded with an acquisition rate of 10 MSP/s and a band-pass filter ranging from 20 kHz to 1 MHz using the software AEwin. An Event-Definition-Time filter of (15 \pm 2) μs was used to detect only signals from source positions located in the range between the two sensors. A medium viscosity silicone grease (KORASILON™, Kurt Obermeier, Germany) was used to provide an adequate acoustic coupling. The sensors were attached to the specimen using standard clamp systems, shown in Figure 91, to ensure a reproducible mounting pressure. The sensor coupling was validated by mutual pulsing of both

sensors and comparison of the detected signal amplitudes in an automatic sensor test (AST). The sound velocity of the initial arrival of the Lamb wave is obtained from the measured time difference between the time of pulsing of sensor 1 and the arrival time at sensor 2 divided by their respective metric distance (118 ± 1 mm for both wavy and plane reference specimens). A pencil lead break test (PLB) was carried out according to ASTM E976 for each specimen before testing. This technique, named Hsu-Nielsen source after its developers, simulates an acoustic emission event by breaking a brittle graphite pencil lead with a diameter of 0.5 mm, located in a suitable fitting, approximately 3 mm (± 0.5 mm) away from its tip by pressing it against the surface of the specimen. This intense artificial acoustic signal simulates a very loud out-of-plane acoustic emission source. This test ensures that the transducers are in good acoustic contact with the specimen being monitored and also checks the accuracy of the source location setup. In addition to the above mentioned tests, signals are measured for approximately one minute with the mechanical measuring system completely at rest before the actual test is carried out. This is done to ensure, that signals, generated outside the measurement area are not recorded. After signal acquisition from mechanical testing, the acoustic emission source position was calculated by Δt -localization techniques using the one-dimensional sensor arrangement. Only localized signals that fulfil the condition $|\Delta t| \leq 20 \mu\text{s}$, were taken into account for further analysis. An application of the pattern recognition method described in [15] yields three signal classes for all eight plane reference and eight wavy specimens investigated. For the pattern recognition method, the acoustic emission signal features of both sensors were calculated from the first 200 μs of the signals after the signal arrival.

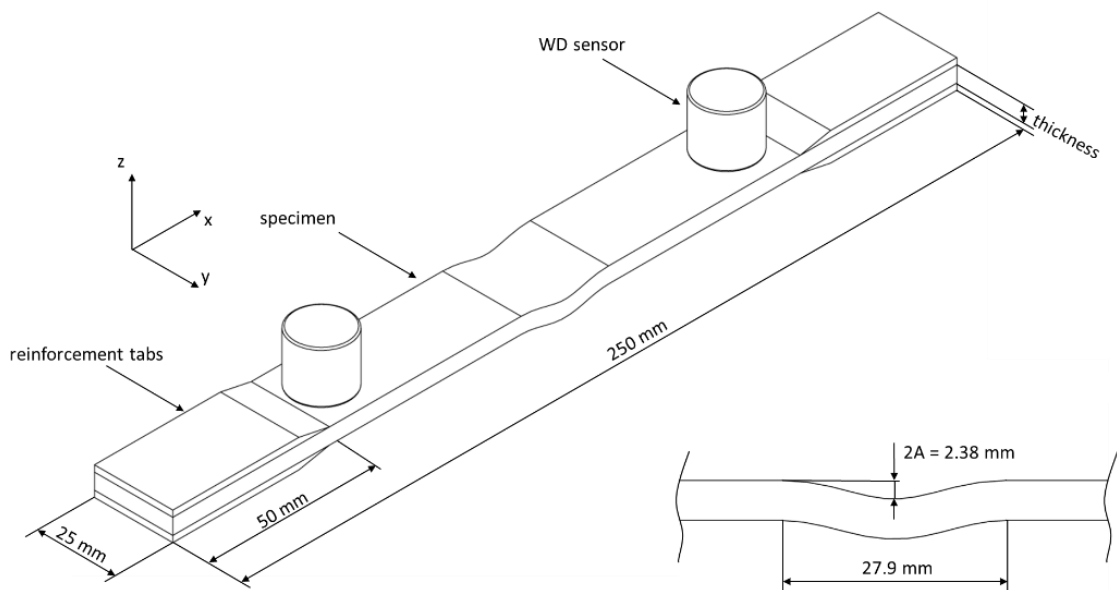


Figure 90. Wavy specimen dimensions and linear arrangement of the acoustic emission sensors.

5.1 EXPERIMENTS UNDER ROOM TEMPERATURE AND DRY CONDITIONS

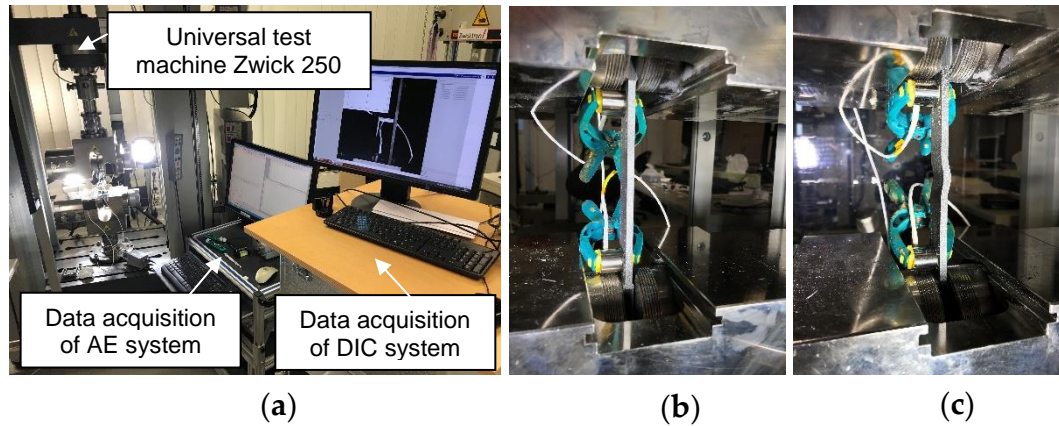


Figure 91. a) Acoustic emission test set-up; b) planar reference specimen; c) wavy specimen.

5.1.2. Results and discussion

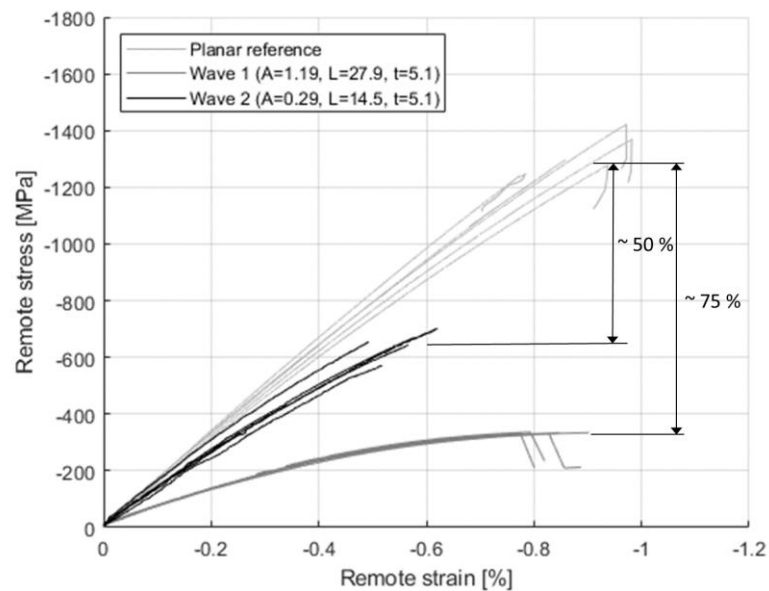
5.1.2.1. Mechanical behavior of planar reference and wavy specimen

The experimental data for planar reference and wavy specimen under compression (Figure 92 and Figure 94) and tensile loading (Figure 93) show a non-linear stress strain response for wavy specimen and a considerable knockdown. Young's modulus in fiber direction and the peak-stress before failure for all tests are shown in Table 13.

The compressive strength is reduced by approximately 75% for the more pronounced wave configuration (wave 1) and 50% for the less pronounced wave (wave 2). The latter also shows a substantial reduction of the strain-to-failure by approximately 45%. Those results are in good accordance with previously reported findings [48]. Although the compression properties were assumed to be more affected by fiber waviness compared to tensile loading [69,70], results from mechanical tests on wave 1 show a drop of 70% in tensile strength for first ply failure, where mode I delamination occur due to positive stresses in thickness direction σ_z (Figure 98 c). A dramatic drop in compressive strength was found for both wave configurations with quasi-isotropic laminate compared to the reference specimen. The compressive strength dropped by approximately 65% (wave 1) and 32% (wave 2). Interestingly, a reduction in stiffness could only be observed for the more pronounced wave (wave 1) but not the other one (wave 2). In compression loaded laminates, containing fiber waviness, the mechanical properties of the 90° -layers are not reduced by the wave. The highly affected 0° -layers account only for 25% of the total laminate. Therefore, the presence of waviness has a reduced influence on QI laminates compared to UD laminate. This results suggest, that the drop in stiffness properties for the more pronounced wave 1 is mainly caused by the geometrical deviation of the wave due to a higher amplitude-to-thickness ratio (A/t). The resulting Young's modulus and strengths for quasi-isotropic laminates are summarized in Table 13.

Table 13. Test data of stiffness and strength properties for IM7-8552 planar reference and wavy specimen.

	Compression		Tension	
	E_{1c} [GPa]	σ_{cm} [MPa]	E_{1t} [GPa]	σ_{tm} [MPa]
Reference UD	160.6	1322.3	172.9	2094.3
Wave 1 UD	78.7	333.5	104.4	584.3
Wave 2 UD	135.9	655.5	-	-
Reference QI	62.2	686.4	64.2	902.4
Wave 1 QI	33.4	237.9	-	-
Wave 2 QI	66.4	465.7	-	-

**Figure 92.** Compression test of UD-laminate – Comparison planar vs. wavy specimen.

5.1 EXPERIMENTS UNDER ROOM TEMPERATURE AND DRY CONDITIONS

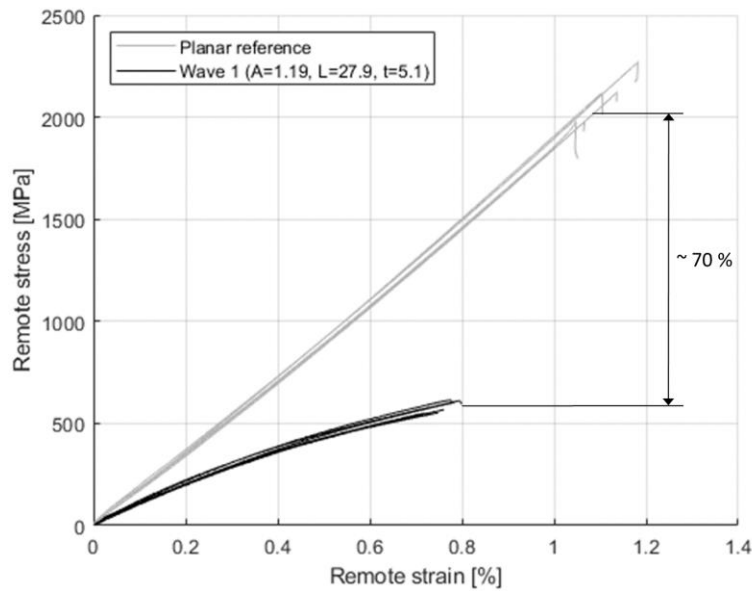


Figure 93. Tensile test of UD-laminate – Comparison planar vs. wavy specimen.

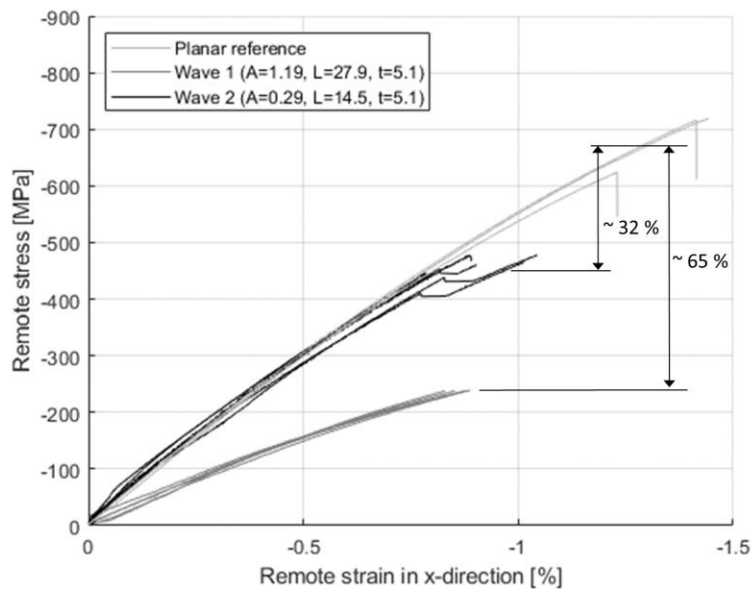


Figure 94. Compression test of QI-laminate – Comparison planar vs. wavy specimen.

The applied unidirectional load leads to a complex 2D strain state at the observed cross-section due to the presence of the wave. In Figure 95 the shear strain ε_{xz} distributions of wavy specimens are shown right before and after final damage within two subsequent frames (10 Hz) for a) wave 1 and b) wave 2 under compression and c) wave 1 under tensile load. Regions of high strain coincide well with the occurrence of macroscopic material failure. This is in accordance with [46], who determined that the associated shear stress τ_{13} is the most significant stress component for damage initiation in wavy composites under axial compression.

While compression loads increase the amplitude-to-wavelength ratio, global applied tensile loads straighten the fiber waviness, leading to an increasing stiffness during loading [242]. Both of which require a geometrically non-linear calculation. The substantial influence of both the amplitude A and thickness t in light of the resulting bending stresses are shown in Eqn. 40. A simplified analytical consideration using the Euler-Bernoulli beam theory (neutral axis coincides with the beam centroid line, bending moment $M_B = F A = \sigma_x b t A$, where A is the amplitude, the moment of inertia for rectangular cross section $J_y = \frac{b t^3}{12}$ and $y = \frac{t}{2}$) leads to

$$\sigma_B = \frac{M_B}{J_y} z = \frac{6 \sigma_x A}{t}. \quad (30)$$

Thus, the resulting bending stresses, with a maximum in the longitudinal center of the wave, increases with increasing amplitude and decreases with increasing thickness. To incorporate the geometric non-linearity the curved beam theory can be utilized.

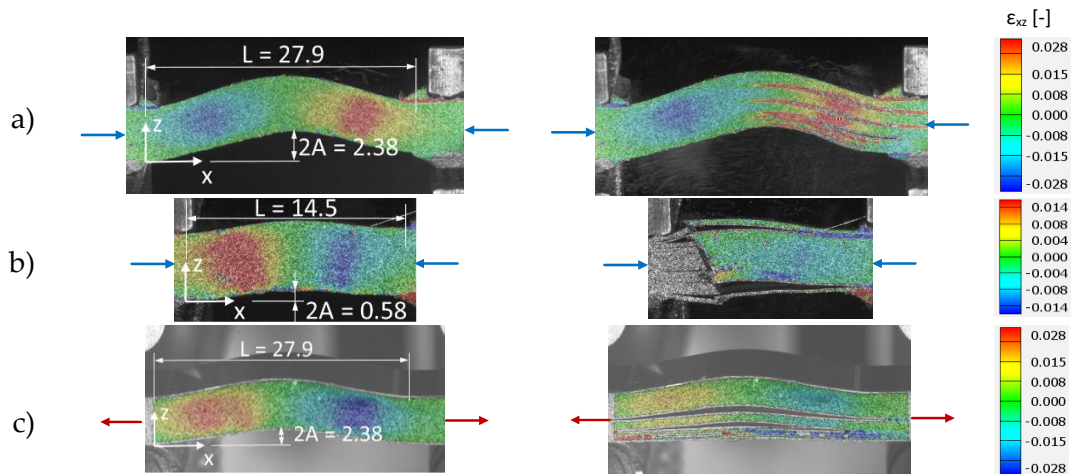


Figure 95. Shear strain ε_{xz} distribution in the frame captured right before and after macroscopic damage for UD specimen configurations. Blue and red arrows indicate the global loading. a) wave 1 in compression; b) wave 2 in compression; c) wave 1 in tension.

The resulting shear stress distribution from a linear-elastic but geometrical non-linear FE simulation evaluated along a centroid curve for varying laminate thicknesses, shown in Figure 96, underlines the thickness-dependent behavior. Shear stresses are highest at the location of the biggest incline/decline and generally increase with thickness. However, when a thickness of $4A$ is reached, the further increase of the resulting shear stress is almost zero. An additional linear elastic FE simulation of varying amplitudes and constant wavelength $L=27.9$ mm and laminate thickness $t=7.14$ mm shows the superposition of bending stresses with the global compressive or tensile load in Figure 97 by plotting the stresses in x -direction at the peak point of the wavy specimen. This results in different stress states (tension or compression) in the center

5.1 EXPERIMENTS UNDER ROOM TEMPERATURE AND DRY CONDITIONS

of the wavy region, depending on the thickness. The compression loaded wave with an amplitude of $A=0.595$ mm shows approximately zero stress σ_x at the peak point due to the superposition of global loading and resulting bending stresses. This mechanism in form of variations of the longitudinal strain component ε_x is also schematically shown in Figure 98 and can be clearly observed in DIC measurements.

There is a transition from tension to compression of ε_x across the thickness when global compression and tension is applied within the tested wave with the higher amplitude (wave 1, c.f. Figure 98 a). Wave 2 (less pronounced waviness) shows a gradient in the strain component but no transition from tensile to compression strains. The effect of superposing bending stresses is amplified during compression testing due to an increasing amplitude-to-wavelength ratio (A/L).

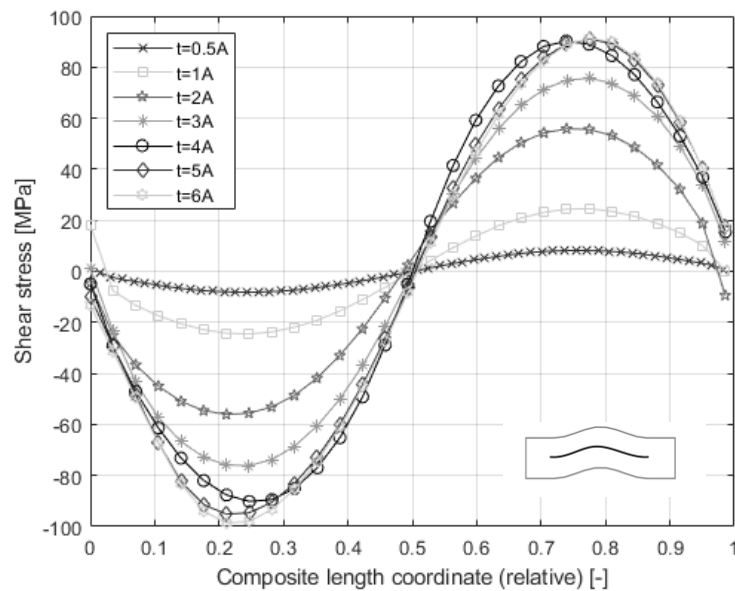


Figure 96. Shear stress distribution along centroid curve for wave 1 ($A = 1.19$ mm, $L = 27.9$ mm) with varying thickness from linear FE-Simulation.

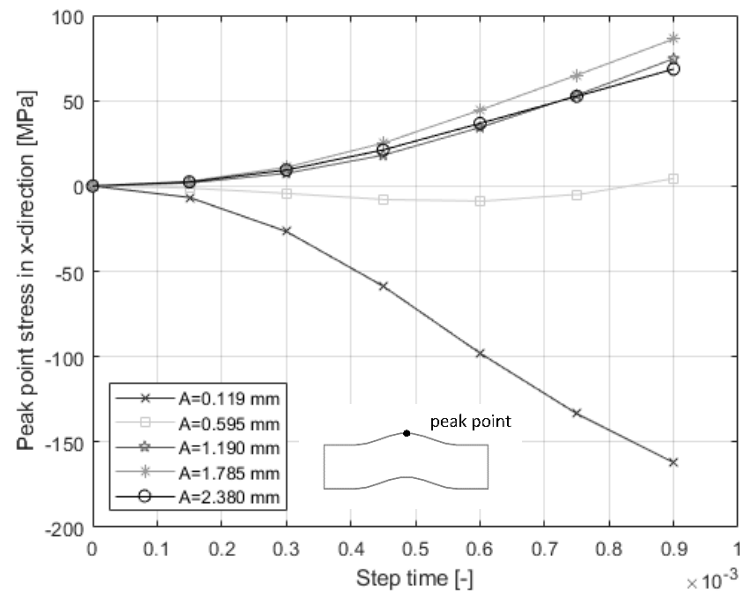


Figure 97. Peak point stress in x-direction ($L = 27.9$ mm, $t = 7.14$ mm) from linear FE-Simulation.

5.1 EXPERIMENTS UNDER ROOM TEMPERATURE AND DRY CONDITIONS

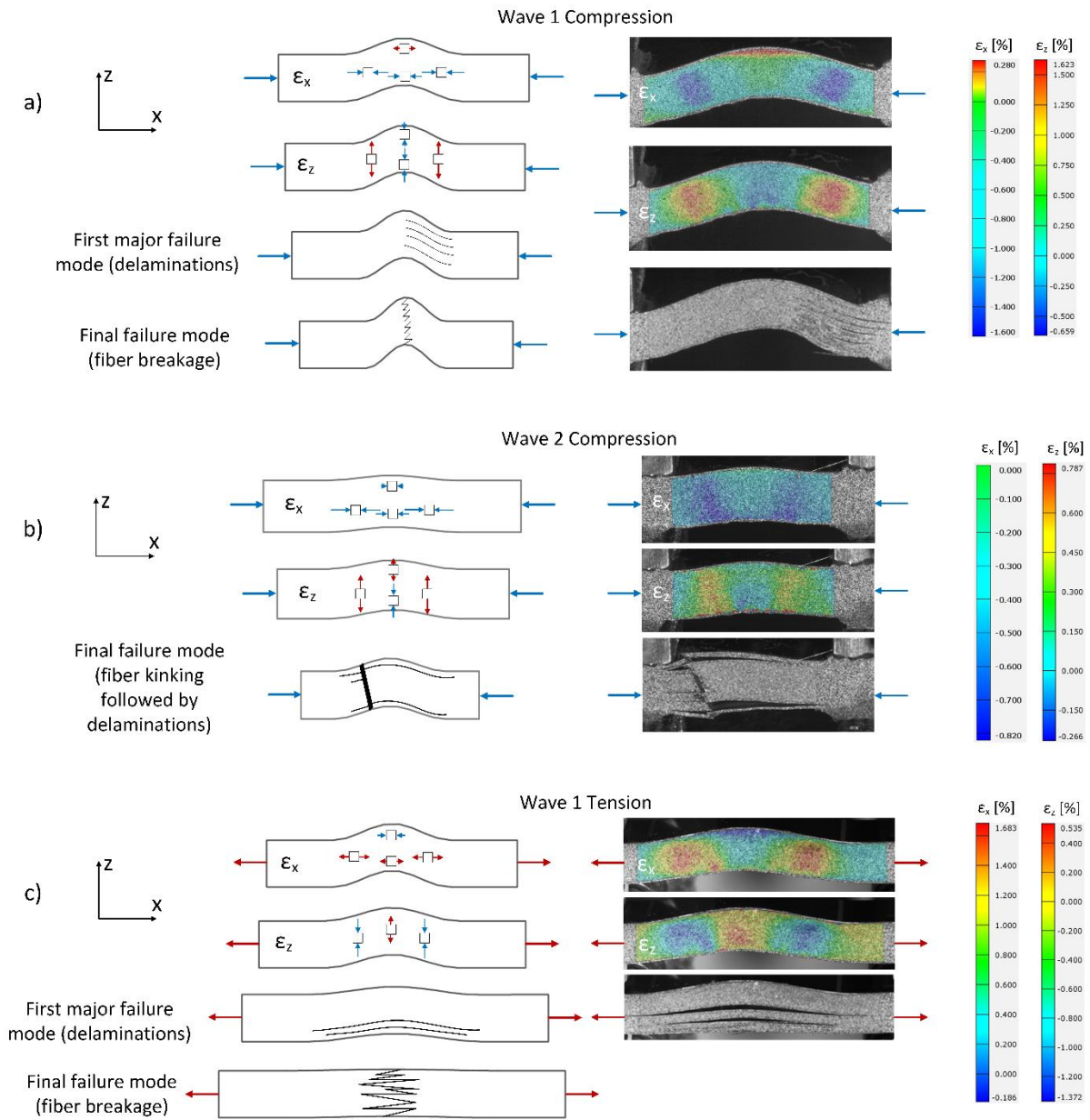


Figure 98. Schematic illustration and corresponding DIC results of damage behavior including normal strains ϵ_x and ϵ_z . a) wave 1 specimens under compression load; b) wave 2 specimens under compression load; c) wave 1 specimens under tensile load.

In addition to the above mentioned shear strains that are considerably influencing the failure behavior, resulting tensile strains ϵ_z , respectively stresses in thickness direction σ_z potentially cause the individual layers to lift off, causing delamination, as shown in Figure 98 a) and c). This leads to the conclusion, that the resulting stresses superpose with shear stress components and also considerably influence the failure behavior. In global tensile loading (Figure 98 c), the resulting through thickness strain component ϵ_z in wave 1 shows a maximum in tension at the center of the wave, leading

to delamination along the whole wave length, potentially initiated at the wave center. Wave 2 shows a maximum tensile strain component ε_z at the turning point of the sinusoidal wave under compression loading. This leads to one-sided delamination initiated at the area of maximum inclination of the sine wave.

Global compression load of wave 2 and the absence of notable bending moments leads to fiber kinking of the specimen schematically depicted in Figure 98 b). The positive strain ε_z in thickness direction leads to less supported fibers and therefore promote the appearance of kink bands. These results suggest that the failure of wave 1 is determined by the bending moments resulting from the geometry (mainly amplitude and thickness). In contrast, for wave 2, the contribution of bending stresses in superposition with the global load is less thus material failure is observe. The failure behavior is more determined by the material properties for lower amplitude-to-thickness ratios.

5.1.2.2. Passive thermography

In-situ passive thermography is used to assess the damage initiation and propagation during quasi-static mechanical loading in compression and tension. Representative images obtained during mechanical testing are shown in Figure 100 (wave 1 in compression), Figure 101 (wave 2 in compression) and Figure 102 (wave 1 in tension). Damage initiation was visible as clear bright spots and the progressing delamination appeared as a bright line. Due to a higher energy release of fiber bundle failure in comparison to the lower energy releases of matrix failure, the type of damage can be clearly identified by single point evaluations of the resulting peak values of thermal intensities as shown in Figure 99. The p-value < 0.0002 , resulting from a one-way ANOVA, determines that the differences between the group means of matrix and fiber bundle failure are statistically significant. The presented digital levels (thermal intensities) of the IR quantum detector are a metric directly related to the temperature. Fiber bundle failure results in approximately two times higher thermal intensities than matrix failure. Clustering these results of (near-)surface damage events on macroscopic level gives the opportunity to distinguish results on smaller scales, e.g. single fiber breakage or small matrix cracks.

5.1 EXPERIMENTS UNDER ROOM TEMPERATURE AND DRY CONDITIONS

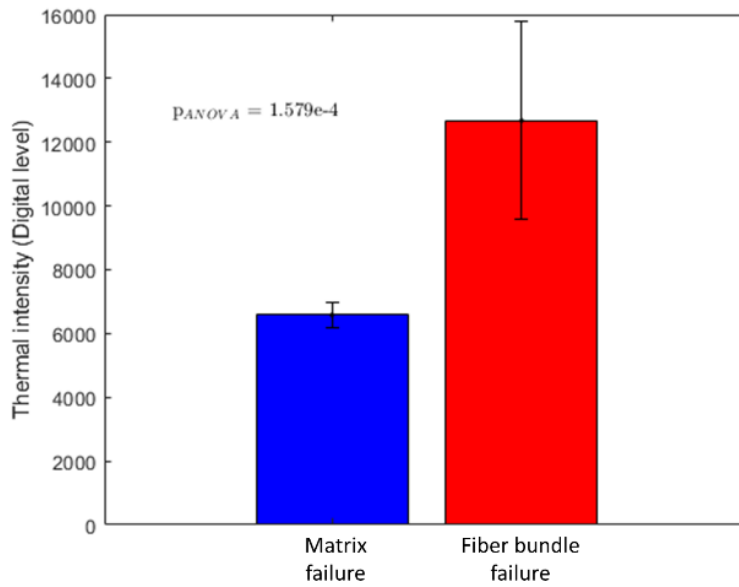


Figure 99. Thermal intensities (digital levels) of first major damage events.

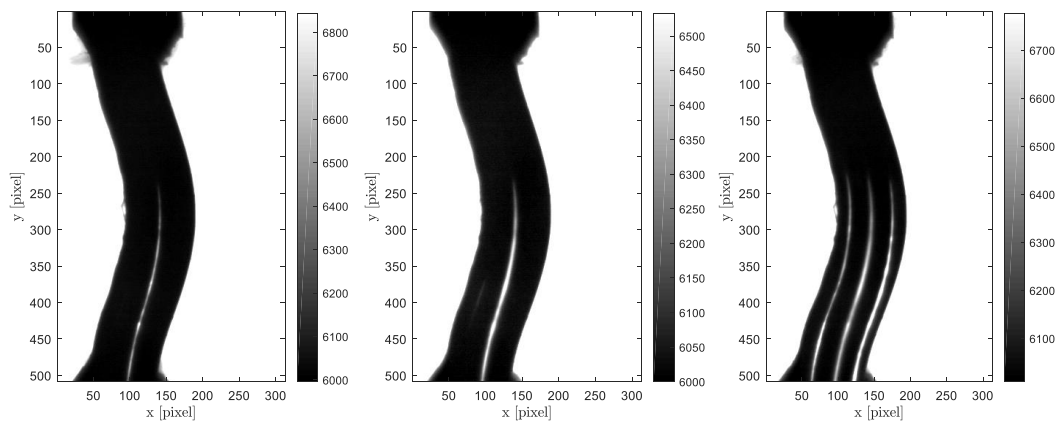


Figure 100. Thermal intensity (digital level) images from IRT of compression test on wave 1 specimen with UD-laminate.

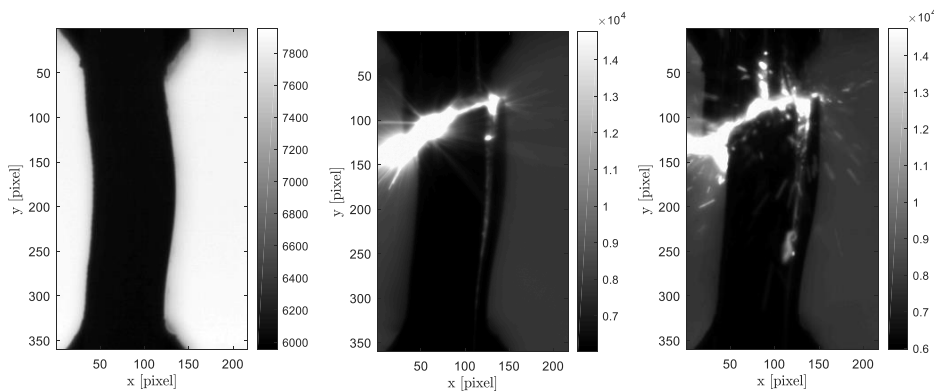


Figure 101. Thermal intensity (digital level) images from IRT of compression test on wave 2 specimen with UD-laminate.

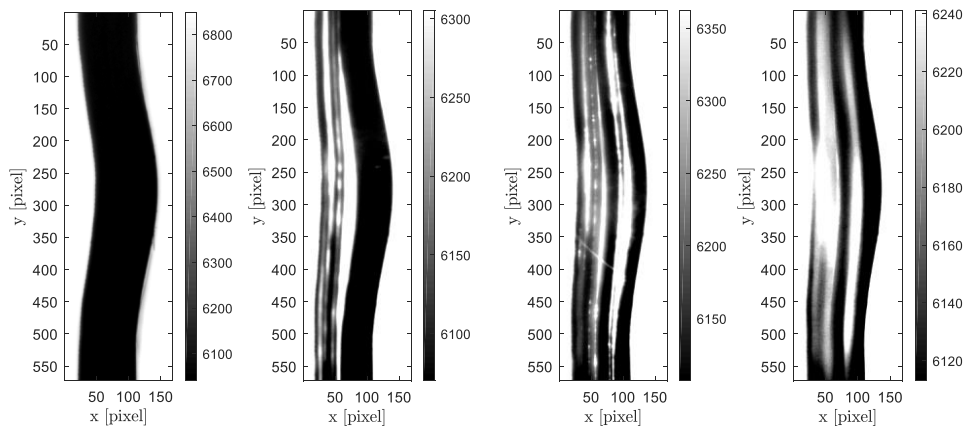


Figure 102. Thermal intensity (digital level) images from IRT of tensile test on wave 1 specimen with UD-laminate.

In Figure 103, a representative result of the averaged thermal intensity associated with the IRT results shown in Figure 100, is shown with the corresponding compression force. The disadvantage of averaging the thermal intensities over the region of interest (wavy region) is that individual failure modes cannot be identified but a general thermal response under mechanical loading can be investigated. Zone 1 is characterized by an almost linear increase of the elastic material response to the external load. In zone 2, a clear increase in intensities indicate the presence of micro-cracks. The increase of micro-cracks can be also observed in a reduced slope of the force signal. The three delamination, shown in Figure 100, appear within three frames with a frame rate of 172 Hz (sample time ~ 17.4 ms) representing the sudden transition from zone 2 to zone 3, leading to a strong increase in temperature and drop of compression force.

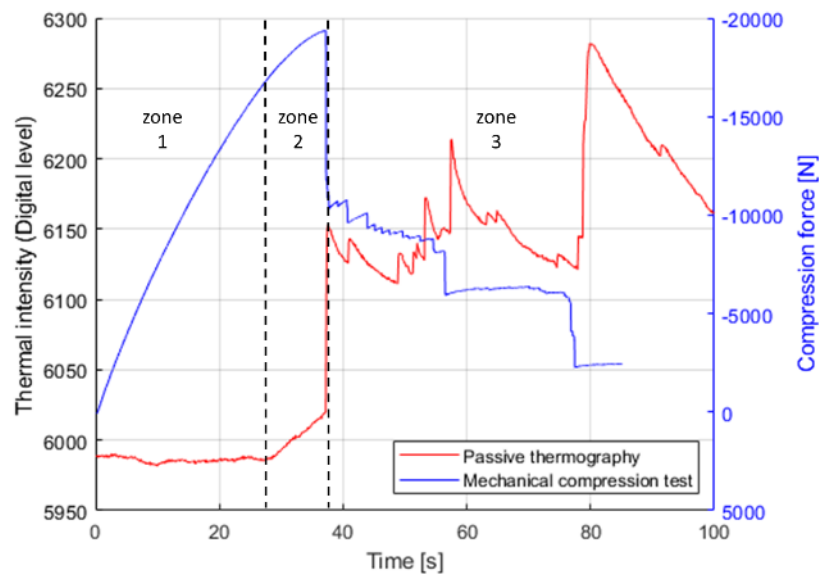


Figure 103. Force-displacement curve and corresponding thermal intensities from IRT of compression test on wave 1 specimen with UD-laminate.

5.1 EXPERIMENTS UNDER ROOM TEMPERATURE AND DRY CONDITIONS

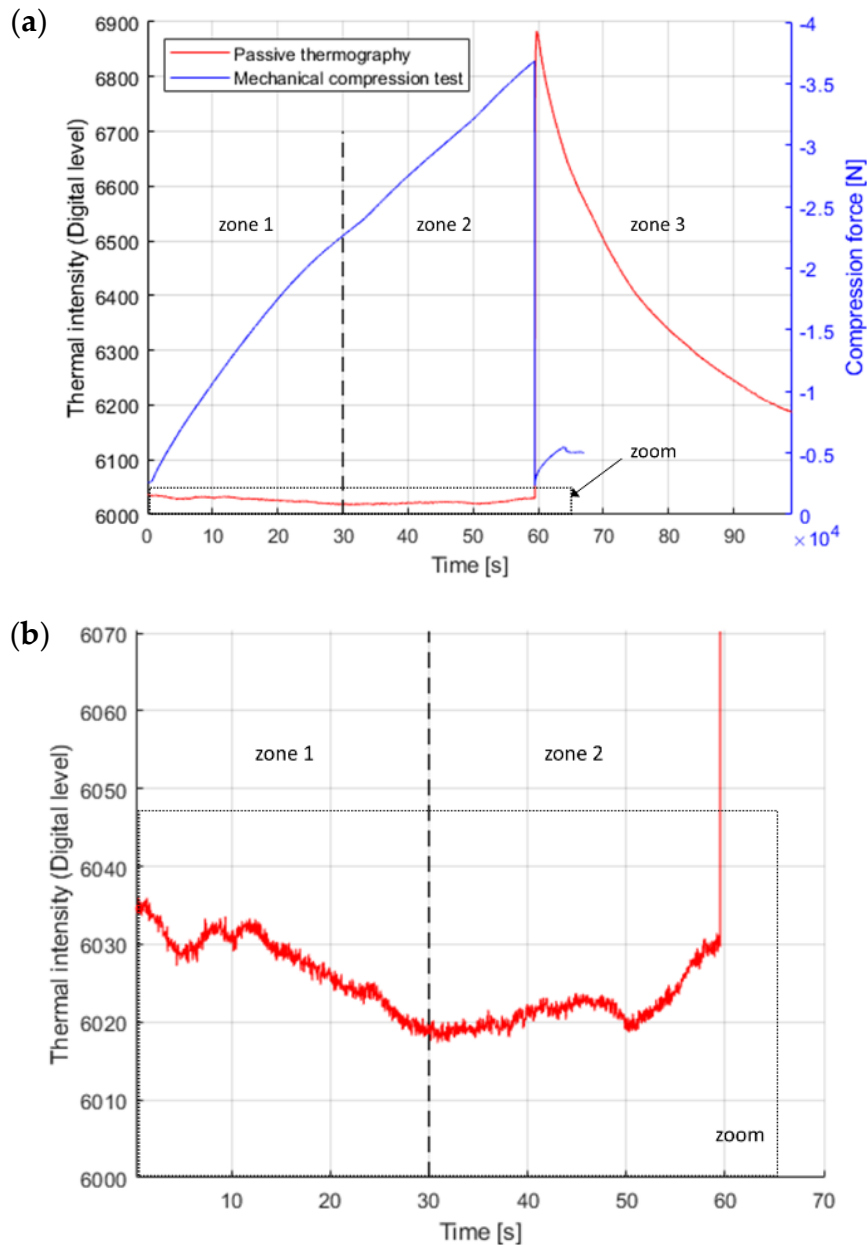


Figure 104. a) Force-displacement curve and corresponding thermal intensities from IRT of compression test on wave 2 specimen with UD-laminate;
 b) Detail of thermal intensity change in zone 1 and zone 2.

The thermo-mechanical behavior [21, 22], where the mechanical energy of testing is completely stored in the material, was observed in the tests. The specimens show an approximately linear decrease in temperature in the initial elastic region (zone 1) as depicted in the zoomed region in Figure 104 (b). The transition from the elastic region zone 1 to zone 2 constitutes a significant decrease in stiffness until final failure in form of fiber kinking occurs. The high energy that is dissipated in fiber kinking is not plotted in Figure 104 as the depicted results are averaged over the wavy region of the specimen as described above and therefore just illustrates a qualitative picture of the damage behavior. A single point evaluation of various damage events is shown in Figure 99.

The small peaks in thermal intensities, depicted in Figure 105, correspond to delamination (Figure 102) in tensile tests. The first two deflections in the force signal are due to damages in the clamping area, which was outside the field of view of the IR camera.

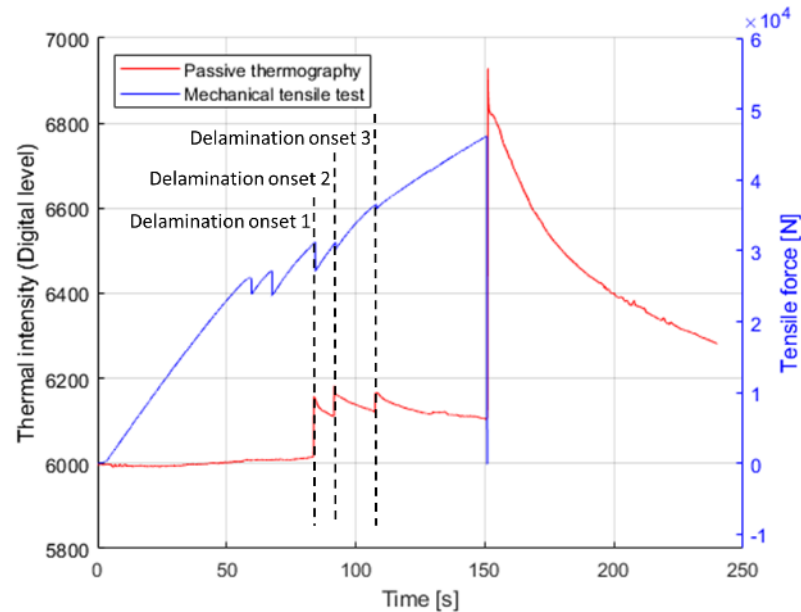


Figure 105. Force-displacement curve and corresponding thermal intensities from IRT of tensile test on wave 1 specimen with UD-laminate.

5.1.2.3. Acoustic emission

AE is used to localize damage initiation and to distinguish between fiber and matrix failure in quasi-isotropic tensile specimen with wave 1 (more pronounced waviness) configuration. The density plot (Figure 106) of damage events clearly shows localized areas in the wavy regions. Matrix cracking in 90° and $\pm 45^\circ$ plies is evenly distributed along the specimen length with a slightly more dense distribution in the wavy region. AE confirmed that the wavy region is more prone to delamination in tension as well as in compression consistent with DIC and IRT results.

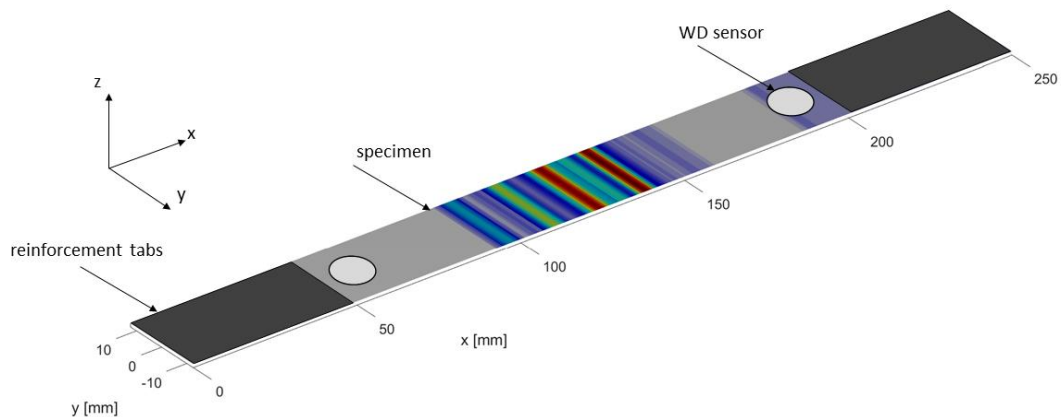


Figure 106. Representative density plot of acoustic emission results with weighting of absolute energy for wavy specimen projected on flat surface.

5.1 EXPERIMENTS UNDER ROOM TEMPERATURE AND DRY CONDITIONS

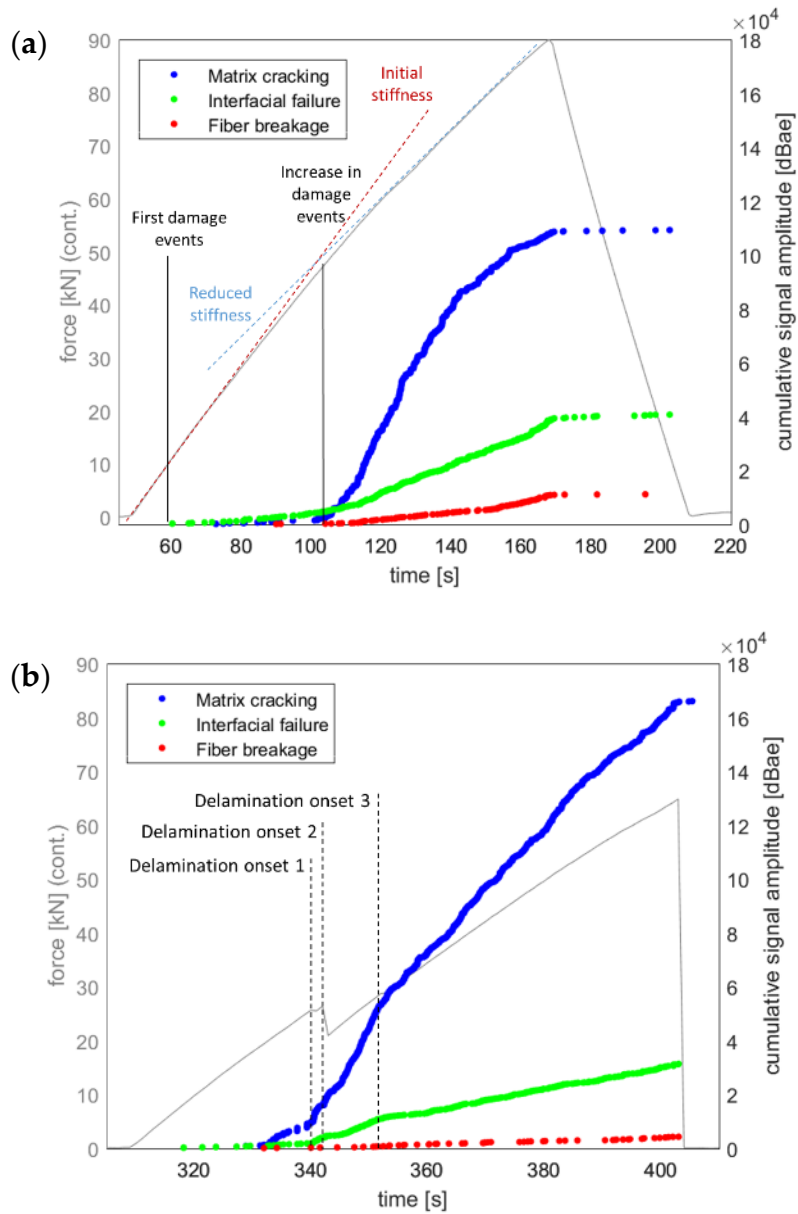


Figure 107. Force and cumulative signal amplitude over time results of acoustic emission testing for a) planar reference specimen and b) wavy specimen.

The reduction of stiffness in plane reference results (Figure 107, a) coincides well with the major increase in damage events. The increase in matrix cracking and interfacial failure after major delamination in wavy specimens (Figure 107, b) can be explained by changes in load paths. The resulting lack of load transmission in failed layers must be compensated by other layers, which have not yet failed. This abrupt increase in load leads to an increasing rate of matrix cracking.

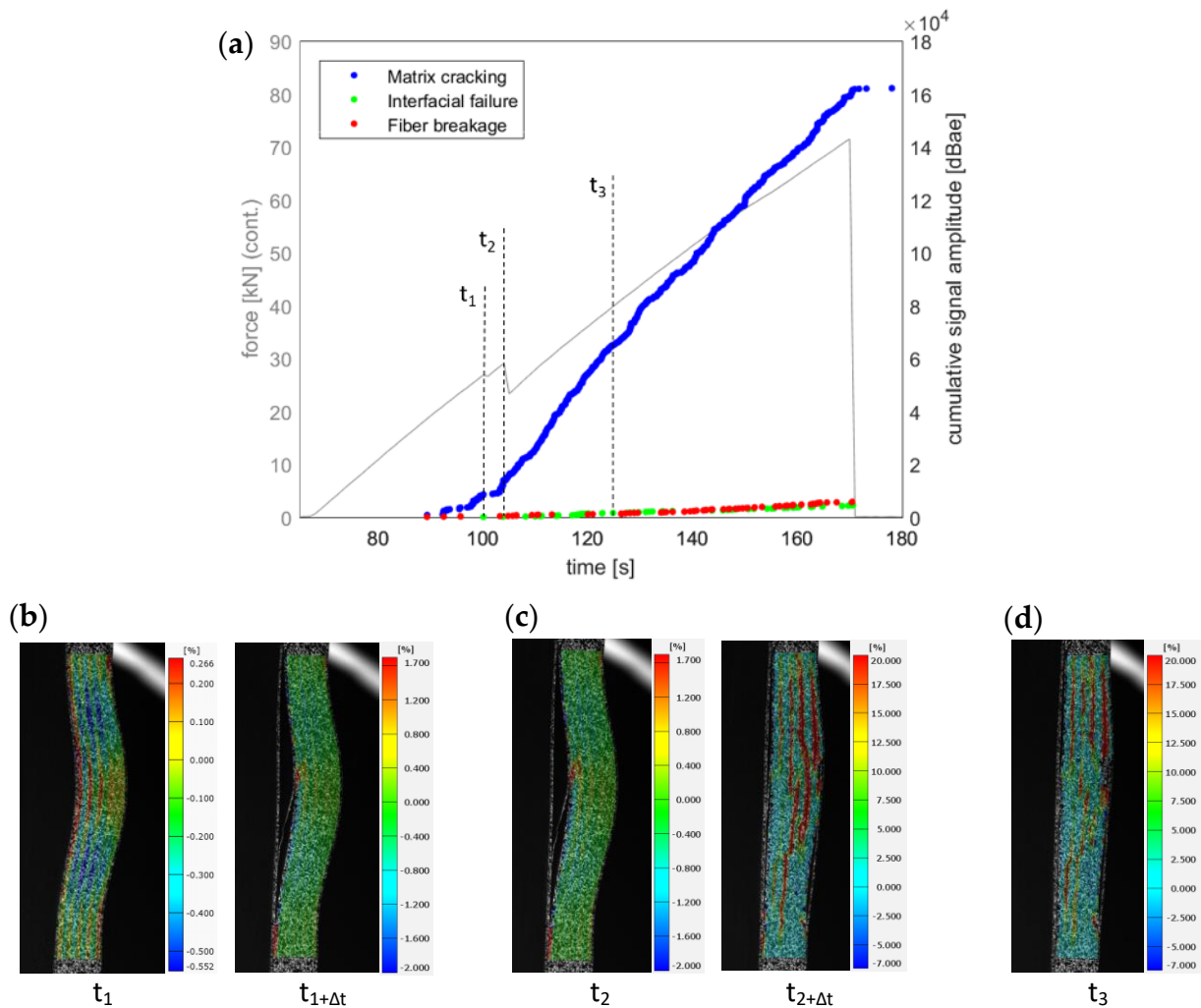


Figure 108. Cumulated signal amplitude over time results of acoustic emission testing (a) and comparison with DIC results ϵ_y obtained from wavy specimen (b-d).

Existing delamination, shown in Figure 108, are closing due to the straightening of the wave, but no increase in stiffness can be observed for quasi-isotropic specimen. Because of this closing mechanism, it is difficult to follow delamination during the whole loading process. The area of delamination appears to be larger in frame t_2 than in frame t_3 , where Δt indicates the subsequent frame of the shown DIC results.

5.1 EXPERIMENTS UNDER ROOM TEMPERATURE AND DRY CONDITIONS

5.1.3. Assessment of test methods

A summarized assessment of the considered test methods is presented in Table 14.

Table 14. Assessment of test methods.

	Digital image correlation	Passive thermography	Acoustic emission
Damage localization method	Optical	Optical	Arrival time of signals
Damage distinction method	Optical distinction of damage modes based on strain signatures	Optical distinction of damage modes based on thermal intensity signatures	Classification based on frequency and intensity of AE signals
Matrix cracking	Good, but strongly dependent on the field of view and the resulting resolution	Good	Good
Delamination	Good	Good	Good
Fiber breakage	Fiber bundles (Good); Single fiber breakage (Difficult)	Good, but depending on the resolution	Good
Local loading condition	Strain field (Very good)	No information, except thermo-mechanical effect	No information
Inspection level	Surface	Surface and near surface damages	Entire Volume
Test part sizes	Small (mm) to large (m) → with <u>major</u> losses of damage event information on larger scales	Small (mm) to large (m) → with <u>minor</u> losses of damage event information on larger scales	Small (cm) to large (m) → <u>no</u> information loss because of the possibility to use more sensors
Uncertainty in evaluation of signals	Low	Low to medium	Medium

5.2. Influence of hot-wet conditioning

Composite materials exposed to harsh environmental conditions, i.e. hot-wet, show considerably reduced mechanical properties, governed by a degrading matrix. To investigate the effect of fiber waviness on the mechanical properties at both room temperature and after 12 months hot-wet conditioning at 70°C and 85% relative humidity, mechanical tests (compressive and tensile loading) were conducted. The influence of matrix degradation due to hot-wet conditioning on the mechanical properties of unidirectional composite materials was found to be significant for laminates with lower thickness, but a minor impact was observed for specimens containing out-of-plane fiber waviness with higher thickness.

5.2.1. *Environmental influences on composite materials*

An aircraft is subjected to a variety of mechanical loads and environmental conditions during its operational life. The long-term performance of composite materials used in aircraft structures is of great importance as they are expected to be in service for 20 years or more, depending on the type of aircraft. The commercial aircraft A380 has a planned life span of 100.000 hours of flight and 20.000 cycles. Aircrafts operate in differing environmental conditions, i.e. temperature differences from ground to air or varying humidity from dry deserts to wet tropical regions. Cured epoxy polymers are generally known to be very stable against thermal, mechanical and climatic stresses. This enables them to be used in high-performance and long-term applications, such as a matrix material for carbon fibers. However, upon contact with liquid or gaseous water, epoxy resins tend to absorb significant amounts of water molecules in service, which then diffuse into the polymer network. Moisture absorption is characterized by a diffusion process, in which water molecules are transported from areas with higher concentration to areas with lower moisture concentration. Typically, fiber reinforced plastics are observed to gain moisture quickly in the beginning and then tend towards saturation, denoted as Fickian behavior [243]. This has a crucial influence on the mechanical behavior of monolithic fiber reinforced plastics, which leads to considerable degradations of mechanical and thermal properties [244,245]. According to [246] the worst-case relative humidity for aircrafts is 85%. The moisture absorption in polymer composites is a function of several variables, e.g. temperature, fiber volume fraction, reinforcement orientation, diffusivity [247]. The penetration of moisture into the composite material follows a diffusion process until complete saturation is achieved. The rate of moisture absorption in polymer composites is increased at elevated temperatures [81]. Long ageing at high temperatures in combination with moisture is harmful to the material. According to [246], the conditioning temperature for epoxy matrices should be kept below 82°C for a 177°C cure material and below 68°C for a 121°C cure material. The temperature must remain well below the glass transition temperature of the

5.2 INFLUENCE OF HOT-WET CONDITIONING

composites in order to avoid any irreversible damage which permanently changes the absorption behavior of the material [248]. To incorporate these environmental effects in the design of new aircrafts, the standard procedure at present is to use hot-wet material properties, obtained from mechanical tests of hygrothermally aged material specimen. Thick composite laminates used in primary structures of aircrafts have thicknesses up to several centimeters. These components will hardly reach saturation during their life span. In this case the use of traditional hot-wet knock down factors is considered to be too conservative leading to the need for investigating these design allowables to optimize weight savings. Chin et al. [249] reported, that it could take up to a few years for fiber reinforced plastics to reach moisture saturation at 40 °C or lower temperature. Numerous studies [250,251] have been carried out on the degradation of material properties due to moisture absorption, all reporting a considerable influence on mechanical and thermal properties. The plasticization of the epoxy matrix and degradation of the fiber-matrix interface due to moisture have been attributed to the degradation of the mechanical properties of composites [243,252].

As the matrix properties and especially the thereby caused shear nonlinearity of the composite plays a dominant role in the failure behavior of wavy layers in composites, hot-wet conditioning (typically 70°C and 85% relative humidity in aviation industry) is also considered to substantially influence this behavior. To the best of the authors knowledge, the effect of hot-wet conditioning on the mechanical performance of laminates containing fiber waviness has not been investigated so far. To understand the complex failure behavior of composite materials containing out-of-plane fiber waviness under compressive and tensile loading, and to investigate the influence of hot-wet aged specimens on the mechanical properties numerous mechanical tests were carried out in this study.

5.2.2. *Experimental methods and test set-ups*

5.2.2.1. Specimen preparation

In addition to the specimen preparation for mechanical tests, described in Section 5.1.1.1, traveler coupons, following ASTM D5229 [253] test standard, were cut and prepared from the laminates, with a size of approximately 40 mm x 40 mm x 5.1 (2.1) mm to measure the mass gain during hygrothermal conditioning. The hot-wet specimens were hygrothermally aged in a climate chamber CTS C-70/600 (Clima Temperatur Systeme, Jennersdorf, Austria) maintained at 70°C and 85% relative humidity for 11 months. During the proces of hygrothermally aging the material, traveler specimens were periodically removed and weighed on a analytical balance Kern ALS 220-4 (KERN & SOHN GmbH, Balingen, Germany) with a resolution of 0.1 mg. Specimens were cooled down to room temperature before being weighed to not influence the scale due to heat transfer. The weight gain of traveler coupons due to moisture absorption (five samples for each laminate thickness and laminate

orientation) was measured weekly during the conditioning process. As carbon fibers do not absorb moisture [251], the effect of moisture is expected to mainly affect the properties of the epoxy matrix. Therefore, mechanical properties which are dominated by matrix material have been considered in the tests. For hot-wet testing, the test specimens were removed from the environmental chamber, placed in a sealed plastic bag and tested at room temperature within two days. Moisture uptake measurements were conducted over a time period of 359 days. Thermal and thermo-mechanical analysis were performed on unaged, hot-wet aged and redried materials. For the drying of the material, a vacuum drying chamber VD115 (Binder, Tuttlingen, Germany) was used. The material was dried at 120°C for 6 hours.

5.2.2.2. Tensile and compression testing

Tensile and compression properties for planar reference and wavy specimen were determined in both room temperature and hot-wet conditions. Tests are carried out in the spirit of ASTM D3039 and ASTM D6641. Material testing was conducted on a universal test machine with a maximum load of 150 kN (Zwick, Ulm, Germany). The tests were displacement controlled with a rate of 2 mm/min. An overview of the conducted tests is given in Table 15.

Table 15. Test plan showing configurations, number of specimens and environmental conditioning.

	Loading	No. of specimen	Layup	Dimension (mm)	Environmental conditioning
Wave 1	Compression	5	0°	130x10	RT
Wave 1	Compression	5	0°	130x10	Hot-wet
Wave 2	Compression	5	0°	115x10	RT
Wave 2	Compression	5	0°	115x10	Hot-wet
Wave 1	Tension	5	0°	250x10	RT
Wave 1	Tension	5	0°	250x10	Hot-wet
Wave 2	Tension	5	0°	250x10	RT
Wave 2	Tension	5	0°	250x10	Hot-wet
Planar reference	Compression	5	0°	110x10	RT
Planar reference	Compression	5	0°	110x10	Hot-wet
Planar reference	Compression	5	90°	110x10	RT
Planar reference	Compression	5	90°	110x10	Hot-wet
Planar reference	Tension	5	0°	250x10	RT
Planar reference	Tension	5	90°	250x25	RT
Planar reference	Tension	5	90°	250x25	Hot-wet
15° Off-axis	Tension	5	15°	250x25	RT
15° Off-axis	Tension	5	15°	250x25	Hot-wet

5.2 INFLUENCE OF HOT-WET CONDITIONING

5.2.2.3. Thermal and thermo-mechanical analysis

Glass transition temperature

The application range of fiber-reinforced plastics is not only limited by their mechanical properties but also by their thermal properties, especially the glass transition temperature T_g [254–257]. The T_g defines the critical service temperature of the composites, as Polymers used above their T_g exhibit a considerable loss of mechanical properties. When T_g is exceeded, the polymer changes from a glass-like state to a rubber-like, so-called entropic-elastic state. Actually, the T_g indicates a temperature range from 20 to 40 °C, within which the polymer properties characteristically change [19]. When the material is exposed to a hygrothermal environment, e.g. aircraft in tropical regions, the T_g usually decreases and hence the critical service temperature changes. It is therefore necessary to know the influence of moisture absorption on the glass transition temperature of a material. There are various temperature-dynamic methods for the determination of the glass transition temperature T_g . The resulting value of T_g can vary due to the varying measuring methods, the dynamics and the different types of evaluation [257]. Consequently, these conditions must be considered when comparing different T_g values.

Dynamic mechanical analysis

The glass transition temperature T_g was determined according to ISO 6721-7 using a Anton Paar Physica MCR 501 (Graz, Austria) dynamic mechanical thermal analyzer (DMTA) at torsional loaded specimens. The analysis was carried out at a heating rate of 2 K min⁻¹, 1 Hz loading frequency and in a temperature range of 30–250 °C. The glass transition temperature T_g was evaluated at the peak of the loss factor $\tan(\delta)$ curve. The dimensions of the specimens were 60 x 10 x 2 mm³ and four specimens were tested from quasi-isotropic lay-ups for each condition, i.e. unaged, hot-wet conditioned and re-dried.

Differential scanning calorimetry

For thermo-analytical investigations of the material, e.g. T_g , differential scanning calorimetry (DSC) was carried out following ISO 11357 using a DSC 3 from Mettler Toledo (Greifensee, Switzerland). The temperature range was set from -50 °C to +280 °C. The heating rate, respectively cooling rate was set to 20 K min⁻¹.

5.2.2.4. Scanning electron microscope

For a detailed analysis of the fracture surface after mechanical testing, images with varying resolutions, i.e. 5, 10 and 50 μm, obtained from a scanning electron microscope (SEM) MIRA3 from TESCAN (Brno, Czech Republic) were investigated.

5.2.3. Results and discussion

5.2.3.1. Moisture absorption

The relative moisture change $M(\%)$ for each sample was determined using Eqn.1, taken from ASTM D 5229:

$$M(\%) = \frac{M_t - M_0}{M_0} \times 100\% \quad (31)$$

where M_t is the measured absorbed moisture mass at time t and M_0 is the initial mass at the dry state.

The rate of moisture absorption and maximum moisture content was observed to be dependent on the stacking sequence of the laminate. QI laminates absorbed moisture at a higher rate than that of UD, although some references, e.g. [250], stated a faster moisture absorption of UD laminates.

Although the samples were conditioned for 359 days, the moisture absorption saturation was not fully reached for thick laminates as the diffusivity process slows down with increasing thickness. The moisture uptake over time is shown in Figure 109. In general, at elevated temperatures and high relative humidity the probability of fiber reinforced polymers exhibiting a non-Fickian behavior is higher [258–260]. According to Dardon et al. [259], this may be ascribed either to structural damage in form of micro-cracks, or to hydrogen bonding of the water.

The diffusion coefficient D in Eqn. (32) proposed by Shen and Springer [243] is a function of temperature and does not depend on the percentage of relative humidity, i.e. it is a constant for materials conditioned at a given temperature.

$$D = \pi \left(\frac{h}{4M_{max}} \right)^2 \left(\frac{M_2 - M_1}{\sqrt{t_2 - t_1}} \right)^2 \quad (32)$$

M_1 and M_2 , are the weight percentage moisture (wt %) taken at times t_1 and t_2 (in seconds) respectively, h is the laminate thickness (in mm) and M_{max} is the equilibrium moisture level (wt %) for the given relative humidity [251].

$$M = M_{max} \left[1 - \exp \left(-7.3 \left(\frac{D \cdot t}{h^2} \right)^2 \right) \right] \quad (33)$$

5.2 INFLUENCE OF HOT-WET CONDITIONING

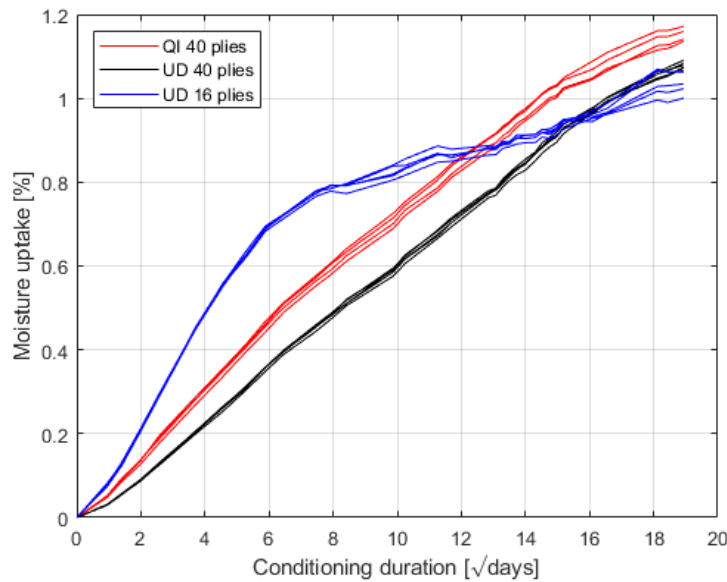


Figure 109. Moisture absorption.

Water molecules that are attached to the hydrophilic groups in the polymer network via hydrogen bonds are referred to as bound water [261]. Epoxy polymers contain many hydrophilic groups, such as the OH or ether groups, which are formed by the polyaddition of the epoxy ring with the, e.g. aminic, hardener. Also unreacted NH groups are strong polar groups with which water molecules form hydrogen bridge bonds [262]. The latter were confirmed by Grave et al. [263], who measured a higher absorbed water content in amine-rich epoxy polymers. The coupling reaction between silane grafted carbon fiber with epoxy resin is shown in Figure 110.

Due to the high polarity, bound water weakens or disturbs the intermolecular interactions between the polymer chains. This requires the mobility of the polymer segments, which causes measurable changes in the epoxy polymer and can be observed e.g. in the form of swelling and plastification [262,264–266].

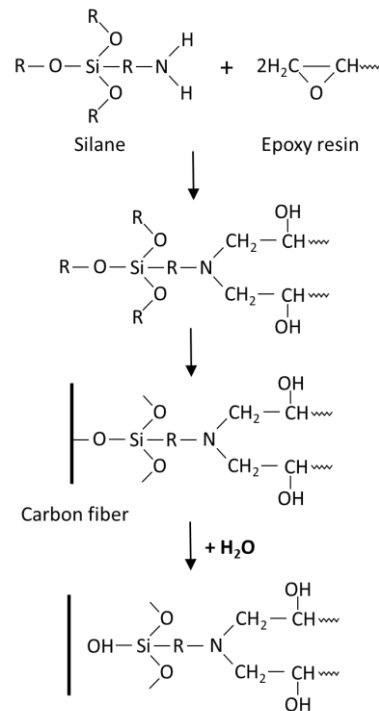


Figure 110. Coupling reaction between silane grafted fiber with epoxy resin, modified from [267]

5.2.3.2. Mechanical behavior of planar specimens with matrix dominated properties

To investigate the influence of hot-wet conditioning on the mechanical properties of composite materials, mechanical tests on matrix dominated specimens, i.e. 15° off-axis tensile tests, 90° tensile and compression tests, have been performed. The experimental data for 15° off-axis tests (Figure 111) has shown a considerable decrease in strength (~30%) but no significant change in elastic properties. Similar observations were made for 90° tensile (Figure 112) and compression (Figure 113) tests with no significant changes in the Young's modulus but drops in strength of ~50 and ~25% respectively.

5.2 INFLUENCE OF HOT-WET CONDITIONING

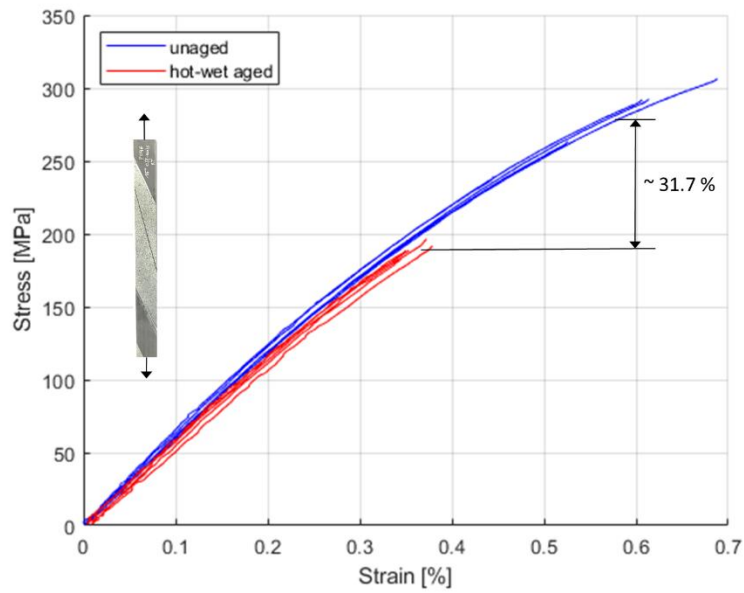


Figure 111. 15° Off axis tensile test of unaged (blue) and hot-wet aged (red) specimens tested at room temperature.

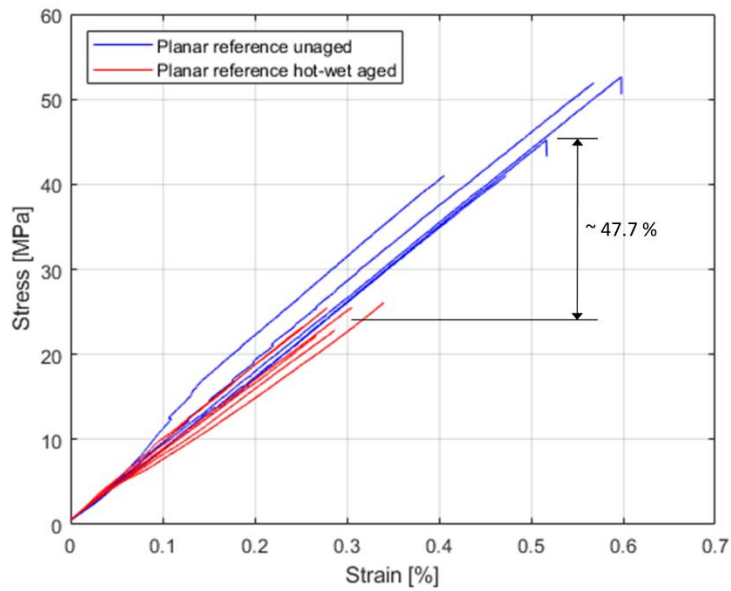


Figure 112. Results for unaged (blue) and hot-wet aged (red) 90° tensile specimens.

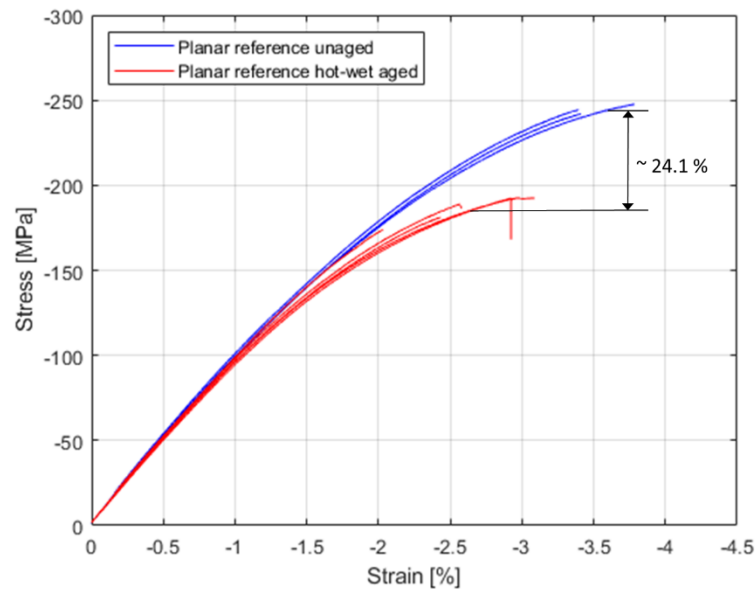


Figure 113. Results for unaged (blue) and hot-wet aged (red) 90° compression specimens.

5.2.3.3. Mechanical behavior of both unaged and hot-wet conditioned planar and wavy specimens

The experimental data for planar reference and wavy specimen under compression (Figure 114) and tensile loading (Figure 115) show a non-linear stress strain response for wavy specimen and a considerable knockdown compared to the planar reference specimen. Young's modulus in fiber direction and the peak-stress before failure for both unaged and hot-wet conditioned tests are shown in Table 16. The compressive strength is reduced by approximately 75% for the more pronounced wave configuration (wave 1) and 50% for the less pronounced wave (wave 2). The latter also shows a substantial reduction by approximately 45% of the strain-to-failure. Those results are in good agreement with previously reported findings [48].

5.2 INFLUENCE OF HOT-WET CONDITIONING

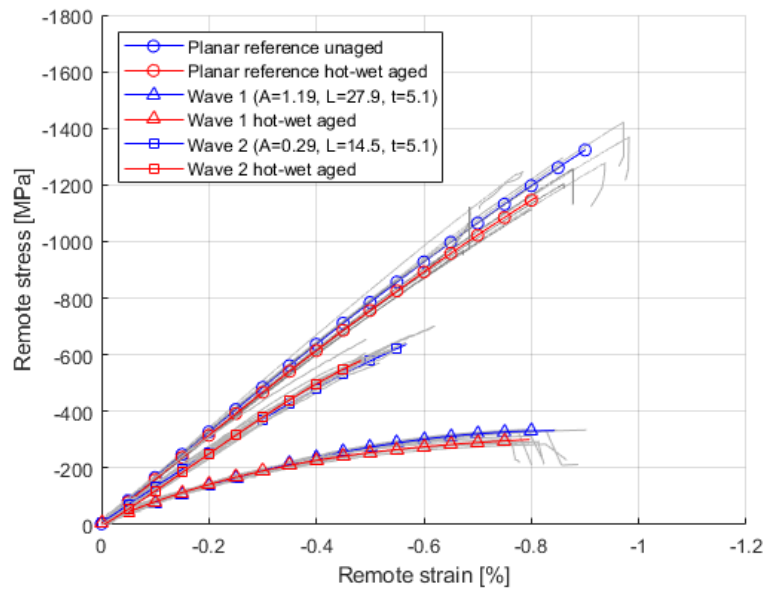


Figure 114. Compression test of UD-laminate – Comparison of unaged (blue) and hot-wet aged (red) planar and wavy specimens.

Although the compression properties were assumed to be more influenced by fiber waviness compared to tensile loading, results from mechanical tests on wave 1 show a drop of 70% in tensile strength. In Figure 115, the stress-strain curve for wave 2 specimen is incomplete, as failure in the tabs occurred due to the high loading forces needed for testing the thick laminate specimens (~ 5 mm). However, the results can be still used for the evaluation of the Young's modulus.

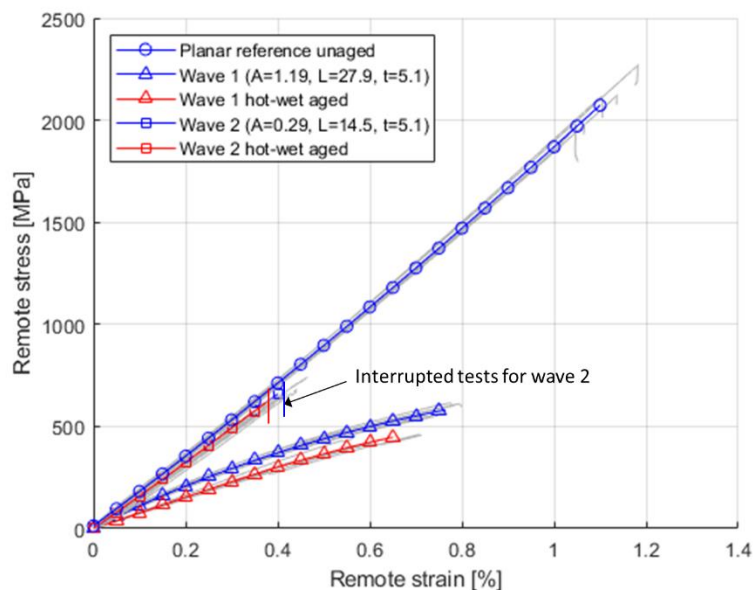


Figure 115. Tensile test of UD-laminate – Comparison of unaged (blue) and hot-wet aged (red) planar and wavy specimens.

Table 16. Test data of stiffness and strength properties for IM7-8552 planar reference and wavy specimen.

		Compression				Tension			
		E_{1c}	STD	σ_{cm}	STD	E_{1t}	STD	σ_{tm}	STD
		[GPa]	[GPa]	[MPa]	[MPa]	[GPa]	[GPa]	[MPa]	[MPa]
15° Off-axis	RT	-	-	-	-	-	-	278.7	27
15° Off-axis	HW	-	-	-	-	-	-	190.4	4.5
90°	RT	10.8	0.6	244.6	2.8	8.95	0.6	46.4	5.7
90°	HW	10.1	0.3	185.8	8	8.19	0.6	24.2	1.7
0°	RT	160.6	7	1322.3	71.8	172.9	4	2094.3	122
0°	HW	155.9	4.2	1155.5	111.8	-	-	-	-
Wave 1	RT	78.7	1.3	333.5	6.1	104.4	2.8	584.3	29.7
Wave 1	HW	69.2	0.5	293.2	10.5	76.5	0.4	449.7	14.6
Wave 2	RT	135.9	1.4	655.5	32.6	162.6	1.8	-	-
Wave 2	HW	124.0	0.9	611.1	17.8	161.8	1.0	-	-

The applied unidirectional load leads to a complex 2D strain state at the observed cross-section due to the presence of the wave. In Figure 116 the shear strain ε_{xz} distributions of wavy specimens are shown right before and after final damage within two subsequent frames (10 Hz) for a) wave 1 and b) wave 2 under compression and c) wave 1 under tensile load. Regions of high strain coincide well with the occurrence of macroscopic material failure. This is in accordance with [46], who determined that the associated shear stress τ_{13} is the most significant stress component for damage initiation in wavy composites under axial compression. Identical failure modes, i.e. no change in failure behavior, were observed for both unaged and hot-wet aged specimens. Except for the tensile test of wave 1, the maximum shear strain ε_{xz} was found to be ~ 0.028 (wave 1, compression), ~ 0.014 (wave 2, compression) independent on the conditioning. Unaged tension loaded wave 1 specimens failed similar to the compression loaded specimens at a shear strain ε_{xz} of ~ 0.028 , whereas hot-wet aged tensile specimens failed at a lower shear strain of ~ 0.014 . This difference can be also observed in the global stress-strain response shown in Figure 115.

Due to the still ongoing moisture absorption of the laminate after 12 months, which can be seen in Figure 109, less damage has probably occurred in thick wavy specimens compared to the planar references. This finding also confirms with the statement, that thick composite laminates which are used in primary structures of aircrafts will hardly reach saturation during their life span. Chin et al. [268] reported, that it may take a few years for fiber reinforced plastics to reach moisture saturation at moderate temperatures.

5.2 INFLUENCE OF HOT-WET CONDITIONING

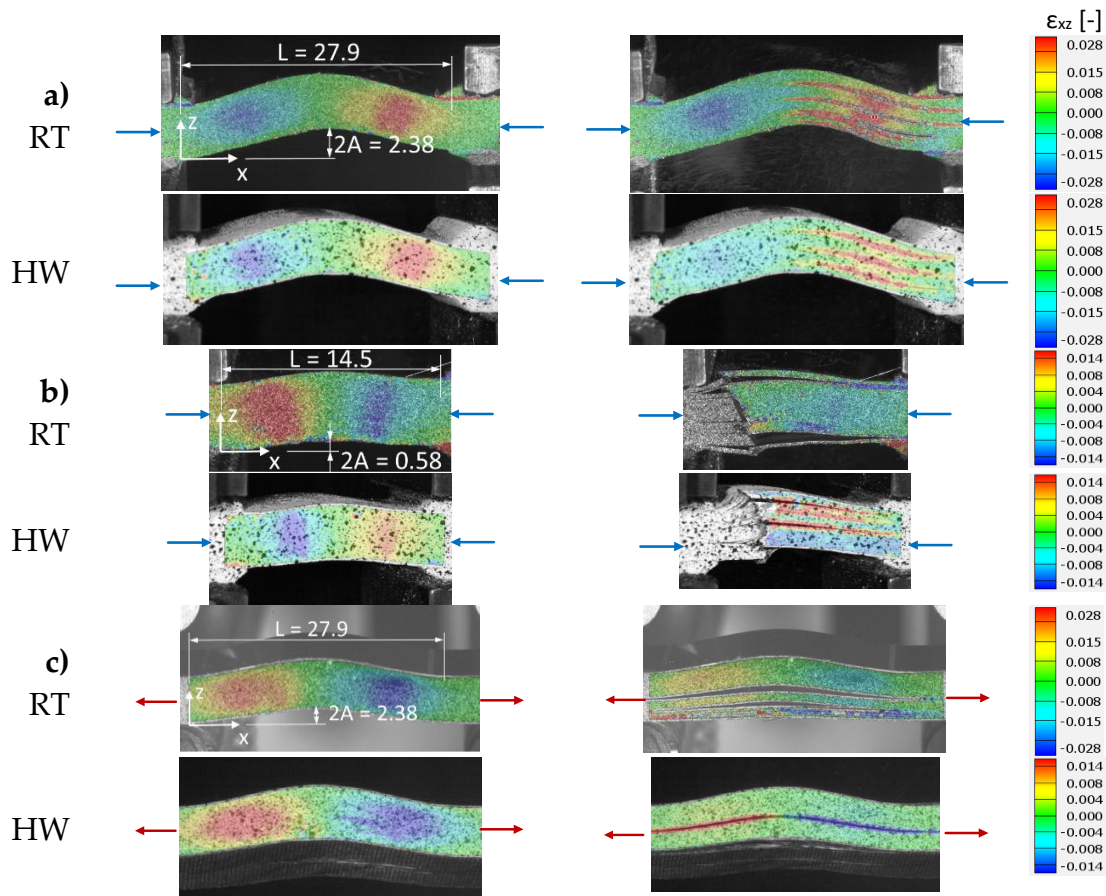


Figure 116. Shear strain ε_{xz} distribution in the frame captured right before and after macroscopic damage for UD specimen configurations. Blue and red arrows indicate the global loading. a) wave 1 in compression; b) wave 2 in compression; c) wave 1 in tension.

The interaction between fiber and polymer matrix is decisive for the properties of fiber reinforced plastics. The numerous interfaces between the fiber reinforcement and the polymer are potential weak points in a CFRP, due to the strong mismatch of material properties of both constituents, e.g. the huge difference in stiffness of carbon fiber ($E_{c-fiber} \approx 200$ to 900 GPa) and epoxy matrix ($E_{EP} \approx 3$ GPa) [269]. Scanning electron microscopy (SEM) images of the obtained fracture surfaces have to be evaluated with caution as they are difficult to interpret. SEM results of 15° off-axis tests are shown in Figure 117 with varying resolutions of 50, 10 and $5 \mu\text{m}$. On the one hand, the fracture surfaces tend to show large areas adhesion failure in hot-wet aged specimens, i.e. the epoxy matrix is completely detached from the surface of the carbon fibers, and on the other hand, unaged specimens tend to show more cohesion failure, i.e. the matrix fails in itself and more epoxy residues remain on the carbon fibers.

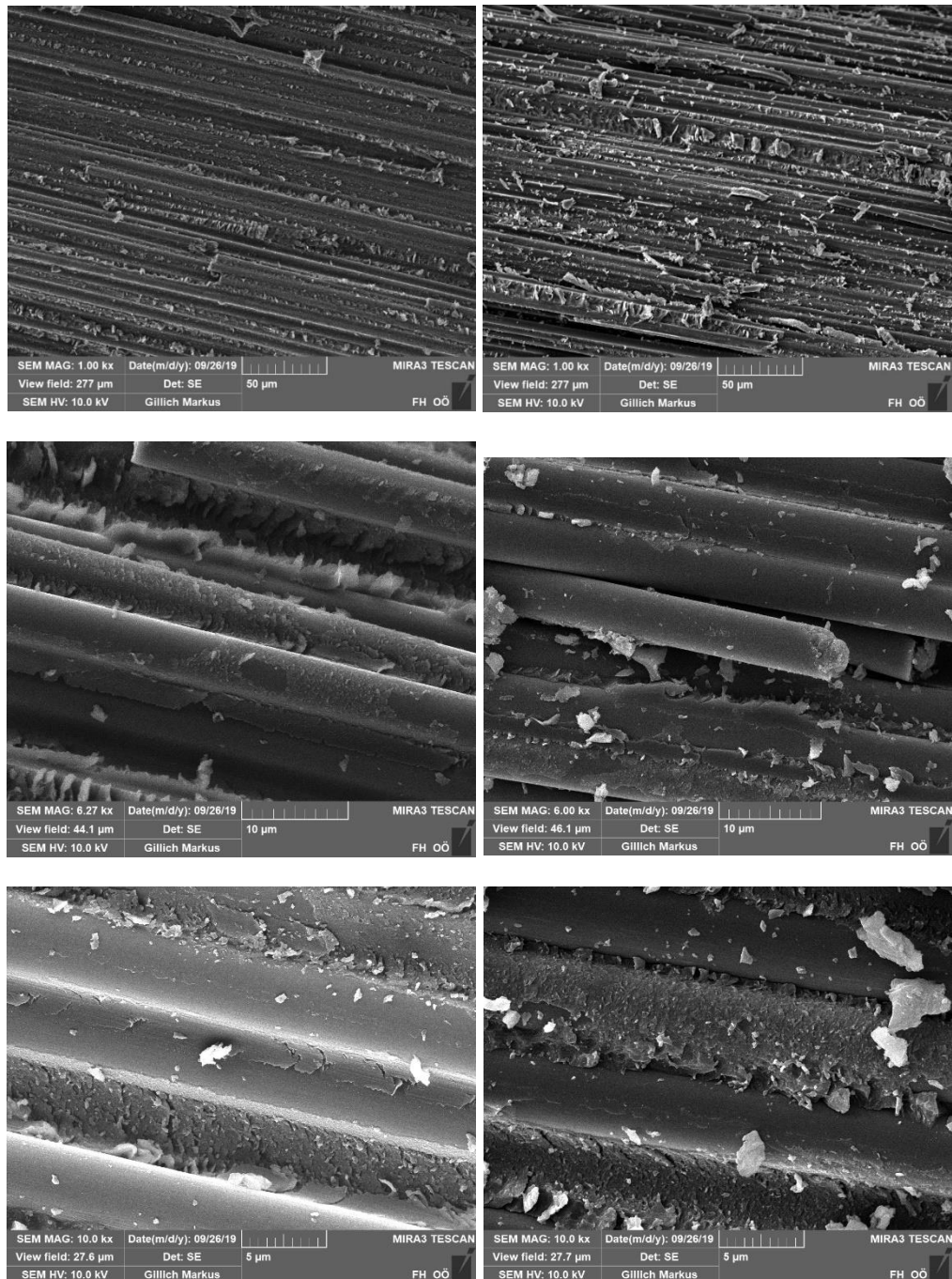


Figure 117. SEM images of a) unaged specimens and b) hot-wet conditioned specimens.

Measurements of the T_g were carried out with both DMA and DSC analysis. The maximum damping, shown in the damping versus temperature diagram from DMA results (Figure 118) was used for the evaluation of the T_g . The moisture absorption caused the glass transition temperature of the epoxy matrix to decrease by $\sim 44^\circ\text{C}$ ($\sim 20\%$), which in turn degraded the high temperature properties of the material. Nevertheless, T_g did not fall below the maximum water temperature of 100°C .

5.2 INFLUENCE OF HOT-WET CONDITIONING

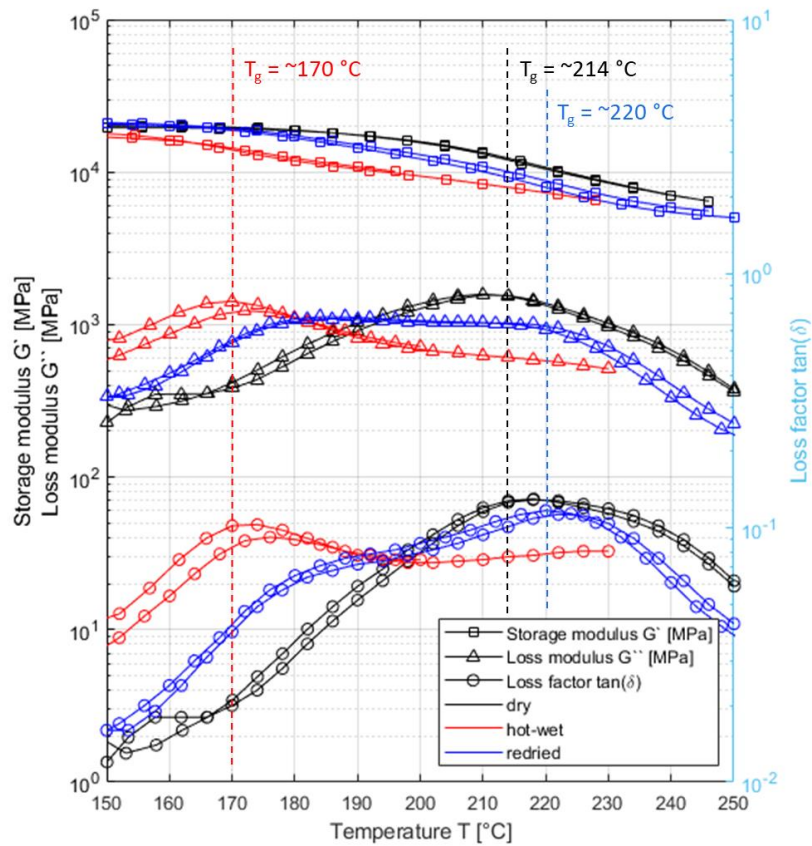


Figure 118. DMTA results for dry, hot-wet and re-dried specimens.

Water absorption in an epoxy polymer can occur reversibly. The absorbed amount of water can be removed by re-drying and the properties, such as the T_g , may again reach the initial value of the dry epoxy polymer. The DSC results (Figure 119) show a post-crosslinking of the dry specimen indicated by exothermic reactions with a peak at $\sim 250^\circ\text{C}$. During the 1st heating the hot-wet conditioned specimen has shown a stronger endothermic reaction compared to dry and re-dried specimen, possibly due to evaporation of bound water. During the 2nd heating step the T_g for all specimen show similar values between $220\text{--}226^\circ\text{C}$.

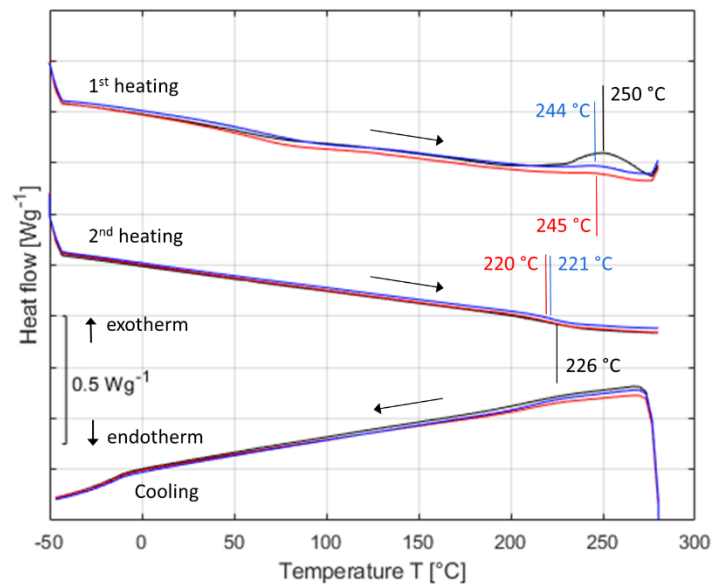


Figure 119. DSC results for dry unaged (black), hot-wet aged (red) and re-dried (blue) specimens.

Depending on the ageing temperature, absorbed water molecules can initiate post-crosslinking reactions in incompletely cured epoxy polymers. Water molecules also have a post-crosslinking effect in non-stoichiometrically balanced, epoxy rich polymers [263,270].

5.3. Conclusions on mechanical testing and the influence of hot-wet conditioning

The knowledge of intrinsic material behavior of fiber reinforced composite materials on microscopic level up to macroscopic or structural level is of crucial importance for the development of suitable material laws for numerical modeling and for a deeper understanding of deformation and damage mechanisms.

The mechanical behavior and damage initiation for two unaged and hot-wet aged wave configurations with UD laminates was successfully tested under compressive and tensile loading. Additionally, extensive material characterization was carried out on planar reference specimens. The experimental data obtained at room temperature has shown a considerable knockdown of mechanical properties of wavy specimen compared to planar references. The compressive strength is reduced by approximately 75% for the more pronounced wave configuration (wave 1) and 50% for the less pronounced wave (wave 2). Wave 2 also shows a substantial reduction of the strain-to-failure by approximately 45%.

Hot-wet aged planar reference specimens with matrix dominated material properties (i.e. 15° off-axis tension, 90° tension and compression and 0° compression), have shown considerable drops in strength of ~30%, ~50% and ~25% respectively but almost no reduction in stiffness. However, the influence of matrix degradation due to

5.3 CONCLUSIONS ON MECHANICAL TESTING AND THE INFLUENCE OF HOT-WET CONDITIONING

hot-wet conditioning on the mechanical properties of unidirectional composite materials containing out-of-plane fiber waviness was less than expected. This difference probably results from different laminate thicknesses of the planar reference specimens (~2 mm) and wavy specimens (~5 mm). The maximum of the shear stress, which is mainly responsible for the failure, occurs at the center of the laminate. At this center position of the laminate, no complete saturation was achieved after a conditioning duration of almost 12 months. Therefore minor influence has been investigated in the experiments compared to the thinner planar specimens. However, laminates with thicknesses of several centimeters, which are used in primary structures of aircrafts, will hardly reach moisture saturation during their lifetime. In subsequent studies, an accelerated moisture absorption in heated water baths will be conducted in order to further investigate the influence of environmental conditions on wavy laminates. Additionally, mechanical tests will be carried out at both room and elevated temperatures.

The used combination of experiments (i.e. digital image correlation, passive thermography, acoustic emission) was able to capture composite material failure in great detail. Inhomogeneous deformations observed in out-of-plane fiber waviness cannot be adequately recorded by traditional extensometers. DIC provides information on mechanisms and a full 2D strain field prior to failure, e.g. the location of strain concentrations. However, capturing damage initiation is limited by the (typically lower) frame-rate as well as the detectable size of an event. Both of which are compensated by passive thermography. Passive thermography signals can be clearly matched with results from DIC and AE. While both methods are limited to the surface of the specimen, information of internal processes was obtained by AE. Specifically, the difference between matrix cracking, interfacial failure and fiber breakage was evident from differences in the acoustic emission signals. It was found, that depending on the laminate configuration (i.e. amplitude, wavelength, thickness) interlaminar shear failure is the dominant failure mechanism that is followed by mode I delamination and layer-wise buckling. For wave configurations with a lower amplitude-to-thickness ratio fiber kinking is the dominant failure mechanism under compression loading. The observed formation of a shear kink-band under compression and shear stress Figure 98 (b) (DIC) and Figure 101 (IRT) is caused by local fiber buckling which is induced by misaligned fibers in the UD materials that continue to rotate under load.

6. ASSESSMENT STRATEGIES IN ENGINEERING PRACTICE

The basic strategies for the assessment of fiber waviness can be categorized as:

- *Empirical* - restricted to effect type and location
- *Generic* - simulation based on basic in-plane and out-of-plane material allowables
- Simulation correlated with subcomponent testing - *Semi-Empirical*

6.1. Challenges in assessing fiber waviness

Loaded wavy layers, although it might be in-plane loading, are causing a complex three-dimensional stress state leading to the necessity of using 3D failure criteria, at least for multidirectional laminates. In engineering practice usually not all out-of-plane lamina or neat resin material allowables are available. This often leads to the necessity of carrying out additional testing effort.

6.2. Knockdown factor (KDF)

The Airbus Technical Report “Manufacturing defect knock down factor for composite parts” (MDKDF) [271] deals with out-of-plane fiber waviness amongst other manufacturing effects. It has to be noted, that the definition of the undulation height h used in the Airbus Technical Report is twice the wave amplitude A which is used throughout this thesis. The difference between these two parameters is schematically shown in Figure 120. From several test campaigns, a link between waviness key parameters (like undulation height (amplitude), wavelength, number of affected plies, etc.) and the mechanical performance is identified.

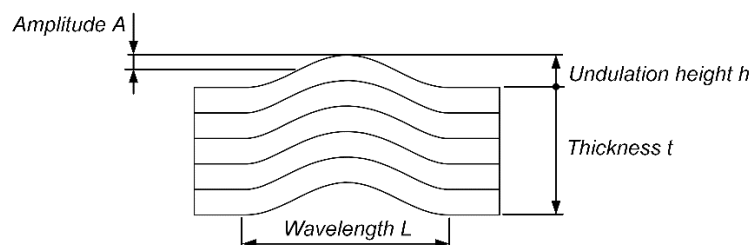


Figure 120. Undulation height vs. wave amplitude.

However, these test results show a large scatter between configurations, which are mainly related to defect morphology, part characteristics, defect root cause, manufacturing process etc. As an example, for plain compression, an undulation with a height of 0.5 mm can induce a KDF from 0.65 to 1.00. Moreover, fiber waviness is often accompanied by other effects (i.e. porosity, thickness deviation, resin accumulation, etc.) which can affect the test conclusions. Thus, no general assessment of the KDF linked to fiber waviness is available today, so that a case by case analysis

6.2 KNOCKDOWN FACTOR (KDF)

is inevitable. To cover the effect of fiber waviness, it is recommended to prove by test evidence that the worst characteristic of the defect that can occur on the part does not lead to a significant mechanical loss or will not lead to different failure modes. On another hand, the report also states, that out-of-plane fiber waviness is difficult to be detected. As shown in Section 4, the wavelength was found to be easier detectable compared to the amplitude. Fiber waviness on edges can be detected by visual inspection after trimming. Airbus states, that for visual inspection an undulation height of 0.3 mm can be considered as a detection threshold. From a stress point of view, fiber waviness that does not affect more than two plies (for parts with a thickness or more than 10 plies) with an amplitude less than one ply thickness must not be considered as an impairment of the stress performance. However, this threshold cannot be identified as an acceptance threshold, as the NDT capability is not yet sufficient for the required level of detection confidence of 90%. Nevertheless, this threshold can be considered for First Part Qualification (FPQ) and quality assessment of manufacturing trials.

The analysis of an EoD (Effect of Defect) test database allows the definition of KDF laws to assess mechanical performance versus wave characteristics, e.g. amplitude. Airbus defined the KDF law in order to cover all the test results available from their test database. Airbus decided to use this single value to simplify KDF laws. This value is roughly in line with the ply thickness and the visual “detection” threshold. Additionally, the test results don’t show any significant influence for an undulation height below 0.2 mm, except in plain compression with low grade material, but this tendency was not observed on other compressive properties which are more relevant regarding sizing (e.g. Compression After Impact (CAI), Filled Hole Compression (FHC)).

Due to confidentiality reasons, the KDF laws for the assessment of out-of-plane fiber waviness from the Airbus MDKDF cannot be presented in this thesis.

When the undulation affects less than 30% of the total amount of plies, the mechanical behavior is closer to the one defined for prints. In the Airbus MDKDF, prints are defined as marks on the surface of the part due to tooling or penetration of foreign objects before or during curing. Prints may also be referred to as indentions, as shown in Section 3.4. If an undulation possesses these morphological characteristics, it is possible to challenge the undulation KDF by using the print KDF

As a summary, the procedure to be applied in case of undulation detection is to have a first assessment of undulation criticality using a calculated KDF from the Airbus MDKDF. But, as the mechanical influence is linked to the part configuration (design, manufacturing process, material, etc.), dedicated mechanical tests can be necessary to validate the applied KDF. Nevertheless, an important point before applying a KDF is to gain evidence through manufacturing trials or FPQ that the undulation is stable, i.e. same morphology (amplitude, wavelength...) and same location (repetitive defect inherent to a process or to a design). It has to be noted, that the KDF calculation according to MDKDF from Airbus does not differentiate between

different ply stacking sequences, i.e. unidirectional or quasi-isotropic. When comparing the calculated KDF with experimental values, it became evident, that the calculated KDF leads to less conservative values for the two considered wave configurations.

6.3. Simulation based approaches

6.3.1. Simplified simulations

In stress analysis, one common way of considering the effect of wavy layers is the deletion, i.e. neglect, of all wavy layers as these layers are considered not to contribute to the stiffness of the laminate compared to aligned layers. However, the wavy layers can influence the failure behavior of the laminate and may therefore affect the strength of the remaining aligned layers. Therefore, this approach has to be used with caution with regard to the strength evaluation at the location of the wavy layers.

In a two-step engineering approach, the maximum load that is present in the wavy region is applied on the remaining undisturbed laminate and evaluated if the laminate is still capable of bearing the load. In addition to that, wavy regions, which typically soften the laminate, may result in a redistribution of the load to the surrounding regions of the part. This increased load in the adjacent region of the laminate has to be evaluated in an additional stress analysis.

Figure 121 schematically shows the procedure of deleting wavy layers in stress analysis.

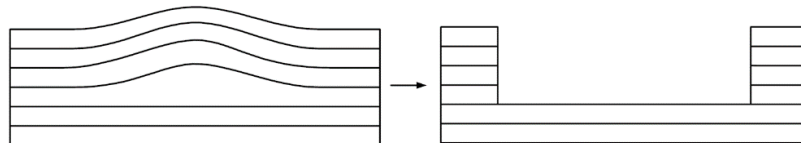


Figure 121. Deletion of wavy elements in simplified simulations.

6.3.2. Numerical and experimental assessment on sub-component level

Another way is based on taking microscopic images of the cross-section of wavy regions and carrying out numerical analysis on sub-component level, such as in Hinterhölzl et al. [219]. The FE discretization of the wavy region, i.e. sub-model geometry, is loaded at its boundaries to assess the local distinct 3D stress state at the vicinity of the affected region. For the stress analysis typical failure criteria (e.g. Puck, LaRC, Hashin, etc.) can be used. In general, for typical load case scenarios in aerospace, strength requirements are specified in terms of limit loads (the maximum loads to be expected in service) and ultimate loads (limit loads multiplied by prescribed safety factors, e.g. 1.5). To validate the simulation results, a correlation with mechanical sub-component tests have to be performed (semi-empirical approach). For this purpose, correlation factors between FEA predictions and real test data are derived for numerous test samples. The reserve factor for limit load and for ultimate load, that is

6.3 SIMULATION BASED APPROACHES

obtained from FE analysis, is then compared with the respective correlation factor. The reserve factors have to be equal or bigger than the respective correlation factor to ensure a positive margin of safety.

7. ANALYTICAL MODELLING

In addition to the experimental and numerical results described in previous Sections, this Section introduces an analytical model that was developed to even further contribute to a better understanding of the material behavior and its effective mechanical properties for global compressive and tensile loading in longitudinal direction. Fiber misalignments in general are known to have a detrimental effect on the compressive strength of composite materials. The presence of wavy layers in a laminate leads to a complex local stress state, even at simple global load states. Interlaminar shear failure is predicted to be the dominant failure mechanism that is followed by delamination and layer-wise buckling. The associated shear stress τ_{13} is, according to Hsiao and Daniel [13] the most significant stress component for wavy composites under axial compression. The World-Wide Failure Exercise [68] has shown, that failure criteria have significant weaknesses which are partly due to a lack in the evaluation of fiber kinking under compression and shear stress. The formation of a shear kink-band is caused by local fiber buckling or matrix flow, which is induced by misaligned fibers in the unidirectional (UD) material that continue to rotate under load.

Due to its severe knockdown effects on the mechanical properties, traditional analytical approaches were extended and validated with results from experimental tests. Previous developed models have mainly focused on UD laminates, where all layers are oriented in the same direction, and have concentrated on the effect of fiber waviness on the stiffness. The analytical model is based on the work of Hsiao & Daniel [46] and Altmann et al. [79] where the waviness in a unidirectional laminate is mathematically represented as in-phase sine-waves. The developed micromechanical model represents an extension of these models for multidirectional laminates and is implemented in a MATLAB GUI to determine the effective elastic properties as well as the resulting complex stress state. The well-established failure Puck criterion [80] was implemented and applied on the calculated stresses to predict local ply failure and determine the strength of the plies consisting of uniform or graded fiber waviness. The analytical model was validated by experimental tests and the results show very good agreement.

The mechanical tests, i.e. compression and tension, which are described in detail in Section 5, were accompanied by digital image correlation (DIC) with a GOM Aramis 3D 12M system to detect the corresponding strain distributions and to better understand the material behavior of laminates containing fiber waviness.

7.1. Effective elastic properties

An analytical approach was used to analyze the homogenized effective mechanical properties of uni- and multidirectional composite laminates containing fiber waviness.

7.1 EFFECTIVE ELASTIC PROPERTIES

Two basic types of waves, i.e. uniform and graded fiber waviness, were analyzed. The geometry of the wave in the cross-sectional plane x - z is assumed to be planar sinusoidal and the geometrical characteristic of the wave does not change in y -direction allowing a 2D planar investigation. For uniform waviness, an identical waviness is assumed for all layers throughout the laminate thickness. For the graded waviness it is assumed that the amplitude of the waviness decreases linearly from a maximum in the laminate mid-plane to zero in the $z = \pm H_w/2$ planes. A representative RVE for a composite laminate with graded ply waviness is schematically shown in Figure 122. The sinusoidal functions contain the wave parameters A and L , describing the maximum amplitude and the wavelength, respectively. The wavelength L corresponds to the length of the RVE in x -direction. The global Cartesian coordinate system xyz has its origin at the center of the laminate. The laminate consists of K plies ($K = 1, 2, 3, \dots$) with arbitrary in-plane (x - y plane) fiber orientations α , i.e. $0^\circ, 30^\circ, 45^\circ, 90^\circ$, and a laminate thickness of h .

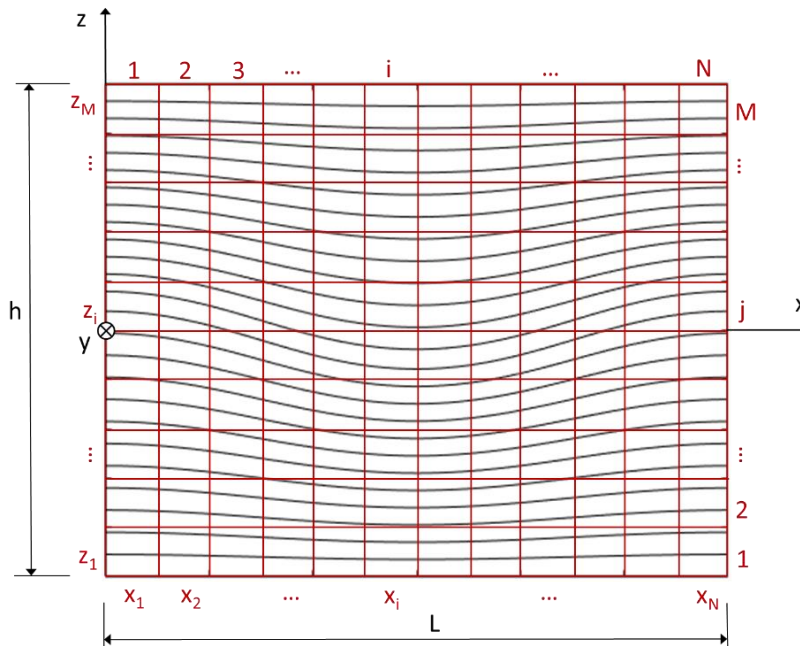


Figure 122. Discretization of the representative volume element for graded waviness.

The compliance matrix ${}_F\mathbf{S}$ in the fiber coordinate system is generally defined by:

$$\begin{aligned}
{}_F\mathbf{S} &= \begin{bmatrix} {}_F\mathcal{S}_{11} & {}_F\mathcal{S}_{12} & {}_F\mathcal{S}_{13} & 0 & 0 & 0 \\ & {}_F\mathcal{S}_{22} & {}_F\mathcal{S}_{23} & 0 & 0 & 0 \\ & & {}_F\mathcal{S}_{33} & 0 & 0 & 0 \\ & & & {}_F\mathcal{S}_{44} & 0 & 0 \\ & \text{sym} & & & {}_F\mathcal{S}_{55} & 0 \\ & & & & & {}_F\mathcal{S}_{66} \end{bmatrix} \\
&= \begin{bmatrix} \frac{1}{E_1} & -\frac{\nu_{12}}{E_1} & -\frac{\nu_{12}}{E_1} & 0 & 0 & 0 \\ & \frac{1}{E_2} & -\frac{\nu_{23}}{E_2} & 0 & 0 & 0 \\ & & \frac{1}{E_2} & 0 & 0 & 0 \\ & & & \frac{2(1+\nu_{23})}{E_2} & 0 & 0 \\ & \text{sym} & & & \frac{1}{G_{12}} & 0 \\ & & & & & \frac{1}{G_{12}} \end{bmatrix} \quad (34)
\end{aligned}$$

where E are the Young's moduli, ν are the Poisson's ratios and G are the shear moduli. For multidirectional laminates containing out-of-plane fiber waviness, two transformations (Figure 123) of the compliance matrix have to be carried out. First, in-plane transformations about the z -axis using the in-plane orientation angle α and second, the out-of-plane transformation about the y -axis using the out-of-plane orientation angle θ .

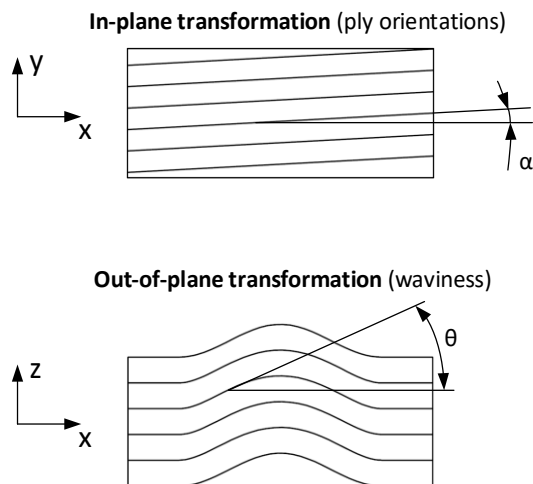


Figure 123. In-plane and out-of-plane transformation.

For **uniform waviness**, i.e. no change in amplitude along the thickness direction of the laminate, the local amplitude ν and local angle θ can be calculated as follows:

7.1 EFFECTIVE ELASTIC PROPERTIES

$$v = A \sin\left(\frac{2\pi x}{L} - \frac{\pi}{2}\right) \quad (35)$$

$$\tan \theta = \frac{dv}{dx} = 2\pi \frac{A}{L} \cos\left(\frac{2\pi x}{L} - \frac{\pi}{2}\right) \quad (36)$$

For **graded waviness**, i.e. the amplitude changes along the thickness direction of the laminate from its maximum at the center to zero at the outer edges, the local amplitude v and local angle θ can be calculated shown in Eqn. (37) and Eqn. (38), respectively:

$$v = A \left(1 - 2\frac{|z|}{h}\right) \sin\left(\frac{2\pi x}{L} - \frac{\pi}{2}\right) \quad (37)$$

$$\tan \theta = \frac{dv}{dx} = 2\pi \frac{A}{L} \left(1 - 2\frac{|z|}{h}\right) \cos\left(\frac{2\pi x}{L} - \frac{\pi}{2}\right) \quad (38)$$

The transformation matrices for the calculation of global compliances are given in Eqn. (39) and (40).

$$\mathbf{T}_{FG_{in-plane}} = \begin{bmatrix} m^2 & n^2 & 0 & 0 & 0 & 2mn \\ n^2 & m^2 & 0 & 0 & 0 & -2mn \\ 0 & 0 & 1 & 0 & 0 & 0 \\ 0 & 0 & 0 & m & n & 0 \\ 0 & 0 & 0 & -n & m & 0 \\ -mn & mn & 0 & 0 & 0 & m^2 - n^2 \end{bmatrix} \quad (39)$$

with $m = \cos \alpha$, $n = \sin \alpha$

$$\mathbf{T}_{FG_{out-of-plane}} = \begin{bmatrix} m^2 & 0 & n^2 & 0 & 2mn & 0 \\ 0 & 1 & 0 & 0 & 0 & 0 \\ n^2 & 0 & m^2 & 0 & -2mn & 0 \\ 0 & 0 & 0 & m & 0 & -n \\ -mn & 0 & mn & 0 & m^2 - n^2 & 0 \\ 0 & 0 & 0 & n & 0 & m \end{bmatrix} \quad (40)$$

with $m = \cos \theta$, $n = \sin \theta$

The compliance matrix ${}_G\mathbf{S}$ in the global coordinate system can then be calculated as follows:

$${}_G\mathbf{S} = \mathbf{T}_{FG_{out-of-plane}}^{-1} \cdot \mathbf{T}_{FG_{in-plane}}^{-1} \cdot {}_F\mathbf{S} \cdot \mathbf{T}_{FG_{in-plane}} \cdot \mathbf{T}_{FG_{out-of-plane}} \quad (41)$$

The superscripts -1 and T denote the inverse and transpose of the transformation matrix, respectively.

For the sake of clarity, the results of the global mechanical material properties in Eqn. (42) are presented for a pure UD laminate only, where only an out-of-plane transformation has to be carried out.

$$\begin{aligned}
 E_{x,ij} = E_x(x_i, z_j) &= \frac{1}{{}_F S_{11} m^4 + (2 {}_F S_{12} + {}_F S_{66}) m^2 n^2 + {}_F S_{22} n^4} \\
 E_{y,ij} = E_y(x_i, z_j) &= \frac{1}{{}_F S_{22}} \\
 G_{xy,ij} = G_{xy}(x_i, z_j) &= \frac{1}{2({}_F S_{22} - {}_F S_{23}) n^2 + {}_F S_{66} m^2} \\
 v_{xy,ij} = v_{xy}(x_i, z_j) &= \frac{{}_F S_{12} m^2 + {}_F S_{23} n^2}{{}_F S_{11} m^4 + (2 {}_F S_{12} + {}_F S_{66}) m^2 n^2 + {}_F S_{22} n^4} \\
 v_{yx,ij} = v_{yx}(x_i, z_j) &= \frac{E_{y,ij}}{E_{x,ij}} v_{xy,ij}
 \end{aligned} \tag{42}$$

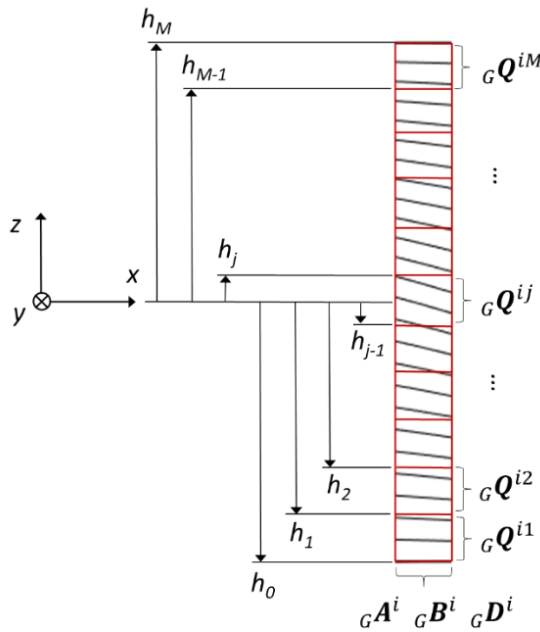


Figure 124. Application of the classical laminate theory on a strip along the x-direction.

The reduced stiffness matrix ${}_G Q^{ij}$ for every ply ij of the element i can be calculated using the derived local stiffnesses from Eqn. (42).

$$\begin{aligned}
 {}_G\mathbf{Q}^{ij} = {}_G\mathbf{Q}(x_i, z_j) &= \begin{bmatrix} Q_{11} & Q_{12} & 0 \\ Q_{12} & Q_{22} & 0 \\ 0 & 0 & Q_{66} \end{bmatrix}^{ij} \\
 &= \begin{bmatrix} \frac{E_x}{1 - \nu_{xy}\nu_{yx}} & \frac{\nu_{xy} E_y}{1 - \nu_{xy}\nu_{yx}} & 0 \\ \frac{\nu_{xy} E_y}{1 - \nu_{xy}\nu_{yx}} & \frac{E_y}{1 - \nu_{xy}\nu_{yx}} & 0 \\ 0 & 0 & G_{xy} \end{bmatrix}^{ij}
 \end{aligned} \tag{43}$$

The stiffness matrices ${}_G\mathbf{A}^i$, ${}_G\mathbf{B}^i$ and ${}_G\mathbf{D}^i$ can be calculated by:

$$\begin{aligned}
 {}_G\mathbf{A}^i &= {}_G\mathbf{A}(x_i) = \sum_{j=1}^M {}_G\mathbf{Q}^{ij} (h_j - h_{j-1}) \\
 {}_G\mathbf{B}^i &= {}_G\mathbf{B}(x_i) = \frac{1}{2} \sum_{j=1}^M {}_G\mathbf{B}^{ij} (h_j^2 - h_{j-1}^2) \\
 {}_G\mathbf{D}^i &= {}_G\mathbf{D}(x_i) = \frac{1}{3} \sum_{j=1}^M {}_G\mathbf{Q}^{ij} (h_j^3 - h_{j-1}^3)
 \end{aligned} \tag{44}$$

with h_j is the relative distance of the ply from the mid-plane, which can be calculated as:

$$h_j = \left(\frac{j}{M} - \frac{1}{2} \right) h \tag{45}$$

using h as the height of the considered volume element.

By using the calculated components of ABD-matrix (Eqn. 14) the general stress-strain relation for combined membrane plate element can be written as:

$$\begin{bmatrix} \mathbf{N} \\ \mathbf{M} \end{bmatrix}^i = \begin{bmatrix} \mathbf{A} & \mathbf{B} \\ \mathbf{B} & \mathbf{D} \end{bmatrix}^i \cdot \begin{bmatrix} \boldsymbol{\varepsilon} \\ \boldsymbol{\kappa} \end{bmatrix}_0^i \quad \text{respectively} \quad \begin{bmatrix} \boldsymbol{\varepsilon} \\ \boldsymbol{\kappa} \end{bmatrix}_0^i = \begin{bmatrix} \mathbf{a} & \mathbf{b} \\ \mathbf{b} & \mathbf{d} \end{bmatrix}^i \cdot \begin{bmatrix} \mathbf{N} \\ \mathbf{M} \end{bmatrix}^i \tag{46}$$

Figure 125 shows a schematic illustration of the homogenization procedure for volume averaging, similar to the homogenization proposed by Takeda [272]. A widely adopted assumption of uniform out-of-plane stresses and in-plane strains throughout each strip is adopted for predicting the effective response of the laminate.

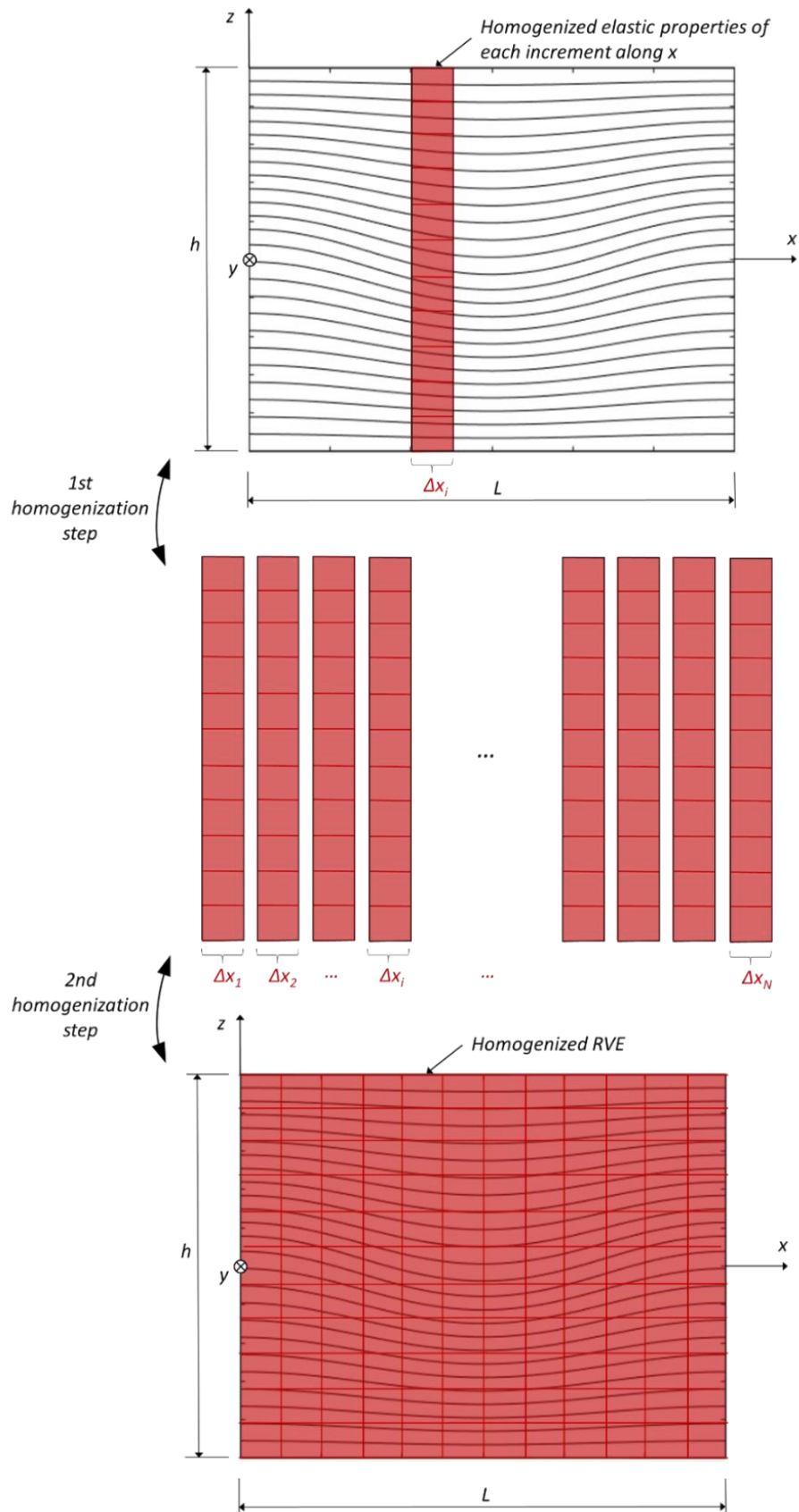


Figure 125. Homogenization procedure for volume averaging.

7.2. Local stresses and strains

Using the inverse of the transformation matrix $\mathbf{T}_{FG}^{-1} = \mathbf{T}_{GF}$, which includes both in-plane and out-of-plane transformations, the transformation relationship for stresses and strains follows:

$$\begin{bmatrix} \sigma_x \\ \sigma_y \\ \sigma_z \\ \tau_{yz} \\ \tau_{xz} \\ \tau_{xy} \end{bmatrix}_G = \mathbf{T}_{GF} \cdot \begin{bmatrix} \sigma_1 \\ \sigma_2 \\ \sigma_3 \\ \tau_{23} \\ \tau_{13} \\ \tau_{12} \end{bmatrix}_F \quad (47)$$

$$\begin{bmatrix} \varepsilon_x \\ \varepsilon_y \\ \varepsilon_z \\ \gamma_{yz}/2 \\ \gamma_{xz}/2 \\ \gamma_{xy}/2 \end{bmatrix}_G = \mathbf{T}_{GF} \cdot \begin{bmatrix} \varepsilon_1 \\ \varepsilon_2 \\ \varepsilon_3 \\ \gamma_{23}/2 \\ \gamma_{13}/2 \\ \gamma_{12}/2 \end{bmatrix}_F \quad (48)$$

By using the Reuther matrix \mathbf{R}

$$\mathbf{R} = \begin{bmatrix} 1 & 0 & 0 & 0 & 0 & 0 \\ 0 & 1 & 0 & 0 & 0 & 0 \\ 0 & 0 & 1 & 0 & 0 & 0 \\ 0 & 0 & 0 & 2 & 0 & 0 \\ 0 & 0 & 0 & 0 & 2 & 0 \\ 0 & 0 & 0 & 0 & 0 & 2 \end{bmatrix} \quad (49)$$

Equation (48) can be written as:

$$\begin{bmatrix} \varepsilon_x \\ \varepsilon_y \\ \varepsilon_z \\ \gamma_{yz} \\ \gamma_{xz} \\ \gamma_{xy} \end{bmatrix}_G = \mathbf{R} \cdot \mathbf{T}_{GF} \cdot \mathbf{R}^{-1} \cdot \begin{bmatrix} \varepsilon_1 \\ \varepsilon_2 \\ \varepsilon_3 \\ \gamma_{23} \\ \gamma_{13} \\ \gamma_{12} \end{bmatrix}_F \quad (50)$$

Using ${}_F\mathbf{S}$ from Eqn. (34), the relationship between stresses and strains in the fiber coordinate system follows Hook's law with:

$$\begin{bmatrix} \varepsilon_1 \\ \varepsilon_2 \\ \varepsilon_3 \\ \gamma_{23} \\ \gamma_{13} \\ \gamma_{12} \end{bmatrix}_F = {}_F\mathbf{S} \cdot \begin{bmatrix} \sigma_1 \\ \sigma_2 \\ \sigma_3 \\ \tau_{23} \\ \tau_{13} \\ \tau_{12} \end{bmatrix}_F \quad (51)$$

The stress strain relation in global coordinates follows by introducing equation (47) and (50) in equation (51)

$$\begin{bmatrix} \varepsilon_x \\ \varepsilon_y \\ \varepsilon_z \\ \gamma_{yz} \\ \gamma_{xz} \\ \gamma_{xy} \end{bmatrix} = \mathbf{R} \cdot \mathbf{T}_{GF} \cdot \mathbf{R}^{-1} \cdot {}_F\mathbf{S} \cdot \mathbf{T}_{FG} \cdot \begin{bmatrix} \sigma_x \\ \sigma_y \\ \sigma_z \\ \tau_{yz} \\ \tau_{xz} \\ \tau_{xy} \end{bmatrix} = {}_G\mathbf{S} \cdot \begin{bmatrix} \sigma_x \\ \sigma_y \\ \sigma_z \\ \tau_{yz} \\ \tau_{xz} \\ \tau_{xy} \end{bmatrix} \quad (52)$$

resulting in the transformed compliance matrix ${}_G\mathbf{S}$:

$${}_G\mathbf{S} = \mathbf{R} \cdot \mathbf{T}_{GF} \cdot \mathbf{R}^{-1} \cdot {}_F\mathbf{S} \cdot \mathbf{T}_{FG} \quad (53)$$

It should be noted, that the transformed compliance matrix ${}_G\mathbf{S}$ generally do not show orthotropic properties. It exists a coupling between shear stresses τ and strains ε , and normal stresses σ and shear strains γ .

$${}_G\mathbf{S} = \begin{bmatrix} {}_G\mathcal{S}_{11} & {}_G\mathcal{S}_{12} & {}_G\mathcal{S}_{13} & 0 & {}_G\mathcal{S}_{15} & 0 \\ & {}_G\mathcal{S}_{22} & {}_G\mathcal{S}_{23} & 0 & {}_G\mathcal{S}_{25} & 0 \\ & & {}_G\mathcal{S}_{33} & 0 & {}_G\mathcal{S}_{35} & 0 \\ & & & {}_G\mathcal{S}_{44} & 0 & {}_G\mathcal{S}_{46} \\ & sym & & & {}_G\mathcal{S}_{55} & 0 \\ & & & & & {}_G\mathcal{S}_{66} \end{bmatrix} \quad (54)$$

The average transformed compliance matrix ${}_G\bar{\mathbf{S}}$ for uniform waviness given in Eqn. (55) can be calculated by integrating ${}_G\mathbf{S}$ over x and dividing by the wavelength L .

$${}_G\bar{\mathbf{S}} = \frac{1}{L} \int_0^L {}_G\mathbf{S} dx \quad (55)$$

Due to the variability of the transformed compliance matrix ${}_G\bar{\mathbf{S}}$ for graded waviness in both x and z -direction, the integration has to be carried out in both directions. Thus, the average transformed compliance matrix for graded waviness follows:

$${}_G\bar{\mathbf{S}} = \frac{1}{h} \frac{1}{L} \int_{-h/2}^{h/2} \int_0^L {}_G\mathbf{S} dx dz \quad (56)$$

For the occupation of ${}_G\bar{\mathbf{S}}$ applies:

7.3 LOCAL ELASTIC PROPERTIES

$${}_G\bar{\mathbf{S}} = \begin{bmatrix} {}_G\bar{S}_{11} & {}_G\bar{S}_{12} & {}_G\bar{S}_{13} & 0 & 0 & 0 \\ & {}_G\bar{S}_{22} & {}_G\bar{S}_{23} & 0 & 0 & 0 \\ & & {}_G\bar{S}_{33} & 0 & 0 & 0 \\ & & & {}_G\bar{S}_{44} & 0 & 0 \\ & \text{sym} & & & {}_G\bar{S}_{55} & 0 \\ & & & & & {}_G\bar{S}_{66} \end{bmatrix} \quad (57)$$

Comparing Eqn. (57) with Eqn. (58), it can be seen that although a coupling between shear stresses τ and strains ε or normal stresses σ and shear strains (angles) γ occurs locally, this coupling is eliminated globally. The representative volume element with fiber waviness behaves orthotropic when considered from a global point of view, but not transversely isotropic. Additionally, it should be noted that the entry S_{22} of the compliance matrix remains unchanged. This is due to the fact that the Young's modulus in y direction is not influenced by the fiber waviness. The following applies ${}_G\bar{S}_{22} = {}_G S_{22} = {}_F S_{22} = \frac{1}{E_z} = \frac{1}{E_y}$. The effective elastic properties for uniform and graded waviness are calculated from Eqn. (55) and Eqn. (56), respectively.

$${}_G\bar{\mathbf{S}} = \begin{bmatrix} \frac{1}{E_x} & -\frac{\nu_{xy}}{E_x} & -\frac{\nu_{xz}}{E_x} & 0 & 0 & 0 \\ & \frac{1}{E_y} & -\frac{\nu_{yz}}{E_y} & 0 & 0 & 0 \\ & & \frac{1}{E_z} & 0 & 0 & 0 \\ & & & \frac{1}{G_{yz}} & 0 & 0 \\ & \text{sym} & & & \frac{1}{G_{xz}} & 0 \\ & & & & & \frac{1}{G_{xy}} \end{bmatrix} \quad (58)$$

7.3. Local elastic properties

Based on the previously derived relationships, the local elasticity constants within a laminate containing fiber waviness can be specified.

Uniform waviness. In the case of the uniform waviness, the laminate properties depend solely on the x -coordinate. For calculating the local properties, the considered volume element is therefore divided along the x -axis into N equal sections with the index $i \in [1, N]$.

According to Eqn. (53), the local transformed compliances ${}_G\mathbf{S}^i = {}_G\mathbf{S}(x_i)$, in the middle x_i of each respective section i are obtained by the following relationship using the transformation matrix $\mathbf{T}_{GF}^i = \mathbf{T}_{GF}(x_i)$.

$${}_G\mathbf{S}^i = \mathbf{R} \cdot \mathbf{T}_{GF}^i \cdot \mathbf{R}^{-1} \cdot {}_F\mathbf{S}^i \cdot \mathbf{T}_{FG}^i \quad (59)$$

$$x_i = \left(\frac{2i-1}{2N} \right) L \quad (60)$$

Graded waviness. With the graded fiber waviness there is an additional dependence of the laminate properties in z -direction due to the varying amplitude, as shown in Figure 122. Accordingly, the discretization of the volume element along the x -axis is carried out into N elements and along the z -axis into M equally sized segments. The index $i \in [1, N]$ again indicates the discretization in x -direction, while $j \in [1, M]$ stands for the discretization in z -direction. Following Eqn. (53), the local transformed compliance matrix ${}_G\mathbf{S}^{ij} = {}_G\mathbf{S}(x_i, z_j)$ in the center of each element ij can be calculated with the transformation matrix $\mathbf{T}_{GF}^{ij} = \mathbf{T}_{GF}(x_i, z_j)$.

$${}_G\mathbf{S}^{ij} = \mathbf{R} \cdot \mathbf{T}_{GF}^{ij} \cdot \mathbf{R}^{-1} \cdot {}_F\mathbf{S}^{ij} \cdot \mathbf{T}_{FG}^{ij} \quad (61)$$

$$x_i = \left(\frac{2i-1}{2N} \right) L \quad (62)$$

$$z_j = \left(\frac{2j-1-M}{2M} \right) h \quad (63)$$

The local elastic properties can then be obtained from Eqn. (58) for both uniform and graded waviness.

7.4. Damage initiation

For the damage initiation the well-established Puck criterion [80] is used.

Fiber failure under tension $\bar{\sigma}_1 \geq 0$

$$f_{EFF}^t(\bar{\sigma}_1) = \frac{\bar{\sigma}_1}{R_{\parallel}^t} \leq 0 \quad (64)$$

Fiber failure under compression $\bar{\sigma}_1 < 0$

$$f_{EFF}^c(\bar{\sigma}_1) = \frac{\bar{\sigma}_1}{(-R_{\parallel}^c)} \leq 0 \quad (65)$$

Inter-fiber failure under tension $\bar{\sigma}_3 \geq 0$ (Mode A)

$$f_{E_{IFF}}^t(\bar{\sigma}_3, \bar{\tau}_{31}) = \sqrt{\left[\left(\frac{1}{R_{\perp}^t} - \frac{p_{\perp\parallel}^t}{R_{\parallel\parallel}^t}\right)\bar{\sigma}_3\right]^2 + \left(\frac{\bar{\tau}_{31}}{R_{\parallel\parallel}^t}\right)^2} + \frac{p_{\perp\parallel}^t}{R_{\perp\parallel}^t}\bar{\sigma}_3 \leq 0 \quad (66)$$

Inter-fiber failure under compression $\bar{\sigma}_3 < 0$ (Mode B)

$$f_{E_{IFF}}^c(\bar{\sigma}_3, \bar{\tau}_{31}) = \sqrt{\left(\frac{p_{\perp\parallel}^c}{R_{\parallel\parallel}^c}\bar{\sigma}_3\right)^2 + \left(\frac{\bar{\tau}_{31}}{R_{\parallel\parallel}^c}\right)^2} + \frac{p_{\perp\parallel}^c}{R_{\perp\parallel}^c}\bar{\sigma}_3 \leq 0 \quad (67)$$

Inter-fiber failure under compression $\bar{\sigma}_3 < 0$ (Mode C)

$$f_{E_{IFF}}^c(\bar{\sigma}_3, \bar{\tau}_{31}) = \left[\left(\frac{\bar{\tau}_{31}}{2(1 + p_{\perp\parallel}^c)R_{\parallel\parallel}^c}\right)^2 + \left(\frac{\bar{\sigma}_3}{R_{\perp\perp}^c}\right)^2\right] \frac{R_{\perp\perp}^c}{-\bar{\sigma}_3} \leq 0 \quad (68)$$

7.5. Validation of analytical results

Hsiao and Daniel [13,46] have carried out fundamental work in the field of fiber waviness in composite materials. In [46] they carried out analytical calculations of Young's modulus and shear modulus as well as the Poisson's ratio for uniform, graded and local fiber waviness. Results obtained by the analytical model, that has been introduced in this Section, are validated against the results from Hsiao and Daniel, shown in Figure 126 to Figure 128 for increasing amplitude-wavelength ratios of Young's moduli, shear moduli and Poisson's ratios, respectively. Generally, it can be seen that the Young's modulus in x -direction is most heavily affected by the fiber waviness. The fibers rotated by the angle θ can bear less load in the x -direction than longitudinally oriented fibers, causing a strong reduction in stiffness in the x direction. Correspondingly, the angled fibers take up more load in the z -direction, which increases the modulus of elasticity in the z -direction. In y -direction there is no influence of the elastic modulus due to the fiber waviness due to transversal isotropic behavior of a UD ply, i.e. $E_2 = E_3$. The effects of the graded fiber waviness are generally less than those of the uniform fiber waviness. This is due to the fact that a smaller proportion of fibers is misaligned. The largest influence on the stiffness is basically the uniform fiber waviness, which extends globally over the entire laminate. As a result of the decreasing amplitudes of the graded fiber waviness, it has a smaller influence. Furthermore, it can be seen that the Young's modulus in the longitudinal direction of the composite material E_x decreases strongly, while E_y remains constant and E_z increases slightly.

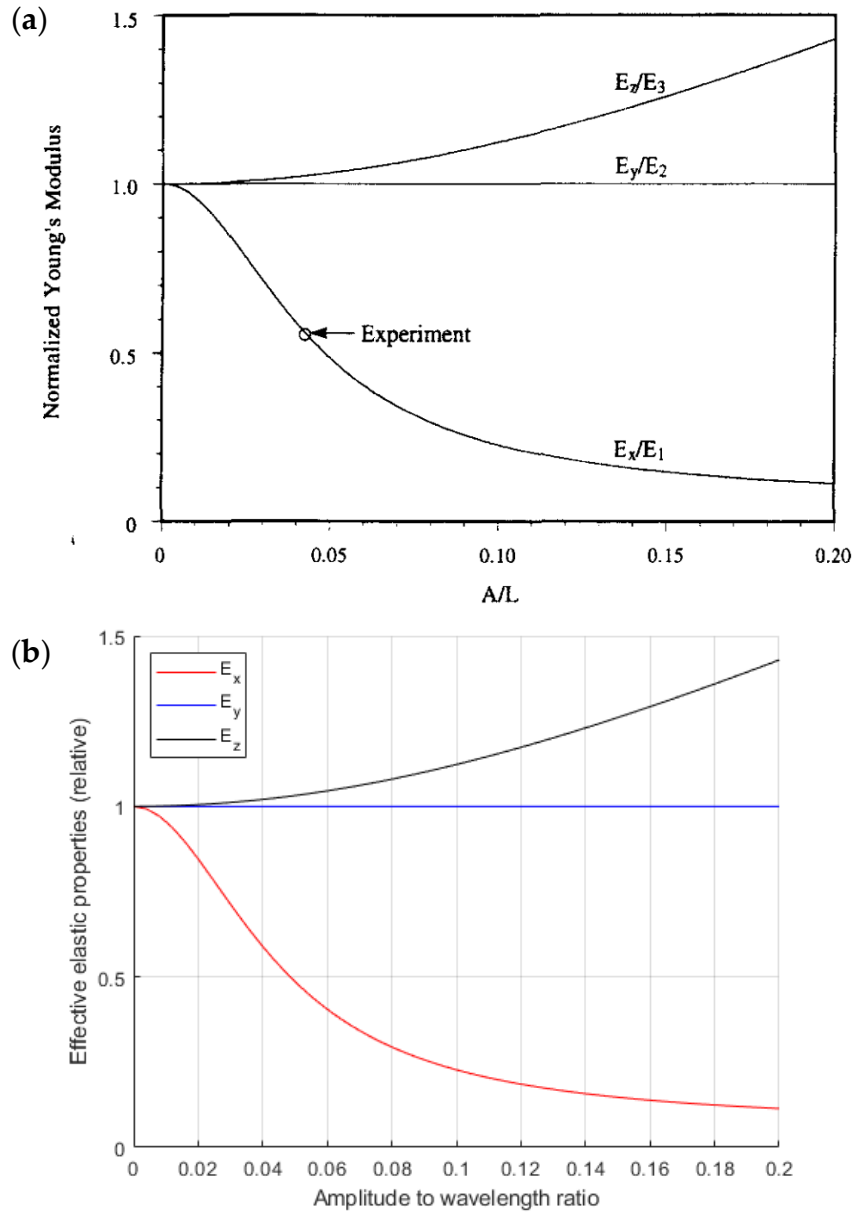


Figure 126. Effective Young's moduli for UD-laminate as a function of waviness parameter A/L for uniform waviness model. a) Results from [46], b) Analytical model implemented in MATLAB.

7.5 VALIDATION OF ANALYTICAL RESULTS

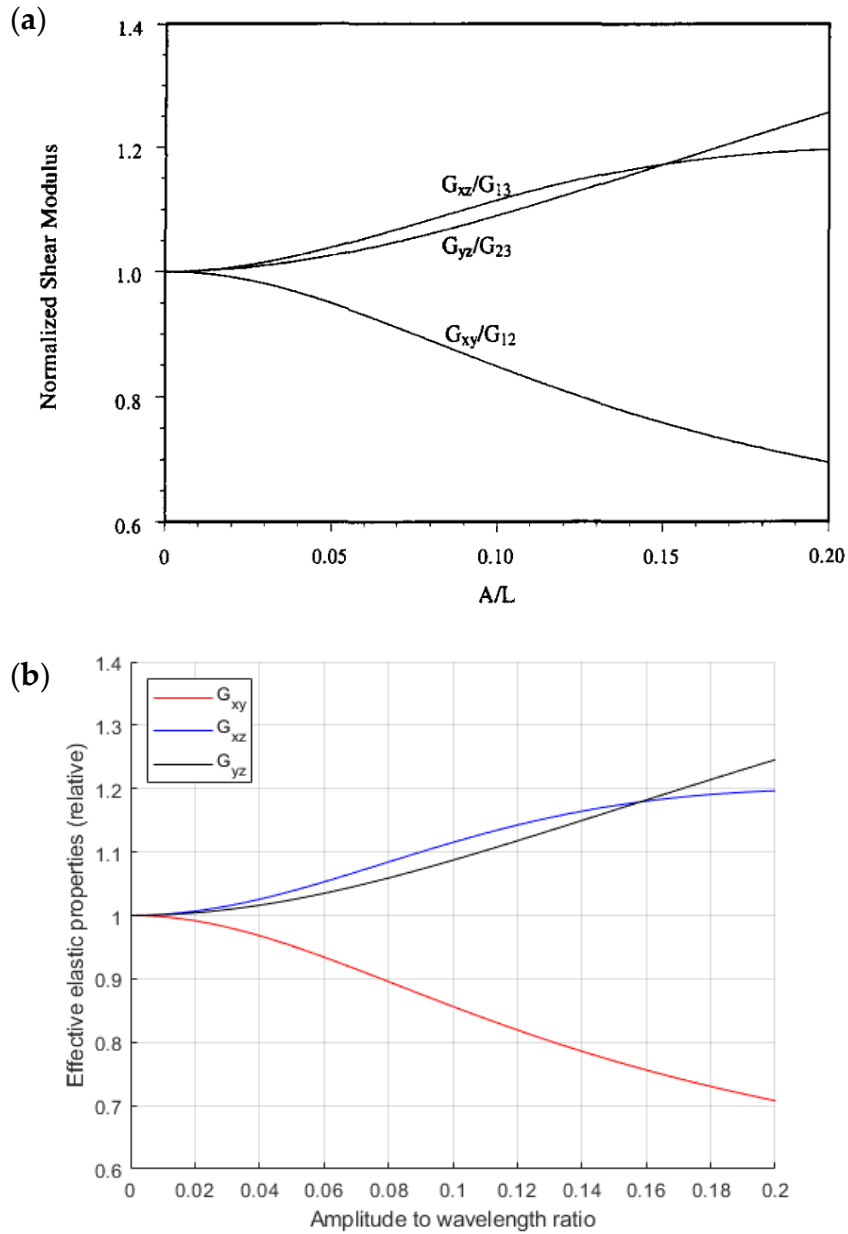


Figure 127. Effective shear moduli for UD-laminate as a function of waviness parameter A/L for uniform waviness model. a) Results from [46], b) Analytical model implemented in MATLAB.

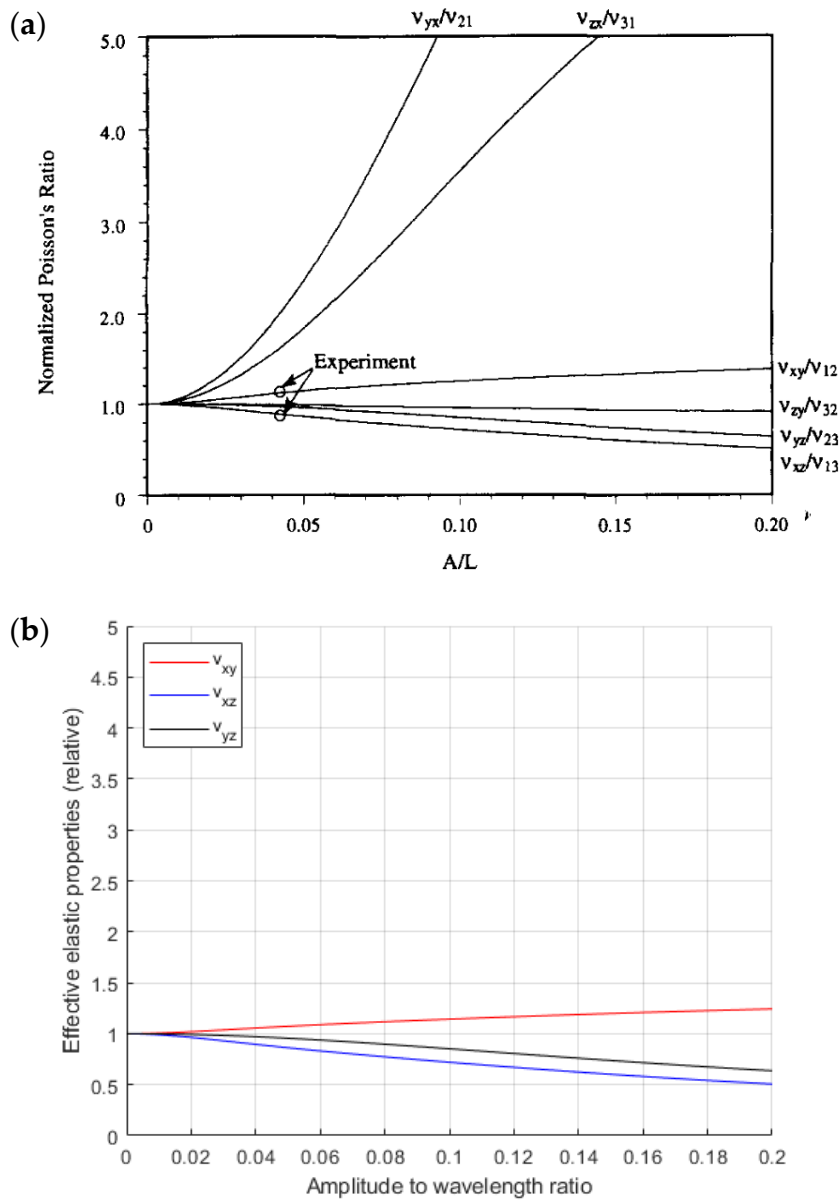


Figure 128. Effective Poisson's ratios for UD-laminate as a function of waviness parameter A/L for uniform waviness model. a) Results from [46], b) Analytical model implemented in MATLAB.

7.6. Comparison with experimental results

Figure 129 shows a comparison of the calculated effective Young's modulus in x -direction for a range of amplitude-to-wavelength ratios between 0-0.2 with experimental data from compression tests of UD laminates with two wave configurations. The analytical calculation of the Young's modulus in global x -direction of 0° laminates (Figure 129 a) shows sufficiently accurate results for both wave configurations in comparison to the conducted mechanical compression tests. The results of the mechanical testing of QI laminates (Figure 129 b) for wave 2 (the less

7.6 COMPARISON WITH EXPERIMENTAL RESULTS

pronounced waviness) resulted in a higher Young's modulus compared to the planar reference samples. This inconclusive result can possibly be related to the different laminate thicknesses of the tested samples (planar reference sample $t=2.1$ mm, wavy samples $t=5.1$ mm). But the wavy samples (wave 2) also showed a higher scattering of the results compared to the reference specimen. Nevertheless, it is also possible to speak of a reliable approximation of the global mechanical properties for multidirectional laminates.

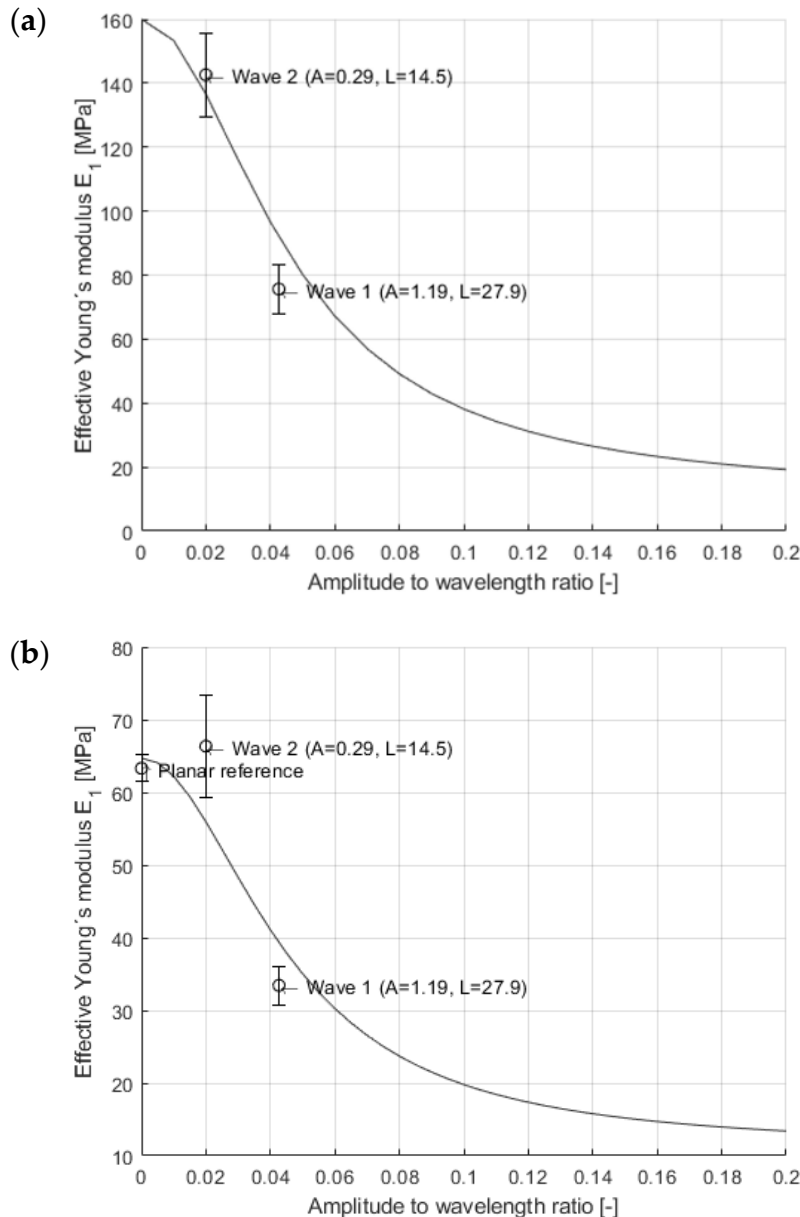


Figure 129. Effective Young's modulus for a) UD- and b) QI-laminate in x-direction.

In addition to experimental testing, the analytical calculated stress distribution along the composite length coordinate, i.e. along the length of the wave, following the approach described in Section 7.2, is compared with results from the performed FE simulations. Please see Section 8.4 for additional results from the FE simulations using

a material model that is incorporated as a user-subroutine which is especially able to account for the shear non-linearities of the matrix. The material parameter for the IM7-8552 material are described in Table 17 in Section 8.3. The axial compression loads applied for wave 1 and wave 2 are, according to the stress-to-failure obtained from numerical results, -288 MPa and -627 MPa, respectively.

The comparison of the local stress component in fiber direction σ_1 obtained from analytical calculations (dashed lines) and FE simulations (continuous lines) show excellent agreement (Figure 130 a). However, the course of wave 1 deviates slightly between analytical and numerical results, but the order of magnitude of the stresses corresponds very well.

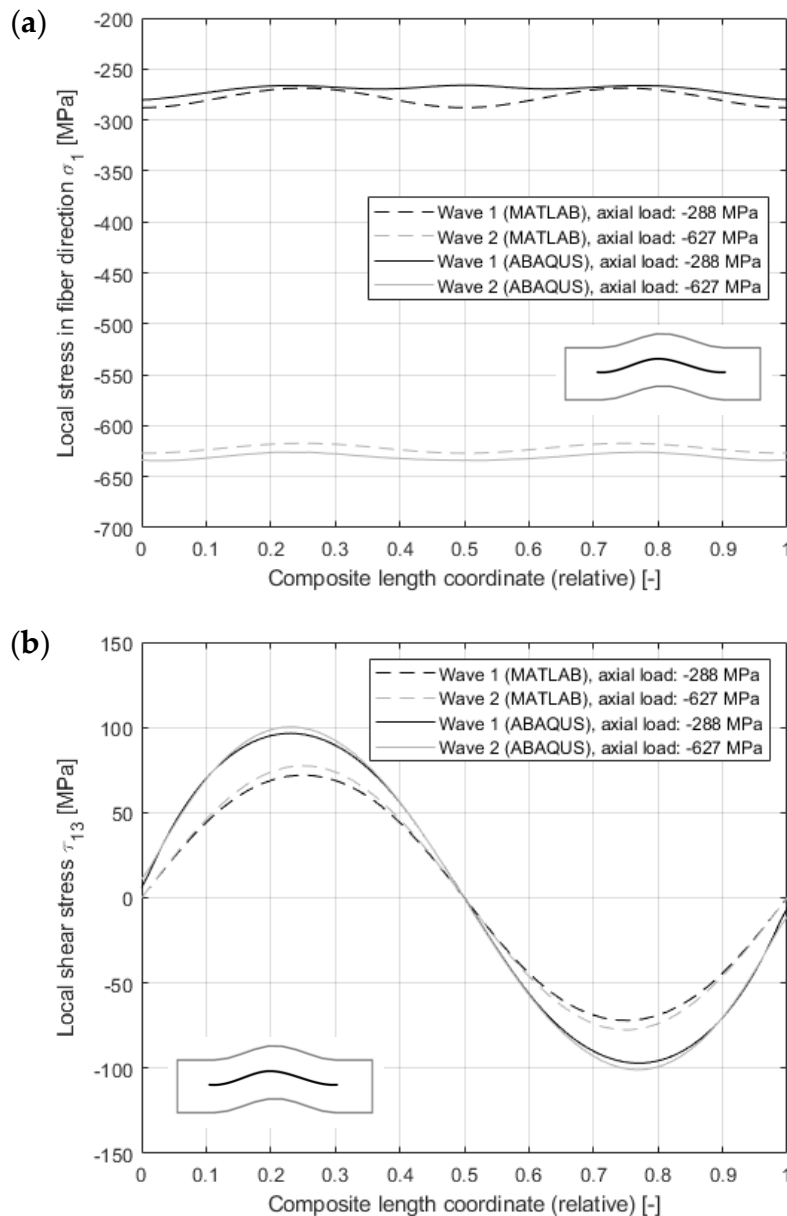


Figure 130. Analytically (MATLAB) and numerically (ABAQUS) obtained values for a) local stresses in fiber direction σ_1 and b) local shear stresses τ_{13} for wave 1 and wave 2 loaded in compression with -288 MPa and -627 MPa, respectively.

7.6 COMPARISON WITH EXPERIMENTAL RESULTS

The shear stress distribution τ_{13} along the (relative) wave length coordinate, plotted in Figure 130 b), which is considered to be the most significant stress component for damage initiation in wavy composites under axial compression, shows a sine shaped curve with maximum amplitudes at the points of the largest inclination of the fibers in 0.25 and 0.75. Interestingly, the shear stress distributions for wave 1 and wave 2 obtained from analytical calculations are identical. The results from numerical simulations are also in the same order of magnitude, regardless of the wave configuration. However, due to its strong impact on failure initiation, the shear stress must be calculated accurately to ensure reliable strength calculations.

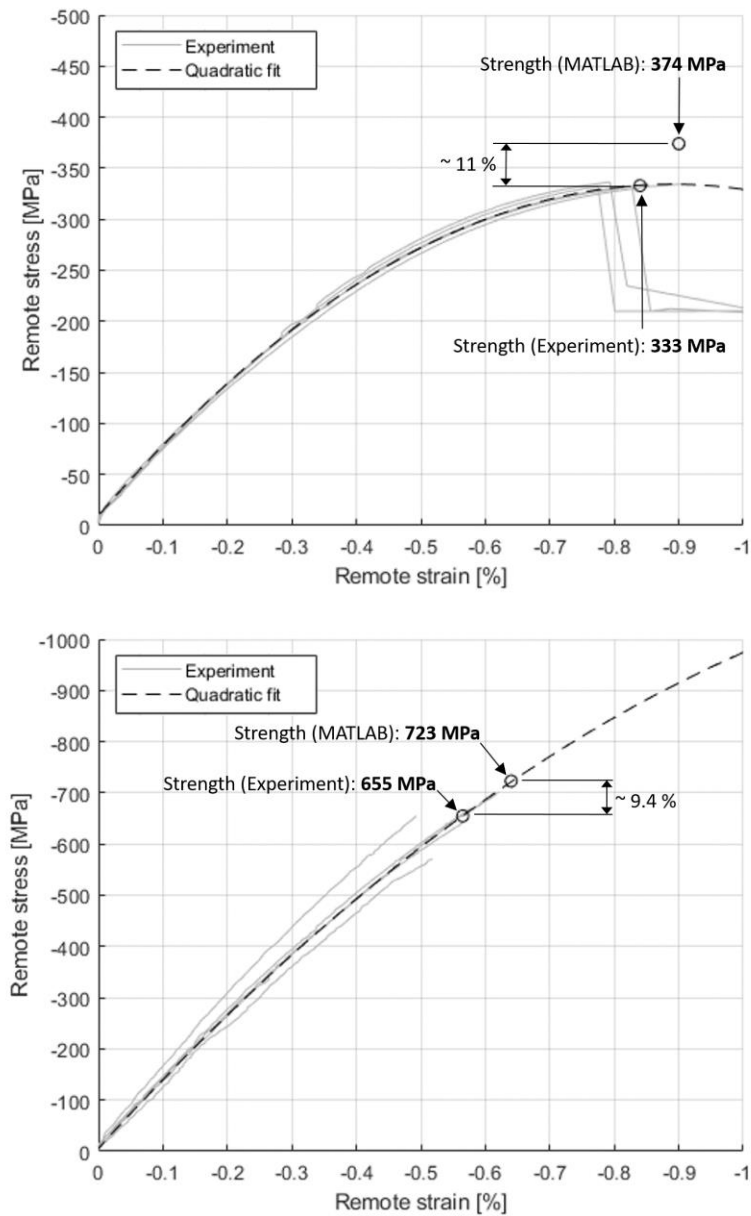


Figure 131. Compression test of UD-laminate with uniform waviness with strength values obtained from analytical model (MATLAB). a) wave 1 (A=1.19, L=27.9) and b) wave 2 (A=0.29, L=14.5).

The damage initiation is determined using the Puck failure criterion, as described in Section 7.4. Figure 131 shows the stress-strain curves and strength values obtained by compression tests on unidirectional laminates with both wave 1 (a) and wave 2 (b) and additionally, the strength values obtained from the analytical model. The deviation between experimental and analytical results for the strength values is 11 % for wave 1 and 9.4 % for wave 2. The dashed lines are quadratic fits from experimental stress-strain curves. It has to be noted, that the analytical strength values are plotted in the diagram without relation to the remote strain. The analytical strength calculation of multidirectional laminates resulted in insufficient values with much higher deviations, indicating the challenge of capturing the whole complexity of stress distributions in laminates with varying ply orientations. In the current status, the analytical model is not capable to account for the highly complex damage behavior of multidirectional laminates.

Figure 132 shows a visualization of the inter-fiber failure (IFF) of the discretized wave 1, i.e. $M=20$ increments for the discretization of the ply height and $N=60$ increments for the composite (wave) length coordinate, when reaching the analytically calculated maximum bearable load of 374 MPa. This figure also illustrates, that the fiber angle does not change in z -direction for uniform waviness, leading to all stress curves are constant in $z \in \left[-\frac{h}{2}, \frac{h}{2}\right]$ and consequently the failure criteria are constant in z .

For comparison, Figure 133 shows the analytical result for inter-fiber failure (IFF) for graded waviness at the same load value of 374 MPa. This load does not lead to IFF in the case of graded fiber waviness, as a lower proportion of the fibers is misaligned. However, it is evident that IFF occurs at the area of the maximum inclination of the fibers.

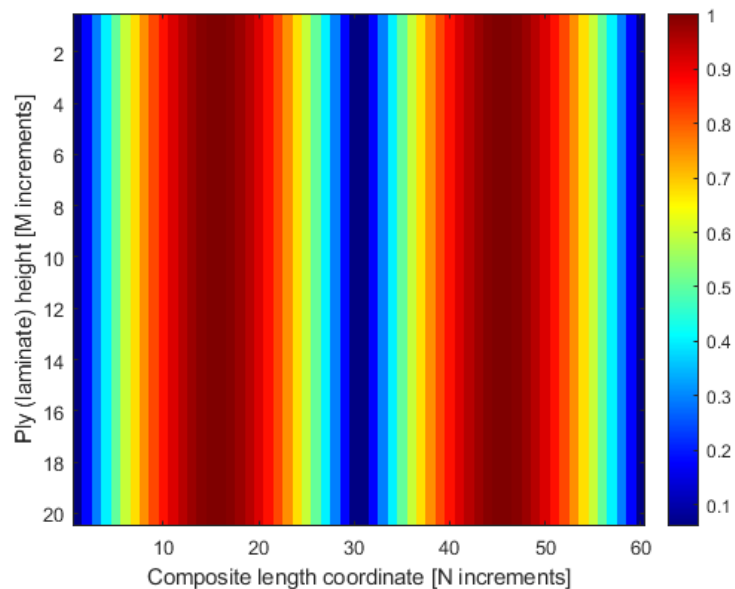


Figure 132. Inter-fiber failure (IFF) of wave 1 with uniform waviness at a loading of 374 MPa obtained from analytical model.

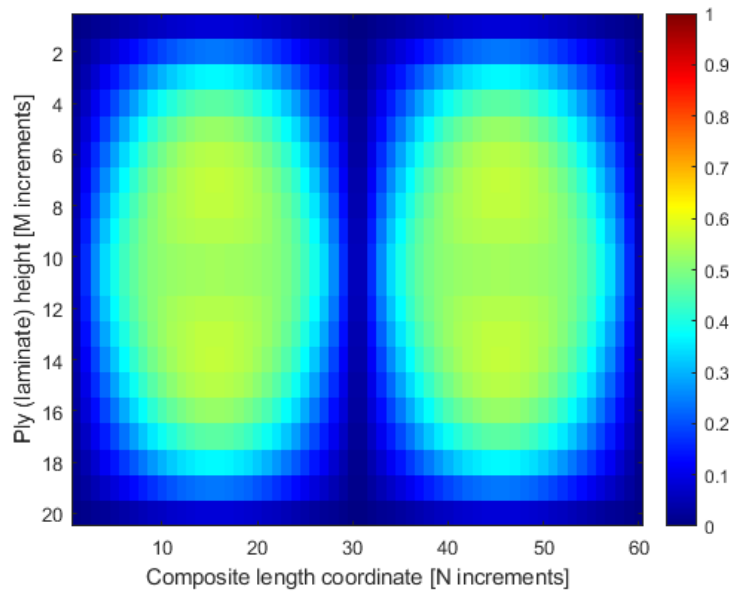


Figure 133. Inter-fiber failure (IFF) of wave 1 with graded waviness at a loading of 374 MPa obtained from analytical model.

7.7. Conclusions on the analytical model

In this thesis, the analytical models of Hsiao & Daniel [46] and Altmann et al. [79], which are only applicable for unidirectional laminates, were extended for the calculation of multidirectional laminates. The analytical approach is able to determine the global, as well as local elastic properties, local stress distributions and based on that, strength calculations using the Puck failure criteria. The model was implemented in the software MATLAB in the form of several user interfaces. The presented model is valid for symmetrical, multidirectional laminates.

It delivers reliable approximations of elastic properties, e.g. stiffnesses, for both uni- and multidirectional laminates. The global elastic properties are significantly influenced by increasing A/L ratio. The Young's modulus E_x in the longitudinal direction is most severely affected. In general, the influence of graded fiber waviness is less than that of uniform fiber waviness, as a lower proportion of fibers are misaligned. The stress analysis has shown that fiber waviness leads to local shear stresses with maxima at the position of the largest deviation, i.e. inclination, of the fiber direction. Graded fiber waviness leads to increased normal stresses in fiber direction σ_1 at the outer edges of the laminate $z = \pm \frac{h}{2}$ as the horizontally aligned fibers in this region carry most of the stresses in x-direction. Comparisons with experimental results (Section 5) and FE simulations (Section 8) have shown good agreement for the prediction of elastic properties and stress distributions. However, the strength prediction only led to sufficient results for unidirectional laminates. The strength evaluation for multidirectional laminates is difficult due to highly complex

interactions in the damage behavior of the varying ply orientations. The lack of accounting for global bending has to be incorporated in the next step to further improve the accuracy of the results.

8. NUMERICAL SIMULATION

The limited capability to predict material failure in composite materials and specifically in wavy composite layers has led to high margins of safety for the design of composite structures. Thus, the full lightweight potential of this class of materials is left unused. To understand the complex failure behavior of composite materials containing out-of-plane fiber waviness under compressive and tensile loading, a non-linear 2D material model was implemented in ABAQUS and validated with extensive experimental test data from compression and tensile tests. Each test was recorded by a stereo camera system for digital image correlation to resolve damage initiation and propagation in detail. This study has shown excellent agreement of numerical simulations with experimental data. In a virtual testing approach, various parameters, i.e. amplitude, wavelength and laminate thickness, have been studied. It was found that the failure mode changed from delamination to kink shear band formation with increasing laminate thickness. The wavelength has shown minor influences compared to amplitude and laminate thickness.

8.1. Constitutive material behavior

The constitutive material behavior of a single UD ply can be modelled by an undamaged non-linear elasto-plastic hardening regime and an elasto-damage softening regime shown in Figure 134. In the hardening regime the stress increases with ascending strain. The degree of non-linearity depends on the angle between loading direction and orientation of the layer. The failure criterion according to Puck [80] is used to determine the damage initiation. The degradation of the continuum is described in the softening regime and controlled by energy-based linear stiffness degradation. Modelling of interface delamination, e.g. cohesive zone modelling (CZM) or virtual crack closure technique (VCCT), is not part of the model. For laminates with all plies in 0° -direction the use of a 2D model in combination with a plain strain assumption has been validated in [48]. Testing the applicability of this approach for QI laminates is still an open task and part of this current study.

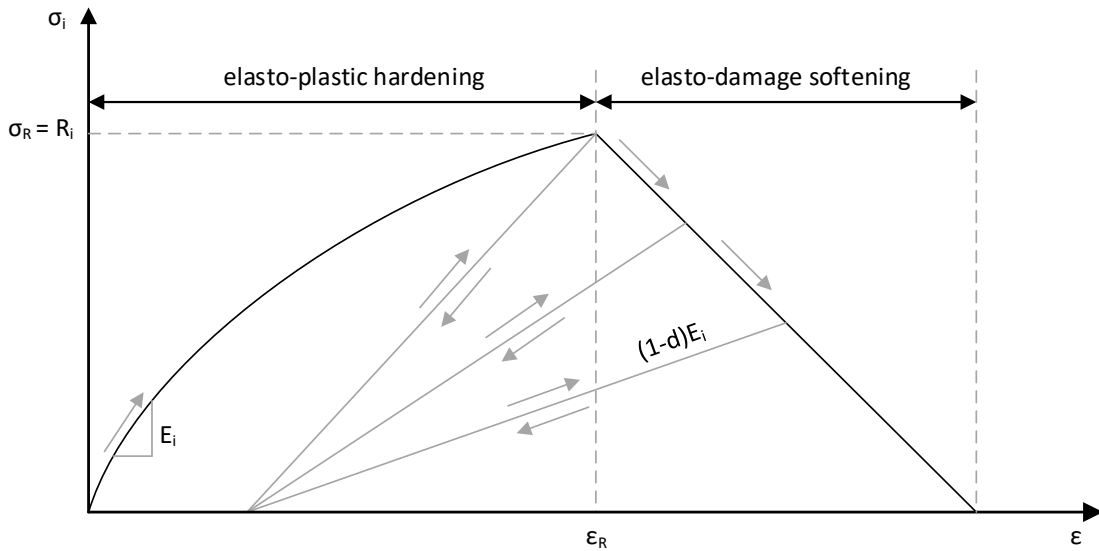


Figure 134. Nonlinear elasto-plastic hardening and elasto-damage softening.

8.1.1. Non-linearity in the elasto-plastic hardening regime

A plasticity model developed by Sun and Chen [273] is implemented to describe the non-linear constitutive behavior of a IM7 unidirectional carbon fiber reinforcement embedded in a 8552 thermosetting epoxy matrix. The plasticity model (plastic potential) is based on a quadratic yield function $f(\sigma_{ij})$, defined in terms of the stress components σ_{ij} in the principal material directions.

The plastic potential is expressed by the general yield function

$$2f = \sigma_{33}^2 + 2a_{66}\sigma_{13}^2 \quad (69)$$

where the material constant a_{66} describes the anisotropy in the plasticity.

The incremental strain $d\varepsilon_{ij}$ can be decomposed into an elastic strain component $d\varepsilon_{ij}^e$ and a plastic strain component $d\varepsilon_{ij}^p$

$$d\varepsilon_{ij} = d\varepsilon_{ij}^e + d\varepsilon_{ij}^p. \quad (70)$$

The in-plane incremental plastic strain components $d\varepsilon_{ij}^p$ are defined in terms of the in-plane yield function f and the plastic multiplier $d\lambda$ via the associated flow rule. Assuming that the longitudinal plastic strain increment $d\varepsilon_{11}^p$ can be neglected since most unidirectional composite materials behave almost linear elastic in longitudinal tension and compression loading [273] the plastic strain component can be described as

8.1 CONSTITUTIVE MATERIAL BEHAVIOR

$$d\varepsilon_{ij}^p = \begin{Bmatrix} d\varepsilon_{11}^p \\ d\varepsilon_{33}^p \\ d\gamma_{13}^p \end{Bmatrix} = \frac{\partial f}{\partial \sigma_{ij}} d\lambda = \begin{Bmatrix} 0 \\ \sigma_{33} \\ 2 a_{66} \sigma_{13} \end{Bmatrix} d\lambda, \quad (71)$$

where γ_{13} denotes the engineering shear strain.

Similarly, the work per unit volume dW performed during elongation $d\varepsilon_{ij}$ can be also decomposed into a reversible elastic work dW^e and an irreversible plastic work dW^p . The incremental plastic work dW^p is defined as

$$dW^p = \sigma_{ij} d\varepsilon_{ij}^p = 2f d\lambda. \quad (72)$$

By introducing the equivalent stress $\bar{\sigma} = \sqrt{3f}$ for the case of a plane stress state, the plastic work increment dW^p can be written as

$$dW^p = \bar{\sigma} d\bar{\varepsilon}^p. \quad (73)$$

Rewriting in terms of the effective plastic strain increment $d\bar{\varepsilon}^p$ leads to

$$d\bar{\varepsilon}^p = \frac{2}{3} \bar{\sigma} d\lambda = \sqrt{\frac{2}{3} (\sigma_{33}^2 + 2a_{66}\sigma_{13}^2)} d\lambda. \quad (74)$$

The incremental plastic stress-strain relation only depends on the values of the plasticity coefficient a_{66} and the plastic multiplier $d\lambda$ which is calculated as

$$d\lambda = \frac{\left(\frac{\partial f}{\partial \sigma}\right)^T \mathbf{C}^0 d\varepsilon}{\frac{4}{9} \bar{\sigma}^2 H_p + \left(\frac{\partial f}{\partial \sigma}\right)^T \mathbf{C}^0 \frac{\partial f}{\partial \sigma}} \quad (75)$$

with the plastic modulus H_p

$$H_p = \frac{d\bar{\sigma}}{d\bar{\varepsilon}^p} = \frac{1}{n_{nl} A_{nl}} \left(\frac{\bar{\varepsilon}^p}{A_{nl}}\right)^{\frac{1-n_{nl}}{n_{nl}}}. \quad (76)$$

H_p is a derivative of the effective stress with respect to the effective plastic strain and using the current effective plastic strain.

Fiber composites are assumed to have no clear yield locus. For this reason, a power law approach can be used to describe the non-linear constitutive behavior in order to fit a master curve of equivalent stress over equivalent strain. The compression and tension regimes must be considered independently of each other.

$$\bar{\boldsymbol{\varepsilon}}^p = A_{nl} \bar{\boldsymbol{\sigma}}^{nl} \quad (77)$$

For a complete description of the non-linear material behavior, the parameter a_{66} must be obtained from off-axis tests (OAT).

In the plane stress state, the prevailing stresses can be indicated as follows

$$\boldsymbol{\sigma} = [\sigma_{11}, \sigma_{33}, \sigma_{13}]^T, \quad (78)$$

with the associated strains

$$\boldsymbol{\varepsilon} = [\varepsilon_{11}, \varepsilon_{33}, \varepsilon_{13}]^T. \quad (79)$$

Assuming a purely elastic material behavior, stress and strain can be related by means of Hook's law (linear elastic material law) by introducing the material stiffness matrix \mathbf{C}^0 , respectively compliance matrix \mathbf{S}^0 .

$$\begin{aligned} \boldsymbol{\sigma} &= \mathbf{C}^0 \boldsymbol{\varepsilon} \\ \boldsymbol{\varepsilon} &= \mathbf{S}^0 \boldsymbol{\sigma} \end{aligned} \quad (80)$$

For the plane stress state, the stiffness matrix C_{ij}^0 can be defined as

$$C_{ij}^0 = \frac{1}{1 - \nu_{13}\nu_{31}} \begin{bmatrix} E_1 & \nu_{31}E_1 & 0 \\ \nu_{13}E_3 & E_3 & 0 \\ 0 & 0 & (1 - \nu_{13}\nu_{31})G_{13} \end{bmatrix}. \quad (81)$$

The corresponding compliance matrix S_{ij}^0 is written as

$$S_{ij}^0 = \begin{bmatrix} \frac{1}{E_1} & -\frac{\nu_{13}}{E_1} & 0 \\ -\frac{\nu_{31}}{E_3} & \frac{1}{E_3} & 0 \\ 0 & 0 & \frac{1}{G_{13}} \end{bmatrix}. \quad (82)$$

8.2. Continuum damage model

8.2.1. Damage variables

In the case of damage progression in the lamina, the constitutive relationship resulting from the progressive damage is considered in the form of a reduction of the stiffness matrix. In this case, a pure elasto-damage is assumed. A damage variable d was introduced in the form of a thermodynamic state variable to determine the damage progression. In the general anisotropic case, the damage of fiber composites

8.2 CONTINUUM DAMAGE MODEL

is described in the form of a 4th order damage tensor \mathbf{D} . In addition, a 4th order damage influence tensor $\mathbf{M}(\mathbf{D})$ is introduced to characterize the damage condition. Applied to the concept of the equivalence of stresses, the effective stresses in the damaged continuum can thus be written as

$$\tilde{\sigma} = \mathbf{M}(\mathbf{D})\sigma \quad (83)$$

with

$$\mathbf{M}(\mathbf{D}) = (\mathbf{I} - \mathbf{D})^{-1} \quad (84)$$

wherein \mathbf{I} represents the 4th order unit tensor. In the case of an uncoupled damage and a unilateral damage propagation in the direction that tears equivalent to the fiber or matrix direction, the damage tensor \mathbf{D} can be written for the plane stress state

$$\mathbf{D} = \begin{bmatrix} d_{11} & 0 & 0 \\ 0 & d_{33} & 0 \\ 0 & 0 & d_{13} \end{bmatrix} = \begin{bmatrix} d_f & 0 & 0 \\ 0 & d_m & 0 \\ 0 & 0 & d_s \end{bmatrix} \quad (85)$$

wherein 1 and 3 denote the fiber and matrix direction, respectively. This allows the damage influence tensor $\mathbf{M}(\mathbf{D})$ to be specified.

$$\mathbf{M}(\mathbf{D}) = \begin{bmatrix} \frac{1}{1-d_{11}} & 0 & 0 \\ 0 & \frac{1}{1-d_{33}} & 0 \\ 0 & 0 & \frac{1}{1-d_{13}} \end{bmatrix} \quad (86)$$

In the case of material damage in the continuum mechanics, the damage variable d is introduced as a thermodynamic state variable. The evolution of the damaged stiffness matrix by internal state variables d are schematically shown in Figure 135 for transverse direction.

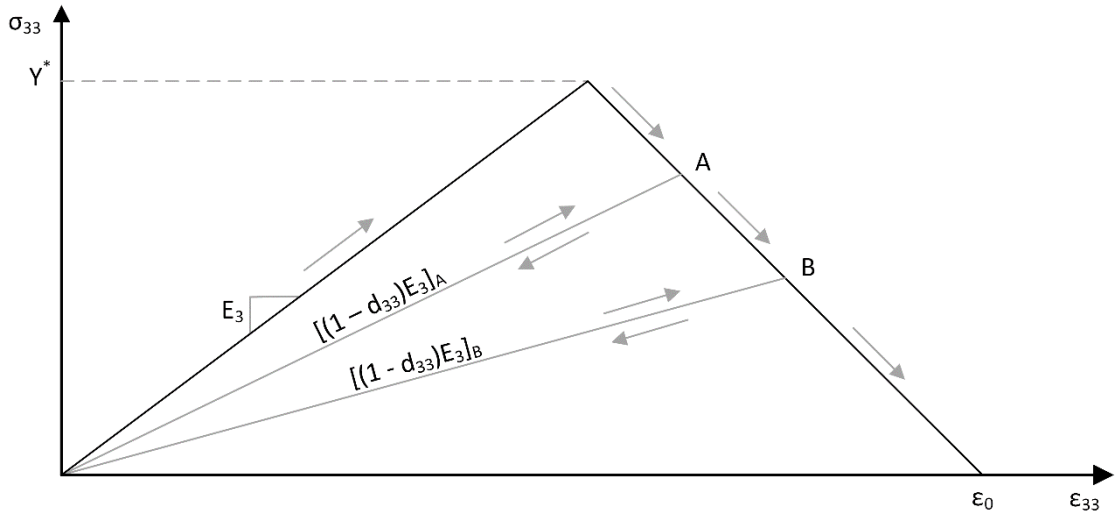


Figure 135. Damaged stiffness matrix by internal state variables d in transverse direction.

The free energy potential f^d can be defined as a function of d . For the damage process free of thermal influence, the following should therefore apply

$$f^d = f^d(\varepsilon_{ij}, d) \quad (87)$$

$$\dot{f}^d = \frac{\partial f^d}{\partial \varepsilon_{ij}} \varepsilon_{ij} + \frac{\partial f^d}{\partial d} \dot{d} \quad (88)$$

$$\Delta = \left(\sigma_{ij} - \frac{\partial f^d}{\partial \varepsilon_{ij}} \right) \varepsilon_{ij} - \frac{\partial f^d}{\partial d} \dot{d} \geq 0. \quad (89)$$

The strain equivalence approach can be used to define

$$\varepsilon = \frac{\tilde{\sigma}}{C^0} = \frac{M(D)\sigma}{C^0} \quad (90)$$

It finally follows for the damaged stiffness matrix $C^d(D)$

$$C^d(D) = M^{-1}(D)C^0 = \begin{bmatrix} \frac{(1-d_{11})E_1}{1 - (1-d_{11})(1-d_{33})\nu_{13}\nu_{31}} & \frac{(1-d_{11})(1-d_{33})\nu_{31}E_1}{1 - (1-d_{11})(1-d_{33})\nu_{13}\nu_{31}} & 0 \\ \frac{(1-d_{11})(1-d_{33})\nu_{13}E_3}{1 - (1-d_{11})(1-d_{33})\nu_{13}\nu_{31}} & \frac{(1-d_{33})E_3}{1 - (1-d_{11})(1-d_{33})\nu_{13}\nu_{31}} & 0 \\ 0 & 0 & (1-d_{13})G_{13} \end{bmatrix} \quad (91)$$

and the elasto-damaged material law

$$\boldsymbol{\sigma}(\mathbf{D}) = \mathbf{C}^d(\mathbf{D})\boldsymbol{\varepsilon}. \quad (92)$$

The damaged compliance matrix $\mathbf{S}^d(\mathbf{D})$ results equivalent to

$$\mathbf{S}^d(\mathbf{D}) = \mathbf{M}(\mathbf{D})\mathbf{S}^0 = \begin{bmatrix} \frac{1}{(1-d_{11})E_1} & -\frac{\nu_{13}}{E_1} & 0 \\ -\frac{\nu_{31}}{E_3} & \frac{1}{(1-d_{33})E_3} & 0 \\ 0 & 0 & \frac{1}{(1-d_{13})G_{13}} \end{bmatrix}. \quad (93)$$

The dissipation inequality for the damaged material behavior results in two conditions. According to Coleman and Gurtin [274], it applies as for the undamaged material

$$\sigma_{ij}(d_{ij}) = \frac{\partial f^d}{\partial \varepsilon_{ij}}. \quad (94)$$

Thus, the following condition can be derived from the dissipation inequality, which must be fulfilled for the inequality to apply

$$-\frac{\partial f^d}{\partial D} \dot{D} \geq 0. \quad (95)$$

The term $\frac{\partial f^d}{\partial D}$ corresponds to the energy release as a result of progressive damage to the material. This term is called energy release rate Y and an energetically conjugated quantity of the damage variable.

$$Y(\boldsymbol{\varepsilon}, \mathbf{D}) = \frac{\partial f^d}{\partial D} \quad (96)$$

$Y\dot{D}$ describes the energy dissipation rate in the material, where Y is the thermodynamic force and \dot{D} is the thermodynamic flow.

8.2.2. Damage initiation

For the damage initiation the well-established Puck criterion [80] is used. The individual failure modes defined by Puck determine the progress of the damage.

Fiber failure under tension $\bar{\sigma}_1 \geq 0$

$$f_{EFF}^t(\bar{\sigma}_1) = \frac{\bar{\sigma}_1}{R_{\parallel}^t} \leq 0 \quad (97)$$

Fiber failure under compression $\bar{\sigma}_1 < 0$

$$f_{EFF}^c(\bar{\sigma}_1) = \frac{\bar{\sigma}_1}{(-R_{\parallel}^c)} \leq 0 \quad (98)$$

Inter-fiber failure under tension $\bar{\sigma}_3 \geq 0$ (Mode A)

$$f_{IFF}^t(\bar{\sigma}_3, \bar{\tau}_{31}) = \sqrt{\left[\left(\frac{1}{R_{\perp}^t} - \frac{p_{\perp\parallel}^t}{R_{\perp\parallel}^t}\right)\bar{\sigma}_3\right]^2 + \left(\frac{\bar{\tau}_{31}}{R_{\perp\parallel}^t}\right)^2} + \frac{p_{\perp\parallel}^t}{R_{\perp\parallel}^t}\bar{\sigma}_3 \leq 0 \quad (99)$$

Inter-fiber failure under compression $\bar{\sigma}_3 < 0$ (Mode B)

$$f_{IFF}^c(\bar{\sigma}_3, \bar{\tau}_{31}) = \sqrt{\left(\frac{p_{\perp\parallel}^c}{R_{\perp\parallel}^c}\bar{\sigma}_3\right)^2 + \left(\frac{\bar{\tau}_{31}}{R_{\perp\parallel}^c}\right)^2} + \frac{p_{\perp\parallel}^c}{R_{\perp\parallel}^c}\bar{\sigma}_3 \leq 0 \quad (100)$$

Inter-fiber failure under compression $\bar{\sigma}_3 < 0$ (Mode C)

$$f_{IFF}^c(\bar{\sigma}_3, \bar{\tau}_{31}) = \left[\left(\frac{\bar{\tau}_{31}}{2(1 + p_{\perp\perp}^c)R_{\perp\parallel}^c}\right)^2 + \left(\frac{\bar{\sigma}_3}{R_{\perp}^c}\right)^2 \right] \frac{R_{\perp}^c}{-\bar{\sigma}_3} \leq 0 \quad (101)$$

8.2.3. Damage evolution law

The components of the damage tensor D , i.e. d_{11} , d_{33} , d_{13} , individually degrade the longitudinal, transverse and shear stiffness, respectively. Since the effects of the damage behave differently under compressive or tensile loading, a total of 5 different damage variables must be determined ($d_{11}^t, d_{11}^c, d_{33}^t, d_{33}^c, d_{13}$). For simplification, linear approaches for the damage evolution are applied.

The linear approach for the constitutive relationship of the material in the softening regime results in

$$\sigma(\varepsilon) = \sigma_R - K(\varepsilon - \varepsilon_0) \quad (102)$$

where K characterizes the descent in the softening regime.

8.2 CONTINUUM DAMAGE MODEL

The damage evolution law is based on the concept of effective stresses in the context of strain equivalence as shown in Figure 136. The approach applies to uniaxial stress, where f_{E_i} is the stress exposure related to a stress state in the undamaged continua.

$$d_i = 1 + \frac{K_i}{E_i} - \frac{1}{(f_{E(\tilde{\sigma})})_i} \left(1 + \frac{K_i}{E_i} \right) \quad i = [11^t, 11^c, 33^t, 33^c, 13] \quad (103)$$

This definition is used to determine the damage progression as a function of the effective stresses.

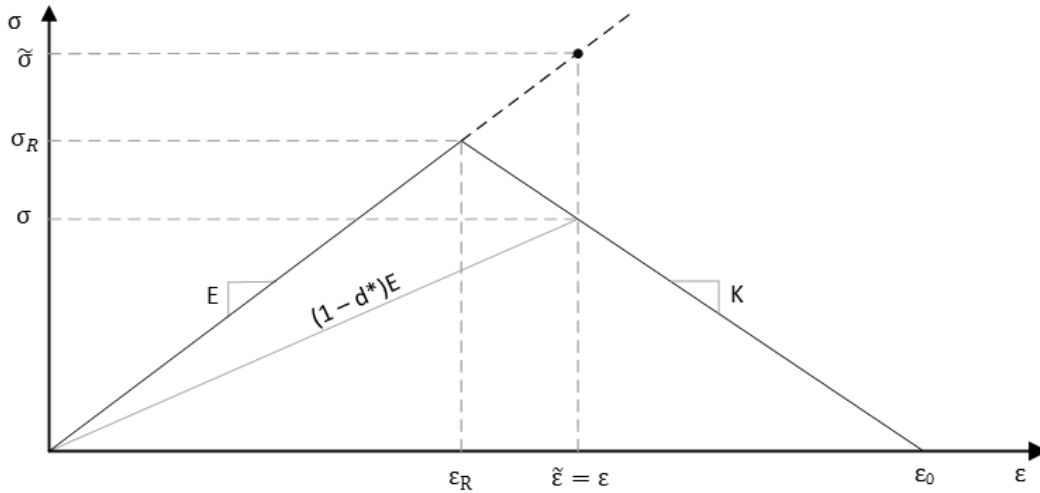


Figure 136. Damage evolution law based on effective stresses and equivalence of strains.

8.2.4. Energy consideration and element size regularization

In continuum damage approaches the damage is represented non-locally, i.e. related to a unit volume (continuum) homogenized in the constitutive relationship. For a better understanding, the non-local energy (i.e. the area under the stress-strain curve) should be defined as follows when considering the damage:

$$W_f = \int \dot{w}_e(\boldsymbol{\varepsilon}, \mathbf{D}) \quad (104)$$

This non-local energy cannot be determined experimentally, so it is not possible to evaluate the equation to determine a damage rate.

Due to the brittle fracture behavior of fiber composites, the formation of macro-cracks due to diffuse micro-damages takes place in a relatively narrow specific area known as the crack process zone (CPZ), shown in Figure 137.

The aim of the numerical damage analysis, which leads to the failure of a composite structure, is the exact physically correct representation of the diffuse damage phenomena. These occur on a microstructural level. This includes

microstructural crack initiation at pores or fiber-matrix interfaces, as well as crack nucleation and crack growth processes up to the formation of macrocracks. As described, the effects of the localized microstructural processes are described by a continuum damage model, which considers a smeared process zone. These narrow, local zones of concentrated growing microcracks and defects can be modelled by different approaches. These can be differentiated by their kinematic description of the displacement or strain field. One possibility, for example, is the representation of the process zone in the form of a curve (3D surface) on which the displacement field shows a jump. An X-FEM approach, for example, is part of this modeling option. By modeling this displacement jump, it is necessary to know the crack front in advance, because for example a node must be doubled, in order to separate it.

A second possibility, which is applied here, is the representation over a delimited band, in which the displacement runs continuously, but the strain field in this area shows a discontinuity. This area forms a band of deforming material separated from the surrounding material. In a FE analysis it is now useful to consider the width of this band relative to the given mesh. The approach equates the width of the band with the width of an element.

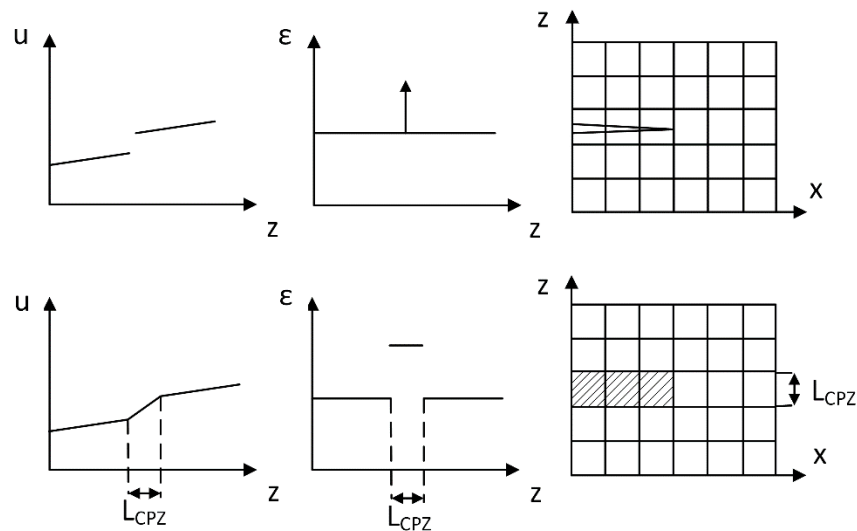


Figure 137. Crack propagation zone.

For example, at notches or holes local discontinuities (strain locality) may occur, which must be smeared in a continuum damage approach, since they often play a decisive role for the failure behavior of the component. This leads to numerical problems, such as a strong dependence on the discretization of the mesh.

Approaches which want to consider the real existing strain or stress controlled softening of the material by a direct mapping of the stress-strain curve are not able to consider stress localizations (at the notch bottom an elastic calculation strives for infinite stresses) and thus causing a strong mesh dependency in the numerical analysis.

8.2 CONTINUUM DAMAGE MODEL

W_f , shown in Figure 138, is the "smeared" energy density per unit volume of the crack process zone.

$$W_f = \int \sigma_{33} \dot{\varepsilon}_{33} = \frac{1}{2} Y^* \varepsilon_0 \quad (105)$$

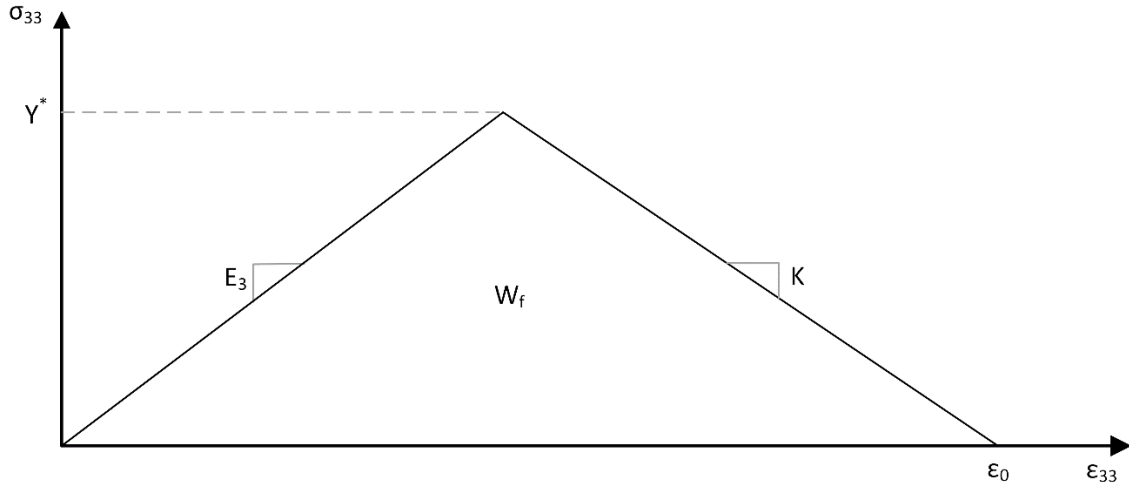


Figure 138. Smeared energy density per unit volume.

This specific energy thus represents the strain energy available for each element volume. This energy corresponds to the complete area under the stress-strain diagram, or the dissipated energy up to the complete deterioration of the material per unit volume. The formation of microdefects in a single layer takes place locally in the direction of the crack front. Here it shall be assumed that the microdefect is orthogonal to the z -axis. It can be assumed that the microcrack nucleation and crack opening processes induce an additional (crack) strain ε_f in the z -direction (Figure 139 and Eqn. (106)), with δ_f being the crack opening displacement and L_{CPZ} the length of the crack propagation zone.

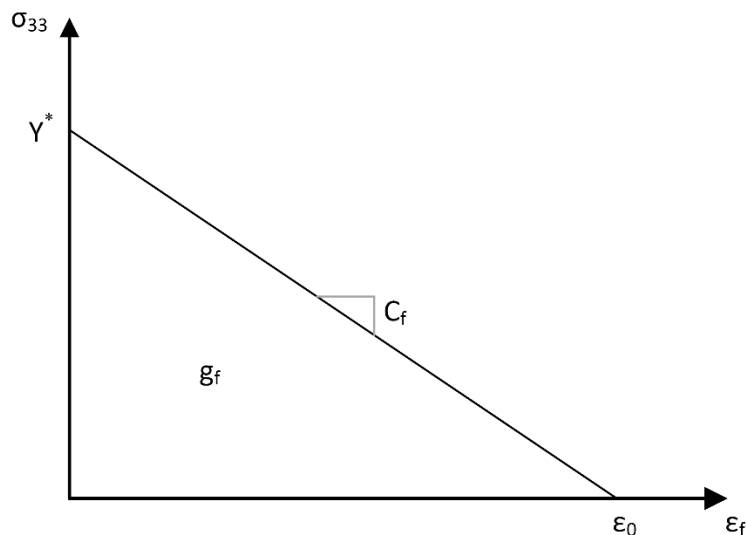


Figure 139. Dissipated energy for crack development due to microcrack nucleation and crack opening processes which induce an additional (crack) strain ε_f in the z -direction.

$$\varepsilon_f = \frac{\delta_f}{L_{CPZ}} = \frac{1}{C_f} (Y^* - \sigma_{33}) = \varepsilon_0 - \frac{\sigma_{33}}{C_f} \quad (106)$$

This results in the following constitutive relationship of the material for the softening area:

$$\begin{pmatrix} \varepsilon_{11} \\ \varepsilon_{33} \\ \varepsilon_{13} \end{pmatrix} = \begin{bmatrix} \frac{1}{E_1} & -\frac{\nu_{13}}{E_1} & 0 \\ -\frac{\nu_{31}}{E_3} & \frac{1}{E_3} - \frac{1}{C_f} & 0 \\ 0 & 0 & \frac{1}{G_{13}} \end{bmatrix} \begin{pmatrix} \sigma_{11} \\ \sigma_{33} \\ \sigma_{13} \end{pmatrix} + \begin{pmatrix} 0 \\ \varepsilon_0 \\ 0 \end{pmatrix} \quad (107)$$

and the increase for the softening regime:

$$\frac{1}{K} = \frac{1}{E_3} - \frac{1}{C_f} \quad (108)$$

The consideration of the fracture energy leads to the following relationship:

$$G_f = g_f L_{CPZ} = L_{CPZ} \int \sigma_{33} \dot{\varepsilon}_f = \frac{1}{2} C_f (\varepsilon_f)^2 L_{CPZ} = \frac{(Y^*)^2}{2C_f} L_{CPZ} \quad (109)$$

$$G_f = \frac{1}{2} \left(\frac{1}{E_3} - \frac{1}{K} \right) (Y^*)^2 L_{CPZ} \quad (110)$$

$$G_f = \frac{1}{2} (Y^* \varepsilon_0) L_{CPZ} \quad (111)$$

In order to enable a relationship between the non-local definition of the continuum damage approach and the local definition of crack formation, the following relationship can be established. The product of the energy density per unit volume with the specific width of the crack process zone corresponds to the fracture energy resulting from the formation of the stress-free crack. In other words, the dissipated energy for the complete deterioration of the material in terms of a unit volume is equal to the dissipated energy for crack development in terms of a unit area.

$$G_f = g_f L_{CPZ} \quad (112)$$

Since the quantities in this equation, i.e. fracture energy and the width of the crack process zone, represent all intrinsic material parameters, the numerical FE consideration would have to be discretized in such a way that the element size corresponds to the intrinsic width of the crack process zone. In the consideration of

8.3 FINITE ELEMENT MODEL

damage processes of fiber composite materials this procedure is not useful. Since the material behavior is not isotropic, for example, an element should be able to map the width of both matrix and fiber breakage, which should be constant over the entire structure under investigation. In addition, the physical width would have to correspond exactly to the numerical element width. Such a method is not appropriate, which is why an approach for regularization is necessary. For this purpose, a new mesh-related width parameter l^* is introduced, which is no longer bound to the physical width of the crack process zone, but represents a regularized numerically defined quantity. By adjusting the area under the stress-strain curve, a dissipated energy in the failed element is obtained as a function of the ratio of physical crack zone width and numerical characteristic element length. It can also be defined that the localization of the strain band is smeared to the element size. The adaptation is done by the relation:

$$W_f = \frac{G_f}{l^*} \quad (113)$$

$$G_f = \frac{1}{2} \left(\frac{1}{E_3} - \frac{1}{K} \right) (Y^*)^2 l^* \quad (114)$$

Both strength and stiffness in the hardening area are independent material parameters. The fracture energy should serve as an intrinsic input parameter. An element size regularization is thus carried out by adjusting the descent in the softening area.

$$K = \frac{E_3 (Y^*)^2 l^*}{(Y^*)^2 l^* - 2G_f E_3} \quad (115)$$

Mode I and II fracture toughness can be empirically determined by material tests using a DCB and ENF test, respectively [275].

The thermodynamic equations provide both the constitutive material behavior as well as the condition that the damage must be irreversible as a result of the evaluation of the Clausius-Duheme inequality $\dot{d} \geq 0$. However, the thermodynamic framework equations do not provide any information about the development laws of the internal state variables. An approach for the evolution of damage must therefore be found.

8.3. Finite element model

The finite element model of both the 15° off-axis tests and wavy geometries, experimental part described in Section 5, are modeled with reduced integration plain strain elements (CPE4R) including hourglass control to avoid zero energy modes. For parameter studies a python script was written to automatically build up FE models with varying parameters, e.g. amplitude, wavelength and laminate thickness. The material model described in Section 2 was implemented as a material user-subroutine

VUMAT in ABAQUS/Explicit [276]. A representative FE model of a wavy specimen including boundary conditions and loading is shown in Figure 140. For better visualization, a coarse mesh is shown. Prior to the numerical simulations, a mesh size study was carried out and 35-40 elements in thickness direction were found to be sufficient. Simulation results of the two wave configurations (wave 1 and 2) were compared with experimental test data. A parameter study was carried out for varying amplitudes ($0.1A-2A$), laminate thicknesses ($0.5A-6A$), where A denotes the baseline amplitude of 1.19 mm, and wavelengths (13.45-41.35 mm). For modelling quasi-isotropic layups with the 2D approach the material properties were transformed for each orientation according to classical laminate theory and applied to the corresponding layers.

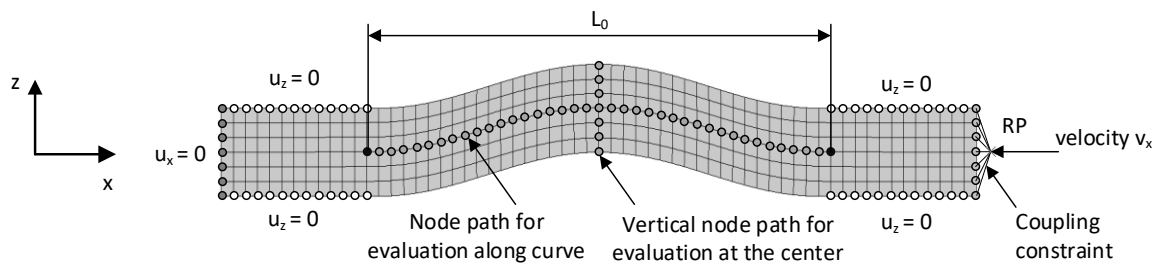


Figure 140. Representative FE model of wavy compression specimen showing node sets for boundary conditions, loading and evaluation.

The material properties of IM7-8552 carbon fiber reinforced epoxy matrix prepreg used for the simulations are given in Table 17. Most simulations were carried out before experimental tests, therefore material parameter from literature were used. These values are consistent with our tested values (c.f. Table 17 and Table 13).

Table 17. Material properties for IM7-8552 used for the simulations.

Longitudinal stiffness	E_1	171.42	[GPa]	[238]
Transverse stiffness	$E_2 = E_3$	9.08	[GPa]	[238]
Poisson's ratio	$\nu_{12} = \nu_{13}$	0.32	[-]	[238]
	ν_{23}	0.43	[-]	[238]
Shear stiffness	$G_{12} = G_{13}$	5.29	[GPa]	[238]
	G_{23}	3.98	[GPa]	[238]
Longitudinal tension strength	R_{\parallel}^t	2326.2	[MPa]	[238]
Longitudinal compression strength	R_{\parallel}^c	1200.1	[MPa]	[238]
Transverse tension strength	R_{\perp}^t	62.3	[MPa]	[238]
Transverse compression strength	R_{\perp}^c	255	[MPa]	[277]
Shear strength	$R_{\perp\parallel}$	86	[MPa]	[278]
Inclination parameter	$p_{\perp\parallel}^t$	0.35	[-]	[279]
Inclination parameter	$p_{\perp\parallel}^c$	0.35	[-]	[279]
Fracture energy in longitudinal tension	G_{\parallel}^t	133	[kJ/m ²]	*
Fracture energy in longitudinal compression	G_{\parallel}^c	150	[kJ/m ²]	*
Fracture energy in transversal tension	G_{\perp}^t	0.277	[kJ/m ²]	[238]

8.4 RESULTS AND DISCUSSION

Fracture energy in transversal compression	G_{\perp}^c	1.31	[kJ/m ²]	[280]
Fracture energy in in-plane shear	$G_{\perp\parallel}$	0.79	[kJ/m ²]	*
Parameter for non-linearity model	a_{66}	2.2		**
Parameter for non-linearity model	A_{nl}	1.2E-14		**
Parameter for non-linearity model	n_{nl}	4.8		**

* Assumed values

** Obtained from experimental data in accordance with [277,281]

8.4. Results and discussion

8.4.1. Model validation

Off-axis tension tests are carried out to determine material parameter needed to describe the nonlinear behavior in combined transverse tension and in-plane shear. According to Körber [277], 15° off-axis specimens are most suitable for the determination of shear properties. In off-axis tests with straight end tabs, it was found that the extension-shear coupling leads to significant stress concentrations near the clamping regions and to a non-uniform strain field. To avoid this, oblique end-tabs were used as proposed by Sun and Chung [282]. The stress-strain response from both simulation and test data for 15° off-axis tensile tests is shown in Figure 141.

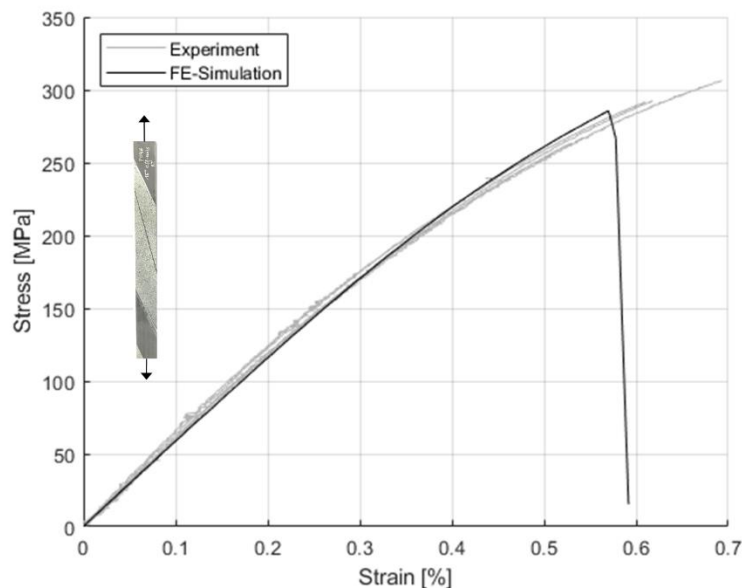


Figure 141. Experimental and FE analysis results for 15° off-axis tensile test (OAT)

The numerical model is able to match the nonlinear material behavior and the damage initiation properly. However, the resulting failure strain/stress was typically too low, thus our model serves as a conservative estimate. Remote stress-strain curves stemming from simulation and experimental results are shown for wave 1 and wave 2 under compressive loading in Figure 142 and Figure 143, respectively. The shear strain

distribution for wave 1 shows excellent agreement of numerical and experimental results. The global stress-strain relationship for wave 2, including the onset of failure, location and failure pattern shows excellent agreement of simulation and test data.

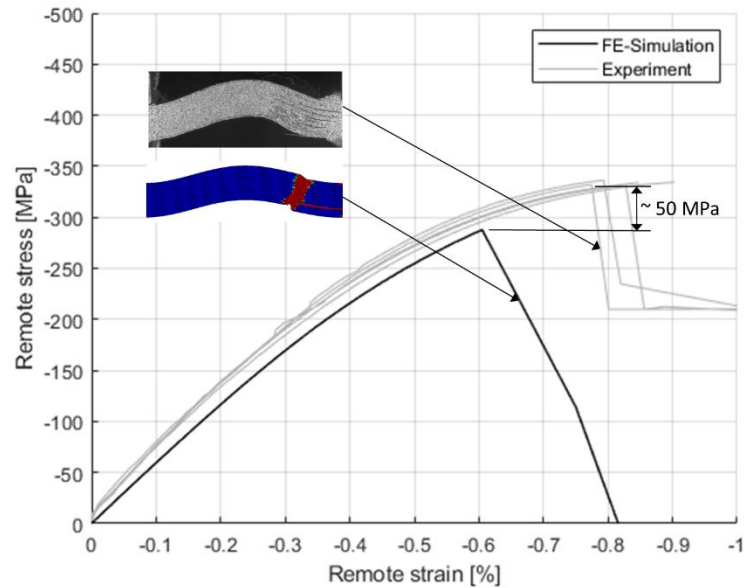


Figure 142. Experimental and FE analysis results for wave 1 with UD laminate under compression ($A = 1.19$ mm, $L = 27.9$ mm, $t = 5.1$ mm).

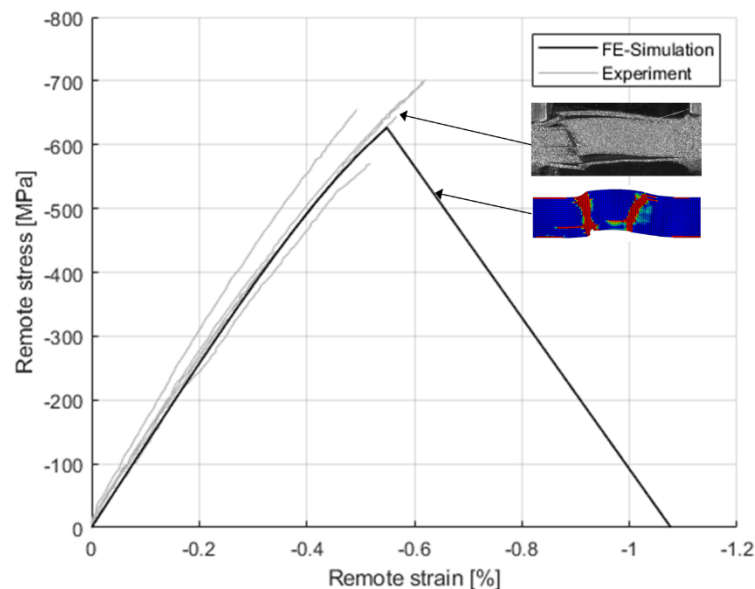


Figure 143. Experimental and FE analysis results for wave 2 with UD laminate under compression ($A = 0.29$ mm, $L = 14.5$ mm, $t = 5.1$ mm).

The typical failure mechanism of a narrow kink-band formation due to matrix yield under compressive loading are indicated at locations of maximum inclinations. The non-linear stress-strain response is increased at higher remote strains. In Figure 142 a slightly conservative damage initiation at approximately 50 MPa below test results is probably due to the use of stress-based failure criteria. When the stress-strain

8.4 RESULTS AND DISCUSSION

curve becomes strongly nonlinear and reaching a plateau, the exact point of damage initiation is more difficult to find. A slight increase in stress leads to a considerable increase in elongation, thus strain-based criteria might be advantageous. The numerical model result is compared with experimental results, determined by digital image correlation (DIC), by comparing the shear strain distribution along the center line of the wave in Figure 144.

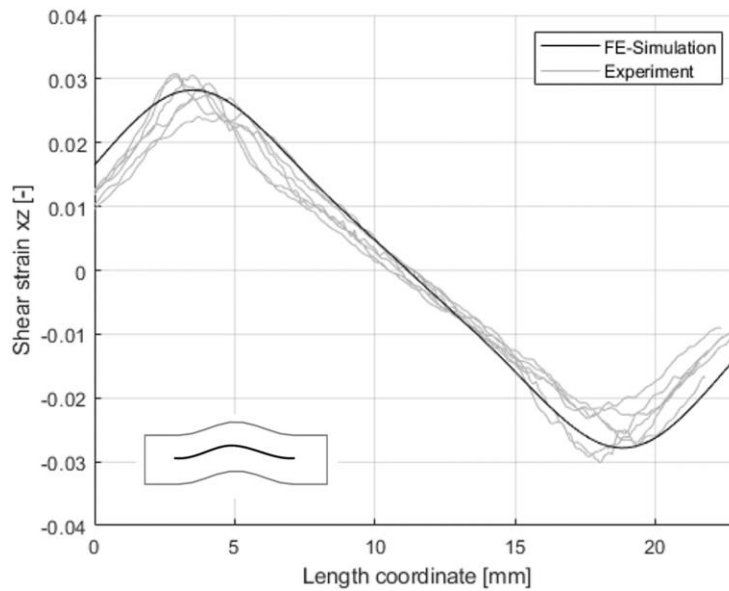


Figure 144. Shear strain ε_{xz} of wave 1 with UD laminate under compression - along curve.

The axial strain ε_x from our simulations and the DIC measurements evaluated along a centered path vertical to the loading direction shows good agreement of numerical and experimental data for both wave configurations with UD laminate in Figure 145 and Figure 146.

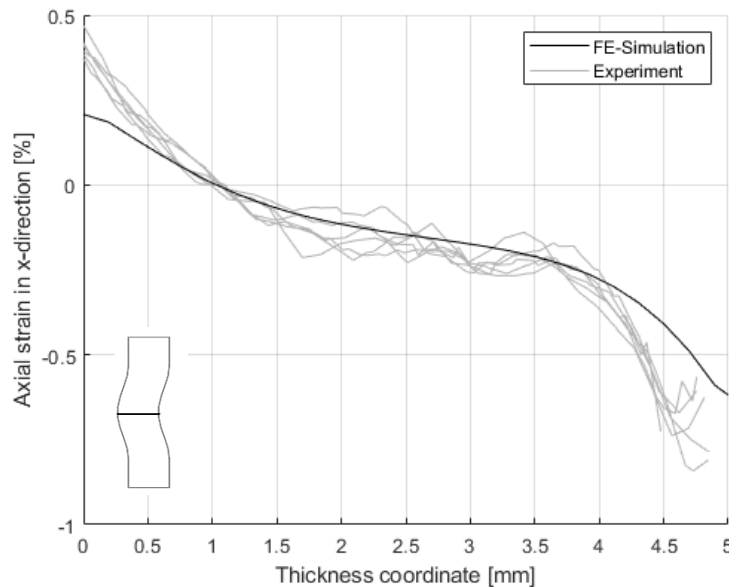


Figure 145. Axial strain in x-direction ε_x of wave 1 with UD laminate under compression - center line.

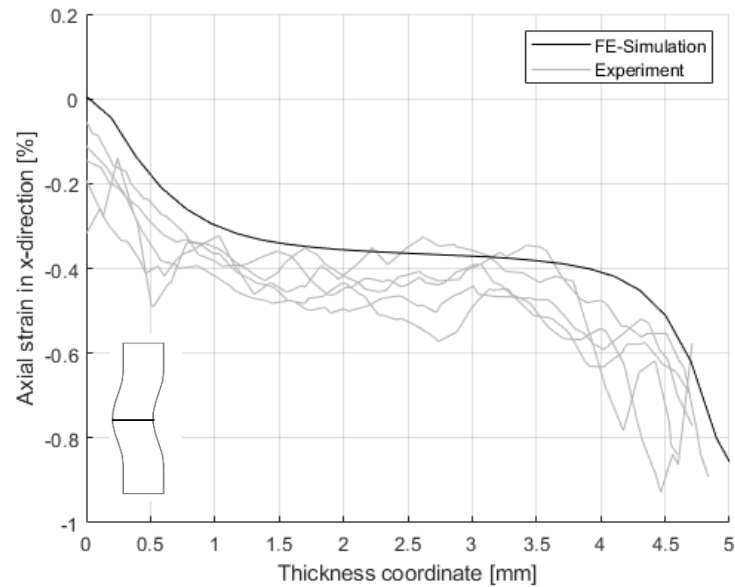


Figure 146. Axial strain in x-direction ε_x of wave 2 with UD laminate under compression - center line.

To evaluate the applicability and limitations of the implemented 2D continuum damage model for more complex materials, it is applied for wave 2 under compressive loading for a quasi-isotropic laminate $(0/45/-45/90)_{5s}$. The global stress-strain response, shown in Figure 147, can only be reproduced insufficiently. The resulting complex 3D stress state leads to a complex failure behavior of QI laminates that cannot be represented by the 2D model, due to neglecting the stress components in y-direction. However, the resulting failure mode as well as the correct location for damage onset were detected correctly at the center of the wave. For the simulation of QI laminates, the model can merely be used as an engineering estimation of the material properties and a qualitative assessment of failure. Therefore, for analyzing QI laminates containing fiber waviness an extension to a three-dimensional model which incorporates nonlinearity parameter for various ply orientations, fiber rotation and cohesive layers for modeling delamination is suggested.

8.4 RESULTS AND DISCUSSION

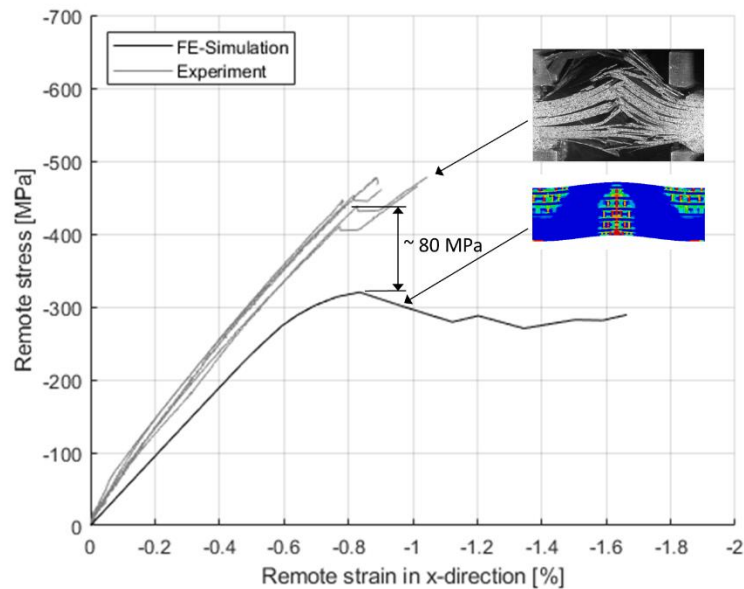


Figure 147. Experimental and FE analysis results for wave 2 with QI laminate under compression ($A = 0.29$ mm, $L = 14.5$ mm, $t = 5.1$ mm).

8.4.2. *Virtual testing*

The model has been successfully validated for UD materials. To reduce the effort of physical testing the model is applied for studying the influence of varying parameters, e.g. amplitudes A , thicknesses t and wavelengths L , in the sense of a virtual test approach. The considerable influence of laminate thickness on the failure behavior has already been described in Section 4.1. The virtual testing results, shown in Figure 148, illustrate the shift from failure dominated by bending stresses to the formation of kink bands with increasing laminate thickness. This confirms our statement, that for lower A/t ratios the testing regime represents a test at material level, whereas the failure behavior above a certain threshold for A/t ratios is strongly influenced by introduced bending moments, thus representing a test on structural level. This results in a pronounced non-linearity in the stress-strain curve of thin laminates (e.g. $t=0.5A$ and $t=1A$) due to the influence of the geometry (geometrical non-linearity).

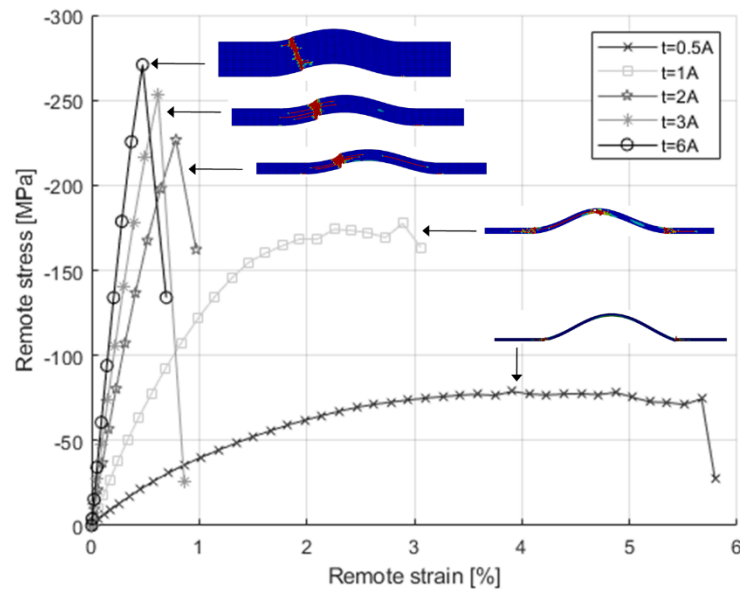


Figure 148. Stress-strain relationship for wavy specimen ($A = 1.19$ mm, $L = 27.9$ mm) with UD laminate and varying thickness using implemented non-linear VUMAT (Puck).

Figure 149 shows the global stress-strain response of compression loaded waviness with varying amplitudes and constant thickness ($t=7.14$ mm) and wavelength ($L=27.9$ mm). Even minor fiber deviations associated with the amplitude lead to a drastic reduction of the mechanical properties, which is known from transformation relations for engineering constants as a function of different fiber orientations [283]. According to that, simulation results show the relative reduction of the stiffness to be smaller at higher amplitudes.

The results from FE simulations of waves with varying wavelength and constant amplitude ($A=1.19$ mm) and thickness ($t=7.14$ mm), shown in Figure 150. The relative drop in compressive strength from $L=41.35$ mm to $L=13.45$ mm is $\sim 46\%$. However, compared to a planar reference specimen those specimens show a reduction of 76% ($L=41.35$ mm) and 87% ($L=13.45$ mm, thus only a 11% absolute difference. This confirms to Lemanski and Sutcliffe [53], who stated that the effect of defect length is relatively small in this configuration.

8.5 CONCLUSION ON THE NUMERICAL SIMULATION

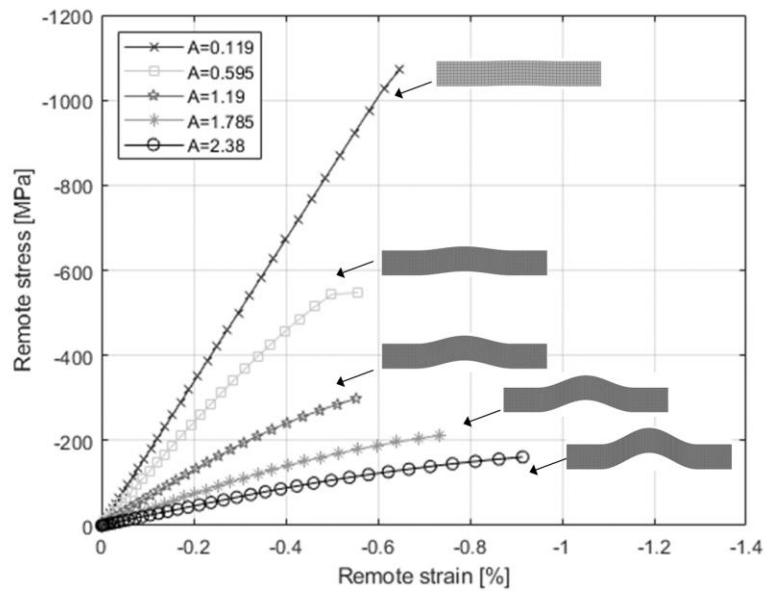


Figure 149. Stress-strain relationship for wavy specimen ($t = 7.14$ mm, $L = 27.9$ mm) with UD laminate and varying amplitude using implemented non-linear VUMAT (Puck).

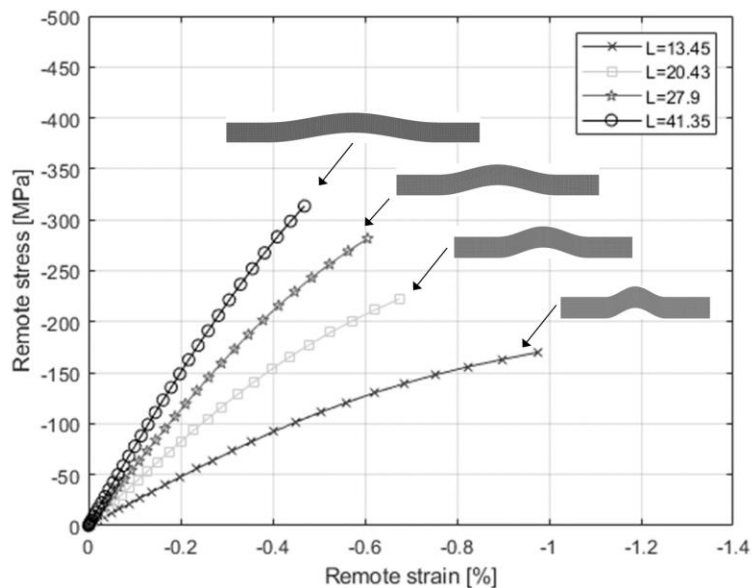


Figure 150. Stress-strain relationship for wavy specimen ($A = 1.19$ mm, $t = 7.14$ mm) with UD laminate and varying wavelength using implemented non-linear VUMAT (Puck).

8.5. Conclusion on the numerical simulation

The mechanical behavior and damage initiation for two wave configurations with UD and QI laminates was successfully tested and simulated under compressive and tensile loading. The understanding of intrinsic material behavior of fiber reinforced composite materials on microscopic level up to macroscopic or structural level is of

crucial importance for the development of suitable material laws for numerical modeling and for a deeper understanding of deformation and damage mechanisms. On top of that, understanding the material behavior of wavy composites is of vital importance for further cost and weight savings. The implemented nonlinear material model was able to capture the material behavior including shear nonlinearities, failure initiation and propagation in unidirectional laminates reasonably accurate. Overall, our results suggest that, depending on the laminate configuration (amplitude, wavelength, thickness) inter-laminar shear failure is the dominant failure mechanism followed by mode I delamination and layer-wise buckling. The nonlinear shear behavior under compressive loading increases with the severity of present fiber waviness and, therefore, plays a dominant role for the initiation and propagation of the failure mechanisms. For wave configurations with a lower amplitude-to-thickness ratio fiber kinking is the dominant failure mechanism under compression loading. The observed formation of a shear kink-band under compression and shear stress (experimental results shown in Section 5 in Figure 95 b) is caused by local fiber buckling, induced by misaligned fibers in the UD materials that continue to rotate under load. In this work, the significant influence of laminate thickness was shown, which has been rarely considered in both industrial practice and academic research so far. The failure behavior for lower amplitude-to-thickness ratios is more determined by the material properties, whereas higher amplitude-to-thickness ratios lead to a higher influence of the geometry due to bending. For this reason, it is suggested to consider the amplitude-to-thickness ratio (A/t) in addition to the commonly used ratio of amplitude-to-wavelength (A/L) for further assessment strategies of fiber waviness. The validity of the model applies for quasi-static loaded unidirectional laminates only. For multidirectional laminates an extension from 2D to 3D is necessary to incorporate the complex 3D stress state.

9. SUMMARY AND CONCLUSIONS

This thesis deals with the versatile topic of fiber waviness in composite materials. For decades, numerous researchers have been working on the understanding of manufacturing origins, non-destructive detection and mechanical effects of fiber waviness. Nevertheless, there is still great uncertainty, especially in the assessment of fiber waviness in view of its influence on the mechanical properties. In the traditionally conservative aerospace industry, in addition to the generally high safety factors, very high knock-down factors are commonly used when it comes to the assessment of manufacturing or in-service defects.

Research question 1: What are the characteristic cases of out-of-plane fiber waviness in industrial applications?

As an introduction to the topic of fiber waviness and to emphasize the importance of understanding the nature of fiber waviness, an overview of various types of out-of-plane fiber waviness (wrinkles) and their origins have been presented in this thesis. Regardless of whether one is dealing with fiber waviness in composite materials from the perspective of a manufacturing engineer or of a part designer, it is essential to have an in-depth understanding of their formation mechanisms. In this thesis, the numerous factors that affect the occurrence of fiber waviness, i.e. process parameters (e.g. temperature, pressure and deformation rate), the selection of the fiber and tooling material and its properties (e.g. CTE) as well as the complexity of the geometry of the final component, are discussed. These influencing parameters often exhibit mutual dependencies and a distinct assignment of a resulting waviness to a specific origin has shown to be difficult. By considering and understanding the numerous mechanisms identified in this thesis, their occurrence can be reduced or, in the best case, completely avoided at an early stage of the product and process development. It is advised to pay great attention at this stage, as further costs for extensive inspection, mechanical assessment or rejected parts can be reduced at this stage.

Research question 2: How can these resulting wrinkles be classified?

Since the characteristics of fiber waviness can be very different, and therefore also their distinctive measurement signals from non-destructive testing and their resulting mechanical properties, a classification scheme was developed. It was found, that different types of waviness can be classified by ten characteristic features, i.e. the number and distribution of waves, a constant or changing wave amplitude, phase characteristics of the wave form, the visibility of the waves, dimensional characteristics, continuity of layers/laminate, portion and position of the wavy region in the laminate, phase characteristics of the material, influence of t/A ratio, and the geometric position of the wavy region in the part. This classification scheme is

intended to serve as a reference framework for future studies on fiber waviness in order to better compare and classify studies of similarly pronounced waves.

Research question 3: Besides ultrasonic testing (UT), which is the standard non-destructive testing (NDT) method used in the aviation industry, are there other NDT methods available, that could provide a better detectability and characterization of out-of-plane fiber waviness?

For safety and performance reasons, the non-destructive detection and evaluation represents an important necessity for the employment of defect-free components for high-performance applications. The NDT&E of composite materials containing embedded out-of-plane fiber waviness has been investigated by conducting various non-destructive tests. The results have shown great potential for the “simple” detection of fiber waviness. However, for a reliable assessment of fiber waviness, only the detection is not sufficient. The wave morphology has to be characterized as precisely as possible. Results from the conducted methods, i.e. ultrasonic testing, acoustic microscopy, infrared thermography, digital shearography and eddy current testing, indicate the possibility of estimating the characteristics of the fiber waviness, i.e. amplitude and wavelength, from the strength of the signal. However, the active thermography and digital shearography have shown to be the most promising methods for industrial application as alternatives to ultrasonic testing. The wavelength has shown to be more easily determined by the conducted NDT methods. Nevertheless, for a subsequent evaluation of the structural integrity, mechanical experiments and numerical simulations that were carried out in this thesis, have shown that the amplitude has greater influence on a decreased mechanical performance and is therefore a more important parameter than the wavelength. Accompanying finite element simulations of the performed infrared thermography and digital shearography tests, have given additional insight into the physics of the test methods applied on fiber waviness. However, due to the various types and characteristics of fiber waviness that can occur in composite manufacturing processes, a general statement on the detectability is not permissible at this point, as different types of waves are expected to behave different and result in different signals. The presented results and statements in this thesis are therefore valid for the investigated type of waviness, i.e. graded out-of-plane fiber waviness, which are completely embedded in the laminate. The results provide a good basis for the determination of the characteristics of embedded fiber waviness, i.e. amplitude, wavelength and depth in the laminate. Moreover, the promising results point out the huge potential of these NDT methods for further research and applications in industry.

Research question 4: How large is the influence of the determined parameters, such as amplitude, wavelength, inclination, thickness, ply lay-up, etc., on the stiffness and strength of the laminate and what are the mutual dependencies between the parameters?

The knowledge of the intrinsic material behavior is of crucial importance for the development of suitable material laws for numerical modeling and analytical stiffness and strength calculations of out-of-plane fiber waviness. For the investigation of the effects of fiber waviness on the mechanical properties, a wavy specimen's geometry with varying amplitudes and wavelengths has been developed. The mechanical behavior and damage initiation for two wave configurations with UD and QI laminates under compressive and tensile loading have been successfully tested and simulated. In general, the global elastic properties are significantly influenced by increasing A/L ratio. The Young's modulus E_x in the longitudinal direction is most severely affected. The influence of graded fiber waviness is less than that of uniform fiber waviness, as a lower proportion of fibers are misaligned. The results further suggest that, depending on the laminate configuration (amplitude, wavelength, thickness) inter-laminar shear failure is the dominant failure mechanism followed by mode I delamination and layer-wise buckling. For wave configurations with a lower amplitude-to-thickness ratio fiber kinking is the dominant failure mechanism under compression loading. The observed formation of a shear kink-band under compression and shear stress is caused by local fiber buckling which is induced by misaligned fibers in the UD materials that continue to rotate under load. The stress/strain analysis (numerical, analytical and experimental) has shown that fiber waviness leads to local shear stresses with maxima at the position of the largest deviation, i.e. inclination, of the fiber direction. The nonlinear shear behavior under compressive loading increases with the severity of present fiber waviness and, therefore, plays a dominant role for the initiation and propagation of the failure mechanisms. In addition to the significant influence of the nonlinear shear behavior, the crucial effect of laminate thickness was shown in this thesis, which has been rarely considered in both industrial practice and academic research so far. The failure behavior for lower amplitude-to-thickness ratios is more determined by the material properties, whereas higher amplitude-to-thickness ratios lead to a higher influence of the geometry due to bending. For this reason, it is suggested to consider the amplitude-to-thickness ratio (A/t) in addition to the commonly used ratio of amplitude-to-wavelength (A/L) for further assessment strategies of fiber waviness. Comparing UD and QI specimen has shown a minor influence on the stiffness of QI specimen was observed. For example, the mechanical properties of 90° -layers are not reduced by the presence of a wave and therefore the influence of fiber waviness on the stiffness of QI laminates is less. The highly affected 0° -layers account only for 25% of the total laminate. However, the compressive strength of QI specimen significantly dropped by approximately 65% (wave 1) and 32% (wave 2), compared to UD laminates with 75% and 50%, respectively.

Research question 5: What is the influence of the matrix, especially under elevated temperatures and relative humidity (i.e. hot/wet conditions)?

In addition to mechanical tests at room temperature, the mechanical behavior and damage initiation for hot-wet aged wave configurations with UD laminates under compressive and tensile loading was investigated. Planar reference specimens with matrix dominated material properties, i.e. 15° off-axis tension, 90° tension and compression and 0° compression, have shown considerable drops in strength of ~30%, ~50% and ~25% respectively but almost no reduction in stiffness. However, the influence of matrix degradation due to hot-wet conditioning on the mechanical properties of unidirectional composite materials containing out-of-plane fiber waviness was less than expected. This difference probably results from different laminate thicknesses of the planar reference specimens (~2 mm) and wavy specimens (~5 mm). The maximum of the shear stress, which is considered to be mainly responsible for the failure, occurs at the center of the laminate. At this center position of the laminate, no complete saturation was achieved after a conditioning duration of almost 12 months. Therefore minor influence has been investigated in the experiments compared to the thinner planar specimens. Finite element simulations of wavy specimens using material parameters obtained from unaged and conditioned planar reference specimens have shown a significant decrease in strength. However, laminates with thicknesses of several centimeters, which are used in primary structures of aircrafts, will hardly reach moisture saturation during their lifetime.

Research question 6: How good is the prediction quality of simple and more complex analytical and numerical approaches in comparison with each other and, above all, with the experiments?

To predict the material behavior as soon as fiber waviness is detected to be present in the material, an analytical and numerical approach was chosen in this thesis. The analytical models of Hsiao & Daniel [4] and Altmann et al. [5], which are only applicable for unidirectional laminates, were extended for the calculation of multidirectional laminates. The analytical approach was able to determine the global, as well as local elastic properties, local stress distributions and based on that, strength calculations using the Puck failure criteria. The model was implemented in the software MATLAB in the form of several user interfaces. The presented model is valid for symmetrical, multidirectional laminates. It delivers reliable approximations of elastic properties, e.g. stiffnesses, for both uni- and multidirectional laminates. Comparisons of the analytical model with experimental results and FE simulations have shown good agreement for the prediction of elastic properties and stress distributions. However, the strength prediction of the analytical model only led to sufficient results for unidirectional laminates. The strength evaluation for multidirectional laminates is difficult due to highly complex interactions in the damage behavior of the varying ply orientations. The lack of accounting for global

8.5 CONCLUSION ON THE NUMERICAL SIMULATION

bending has to be incorporated in the next step to further improve the accuracy of the results.

The nonlinear material model that was implemented in ABAQUS as a material user-subroutine was able to capture the material behavior including shear nonlinearities, failure initiation and propagation in unidirectional laminates reasonably accurate. The validity of the model applies for quasi-static loaded unidirectional laminates only. To evaluate the applicability and limitations of the implemented 2D continuum damage model for more complex materials, it was applied under compressive loading for a quasi-isotropic laminate.

The global stress-strain response could only be reproduced insufficiently. The resulting complex 3D stress state leads to a complex failure behavior of QI laminates that cannot be represented by the 2D model, due to neglecting the stress components in y-direction. For the simulation of QI laminates, the model can merely be used as an engineering estimation of the material properties and a qualitative assessment of failure.

Both analytical and numerical models have weaknesses in the evaluation of the strength of multidirectional laminates. The analytical model cannot capture the complex interaction of plies with varying orientations. The 2D numerical model was developed for UD laminates with all fibers in the same direction.

Research question 7: Is a reliable and computationally efficient study over the large parameter space of out-of-plane fiber waviness possible using a virtual testing approach (analytical or numerical) as a substitute to a very high experimental effort?

Analytical and numerical results of UD specimens are well correlating with experimental data. This allows the assumption, that the presented analytical model and numerical simulations using the implemented material model are capable for a computationally efficient parameter study in the sense of a virtual testing approach. Based on the experimentally validated finite element model, a parameter study was carried out in this thesis with varying wave amplitudes ($0.1A-2A$), wavelengths and laminate thickness ($0.5A-6A$), where A denotes the baseline amplitude of 1.19 mm, and wavelengths (13.45-41.35 mm). The analytical model allows for a fast and reliable assessment of stiffness reductions of both uni- and multidirectional laminates for varying A/L ratios. The strength reduction can be used as a first estimation for unidirectional laminates. However, the strength evaluation of multidirectional laminates led to inconclusive results.

10. OUTLOOK

In further research, additional investigations on a range of varying types of waviness morphologies and positions, i.e. depths, in the laminate have to be carried out from both mechanically destructive and non-destructive perspectives.

In addition to the findings of this thesis that are limited to the mechanical behavior of fiber waviness under quasi-static loading, the effects of fiber waviness under fatigue loading need to be studied in more detail.

Additional mechanical tests could be carried out at elevated temperatures and humidity. An accelerated moisture absorption in heated water baths could be conducted in order to further investigate the influence of environmental conditions on wavy laminates.

Similar investigations should also be undertaken for analyzing other manufacturing defects such as voids and delamination.

In view of material modelling, for analyzing QI laminates containing fiber waviness an extension to a three-dimensional model which incorporates nonlinearity parameter for various ply orientations, fiber rotation and cohesive layers for modeling delamination is suggested.

REFERENCES

- [1] Potter K, Khan B, Wisnom M, Bell T, Stevens J. Variability, fibre waviness and misalignment in the determination of the properties of composite materials and structures. *Compos Part A Appl Sci Manuf* 2008;39:1343–54. doi:10.1016/j.compositesa.2008.04.016.
- [2] Potter KD. Understanding the origins of defects and variability in composites manufacture. *17 Th Int Conf Compos Mater* 2009:27–31.
- [3] Belnoue JPH, Mesogitis T, Nixon-Pearson OJ, Kratz J, Ivanov DS, Partridge IK, et al. Understanding and predicting defect formation in automated fibre placement pre-preg laminates. *Compos Part A Appl Sci Manuf* 2017;102:196–206. doi:10.1016/j.compositesa.2017.08.008.
- [4] Boisse P, Colmars J, Hamila N, Naouar N, Steer Q. Bending and wrinkling of composite fiber preforms and prepregs. A review and new developments in the draping simulations. *Compos Part B Eng* 2018;141:234–49. doi:10.1016/j.compositesb.2017.12.061.
- [5] Sjölander J, Hallander P, Åkermo M. Forming induced wrinkling of composite laminates: A numerical study on wrinkling mechanisms. *Compos Part A Appl Sci Manuf* 2016;81:41–51. doi:10.1016/j.compositesa.2015.10.012.
- [6] Nelson JW, Riddle TW, Cairns DS, Investigator P. *Effects of Defects in Composite Wind Turbine Blades : Round 1* 2012.
- [7] Ishikawa T, Chou T. Stiffness and strength behaviour of woven fabric composites. *J Mater Sci* 1982;17:3211–20. doi:10.1007/BF01203485.
- [8] Bogdanovič AE., Pastore CM. *Mechanics of textile and laminated composites*. 1st ed. London [u.A.]: Chapman & Hall; 1996.
- [9] Lomov S V., Huysmans G, Luo Y, Parnas RS, Prodromou A, Verpoest I, et al. Textile composites: Modelling strategies. *Compos - Part A Appl Sci Manuf* 2001;32:1379–94. doi:10.1016/S1359-835X(01)00038-0.
- [10] Lomov S V., Ivanov DS, Truong TC, Verpoest I, Baudry F, Vanden Bosche K, et al. Experimental methodology of study of damage initiation and development in textile composites in uniaxial tensile test. *Compos Sci Technol* 2008;68:2340–9. doi:10.1016/j.compscitech.2007.07.005.
- [11] Davidson P, Waas a M. Effect of Fiber Waviness on the Compressive Strength of Unidirectional Carbon Fiber Composites. 53rd AIAA/ASME/ASCE/AHS/ASC Struct Struct Dyn Mater Conf 2012:1–16.
- [12] Thor M, Mandel U, Nagler M, Maier F, Tauchner J, Sause MGR, et al. Numerical and experimental investigation of out-of-plane fiber waviness on the mechanical properties of composite materials. *Int J Mater Form* 2020. doi:10.1007/s12289-020-01540-5.
- [13] Hsiao HM, Daniel IM. Effect of fiber waviness on stiffness and strength reduction of unidirectional composites under compressive loading. *Compos Sci Technol* 1996;56:581–93. doi:10.1016/0266-3538(96)00045-0.

- [14] Cimini Jr. CA, Tsai SW. Ply Waviness on in-Plane Stiffness of Composite Laminates. 12th Int Conf Compos Mater n.d.
- [15] El-Hajjar RF, Petersen DR. Gaussian function characterization of unnotched tension behavior in a carbon/epoxy composite containing localized fiber waviness. *Compos Struct* 2011;93:2400–8. doi:10.1016/j.compstruct.2011.03.029.
- [16] Caiazzo A, Orlet M, McShane H, Strait L, Rachau C. The effects of marcel defects on composite structural properties. *Compos Struct Theory Pract* 2000;1383:158–87. doi:Doi 10.1520/Stp14509s.
- [17] Heuer H, Schulze MH, Meyendorf N. Non-destructive evaluation (NDE) of composites: Eddy current techniques. In: Karbhari VM, editor. *Non-Destructive Eval. Polym. Matrix Compos. Tech. Appl.*, Cambridge, UK: Woodhead Publishing Limited; 2013, p. 33–55. doi:10.1533/9780857093554.1.33.
- [18] Voltzer K. *Online-Prozessüberwachung von Automated Fiber Placement Prozessen auf Basis der Thermografie*. Gottfried Wilhelm Leibniz Universität Hannover, 2018.
- [19] Berger D, Egloff A, Summa J, Schwarz M, Lanza G, Herrmann HG. Conception of an Eddy Current In-process Quality Control for the Production of Carbon Fibre Reinforced Components in the RTM Process Chain. *Procedia CIRP* 2017;62:39–44. doi:10.1016/j.procir.2016.06.011.
- [20] Sutcliffe MPF, Lemanski SL, Scott AE. Measurement of fibre waviness in industrial composite components. *Compos Sci Technol* 2012;72:2016–23. doi:10.1016/j.compscitech.2012.09.001.
- [21] Joyce PJ, Kugler D, Moon TJ. A Technique for Characterizing Process-Induced Fiber Waviness in Unidirectional Composite Laminates-Using Optical Microscopy. *J Compos Mater* 1997;31:1694–727. doi:10.1177/002199839703101702.
- [22] Kastner J, Plank B, Heinzl C. *Advanced X-ray computed tomography methods: High resolution CT, quantitative CT, 4DCT and phase contrast CT*. Proc. Digit. Ind. Radiol. Comput. Tomogr., Ghent, Belgium: 2015.
- [23] Sutcliffe MPF, Lemanski SL, Scott AE. Measurement of fibre waviness in industrial composite components. *Compos Sci Technol* 2012;72:2016–23. doi:10.1016/j.compscitech.2012.09.001.
- [24] Yoshimura A, Hosoya R, Koyanagi J, Ogasawara T. X-ray computed tomography used to measure fiber orientation in CFRP laminates. *Adv Compos Mater* 2016;25:19–30. doi:10.1080/09243046.2014.959240.
- [25] Schmerr LW. *Fundamentals of Ultrasonic Nondestructive Evaluation: A Modeling Approach*. 2nd ed. Springer International Publishing; 2016. doi:10.1007/978-3-319-30463-2.
- [26] Elhajjar R, Haj-Ali R, Wei BS. An Infrared Thermoelastic Stress Analysis Investigation for Detecting Fiber Waviness in Composite Structures. *Polym - Plast Technol Eng* 2014;53:1251–8. doi:10.1080/03602559.2014.886116.
- [27] Campbell FC. *Manufacturing Processes for Advanced Composites*. 2004.

doi:10.1016/B978-1-85617-415-2.X5000-X.

- [28] Pain D, Drinkwater BW. Detection of fibre waviness using ultrasonic array scattering data. *J Nondestruct Eval* 2013;32:215–27. doi:10.1007/s10921-013-0174-z.
- [29] James R, Faisal Haider M, Giurgiutiu V, Lilienthal D. Eddy current non-destructive evaluation of manufacturing flaws and operational damage in CFRP composites 2019;57. doi:10.1117/12.2515505.
- [30] Nielsen SA. A review of reference methods for automated ultrasonic evaluation of composite structures. *ICCM Int Conf Compos Mater* 2015;2015-July:19–24.
- [31] Smith RA, Mukhopadhyay S, Lawrie A, Hallett SR. Applications of ultrasonic NDT to aerospace composites. *5th Int Symp NDT Aerosp* 2013;44:13–5.
- [32] Nelson LJ, Smith RA. Three-dimensional fibre-orientation characterisation in monolithic carbon-fibre composites. *11th Eur Conf Non-Destructive Test* 2014:1–12.
- [33] Chakrapani SK, Dayal V, Hsu DK, Barnard DJ, Gross A. Characterization of waviness in wind turbine blades using air coupled ultrasonics. *AIP Conf Proc* 2011;1335:956–62. doi:10.1063/1.3592041.
- [34] Thompson JG, Georgeson GE, Tat HH, Holmes TM. Characterization of wrinkles and periodic variations in material using infrared thermography. *US 10 094 794 B2*, 2018.
- [35] Heuer H, Schulze M, Pooch M, Gäbler S, Nocke A, Bardl G, et al. Review on quality assurance along the CFRP value chain - Non-destructive testing of fabrics, preforms and CFRP by HF radio wave techniques. *Compos Part B Eng* 2015;77:494–501. doi:10.1016/j.compositesb.2015.03.022.
- [36] Mook G, Lange R, Koeser O. Non-destructive characterisation of carbon-fibre-reinforced plastics by means of eddy-currents. *Compos Sci Technol* 2001;61:865–73. doi:10.1016/S0266-3538(00)00164-0.
- [37] Cheng J, Qiu J, Xu X, Ji H, Takagi T, Uchimoto T. Research advances in eddy current testing for maintenance of carbon fiber reinforced plastic composites. *Int J Appl Electromagn Mech* 2016;51:261–84. doi:10.3233/JAE-150168.
- [38] Zeng Z, Wang J, Liu X, Lin J, Dai Y. Detection of fiber waviness in CFRP using eddy current method. *Compos Struct* 2019;229:111411. doi:10.1016/j.compstruct.2019.111411.
- [39] Mizukami K, Mizutani Y, Kimura K, Sato A, Todoroki A, Suzuki Y. Detection of in-plane fiber waviness in cross-ply CFRP laminates using layer selectable eddy current method. *Compos Part A Appl Sci Manuf* 2016;82:108–18. doi:10.1016/j.compositesa.2015.11.040.
- [40] Mizukami K, Mizutani Y, Kimura K, Sato A, Todoroki A, Suzuki Y, et al. Visualization and size estimation of fiber waviness in multidirectional CFRP laminates using eddy current imaging. *Compos Part A Appl Sci Manuf* 2016;90:261–70. doi:10.1016/j.compositesa.2016.07.008.

- [41] Bouloudenine A, Feliachi M, Latreche MEH. Development of circular arrayed eddy current sensor for detecting fibers orientation and in-plane fiber waviness in unidirectional CFRP. *NDT E Int* 2017;92:30–7. doi:10.1016/j.ndteint.2017.07.011.
- [42] Mizukami K, Ogi K. Non-contact visualization of fiber waviness distribution in carbon fiber composites using eddy current testing. *Adv Compos Mater* 2018;27:135–46. doi:10.1080/09243046.2017.1344917.
- [43] Mizukami K. Evaluation of size of surface and subsurface waviness in carbon fiber composites using eddy current testing: a numerical study. *Adv Compos Mater* 2018;27:589–604. doi:10.1080/09243046.2017.1417092.
- [44] Mizukami K, Mizutani Y, Todoroki A, Suzuki Y. Detection of in-plane and out-of-plane fiber waviness in unidirectional carbon fiber reinforced composites using eddy current testing. *Compos Part B Eng* 2016;86:84–94. doi:10.1016/j.compositesb.2015.09.041.
- [45] Budiansky B, Fleck N a. Compressive Kinking of Fiber Composites: A Topical Review. *Appl Mech Rev* 1994;47:S246. doi:10.1115/1.3124417.
- [46] Hsiao HM, Daniel IM. Elastic properties of composites with fiber waviness. *Compos Part A Appl Sci Manuf* 1996;27:931–40. doi:10.1016/1359-835X(96)00034-6.
- [47] Piggott MR. The effect of fibre waviness on the mechanical properties of unidirectional fibre composites: A review. *Compos Sci Technol* 1995;53:201–5. doi:10.1016/0266-3538(95)00019-4.
- [48] Altmann A, Taubert R, Mandel U, Hinterhoelzl R, Drechsler K. A continuum damage model to predict the influence of ply waviness on stiffness and strength in ultra-thick unidirectional Fiber-reinforced Plastics. *J Compos Mater* 2015;0021998315612536-. doi:10.1177/0021998315612536.
- [49] Adams DOH, Bell SJ. Compression strength reductions in composite laminates due to multiple-layer waviness. *Compos Sci Technol* 1995;53:207–12. doi:10.1016/0266-3538(95)00020-8.
- [50] Steeves CA, Fleck NA. Compressive strength of composite laminates with terminated internal plies. *Compos Part A Appl Sci Manuf* 2005;36:798–805. doi:10.1016/j.compositesa.2004.10.024.
- [51] Wang J, Potter KD, Etches J. Experimental investigation and characterisation techniques of compressive fatigue failure of composites with fibre waviness at ply drops. *Compos Struct* 2013;100:398–403. doi:10.1016/j.compstruct.2013.01.010.
- [52] Elhajjar RF, Shams SS. Compression testing of continuous fiber reinforced polymer composites with out-of-plane fiber waviness and circular notches 2014;35:45–55.
- [53] Lemanski SL, Sutcliffe MPF. Compressive failure of finite size unidirectional composite laminates with a region of fibre waviness. *Compos Part A Appl Sci Manuf* 2012;43:435–44. doi:10.1016/j.compositesa.2011.11.007.

- [54] Zhu J, Wang J, Zu L. Influence of out-of-plane ply waviness on elastic properties of composite laminates under uniaxial loading. *Compos Struct* 2015;132:440–50. doi:10.1016/j.compstruct.2015.05.062.
- [55] Li Y, Stier B, Bednarczyk B, Simon JW, Reese S. The effect of fiber misalignment on the homogenized properties of unidirectional fiber reinforced composites. *Mech Mater* 2016;92:261–74. doi:10.1016/j.mechmat.2015.10.002.
- [56] Vogler TJ, Hsu S-Y, Kyriakides S. Composite failure under combined compression and shear. *Int J Solids Struct* 2000;37:1765–91. doi:10.1016/S0020-7683(98)00323-0.
- [57] Pinho ST, Iannucci L, Robinson P. Physically based failure models and criteria for laminated fibre-reinforced composites with emphasis on fibre kinking. Part II: FE implementation. *Compos Part A Appl Sci Manuf* 2006. doi:10.1016/j.compositesa.2005.06.008.
- [58] Pinho ST, Iannucci L, Robinson P. Physically-based failure models and criteria for laminated fibre-reinforced composites with emphasis on fibre kinking: Part I: Development. *Compos Part A Appl Sci Manuf* 2006;37:63–73. doi:10.1016/j.compositesa.2005.04.016.
- [59] Budiansky B, Fleck NA. Compressive failure of fibre composites. *J Mech Phys Solids* 1993;41:183–211. doi:10.1016/0022-5096(93)90068-Q.
- [60] Jelf PM, Fleck NA. Compression Failure Mechanisms in Unidirectional Composites. *J Compos Mater* 1992;26:2706–26. doi:10.1177/002199839202601804.
- [61] Niu K, Talreja R. Modeling of compressive failure in fiber reinforced composites. *Int J Solids Struct* 2000;37:2405–28. doi:10.1016/S0020-7683(99)00010-4.
- [62] Slaughter WS, Fleck NA. Microbuckling of fiber composites with random initial fiber waviness. *J Mech Phys Solids* 1994;42:1743–66. doi:10.1016/0022-5096(94)90070-1.
- [63] Lemanski SL, Wang J, Sutcliffe MPF, Potter KD, Wisnom MR. Modelling failure of composite specimens with defects under compression loading. *Compos Part A Appl Sci Manuf* 2013;48:26–36. doi:10.1016/j.compositesa.2012.12.007.
- [64] Daniel IM, Luo JJ, Schubel PM, Werner BT. Interfiber/interlaminar failure of composites under multi-axial states of stress. *Compos Sci Technol* 2009;69:764–71. doi:10.1016/j.compscitech.2008.04.016.
- [65] Bogetti TA, Gillespie JW, Lamontia MA. The Influence of Ply Waviness with Nonlinear Shear on the Stiffness and Strength Reduction of Composite Laminates. *J Thermoplast Compos Mater* 1994;7:76–90. doi:10.1177/089270579400700201.
- [66] Pimenta S, Gutkin R, Pinho ST, Robinson P. A micromechanical model for kink-band formation: Part I — Experimental study and numerical modelling. *Compos Sci Technol* 2009;69:948–55. doi:10.1016/j.compscitech.2009.02.010.

- [67] Pimenta S, Gutkin R, Pinho ST, Robinson P. A micromechanical model for kink-band formation: Part II – Analytical modelling. *Compos Sci Technol* 2009;69:956–64. doi:10.1016/j.compscitech.2009.02.003.
- [68] Hinton MJ, Kaddour AS, Soden PD. *The world-wide failure exercise*. Elsevier Science Ltd.; 2004.
- [69] Chun H, Shin J, Daniel IM. Effects of material and geometric nonlinearities on the tensile and compressive behavior of composite materials with fiber waviness 2001;61:125–34.
- [70] Altmann A, Gesell P, Drechsler K. Strength prediction of ply waviness in composite materials considering matrix dominated effects. *Compos Struct* 2015;127:51–9. doi:10.1016/j.compstruct.2015.02.024.
- [71] Croft K, Lessard L, Pasini D, Hojjati M, Chen J, Yousefpour A. Experimental study of the effect of automated fiber placement induced defects on performance of composite laminates. *Compos Part A Appl Sci Manuf* 2011;42:484–91. doi:10.1016/j.compositesa.2011.01.007.
- [72] Lan M, Cartié D, Davies P, Baley C. Influence of embedded gap and overlap fiber placement defects on the microstructure and shear and compression properties of carbon-epoxy laminates. *Compos Part A Appl Sci Manuf* 2016;82:198–207. doi:10.1016/j.compositesa.2015.12.007.
- [73] Wisnom MR. Shear fracture of unidirectional composites without initial cracks 1994;52:9–17.
- [74] Bloom LD, Wang J, Potter KD. Damage progression and defect sensitivity: An experimental study of representative wrinkles in tension. *Compos Part B Eng* 2013;45:449–58. doi:10.1016/j.compositesb.2012.05.021.
- [75] Mukhopadhyay S, Jones MI, Hallett SR. Compressive failure of laminates containing an embedded wrinkle; Experimental and numerical study. *Compos Part A Appl Sci Manuf* 2015;73:132–42. doi:10.1016/j.compositesa.2015.03.012.
- [76] Mukhopadhyay S, Jones MI, Hallett SR. Tensile failure of laminates containing an embedded wrinkle; numerical and experimental study. *Compos Part A Appl Sci Manuf* 2015;77:219–28. doi:10.1016/j.compositesa.2015.07.007.
- [77] Mukhopadhyay S, Nixon-Pearson OJ, Hallett SR. An experimental and numerical study on fatigue damage development in laminates containing embedded wrinkle defects. *Int J Fatigue* 2018;107:1–12. doi:10.1016/j.ijfatigue.2017.10.008.
- [78] Wilhelmsson D, Asp LE, Gutkin R, Edgren F. Fibre waviness induced bending in compression tests of unidirectional NCF composites. *ICCM Int Conf Compos Mater* 2017;2017-Augus:20–5.
- [79] Altmann A, Gesell P, Drechsler K. Strength prediction of ply waviness in composite materials considering matrix dominated effects. *Compos Struct* 2015;127:51–9. doi:10.1016/j.compstruct.2015.02.024.
- [80] Puck A, Schürmann H. Failure analysis of FRP laminates by means of physically based phenomenological models. *Fail. Criteria Fibre-Reinforced-*

- Polymer Compos., 2004. doi:10.1016/B978-008044475-8/50028-7.
- [81] Schürmann H. Konstruieren mit Faser-Kunststoff-Verbunden. 2007. doi:10.1007/978-3-540-72190-1.
- [82] Dodwell TJ, Butler R, Hunt GW. Out-of-plane ply wrinkling defects during consolidation over an external radius. *Compos Sci Technol* 2014;105:151–9. doi:10.1016/j.compscitech.2014.10.007.
- [83] Boisse P, Hamila N, Madeo A. Modelling the development of defects during composite reinforcements and prepreg forming. *Philos Trans R Soc A Math Phys Eng Sci* 2016;374. doi:10.1098/rsta.2015.0269.
- [84] Hou M. Stamp Forming of Fabric-Reinforced Thermoplastic Composites. *Polym Compos* 1996;17:596–603.
- [85] O'Brádaigh CM, Pipes RB, Mallon PJ. Issues in diaphragm forming of continuous fiber reinforced thermoplastic composites. *Polym Compos* 1991;12:246–56. doi:10.1002/pc.750120406.
- [86] Potter K. Manufacturing defects as a cause of failure in polymer matrix composites. *Fail. Mech. Polym. Matrix Compos. Criteria, Test. Ind. Appl.*, 2012. doi:10.1016/B978-1-84569-750-1.50002-1.
- [87] Dong C. Experimental investigation on the fiber preform deformation due to mold closure for composites processing. *Int J Adv Manuf Technol* 2014;71:585–91. doi:10.1007/s00170-013-5517-5.
- [88] Boisse P, Hamila N, Vidal-Sallé E, Dumont F. Simulation of wrinkling during textile composite reinforcement forming. Influence of tensile, in-plane shear and bending stiffnesses. *Compos Sci Technol* 2011;71:683–92. doi:10.1016/j.compscitech.2011.01.011.
- [89] Tam AS, Gutowski TG. The kinematics for forming ideal aligned fibre composites into complex shapes. *Compos Manuf* 1990;1:219–28. doi:10.1016/0956-7143(90)90044-W.
- [90] Hallander P, Åkermo M, Mattei C, Petersson M, Nyman T. An experimental study of mechanisms behind wrinkle development during forming of composite laminates. *Compos Part A Appl Sci Manuf* 2013;50:54–64. doi:10.1016/j.compositesa.2013.03.013.
- [91] Åkermo M, Larberg YR, Sjölander J, Hallander P. Influence of interply friction on the forming of stacked UD prepreg. *ICCM Int Conf Compos Mater* 2013;2013-July:919–28.
- [92] Hallander P, Sjölander J, Åkermo M. Forming induced wrinkling of composite laminates with mixed ply material properties; an experimental study. *Compos Part A Appl Sci Manuf* 2015;78:234–45. doi:10.1016/j.compositesa.2015.08.025.
- [93] Hallander P, Sjölander J, Petersson M, Åkermo M. Interface manipulation towards wrinkle-free forming of stacked UD prepreg layers. *Compos Part A Appl Sci Manuf* 2016;90:340–8. doi:10.1016/j.compositesa.2016.07.013.
- [94] Wang J, Paton R, Page JR. Draping of woven fabric preforms and prepreps for production of polymer composite components. *Compos Part A Appl Sci Manuf*

- 1999;30:757–65. doi:10.1016/S1359-835X(98)00187-0.
- [95] Lin H, Wang J, Long AC, Clifford MJ, Harrison P. Textile wrinkling in composite forming 2005:1–10.
- [96] Hou M, Friedrich K. 3-D stamp forming of thermoplastic matrix composites. *Appl Compos Mater* 1994. doi:10.1007/BF00567575.
- [97] Murtagh AM, Mallon PJ. Characterisation of shearing and frictional behaviour during sheet forming. In: Bhattacharyya D, editor. *Compos. Sheet Form.*, Amsterdam: Elsevier; 1997, p. 163–214. doi:10.1016/S0927-0108(97)80007-0.
- [98] Christie GR, Collins IF, Bhattacharyya D. Out-of-plane buckling of fiber-reinforced thermoplastic sheets under homogeneous biaxial conditions. *J Appl Mech Trans ASME* 1995. doi:10.1115/1.2896008.
- [99] Monaghan MR, Mallon PJ, O’bradaigh CM, Pipes RB. The Effect of Diaphragm Stiffness on the Quality of Diaphragm Formed Thermoplastic Composite Components. *J Thermoplast Compos Mater* 1990. doi:10.1177/089270579000300303.
- [100] Hull BD, Rogers TG, Spencer AJM. Theory of fibre buckling and wrinkling in shear flows of fibre-reinforced composites. *Compos Manuf* 1991. doi:10.1016/0956-7143(91)90138-7.
- [101] Margossian A. Forming of tailored thermoplastic composite blanks: material characterisation, simulation and validation 2017.
- [102] Mallick PK. *Processing of Polymer Matrix Composites*. Boca Raton, FL: CRC Press; 2018. doi:10.1201/9781315157252.
- [103] Soll W, Gutowski TG. Forming Thermoplastic Composite Parts. *SAMPE J* 1988:15–9.
- [104] Aström BT. Thermoplastic composite sheet forming: Materials and manufacturing techniques. In: Bhattacharyya D, editor. *Compos. Sheet Form.*, Amsterdam: Elsevier; 1997, p. 27–73. doi:10.1016/S0927-0108(97)80004-5.
- [105] Bhattacharyya D. *Composite Sheet Forming*. Amsterdam: Elsevier Science B.V.; 1997.
- [106] Friedrich K, Hou M, Krebs J. Thermoforming of continuous fibre/thermoplastic composite sheets. In: Bhattacharyya D, editor. *Compos. Sheet Form.*, Amsterdam: Elsevier; 1997, p. 91–162. doi:10.1016/S0927-0108(97)80006-9.
- [107] Li H, Gutowski TG. The forming of thermoset composites. In: Bhattacharyya D, editor. *Compos. Sheet Form.*, Amsterdam: Elsevier; 1997, p. 441–72.
- [108] Wakeman MD, Manson JAE. Composites manufacturing - thermoplastics. In: Long AC, editor. *Des. Manuf. Text. Compos.*, Cambridge, UK: Woodhead; 2005, p. 197–241. doi:10.1533/9781845690823.197.
- [109] Li HL, Koch P, Prevorsek DC, Oswald HJ. Cold forming of plastics part I. Draw forming of thermoplastic sheets. *Polym Eng Sci* 1971;11. doi:10.1002/pen.760110205.
- [110] Broutman LJ, Kalpakjian S, Chawla J. Deep drawability of biaxially rolled thermoplastic sheets. *Polym Eng Sci* 1972;12:150–6. doi:10.1002/pen.760120212.

- [111] Blom AW, Lopes CS, Kromwijk PJ, Gurdal Z, Camanho PP. A Theoretical Model to Study the Influence of Tow-drop Areas on the Stiffness and Strength of Variable-stiffness Laminates. *J Compos Mater* 2009;43:403–25. doi:10.1177/0021998308097675.
- [112] Blom AW. Structural performance of fiber-placed, variable-stiffness composite conical and cylindrical shells. Delft University of Technology, 2010.
- [113] Hörmann P. Thermoset automated fibre placement - on steering effects and their prediction. Technische Universität München, 2016.
- [114] Lukaszewicz DHJA, Ward C, Potter KD. The engineering aspects of automated prepreg layup: History, present and future. *Compos Part B Eng* 2012;43:997–1009. doi:10.1016/j.compositesb.2011.12.003.
- [115] Heinecke F, Willberg C. Manufacturing-Induced Imperfections in Composite Parts Manufactured via Automated Fiber Placement. *J Compos Sci* 2019;3:56. doi:10.3390/jcs3020056.
- [116] Beakou A, Cano M, Le Cam JB, Verney V. Modelling slit tape buckling during automated prepreg manufacturing: A local approach. *Compos Struct* 2011;93:2628–35. doi:10.1016/j.compstruct.2011.04.030.
- [117] Bakhshi N, Hojjati M. Time-dependent wrinkle formation during tow steering in automated fiber placement. *Compos Part B Eng* 2019;165:586–93. doi:10.1016/j.compositesb.2019.02.034.
- [118] Lukaszewicz DHJA, Potter KD, Eales J. A concept for the in situ consolidation of thermoset matrix prepreg during automated lay-up. *Compos Part B Eng* 2013;45:538–43. doi:10.1016/j.compositesb.2012.09.008.
- [119] Lichtinger R, Hörmann P, Stelzl D, Hinterhölzl R. The effects of heat input on adjacent paths during Automated Fibre Placement. *Compos Part A Appl Sci Manuf* 2015;68:387–97. doi:10.1016/j.compositesa.2014.10.004.
- [120] Chinesta F, Leygue A, Bognet B, Ghnatios C, Poulhaon F, Bordeu F, et al. First steps towards an advanced simulation of composites manufacturing by automated tape placement. *Int J Mater Form* 2014;7:81–92. doi:10.1007/s12289-012-1112-9.
- [121] Matveev MY, Schubel PJ, Long AC, Jones IA. Understanding the buckling behaviour of steered tows in Automated Dry Fibre Placement (ADFP). *Compos Part A Appl Sci Manuf* 2016;90:451–6. doi:10.1016/j.compositesa.2016.08.014.
- [122] Kim BC, Hazra K, Weaver P, Potter K. Limitations of fibre placement techniques for variable angle tow composites and their process-induced defects. *ICCM Int Conf Compos Mater* 2011.
- [123] Rajan S, Sutton MA, Wehbe R, Tatting B, Gürdal Z, Kidane A, et al. Experimental investigation of prepreg slit tape wrinkling during automated fiber placement process using StereoDIC. *Compos Part B Eng* 2019;160:546–57. doi:10.1016/j.compositesb.2018.12.017.
- [124] Viisainen V, Zhou J, Sutcliffe M, Street T. Development of a Composite Forming Limit Diagram: A Feasibility Study. 22nd ICCM Int. Conf. Compos.

- Mater., Melbourne: 2019.
- [125] Hoa S V. Principles of the manufacturing of composite materials. Lancaster, Pennsylvania: DEStech Publications, Inc.; 2009.
- [126] Hubert P, Centea T, Grunefelder L, Nutt S, Kratz J, Levy A. Out-of-Autoclave Prepreg Processing. vol. 2. Elsevier Ltd.; 2018. doi:10.1016/b978-0-12-803581-8.09900-8.
- [127] Lightfoot JS, Wisnom MR, Potter K. A new mechanism for the formation of ply wrinkles due to shear between plies. *Compos Part A Appl Sci Manuf* 2013;49:139–47. doi:10.1016/j.compositesa.2013.03.002.
- [128] Levy A, Hubert P. Vacuum-bagged composite laminate forming processes: Predicting thickness deviation in complex shapes. *Compos Part A Appl Sci Manuf* 2019;126:105568. doi:10.1016/j.compositesa.2019.105568.
- [129] Hubert P, Poursartip A. Aspects of the compaction of composite angle laminates: an experimental investigation. *J Compos Mater* 2001. doi:10.1106/X8D7-PR9V-U6F2-0JEK.
- [130] ASTM International. D1894-11 - Standard Test Method for Static and Kinetic Coefficients of Friction of Plastic Film and Sheeting. *ASTM Int* 2013. doi:10.1520/D1894-11.2.
- [131] Sachs U, Akkerman R, Fetfatsidis K, Vidal-Sallé E, Schumacher J, Ziegmann G, et al. Characterization of the dynamic friction of woven fabrics: Experimental methods and benchmark results. *Compos Part A Appl Sci Manuf* 2014;67:289–98. doi:10.1016/j.compositesa.2014.08.026.
- [132] Farnand K, Zobeiry N, Poursartip A, Fernlund G. Micro-level mechanisms of fiber waviness and wrinkling during hot drape forming of unidirectional prepreg composites. *Compos Part A Appl Sci Manuf* 2017;103:168–77. doi:10.1016/j.compositesa.2017.10.008.
- [133] The Boeing Company. Patent Application Publication (10) Pub . No .: US 2016 / 0123850 A1. US 2016/0176500 A1, 2016.
- [134] Breuer UP. Commercial aircraft composite technology. Kaiserslautern: Springer International Publishing AG Switzerland; 2016. doi:10.1007/978-3-319-31918-6.
- [135] Hassan MH, Othman AR, Kamaruddin S. A review on the manufacturing defects of complex-shaped laminate in aircraft composite structures. *Int J Adv Manuf Technol* 2017;91:4081–94. doi:10.1007/s00170-017-0096-5.
- [136] Heimbs S, Middendorf P, Maier M. Honeycomb Sandwich Material Modeling for Dynamic Simulations of Aircraft Interior Components. 9th Int. LS-DYNA Users Conf., Dearborn: 2006.
- [137] Lamontia MA, Funck SB, Gruber MB, Cope RD, Waibel BJ, Gopez NM. Manufacturing flat and cylindrical laminates and built up structure using automated thermoplastic tape laying, fiber placement, and filament winding. *SAMPE J* 2003;39:30–8.
- [138] Riss F, Schilp J, Reinhart G. Load-dependent optimization of honeycombs for sandwich components-new possibilities by using additive layer

- manufacturing. *Phys Procedia* 2014;56:327–35. doi:10.1016/j.phpro.2014.08.178.
- [139] Fischer FJC, Mezakeu Tongnan Y, Beyrle M, Gerngross T, Kupke M. Characterization of Production-Induced Defects in Carbon Fiber Reinforced Thermoplastic Technology. 7th Int Symp NDT Aerosp 2015:1–19.
- [140] Lightfoot JS, Wisnom MR, Potter K. Defects in woven preforms: Formation mechanisms and the effects of laminate design and layup protocol. *Compos Part A Appl Sci Manuf* 2013;51:99–107. doi:10.1016/j.compositesa.2013.04.004.
- [141] Elhajjar R, Grant P, Ashforth C. *Composite Structures: Effects of Defects*. New York: John Wiley & Sons Ltd; 2019. doi:10.1002/9781118997710.
- [142] Ersoy N, Garstka T, Potter K, Wisnom MR, Porter D, Clegg M, et al. Development of the properties of a carbon fibre reinforced thermosetting composite through cure. *Compos Part A Appl Sci Manuf* 2010;41:401–9. doi:10.1016/j.compositesa.2009.11.007.
- [143] Krebs J, Friedrich K, Bhattacharyya D. A direct comparison of matched-die versus diaphragm forming. *Compos Part A Appl Sci Manuf* 1998;29:183–8. doi:10.1016/S1359-835X(97)82706-6.
- [144] Tam AS, Gutowski TG. Ply-Slip during the Forming of Thermoplastic Composite Parts. *J Compos Mater* 1989;23:587–605. doi:10.1177/002199838902300604.
- [145] Hou M, Friedrich K. Zum Thermoformen von Hochleistungsverbundwerkstoffen mit thermoplastischer Matrix. *Proc. AVK Conf.*, Berlin: Arbeitsgemeinschaft Verstärkte Kunststoffe e.V (AVK); 1991, p. 12–4.
- [146] Hou M, Friedrich K, Scherer R. Optimization of stamp forming of thermoplastic composite bends. *Compos Struct* 1994;27:157–67. doi:10.1016/0263-8223(94)90077-9.
- [147] Scherer R, Friedrich K. Experimental Background for Finite Element Analysis of the Interply-Slip Process during Thermoforming of Thermoplastic Composites. In: Füller J, Grüninger G, Schulte K, Bunsell AR, Massiah A, editors. *Dev. Sci. Technol. Compos. Mater.*, Dordrecht: Springer; 1990, p. 1001–6. doi:10.1007/978-94-009-0787-4_144.
- [148] Pandey RK, Sun CT. Mechanisms of wrinkle formation during the processing of composite laminates. *Compos Sci Technol* 1999;59:405–17. doi:10.1016/S0266-3538(98)00080-3.
- [149] Cakmak M, Dutta A. Instrumented thermoforming of advanced thermoplastic composites. II: Dynamics of double curvature part formation and structure development from PEEK/carbon fiber prepreg tapes. *Polym Compos* 1991;12:338–53.
- [150] Wiersma HW, Peeters LJB, Akkerman R. Prediction of springforward in continuous-fibre/polymer L-shaped parts. *Compos Part A Appl Sci Manuf* 1998;29:1333–42. doi:10.1016/S1359-835X(98)00062-1.
- [151] Ding A, Li S, Sun J, Wang J, Zu L. A comparison of process-induced residual

- stresses and distortions in composite structures with different constitutive laws. *J Reinf Plast Compos* 2016;35:807–23. doi:10.1177/0731684416629764.
- [152] Cogswell FN. The experience of thermoplastic structural composites during processing. *Compos Manuf* 1991;2:208_216.
- [153] Zhang Y, Xia Z, Ellyin F. Evolution and influence of residual stresses/strains of fiber reinforced laminates. *Compos Sci Technol* 2004;64:1613–21. doi:10.1016/j.compscitech.2003.11.012.
- [154] Karami G, Garnich M. Micromechanical study of thermoelastic behavior of composites with periodic fiber waviness. *Compos Part B Eng* 2005;36:241–8. doi:10.1016/j.compositesb.2004.09.005.
- [155] Ersoy N, Potter K, Wisnom MR, Clegg MJ. An experimental method to study the frictional processes during composites manufacturing. *Compos Part A Appl Sci Manuf* 2005;36:1536–44. doi:10.1016/j.compositesa.2005.02.010.
- [156] Ruiz E, Trochu F. Numerical analysis of cure temperature and internal stresses in thin and thick RTM parts. *Compos Part A Appl Sci Manuf* 2005;36:806–26. doi:10.1016/j.compositesa.2004.10.021.
- [157] Kugler D, Moon TJ. Identification of the Most Significant Processing Parameters on the Developments of Fiber Wavinesses in Thin Laminates. *J Compos Mater* 2002;36:1451–79. doi:10.1106/002199802023575.
- [158] Belnoue JPH, Nixon-Pearson OJ, Thompson AJ, Ivanov DS, Potter KD, Hallett SR. Consolidation-driven defect generation in thick composite parts. *J Manuf Sci Eng Trans ASME* 2018;140. doi:10.1115/1.4039555.
- [159] De Luca P, Lefébure P, Pickett AK. Numerical and experimental investigation of some press forming parameters of two fibre reinforced thermoplastics: APC2-AS4 and PEI-CETEX. *Compos Part A Appl Sci Manuf* 1998;29:101–10. doi:10.1016/S1359-835X(97)00060-2.
- [160] Lan M, Cartié D, Davies P, Baley C. Microstructure and tensile properties of carbon-epoxy laminates produced by automated fibre placement: Influence of a caul plate on the effects of gap and overlap embedded defects. *Compos Part A Appl Sci Manuf* 2015;78:124–34. doi:10.1016/j.compositesa.2015.07.023.
- [161] Murri GB. Influence of Ply Waviness on Fatigue Life of Tapered Composite Flexbeam Laminates 1999.
- [162] Hart-Smith LJ. Designing with advanced fibrous composites. Douglas paper 8011, Brisbane: Presented to Australian Bicentennial International Congress on Mechanical Engineering; 1988.
- [163] Gereke T, Döbrich O, Hübner M, Cherif C. Experimental and computational composite textile reinforcement forming: A review. *Compos Part A Appl Sci Manuf* 2013;46:1–10. doi:10.1016/j.compositesa.2012.10.004.
- [164] Dai S, Cunningham PR, Marshall S, Silva C. Influence of fibre architecture on the tensile, compressive and flexural behaviour of 3D woven composites. *Compos Part A Appl Sci Manuf* 2015;69:195–207. doi:10.1016/j.compositesa.2014.11.012.

- [165] Long AC, Rudd CD, Blagdon M, Smith P. Characterizing the processing and performance of aligned reinforcements during preform manufacture. *Compos Part A Appl Sci Manuf* 1996;27:247–53. doi:10.1016/1359-835X(95)00051-3.
- [166] Prodromou AG, Chen J. On the relationship between shear angle and wrinkling of textile composite preforms. *Compos Part A Appl Sci Manuf* 1997;28:491–503. doi:10.1016/S1359-835X(96)00150-9.
- [167] Hosseini A, Kashani MH, Sassani F, Milani AS, Ko FK. Identifying the distinct shear wrinkling behavior of woven composite preforms under bias extension and picture frame tests. *Compos Struct* 2018;185:764–73. doi:10.1016/j.compstruct.2017.11.033.
- [168] Hamila N, Boisse P, Sabourin F, Brunet M. A semi-discrete shell finite element for textile composite reinforcement forming simulation. *Int J Numer Methods Eng* 2009;79:1443–66.
- [169] Allaoui S, Hivet G, Soulat D, Wendling A, Ouagne P, Chatel S. Experimental preforming of highly double curved shapes with a case corner using an interlock reinforcement. *Int J Mater Form* 2014;7:155–65. doi:10.1007/s12289-012-1116-5.
- [170] Allaoui S, Boisse P, Chatel S, Hamila N, Hivet G, Soulat D, et al. Experimental and numerical analyses of textile reinforcement forming of a tetrahedral shape. *Compos Part A Appl Sci Manuf* 2011;42:612–22. doi:10.1016/j.compositesa.2011.02.001.
- [171] Launay J, Hivet G, Duong A V., Boisse P. Experimental analysis of the influence of tensions on in plane shear behaviour of woven composite reinforcements. *Compos Sci Technol* 2008;68:506–15. doi:10.1016/j.compscitech.2007.06.021.
- [172] Lomov S V., Verpoest I. Model of shear of woven fabric and parametric description of shear resistance of glass woven reinforcements. *Compos Sci Technol* 2006;66:919–33. doi:10.1016/j.compscitech.2005.08.010.
- [173] Harrison P, Abdiwi F, Guo Z, Potluri P, Yu WR. Characterising the shear-tension coupling and wrinkling behaviour of woven engineering fabrics. *Compos Part A Appl Sci Manuf* 2012;43:903–14. doi:10.1016/j.compositesa.2012.01.024.
- [174] Allaoui S, Cellard C, Hivet G. Effect of inter-ply sliding on the quality of multilayer interlock dry fabric preforms. *Compos Part A Appl Sci Manuf* 2015;68:336–45. doi:10.1016/j.compositesa.2014.10.017.
- [175] Lomov S V., Belov EB, Bischoff T, Ghosh SB, Truong Chi T, Verpoest I. Carbon composites based on multiaxial multiply stitched preforms. Part 1. Geometry of the preform. *Compos Part A Appl Sci Manuf* 2002;33:1171–83. doi:10.1016/S1359-835X(02)00090-8.
- [176] Cao Y, Feng Y, Wang W, Wu D, Zhu Z. Estimation of lamina stiffness and strength of quadriaxial non-crimp fabric composites based on semi-laminar considerations. *Appl Sci* 2016;6. doi:10.3390/app6090267.

- [177] Saboktakin A. 3D textile preforms and composites for aircraft structures: A review. *Int J Aviat Aeronaut Aerosp* 2019;6. doi:10.15394/ijaaa.2019.1299.
- [178] Uhlig K, Tosch M, Bittrich L, Leipprand A, Dey S, Spickenheuer A, et al. Meso-scaled finite element analysis of fiber reinforced plastics made by Tailored Fiber Placement. *Compos Struct* 2016;143:53–62. doi:10.1016/j.compstruct.2016.01.049.
- [179] Hazra K, Saverymuthapulle M, Hawthorne M, Stewart DL, Weaver P, Potter K. Investigation of mechanical properties of tow steered CFRP panels. *ICCM19 Int Conf Compos Mater* 2009.
- [180] Mouritz AP. Review of z-pinned composite laminates. *Compos Part A Appl Sci Manuf* 2007;38:2383–97. doi:10.1016/j.compositesa.2007.08.016.
- [181] Tong L, Mouritz AP, Bannister MK. *3D Fibre Reinforced Polymer Composites*. Oxford: Elsevier Science Ltd.; 2002.
- [182] Takeda N, Okabe Y, Kuwahara J, Kojima S, Ogisu T. Development of smart composite structures with small-diameter fiber Bragg grating sensors for damage detection: Quantitative evaluation of delamination length in CFRP laminates using Lamb wave sensing. *Compos Sci Technol* 2005;65:2575–87. doi:10.1016/j.compscitech.2005.07.014.
- [183] Shivakumar K, Emmanwori L. Mechanics of Failure of Composite Laminates with an Embedded Fiber Optic Sensor. *J Compos Mater* 2004. doi:10.1177/0021998304042393.
- [184] Luyckx G, Voet E, Lammens N, Degrieck J. Strain measurements of composite laminates with embedded fibre bragg gratings: Criticism and opportunities for research. *Sensors* 2011;11:384–408. doi:10.3390/s110100384.
- [185] Satori K, Fukuchi K, Kurosawa Y, Hongo A, Takeda N. Polyimide-coated small-diameter optical fiber sensors for embedding in composite laminate structures. *Smart Struct. Mater. 2001 Sens. Phenom. Meas. Instrum. Smart Struct. Mater.*, 2001. doi:10.1117/12.435531.
- [186] Suarez E, Sause MGR, Gallego A. Influence of an optical fiber embedded on unidirectional CFRP laminates evaluated with the Acoustic Emission and 3D Digital Image Correlation techniques. *Prog. Acoust. Emiss. XVIII, Kyoto, Japan: 2016*.
- [187] Skontorp A. Composites with embedded optical fibers at structural details with inherent stress concentrations. *J Compos Mater* 2002;36:2501–15. doi:10.1177/002199802761405268.
- [188] Sarantinos N, Tsantzalis S, Ucsnik S, Kostopoulos V. Review of through-the-thickness reinforced composites in joints. *Compos Struct* 2019;229:111404. doi:10.1016/j.compstruct.2019.111404.
- [189] Davidson P, Waas AM. The effects of defects on the compressive response of thick carbon composites: An experimental and computational study. *Compos Struct* 2017;176:582–96. doi:10.1016/j.compstruct.2017.05.046.
- [190] Hamidi YK, Altan MC. Process induced defects in liquid molding processes of

- composites. *Int Polym Process* 2017;32:527–44. doi:10.3139/217.3444.
- [191] Lightfoot JS, Wisnom MR, Potter K. Defects in woven preforms: Formation mechanisms and the effects of laminate design and layup protocol. *Compos Part A Appl Sci Manuf* 2013;51:99–107. doi:10.1016/j.compositesa.2013.04.004.
- [192] Barnes JA, Cogswell FN. Transverse flow processes in continuous fibre-reinforced thermoplastic composites. *Composites* 1989;20:38–42. doi:10.1016/0010-4361(89)90680-0.
- [193] Hallett SR, Belnoue JP-H, Nixon-Pearson OJ, Mesogitis T, Kratz J, Ivanov DS, et al. Understanding and Prediction of Fibre Waviness Defect Generation. *Am Soc Compos Thirty-First Tech Conf* 2016.
- [194] Parlevliet PP, Bersee HEN, Beukers A. Residual stresses in thermoplastic composites - a study of the literature. Part III: Effects of thermal residual stresses. *Compos Part A Appl Sci Manuf* 2007;38:1581–96. doi:10.1016/j.compositesa.2006.12.005.
- [195] Baran I, Cinar K, Ersoy N, Akkerman R, Hattel JH. A Review on the Mechanical Modeling of Composite Manufacturing Processes. *Arch Comput Methods Eng* 2016;24:365–95. doi:10.1007/s11831-016-9167-2.
- [196] Parlevliet PP, Bersee HEN, Beukers A. Residual stresses in thermoplastic composites - A study of the literature - Part I: Formation of residual stresses. *Compos Part A Appl Sci Manuf* 2006;37:1847–57.
- [197] Altmann A. Matrix dominated effects of defects on the mechanical properties of wind turbine blades. 2015.
- [198] Bhalerao M. On process-induced fiber waviness in composites: theory and experiments. The University of Texas at Austin, 1996.
- [199] KIUCHI T, TODOROKI A, MATSUZAKI R, MIZUTANI Y. Fiber-Waviness Model in Filament Winding Process. *Trans Japan Soc Mech Eng Ser A TRANSACTIONS JAPAN Soc Mech Eng Ser A* 2017;75:243–50. doi:10.1299/kikaia.75.243.
- [200] Baker A, Dutton S, Kelly D. *Composite Materials for Aircraft Structures*, Second Edition. 2012. doi:10.2514/4.861680.
- [201] Kugler D, Moon TJ. The effects of Mandrel material and tow tension on defects and compressive strength of hoop-wound, on-line consolidated, composite rings. *Compos - Part A Appl Sci Manuf* 2002;33:861–76. doi:10.1016/S1359-835X(02)00018-0.
- [202] Eduljee RF, Gillespie JW. Elastic response of post- and in situ consolidated laminated cylinders. *Compos Part A* 1996;27:437–46.
- [203] Rudd CD, Turner MR, Long AC, Middleton V. Tow placement studies for liquid composite moulding. *Compos Part A Appl Sci Manuf* 1999;30:1105–21. doi:10.1016/S1359-835X(99)00010-X.
- [204] Calius EP, Springer GS. A model of filament-wound thin cylinders. *Int J Solids Struct* 1990;26:271–97. doi:10.1016/0020-7683(90)90041-S.
- [205] Lee SY, Springer GS. *Filament Winding Cylinders: III. Selection of the Process*

- Variables. *J Compos Mater* 1990;24:1270–98. doi:10.1177/002199839002401204.
- [206] Gillham JK. Formation and properties of thermosetting and high tg polymeric materials. *Makromol Chemie Macromol Symp* 1987. doi:10.1002/masy.19870070108.
- [207] Svanberg JM, Holmberg JA. An experimental investigation on mechanisms for manufacturing induced shape distortions in homogeneous and balanced laminates. *Compos - Part A Appl Sci Manuf* 2001;32:827–38. doi:10.1016/S1359-835X(00)00173-1.
- [208] Wisnom MR, Gigliotti M, Ersoy N, Campbell M, Potter KD. Mechanisms generating residual stresses and distortion during manufacture of polymer-matrix composite structures. *Compos Part A Appl Sci Manuf* 2006;37:522–9. doi:10.1016/j.compositesa.2005.05.019.
- [209] Bogetti TA, Gillespie JW. Process-Induced Stress and Deformation in Thick-Section Thermoset Composite Laminates. *J Compos Mater* 1992;26:626–60. doi:10.1177/002199839202600502.
- [210] Coogler K, Harries KA, Wan B, Rizos DC, Petrou MF. Critical evaluation of strain measurements in glass fiber-reinforced polymer bridge decks. *J Bridg Eng* 2005. doi:10.1061/(ASCE)1084-0702(2005)10:6(704).
- [211] Sebastian WM. Fibre waviness in pultruded bridge deck profiles: Geometric characterisation and consequences on ultimate behaviour. *Compos Part B Eng* 2018;146:270–80. doi:10.1016/j.compositesb.2018.03.042.
- [212] Turvey GJ, Zhang Y. Characterisation of the rotational stiffness and strength of web-flange junctions of pultruded GRP WF-sections via web bending tests. *Compos Part A Appl Sci Manuf* 2006;37:152–64. doi:10.1016/j.compositesa.2005.04.022.
- [213] Sebastian WM, Keller T, Ross J. Influences of polymer concrete surfacing and localised load distribution on behaviour up to failure of an orthotropic FRP bridge deck. *Compos Part B Eng* 2013;45:1234–50. doi:10.1016/j.compositesb.2012.07.050.
- [214] Feo L, Mosallam AS, Penna R. Mechanical behavior of web-flange junctions of thin-walled pultruded I-profiles: An experimental and numerical evaluation. *Compos Part B Eng* 2013;48:18–39. doi:10.1016/j.compositesb.2012.11.001.
- [215] Yanes-Armas S, de Castro J, Keller T. Energy dissipation and recovery in web-flange junctions of pultruded GFRP decks. *Compos Struct* 2016;148:168–80. doi:10.1016/j.compstruct.2016.03.042.
- [216] Yanes-Armas S, de Castro J, Keller T. System transverse in-plane shear stiffness of pultruded GFRP bridge decks. *Eng Struct* 2016;107:34–46. doi:10.1016/j.engstruct.2015.11.003.
- [217] Kuo CM, Takahashi K, Chou TW. Effect of Fiber Waviness on the Nonlinear Elastic Behavior of Flexible Composites. *J Compos Mater* 1988;22:1004–25. doi:10.1177/002199838802201101.
- [218] Camanho PP, Dávila CG, Pinho ST, Iannucci L, Robinson P. Prediction of in

situ strengths and matrix cracking in composites under transverse tension and in-plane shear. *Compos Part A Appl Sci Manuf* 2006;37:165–76. doi:10.1016/j.compositesa.2005.04.023.

- [219] Hinterhölzl RM, Haller H, Luger M, Klar R. Strategy for a simulation based assessment of effects of manufacturing process induced fiber deflections on the structural behavior of a thick walled composite part. *Proc 5th Int Conf “Supply Wings” Airtech* 2010.
- [220] Kastner J, Plank B, Kottler C, Revol V. Comparison of phase contrast X-ray computed tomography methods for non-destructive testing of materials. *Proc. 18th World Conf. Non-Destructive Test., Durban: 2012.*
- [221] Kastner J, Heinzl C. X-Ray Tomography. In: Ida N, Meyendorf N, editors. *Handb. Adv. Non-Destructive Eval., Springer International Publishing; 2019, p. 1–72.*
- [222] Gusenbauer C, Reiter M, Salaberger D, Plank B, Kastner J, Wels C. High-resolution X-ray computed tomography of inhomogeneous materials. *Proc. 12th Eur. Conf. Non-destructive Test., Gothenburg, Sweden: 2018, p. 1–8.*
- [223] Smith R. Composite Defects and Their Detection. *Mater Sci Eng* 1997;III:14.
- [224] Michaels TE, Davidson BD. Ultrasonic inspection detects hidden damage in composites. *Adv Mater Process* 1993;143:34–8.
- [225] Maldague XP V. *Nondestructive Evaluation of Materials by Infrared Thermography.* London: Springer-Verlag; 1993. doi:10.1007/978-1-4471-1995-1.
- [226] Maldague XP. *Theory and Practice of Infrared Technology for Nondestructive Testing.* New York: Wiley; 2001.
- [227] Meola C, Carlomagno GM. Recent advances in the use of infrared thermography. *Meas Sci Technol* 2004;15:R27–58. doi:10.1088/0957-0233/15/9/R01.
- [228] Pohl J. *Active Thermographic Testing of CFRP with Ultrasonic and Flash Light Activation* 2016:1–10.
- [229] Busse G, Wu D, Karpen W. Thermal wave imaging with phase sensitive modulated thermography. *J Appl Phys* 1992;71:3962–3965. doi:10.1063/1.351366.
- [230] Hendorfer G, Mayr G, Zauner G, Haslhofer M, Pree R. Quantitative determination of porosity by active thermography. *AIP Conf Proc* 2006;26A:702–8. doi:10.1063/1.2718039.
- [231] Shepard SM. *Temporal Noise Reduction, Compression and Analysis of Thermographic Image Data Sequence.* US Patent (6,516,084), 2000.
- [232] Chen YS, Hung YY, Ng SP, Huang YH, Liu L. Review and comparison of shearography and active thermography for nondestructive testing and evaluation (NDT&E). *ICEM 2008 Int Conf Exp Mech* 2008 2008;7375:73754W. doi:10.1117/12.839322.
- [233] Hung YY, Ho HP. Shearography: An optical measurement technique and applications. *Mater Sci Eng R Reports* 2005;49:61–87.

- doi:10.1016/j.mser.2005.04.001.
- [234] Thor M, Sause MGR, Hinterhölzl RM. Mechanisms of Origin and Classification of Out-of-Plane Fiber Waviness in Composite Materials — A Review. *J Compos Sci* 2020;4:1–39. doi:10.3390/jcs4030130.
- [235] Hexcel Corporation. Data Sheet HexPly 8552. 2016.
- [236] Mayr G, Pöchacker S, Gresslehner K-H, Hendorfer G. Transient Measurement of Anisotropic Thermal Diffusivity of CFRP-Multilayer with Pulsed Thermography, 2016, p. 1.
- [237] Maldague XPV, Moore PO. *Nondestructive Testing Handbook: Infrared and Thermal Testing*. Third Edit. Columbus: American Society for Nondestructive Testing; 2001.
- [238] Camanho PP, Maimí P, Dávila CG. Prediction of size effects in notched laminates using continuum damage mechanics. *Compos Sci Technol* 2007. doi:10.1016/j.compscitech.2007.02.005.
- [239] Li Y, Zhang W, Yang Z-W, Zhang J-Y, Tao S-J. Low-velocity impact damage characterization of carbon fiber reinforced polymer (CFRP) using infrared thermography. *Infrared Phys Technol* 2016;91–102. doi:10.1016/j.infrared.2016.01.019.
- [240] Thérroux L-D, Dumoulin J, Maladague X. Square Heating Applied to Shearography and Active Infrared Thermography Measurements Coupling: From Feasibility Test in Laboratory to Numerical Study of Pultruded CFRP Plates Glued on Concrete Specimen. *Strain* 2014;404–16. doi:10.1111/str.12086.
- [241] Stotter B, Stockner G, Gresslehner K-H, Hendorfer G. Development of a method for scanning component inspections using active thermography, 2013, p. 33.
- [242] Garnich MR, Karami G. Finite element micromechanics for stiffness and strength of wavy fiber composites. *J Compos Mater* 2004;38:273–92. doi:10.1177/0021998304039270.
- [243] Shen C-H, Springer GS. Moisture Absorption and Desorption of Composite Materials. *J Compos Mater* 1975;10:2–20.
- [244] Arnold JC. 6.10 - Environmental Effects on Crack Growth in Composites. *Compr. Struct. Integr.*, 2007. doi:10.1016/B978-008043749-1/00318-8.
- [245] Sala G. Composite degradation due to fluid absorption. *Compos Part B Eng* 2000;31:357–73. doi:10.1016/S1359-8368(00)00025-1.
- [246] US Department of Defense. MIL-HDBK-17-1F: Composite Materials Handbook Volume 1: Polymer Matrix Composites - Guidelines for Characterisation of Structural Materials. *Compos Mater Handb Ser* 2002;1:1–586.
- [247] Thomason JL. The interface region in glass fibre-reinforced epoxy resin composites: 2. Water absorption, voids and the interface. *Composites* 1995;26:477–85. doi:10.1016/0010-4361(95)96805-G.
- [248] Botelho EC, Pardini LC, Rezende MC. Hygrothermal effects on the shear properties of carbon fiber/epoxy composites. *J Mater Sci* 2006;41:7111–8.

doi:10.1007/s10853-006-0933-7.

- [249] Grammatikos SA, Zafari B, Evernden MC, Mottram JT, Mitchels JM. Moisture uptake characteristics of a pultruded fibre reinforced polymer flat sheet subjected to hot/wet aging. *Polym Degrad Stab* 2015;121:407–19. doi:10.1016/j.polymdegradstab.2015.10.001.
- [250] Revathi A, Sendil M, Shylaja S, Jagannathan N, Manjunatha C. Effect of Hot-Wet Conditioning on the Mechanical and Thermal Properties of IM7/ 8552 Carbon Fiber Composite. *Indian J Adv Chem Sci* 2014;2:84–8.
- [251] Ryan JM, Adams R, Brown SGR. Moisture Ingress Effect on Properties of CFRP. *ICCM 17* 2009.
- [252] De'Nève B, Shanahan MER. Water absorption by an epoxy resin and its effect on the mechanical properties and infra-red spectra. *Polymer (Guildf)* 1993. doi:10.1016/0032-3861(93)90254-8.
- [253] ASTM D5229-2004. ASTM D 5229– 92 – Standard Test Method for Moisture Absorption Properties and Equilibrium Conditioning of Polymer Matrix Composite Materials. *Annu B ASTM Stand* 2010. doi:10.1520/D5229.
- [254] Stelzer R, Friedrich K. Mechanical properties and failure behaviour of carbon fibre-reinforced polymer composites under the influence of moisture. *Compos Part A Appl Sci Manuf* 1997;28:595–604. doi:10.1016/S1359-835X(96)00154-6.
- [255] Costa ML, De Almeida SFM, Rezende MC. Hygrothermal effects on dynamic mechanical analysis and fracture behavior of polymeric composites. *Mater Res* 2005;8:335–40. doi:10.1590/S1516-14392005000300019.
- [256] Khan LA, Nesbitt A, Day RJ. Hygrothermal degradation of 977-2A carbon/epoxy composite laminates cured in autoclave and Quickstep. *Compos Part A Appl Sci Manuf* 2010;41:942–53. doi:10.1016/j.compositesa.2010.03.003.
- [257] Adamow KM. Einfluss von Wasser auf die Kohlenstofffaser / Epoxid-Polymermatrix Wechselwirkung. University of Bremen, 2014.
- [258] Dhakal HN, Zhang ZY, Richardson MOW. Effect of water absorption on the mechanical properties of hemp fibre reinforced unsaturated polyester composites. *Compos Sci Technol* 2007;67:1674–83. doi:10.1016/j.compscitech.2006.06.019.
- [259] Dardon H, Fukuda H, Reifsnider KL, Verchery G. Recent Developments in Durability Analysis of Composite Systems. Taylor & Francis; 2000.
- [260] Bucinell RB, on High Modulus Fibers ACD-30, Composites T, on Fatigue ACE-8, Fracture. *Composite Materials: Fatigue and Fracture*. Seventh volume. ASTM; 1998.
- [261] Zhou JM, Lucas JP. Hygrothermal effects of epoxy resin. Part I: the nature of water in epoxy. *Polymer (Guildf)* 1999;40:5505–12.
- [262] Apicella A, Nicolais L. Effect of water on the properties of epoxy matrix and composite. *Epoxy Resins Compos. I*, Berlin, Heidelberg: Springer Berlin Heidelberg; 1985, p. 69–77.
- [263] Grave C, McEwan I, Pethrick RA. Influence of Stoichiometric Ratio on Water

- Absorption in Epoxy Resins. Proceedings, Annu Conf - Can Soc Civ Eng 1998;69:2369–76.
- [264] Nogueira P, Ramírez C, Torres A, Abad MJ, Cano J, López J, et al. Effect of water sorption on the structure and mechanical properties of an epoxy resin system. *J Appl Polym Sci* 2001;80:71–80. doi:10.1002/1097-4628(20010404)80:1<71::AID-APP1077>3.0.CO;2-H.
- [265] Musto P, Ragosta G, Mascia L. Vibrational spectroscopy evidence for the dual nature of water sorbed into epoxy resins. *Chem Mater* 2000;12:1331–41. doi:10.1021/cm9906809.
- [266] Weir MD, Bastide C, Sung CSP. Characterization of interaction of water in epoxy by UV reflection spectroscopy. *Macromolecules* 2001;34:4923–6. doi:10.1021/ma0017900.
- [267] Xie Y, Hill CAS, Xiao Z, Militz H, Mai C. Silane coupling agents used for natural fiber/polymer composites: A review. *Compos Part A Appl Sci Manuf* 2010;41:806–19. doi:10.1016/j.compositesa.2010.03.005.
- [268] Chin JW, Aouadi K, Haight MR, Hughes WL, Nguyen T. Effects of water, salt solution and simulated concrete pore solution on the properties of composite matrix resins used in civil engineering applications. *Polym Compos* 2001;22:282–97. doi:10.1002/pc.10538.
- [269] Hughes JDH. The carbon fibre/epoxy interface-A review. *Compos Sci Technol* 1991;41:13–45. doi:10.1016/0266-3538(91)90050-Y.
- [270] Wu L, Hoa S V., Minh-Tan, Ton-That. Effects of composition of hardener on the curing and aging for an epoxy resin system. *J Appl Polym Sci* 2006;99:580–8. doi:10.1002/app.22493.
- [271] Desailoud M, Schmid-Fuertes T, Temmen H. Manufacturing defect knock down factor for composite parts - Exportable Version. Airbus Tech Rep V029RP1035199_EXP 2016:1–132.
- [272] Takeda T. Micromechanics model for three-dimensional effective elastic properties of composite laminates with ply wrinkles. *Compos Struct* 2018;189:419–27. doi:10.1016/j.compstruct.2017.10.086.
- [273] Sun CT, Chen JL. A Simple Flow Rule for Characterizing Nonlinear Behavior of Fiber Composites. *J Compos Mater* 1989. doi:10.1177/002199838902301004.
- [274] Coleman BD, Gurtin ME. Thermodynamics with internal state variables. *J Chem Phys* 1967. doi:10.1063/1.1711937.
- [275] Maimí P, Camanho PP, Mayugo JA, Dávila CG. A continuum damage model for composite laminates: Part II – Computational implementation and validation. *Mech Mater* 2007;39:909–19. doi:10.1016/j.mechmat.2007.03.006.
- [276] Dassault Systèmes Simulia Corp. Abaqus Analysis User's Guide, Version 2017. Providence, USA: 2017.
- [277] Körber H. Mechanical response of advanced composites under high strain rates. University of Porto, 2010.
- [278] Mandel U, Taubert R, Hinterhölzl R. Mechanism based nonlinear constitutive

- model for composite laminates subjected to large deformations. *Compos Struct* 2015;132:98–108. doi:10.1016/j.compstruct.2015.04.029.
- [279] Puck A, Kopp J, Knops M. Guidelines for the determination of the parameters in Puck's action plane strength criterion. *Compos Sci Technol* 2002. doi:10.1016/S0266-3538(01)00202-0.
- [280] Mandel U, Taubert R, Hinterhölzl R. Laminate damage model for composite structures. *Compos Struct* 2016;136:441–9. doi:10.1016/j.compstruct.2015.10.032.
- [281] Mandel U. Mechanism Based Constitutive Model for Composite Laminates. Technical University of Munich, 2016.
- [282] Sun CT, Chung I. An oblique end-tab design for testing off-axis composite specimens. *Composites* 1993;24:614–23. doi:10.1016/0010-4361(93)90124-Q.
- [283] Daniel IM, Ishai O. Engineering mechanics of composite materials. *Mech Compos Mater* 1994:881–6. doi:10.1016/B978-0-08-006421-5.50049-6.